

Mineralized Bionanoparticle Pickering Emulsions

DISSERTATION

zur Erlangung des akademischen Grades eines
Doktors der Naturwissenschaften (Dr. rer. nat.)
im Fach Chemie der Fakultät für Biologie, Chemie und
Geowissenschaften
der Universität Bayreuth

vorgelegt von
Günther Jutz
geboren in Memmingen

Bayreuth, 2008

Vollständiger Abdruck der von der Fakultät für Biologie, Chemie und Geowissenschaften der Universität Bayreuth genehmigten Dissertation zur Erlangung des akademischen Grades eines Doktors der Naturwissenschaften (Dr. rer. nat.).

Die vorliegende Arbeit wurde in der Zeit von Januar 2005 bis Juli 2008 am Lehrstuhl für Physikalische Chemie der Universität Bayreuth in der Arbeitsgruppe von Herrn Prof. Dr. Alexander Böker (Lichtenberg-Professur der VolkswagenStiftung) angefertigt.

Promotionsgesuch eingereicht am: 16.07.2008

Zulassung durch die Promotionskommission: 23.07.2008

Wissenschaftliches Kolloquium: 18.12.2008

Amtierender Dekan: Prof. Dr. Müller

Prüfungsausschuß:

Prof. Dr. A. Böker (Erstgutachter)

Prof. Dr. A. H. E. Müller (Zweitgutachter)

Prof. Dr. J. Breu (Vorsitzender)

Prof. Dr. Th. Scheibel

Table of Content

Table of Content	I
List of Abbreviations	V
Table of Symbols	VII
1 Introduction.....	1
1.1 Biomolecules for New Materials and Device Fabrication.....	1
1.1.1 Development of Nanostructured Materials.....	1
1.1.2 Self-Assembling Protein Materials for Nano- and Biotechnology.....	2
1.1.2.1 Viruses as Polyvalent Scaffolds.....	4
1.1.2.2 Protein Cages as Templates for Constrained Nanomaterials Synthesis	6
1.1.2.3 Protein Cages as Scaffolds and Templates for Materials Synthesis	7
1.1.2.4 Surface Patterning with Self-Assembled Bionanoparticles	7
1.2 Pickering Emulsions and Protein Adsorption at liquid-liquid Interfaces	9
1.2.1 Pickering Emulsions	9
1.2.2 Protein Adsorption at liquid-liquid Interfaces	13
1.2.3 Quantitative Modelling of Protein Adsorption at liquid-liquid Interfaces	13
1.2.3.1 Surface Tension of Protein Solutions	14
1.2.3.2 The Concept of Varying Partial Molar Areas of Adsorbed Proteins ²¹⁸	16
1.2.3.3 Modelling of Protein Adsorption at liquid Interfaces.....	18
1.3 Bio-Inorganic Composite Materials.....	21
1.3.1 Biominerals in Nature.....	21
1.3.2 Biomimetic Bone Tissues	23
1.4 Hydroxy Apatite Coating in a Biomimetic Process.....	26
1.5 Bionanoparticles: Plant Viruses, Ferritin and Proteins.....	29
1.5.1 Plant Viruses	29
1.5.1.1 Cowpea mosaic virus (CPMV) ²⁹¹⁻²⁹⁵	29
1.5.1.2 Turnip Yellow Mosaic Virus (TYMV) ³⁰⁰⁻³⁰⁵	30
1.5.1.3 Tobacco Mosaic Virus (TMV) ³⁰⁸⁻³¹⁰	32
1.5.2 Ferritin	33
1.5.3 Bovine/Human Serum Albumin (BSA/HSA) ³³⁰⁻³³²	35
1.5.4 α_2 -Heremans-Schmid glycoprotein (Ahsg)/fetuin-A ³³⁴	36
1.5.5 Physical Properties of Bionanoparticles	37
1.6 Outline and Relevance of the Presented Research Work	39
2 Theoretical Background and Methods.....	43
2.1 Modelling Protein Adsorption at liquid-liquid Interfaces.....	43
2.1.1 Quantitative Description of Equilibrium Surface Tension of Protein Solutions ²⁰³	43
2.1.1.1 Adsorption at Low Protein Concentrations	43
2.1.1.2 Adsorption at High Protein Concentrations.....	47
2.1.2 Quantitative Description of Dynamic Surface Tensions	48
2.1.3 Approximate Solutions for Dynamic Surface Tensions ³⁷⁹	51
2.1.4 Depletion of Droplets.....	53
2.2 Determination of Interfacial Tension by Axisymmetric Drop Shape Analysis	54
2.3 Light Scattering Techniques	58

2.3.1	Static Light Scattering ⁴⁰⁷	58
2.3.2	Dynamic Light Scattering ^{410, 411}	61
2.4	Size Exclusion Chromatography	64
2.5	Transmission Electron Microscopy	68
2.6	Scanning Electron Microscopy	70
2.7	Atomic Force Microscopy (AFM)	74
2.8	UV-Vis Spectroscopy	77
3	Experimental Section	79
3.1	Chemicals	79
3.2	Virus Preparation	80
3.3	Conjugation Reactions to CPMV	81
3.4	Preparation of Pickering Emulsions	81
3.5	Preparation of glass A	82
3.6	Preparation of SBF	82
3.7	Preparation of Supersaturated Calcium Phosphate Solution Containing Citrate (Ca/P/cit)	84
3.8	Profile Analysis Tensiometry	84
3.9	Size Exclusion Chromatography	85
3.10	Dynamic Light Scattering	86
3.11	UV-Vis Spectroscopy	87
3.12	SDS-Polyacrylamide Gel Electrophoresis (SDS-PAGE)	87
3.13	MALDI-TOF Mass Spectrometry	88
3.14	Confocal Fluorescence Laser Scanning Microscopy	88
3.15	Transmission Electron Microscopy and Sample Preparation	89
3.16	Scanning Electron Microscopy and Sample Preparation	89
3.17	Atomic Force Microscopy	90
3.18	X-ray Diffraction	90
3.19	Further Instruments	90
4	Characterization of Viruses	91
4.1	Characterization of Viruses and Proteins with Aqueous SEC and Light Scattering Detection	91
4.2	Characterization of Viruses and Proteins with Dynamic Light Scattering	95
4.3	Bionanoparticle Characterization with SDS-PAGE	100
4.4	Bionanoparticle Characterization with Transmission Electron Microscopy	102
4.5	Dye-labelled Cowpea Mosaic Virus	107
5	Protein Adsorption at liquid-liquid Interfaces	111
5.1	Surface Tension Measurements of Proteins at liquid-liquid Interfaces	111
5.2	Modelling of Protein Surface Pressure Isotherms	117
5.3	Modelling Dynamic Interfacial Tension Curves of Proteins	123
5.4	Bionanoparticle Adsorption at liquid-liquid Interfaces	127
6	Investigation of Bionanoparticle Assemblies at Interfaces	133
6.1	Bionanoparticles at liquid-liquid Interfaces	133
6.2	Bionanoparticle Membranes	135
6.3	Bionanoparticles Trapped at PDMS-Surfaces	138
6.3.1	Investigation of the Surface Structure with SEM	138
6.3.2	Investigation of the Surface Structure with AFM	141
6.3.3	Fluorescence Microscopy of Antibody-Labelled Bionanoparticle Pickering Emulsions	147
7	Hydroxy Apatite Mineralization at Surfaces and Interfaces	149

7.1	Hydroxy Apatite Formation on PET in a Biomimetic Process.....	150
7.1.1	Preparation and Characterization of Bioactive Glass A	150
7.1.2	Hydroxy Apatite Formation on Surfaces in SBF Solution	152
7.1.3	Hydroxy Apatite Formation on PET in SBF	153
7.2	Hydroxy Apatite Formation on PET in 1.5 SBF with Citrate	157
7.3	Hydroxy Apatite Formation on PET in an Oversaturated Calcium Phosphate Solution	160
7.4	Mineralization of Bionanoparticle Coated Surfaces.....	164
7.4.1	Biomimetic Hydroxy Apatite Mineralization of Bionanoparticle- Coated Surfaces.....	166
7.4.2	Hydroxy Apatite Mineralization of Bionanoparticle Coated Surfaces in 1.5 SBF with Citrate.....	170
7.4.3	Hydroxy Apatite Mineralization of Bionanoparticle Coated Surfaces in an Oversaturated Calcium Phosphate Solution.....	171
7.5	Investigation of the Hydroxy Apatite Mineral Layer	173
7.6	Comparison of Mineralization Conditions	176
7.7	Mineralization of Pickering Emulsions	178
8	Summary.....	187
9	Zusammenfassung.....	189
	References.....	191

List of Abbreviations

AFM	atomic force microscopy
ATRP	atom transfer radical polymerization
BSA	bovine serum albumin
BSE	back scattered electrons
CCMV	cowpea chlorotic mottle virus
cDNA	complementary DNA
CP	coat protein
CPMV	cowpea mosaic virus
cryo-TEM	cryo-transmission electron microscopy
DLS	dynamic light scattering
DDLS	depolarized dynamic light scattering
DMSO	dimethyl sulfoxide
DNA	deoxyribonucleic acid
EDX	energy dispersive X-ray analysis
FPLC	fast protein liquid chromatography
FRET	fluorescence resonance energy transfer
HAP	hydroxy apatite
HSA	human serum albumin
LS	light scattering
MALDI-TOF MS	matrix-assisted laser desorption ionization time-of-flight mass spectrometry
MAP	multiple antigene peptide
NHS	<i>N</i> -hydroxy succinimide
MW	molecular weight
NMR	nuclear magnetic resonance
ORF	open reading frame
PDMS	poly(dimethyl siloxane)
PEG	poly(ethylene glycol)
PET	poly(ethylene terephthalate)
pH	negative common logarithm of proton concentration ($-\lg[\text{H}^+]$)
pI	isoelectric point

PMMA	poly(methyl methacrylate)
PTFE	poly(tetrafluoro ethylene)
RdRp	RNA dependent RNA polymerase
RI	refractive index
rms	root means square
RNA	ribonucleic acid
rpm	rounds per minute
SBF	simulated body fluid
SDS-PAGE	sodium dodecylsulphate polyacrylamide gel electrophoresis
SE	secondary electrons
SEC	size exclusion chromatography
SEM	scanning electron microscopy
sgRNA	subgenomic RNA
SLS	static light scattering
ssRNA	single stranded RNA
STM	scanning tunnelling microscopy
TCEP	tris (2-carboxyethyl) phosphine hydrochloride
TEM	transmission electron microscopy
TMV	tobacco mosaic virus
tris	2-amino-2-hydroxymethyl propane 1,3-diol
tRNA	transfer ribonucleic acid
TYMV	turnip yellow mosaic virus
UV-Vis	ultraviolet-visible
wt%	weight percent
XRD	X-ray diffraction

The mineralization solutions are abbreviated for easier reading. Please refer to the indicated chapters for the details of the solution composition:

1.0 SBF, 1.5 SBF, 1.5 SBF/cit	chapter 3.6
Ca/P/cit	chapter 3.7

Table of Symbols

Symbols that are generally used and not explained with the equations (numerical values from ref.¹):

T	absolute temperature [K]
R	molar gas constant: $8.314510 \text{ Jmol}^{-1}\text{K}^{-1}$
N_A	Avogadro constant: $6.0221367 \cdot 10^{23} \text{ mol}^{-1}$
k_B	Boltzmann constant: $1.380658 \cdot 10^{-23} \text{ JK}^{-1}$
g	gravitational acceleration $9.80665 \text{ m}^{\text{s}^{-2}}$

1 Introduction

1.1 Biomolecules for New Materials and Device Fabrication

1.1.1 Development of Nanostructured Materials

Miniaturization towards nanoscale materials and devices is one of the leading trends in science and research and development in this century. The production of nanoscale materials and the characterization of nanostructures by real-space imaging techniques have significantly advanced during the last two decades. Electron microscopy techniques were developed more than 70 years ago but the pivotal milestone in nanoscience was the development of the scanning tunnelling microscope (STM)² and of the atomic force microscope (AFM)³. Nanochemistry had its breakthrough with the development of facile solution syntheses of nanoparticles. Early achievements were the synthesis of monodispersed gold^{4, 5} and cadmium selenide nanoparticles⁶.

The development of lithographic techniques paralleled the development of electronic parts for computers. The generation of small structures was traditionally a top-down process: The application of masks, illumination and etching steps generated the desired structures on an initially unpatterned material. The use of electromagnetic radiation (mostly ultraviolet light) implies the well-known “diffraction limit”. Structures below the wavelength of the used light are not feasible, though smaller structures can be generated with some experimental effort or the use of other radiation sources (electron beams, synchrotron radiation, X-ray...).⁷ Nevertheless, lithography is connected with intrinsic limitations and despite recent success⁸ a radical change in chip making technology and nanofabrication will be inevitable in order to keep the current speed of development.⁷

In this moment, bottom-up approaches, i. e. the generation of complex nanoscale patterns which start from nanoscaled building blocks come into play. By now, the synthesis of nanoparticles reached astonishing levels: A multitude of materials, ranging from inorganic to polymeric nanoparticles or biological building blocks with many different electronic, magnetic and optical properties have been synthesized and

characterized in great detail. The pivotal point is now the directed or self-assembly of the nanoparticles to arbitrarily defined structures. Such structures can be used in high-resolution soft lithography to make next-generation nanodevices.⁷ A typical example for the different approaches are electronics: while classical semiconductor-based electronics are based on top-down processes, the field of (bio-) nanoelectronics followed a bottom-up approach when it emerged from molecular understanding of biochemical signal transduction and engineering and interfacing of single molecules.⁹

Progress in nanotechnology is aiming at miniaturization and is accompanied by an increased complexity. This is not just a matter of geometrical structuration but also a matter of specific functionalities that are positioned at discrete locations and defined distances. Nature sets the benchmark for functional structures down to atomic scales. The machinery of life with its highly precise working mechanisms is the yet unreached model for any man-made machine. Proteins with a simple set of 20 amino acid building blocks but yet highly complex three-dimensional structures are a class of biomaterials that is now quite well understood. They can be obtained in fairly large amounts after extraction and purification from biological sources as well as by various synthetic strategies in the laboratory. DNA or RNA in various forms is the code that predetermines all materials and functions of living systems. In the last two decades trailblazing developments led to tools for analysis and synthesis of this class of biopolymers. The use of biomolecules is considered as an evident step in the synthesis and construction of next generation nanomaterials and devices.¹⁰ A whole new branch termed bionanotechnology seeks for scientific as well as economic breakthroughs in the development of bio-inorganic nanomaterials with novel properties for computation and nanotechnology, new methods in diagnosis and analytics, devices or new drugs and drug delivery systems.^{11, 12}

1.1.2 Self-Assembling Protein Materials for Nano- and Biotechnology

The complexity of biomolecules makes them interesting materials for the development of novel nanodevices. Self-assembled protein complexes, protein cage systems and particularly ferritin and plant viruses have been extensively used in the last few years as

building blocks and templates in nanochemistry and molecular biology.^{13, 14} They are robust assemblies and can be obtained from biological sources or through *in vitro* expression and self-assembly.

Proteins and biological scaffolds have - unlike most synthetic polymers - a more or less fixed three-dimensional conformation through covalent bonds or non-covalent interactions. This structural rigidity and the highly functional surface of proteins drive self-assembly of protein subunits in solution to oligomeric filamentous, cage-like or tubular structures and to regular patterns on various surfaces and interfaces.¹⁵ Symmetry plays an important role in that process.¹⁵ Binding sites and functional groups on such self-assembled layers are held at precisely defined orientations. While protein crystals are rare *in vivo*, many examples of symmetric protein complexes have been found and characterized with the advance of electron microscopy and X-ray crystallography. The helical symmetry in tobacco mosaic virus was found¹⁶ and the cubic symmetry of spherical viruses proposed¹⁷ as early as 1955/56 and the structure of many viruses is known today in great detail.¹⁸ The quasi-equivalent assembly of protein subunits in icosahedral virus capsids is a particularly early recognized and well investigated example of protein assembly.^{19, 20} Exploiting these principles, folded protein structures have been constructed by rational design. Nanotubes²¹, filaments²² and cages²³ have been created through self-assembly. Bacterial surface layers (termed S-layers) are prominent examples of ordered two-dimensional arrays of natural proteins at interfaces.²⁴

The outer surface of proteins and protein cages has been employed as polyvalent scaffolds similarly to dendrimers or multiple antigenic peptides (MAPs). Such modified protein materials have been used e. g. as vaccines. The interior cavity has been utilized as size-constrained reaction vessel for the production of nanomaterials. The well-defined and monodisperse nature of biomolecules yields a useful scaffold for the production of composite bioinorganic nanoparticles. Besides site-specific chemical reactions, biomolecules can be produced under genetic control which allows ultimate control of structure and constitutes a major advantage.²⁵ The next paragraphs give a short overview of recent developments in bionanoscience and -technology related to the materials and principles that have been employed in this work.

1.1.2.1 Viruses as Polyvalent Scaffolds

Polyvalent scaffolds that display the respective antibodies are a central topic in the development of modern artificial vaccines. Display of as many as possible antigens on a scaffold is necessary to elicit efficient immune response.^{26, 27} The laborious syntheses of well-defined peptide dendrimers led to the development of multiple antigenic peptides (MAPs).^{28, 29} The distances in dendrimers are basically defined by steric or electrostatic repulsion. However, it was shown that defined structural constraints are important for immunogenicity of heterologous displayed peptides.³⁰ In protein complexes, binding sites and functional groups are held at defined orientations. Virus-like particles proved to be an ideal polyvalent platform with rigid conformation.³¹ The strong immunogenic properties of virus-like particles made them a promising candidate for novel vaccines.^{32, 33} If pathological sequences from the genetic material of a virus are deleted, delivery and transient or permanent expression of foreign genes (viral therapy) can be envisaged to overcome malfunctioning of the body.^{34, 35} Cowpea mosaic viruses (CPMV) that had been genetically engineered to express heterologous short peptide sequences (epitopes) on their surface lead to stronger immunogenic response than the single antigen. As there have not been any reports about the pathogenic nature of plant viruses to mammals, CPMV might be therefore a potent candidate for the development of epitope-based vaccines.^{36, 37} The large channels in CPMV crystals allow adaption to inserted loops and bound antibodies and a precise crystallographic characterization.^{37, 38} Presentation of antigens in bacterial viruses (phage display technology)^{39, 40} and other display type libraries revolutionized screening processes in polypeptide research^{41, 42} and immunology⁴³.

Recently, the topological analogy of plant viruses to dendrimers has been exploited in a number of organic reactions.^{44, 45} Many researchers made use of the unique dendrimer-like polyvalent properties of the protein capsid for the synthesis of monodisperse and highly functional bionanoparticles. The close proximity of different labels was shown by fluorescence resonance energy transfer (FRET) of differently introduced fluorescein and rhodamine dyes.⁴⁶ The advantage of viruses over dendrimers is that their structure is defined and known to atomic resolution.

A vast literature emerged from the first report on using cowpea mosaic virus particles as addressable nanoscale building blocks.⁴⁷⁻⁴⁹ Besides carboxylic groups,⁵⁰ especially uniquely addressable amino-groups from lysine residues have been used in conjugation reactions on the CPMV capsid's exterior.^{48, 51} A maximum of four lysine residues per asymmetric unit can be addressed if the ratio of activated dye to protein is increased to 4000. Under less forcing conditions just one lysine residue (KS38) on the small subunit is labelled.^{52, 53} The number of attached dye molecules can be controlled through the excess amount of dye and the conjugation chemistry. A proper order allows the sequential addressing of functional groups. Interior sulfhydryl groups from cysteine residues on the small subunit can be addressed to a limited extent through maleimide coupling chemistry under forcing conditions.^{49, 53} Adjacent tyrosine residues could be oxidized leading to intersubunit crosslinking and oxidatively labelled with sulfhydryl compounds.⁵⁴ Genetic engineering allowed altering the displayed functional groups on the virus capsid and presenting different addressable groups.^{49, 51, 52, 54} Mutants with reactive cysteine moieties on protruding loops have been designed by genetic engineering. The location of mutation was verified after decoration with charge-stabilized gold nanoparticles^{51, 55} or monofunctional nanogold labels^{47, 49, 52, 56} and image reconstruction from cryo-TEM. Different binding sites in the capsid clearly led to different binding patterns. Limited stability of the virus in aqueous organic solvents (stability for up to 50 % DMSO in buffered solution as well as for pH = 3-9 for prolonged time at room temperature or at 60 °C for at least an hour has been reported) seems to be the only restriction for conjugation reactions. Via well established cross-linking chemistries⁵⁷ using either direct activation or bifunctional crosslinking agents many different labels as for example dyes,^{46-50, 52, 53} carbohydrates,⁴⁶ polymers,^{53, 58} nanoparticles,^{47, 49, 51, 52, 56} quantum dots,^{59, 60} antigens,^{46, 48, 49, 53} oligonucleotides,⁶¹ proteins and enzymes⁶² and other labels^{50, 60} have been introduced onto the virus capsid. A promising orthogonal method for conjugation reactions is click-chemistry.⁶³ By this method, dyes,^{44, 54} polymers,^{44, 64} proteins,⁴⁴ carbohydrates⁴⁴ and other labels have been introduced with high efficiency and excellent yields.

Recently, also turnip yellow mosaic virus (TYMV) has been employed as a polyvalent scaffold. Reactions with dyes under NHS-activation have been used to address lysine amino groups and carboxylic groups.⁶⁵ Characterization methods include agarose gel

electrophoresis of whole viruses,^{50, 55} UV-Vis, FPLC, SDS-PAGE analysis and MALDI-TOF MS of the whole and digested subunit, similarly to the investigations of reactions with CPMV.

Functionalization of the ferritin protein cage was performed to obtain particles with reversed overall charge (“cationic ferritin”)⁶⁶ and hydrophobic solution properties (“hydrophobic ferritin”)^{67, 68}. Chemoselective derivatization has been shown by Wang and coworkers by versatile click reaction and ATRP.^{69, 70} They found that four lysine amino groups per subunit are reactive but steric crowding prevents further reaction if one dye is attached to a subunit.

1.1.2.2 Protein Cages as Templates for Constrained Nanomaterials Synthesis

When the first crystal structure of ferritin was reported in 1991,⁷¹ Mann and Meldrum made use of the protein structure as a size-constrained reaction vessel.⁷² Since then, this approach has been exploited in many similar works^{73, 74} and was later expanded to plant viruses.⁷⁵⁻⁷⁷ The directed mineralization inside the capsid is prerequisite for the controlled synthesis of nanoscale materials without non-specific bulk precipitation. *In vivo*, the formation of the ferritin core is enzymatically controlled through ferroxidase. For non-ferroxidase substrates or mineralization of virus capsids which is not specifically protein-assisted, the spatial selectivity is controlled by charged nucleation sites at the protein interface.⁷³ Manganese,^{72, 78, 79} cobalt⁷³ and cadmium minerals⁸⁰ were synthesized inside the cage, ferrihydrite conversion to iron sulphide was also reported.⁷⁴ The entrapment of a molecular gadolinium-chelate complex led to materials with promising applications in NMR imaging.⁸¹ The potential of ferritin as photocatalyst is another interesting application of the mineral/protein complex.⁸² Besides apoferritin, viruses have been extensively used as cages or scaffolds for material synthesis.⁸³ Cowpea chlorotic mottle virus (CCMV) is one of the best characterized viruses and has been used in the synthesis of various encapsulated inorganic nanomaterials.⁷⁵⁻⁷⁷ A unique feature of CCMV is the pH- and metal-dependent gating/swelling property that can be utilized for the selective entrapment and release of material.^{76, 77} The reverse

process i. e. encapsidation of precursor nanoparticles with self-assembling virus coat proteins has been shown to be feasible, too.⁸⁴ Heat shock proteins and chaperones are another interesting class of protein assemblies with cage-like architectures.⁸⁵⁻⁸⁷

1.1.2.3 Protein Cages as Scaffolds and Templates for Materials Synthesis

Viruses can serve as building blocks or can be used as scaffold itself for the development of novel nanoscale materials. Of particular interest are one-dimensional conducting nanostructures that can be used to build nanoelectronic devices. The classical templates for filamental or rod-like structures are tobacco mosaic virus (TMV), phages or DNA. TMV has been employed as scaffold for the deposition of minerals and metal oxides,⁸⁸⁻⁹² metallic nanoparticles and coatings⁹³⁻⁹⁶ and conducting polymers⁹⁷⁻¹⁰⁰ to construct nanowires. Binding motives for different inorganic materials on phage coat proteins have been identified by screening of bacteriophage libraries.^{25, 101} The highly anisotropic shape allowed production of many new and interesting self-assembled hybrid materials.¹⁰² DNA has also been used to build nanowires.^{103, 104} DNA can be bound to surfaces through condensation of sticky ends which allowed the electrical characterization of single DNA-nanowires.^{105, 106} CPMV and other spherical viruses have been decorated with quantum dots^{51, 56, 107-109} and conjugated with carbon nanotubes¹⁰⁷ to construct bionanoparticle hybrids.

1.1.2.4 Surface Patterning with Self-Assembled Bionanoparticles

During the course of the Protein Array Project, the adsorption and manipulation of two-dimensional arrays of ferritin on various surfaces has been investigated in great detail.¹¹⁰⁻¹¹³ Ferritin was spread at the buffer-air interface and formed stable membranes after crosslinking that spanned large areas on a holey carbon film as seen in TEM.¹¹⁰ To obtain large crystalline areas, recombinant apoferritin devoid of the natural subunit inhomogeneity was frequently used.¹¹⁴ However, good results were also obtained from horse spleen ferritin that was assembled at the water-hexane interface.¹¹¹ The positively charged dehydroabietyl amine that was solved in the organic phase aided the formation

of regular protein arrays at the interface. After pick-up on a hydrophobically coated silicon wafer, ferritin arrays could be thermally treated to remove the protein shell and fix the iron oxide core on the substrate.¹¹⁵ Regular quantum dot arrays prepared from ferritin with various different mineral cores are suitable for application in nanoelectronics.^{116, 117} Liposomes have also been employed as matrix for the assembly of ferritin, by electrostatic or ligand-receptor interactions, and yielded fully biological structures.¹¹² Ferritin was also used in the wetting assisted preparation of two-dimensional nanoparticle arrays embedded in thin silica films.¹¹⁸ The possibility to fill the ferritin cavity with different inorganic materials makes it a versatile platform for nanoparticle arrays.

The adsorption of plant viruses and proteins in general is essentially governed by electrostatic interactions that are determined by the surface charge and the isoelectric point (pI) of the particle. At solution conditions above pI, viruses should adsorb strongly to positively charged surfaces and weakly on negatively charged surfaces; for solution conditions below pI the reverse should hold true. Functional nanoarrays have been achieved by the assembly of viruses through electrostatic adsorption¹¹⁹⁻¹²², covalent immobilization^{123, 124} and selective binding^{60, 125}. Soft polymer surfaces led to denser and more regular patterns than hard surfaces.¹²⁰

Self-assembled protein materials have been utilized in few applications. They are promising scaffolds for tissue engineering¹²⁶ and directed mineralization for bone formation¹²⁷. Many different applications have been disclosed for bacterial S-layers, e. g. to construct ultra-filtration membranes, vaccine adjuvants or as template for the preparation of regularly arranged nanoparticles and as interfaces for biosensor applications.^{128, 129}

1.2 Pickering Emulsions and Protein Adsorption at liquid-liquid Interfaces

Interfaces play an important role in many processes in nature and technology. Biological systems are compartmentalized by membranes and interact with the environment through recognition processes at these interfaces. In technology, processes at surfaces play an important role in catalysis, mining, food technology, hygiene and cleaning etc. In the context of nano- and nanobiotechnology recognition and sensing are important fields of interest.¹³⁰

Pickering emulsions are solid-stabilized emulsions.¹³¹ While they attracted considerable interest from nanotechnology research only recently, protein adsorption at liquid interfaces has been investigated for decades.¹³² A brief overview of both topics is given in the next two chapters. The typical methods for characterization of Pickering emulsions have been employed here as well for bionanoparticle Pickering emulsions, but the approach to modelling of the adsorption kinetics of proteins can be found in classical colloid chemistry.

1.2.1 Pickering Emulsions

The liquid-liquid interface has been recognized recently as template for the self-assembly of solid particles, however, Pickering emulsions are known for almost a hundred years.^{133, 134} Conventional emulsions, i. e. dispersions of oil-in-water or reverse, are stabilized by surfactants or polymers. The physics and chemistry of these systems have formed the large and strong branch of colloid science. Although dispersions stabilized by solid particles have significant technological implications, few aspects attracted academic interest in this area. Solid stabilized emulsions play an important role in the recovery of crude oil, separation of oil fluids, wastewater treatment, cosmetic formulations and food technology.^{135, 136} These systems are highly complex. Scientific approaches have to use simplified model systems to elucidate the states and kinetic processes. Well-defined nano- and microparticles and proteins can be used.

Soon after the first stimulating report on novel investigations on Pickering emulsions,¹³⁷ it seems nearly impossible to review the work that has been done in that field since then,¹³⁸ partially because some systems are at the borderline between liquid-solid and pure liquid-liquid-interfaces (e. g. in wetting assisted assemblies, Langmuir-Blodgett-techniques, soft polymer interfaces etc.). Assemblies at pure liquid-liquid interfaces suffer from inherent limitations in analytical access and several approaches have been reported to transfer the assemblies for investigations from fluid interfaces to solid surfaces.

In the early works, sub- to micrometer sized polymer colloids have been used to stabilize water-in-oil emulsions.¹³⁷ The particles are readily trapped at the interface by a deep energy well. With the help of confocal laser scanning microscopy and scanning electron microscopy it could be shown that the adsorbed particles form dense and regular assemblies at the interface. After fixing the assemblies by electrostatic interactions or sintering, the yet flexible capsules could be transferred to a single phase without disruption. Size-selective permeabilities, traced with fluorescently labelled colloids, are in agreement with simple geometric considerations about the formed interstices. Based on these findings many new applications in the field of drug delivery, cell encapsulation or tissue engineering have been proposed.¹³⁷ The whole system profits from the wide variety of possible conditions.

Recently, cadmium selenide-nanoparticles have been employed to form stable sheets and membranes after crosslinking.^{139, 140} As the interfacial energy well depends on the radius according to $\Delta E = -(\pi R^2/\gamma_{o-w})[\gamma_{o-w} - (\gamma_{p-w} - \gamma_{p-o})]^2$, thermal energy can activate the escape of nanosized particles from the interface. The displacement of small nanoparticles by larger ones has been shown with fluorescence microscopy¹⁴¹ as well as interfacial tension measurements¹⁴². Rapidly, the water/oil interface has been recognized as the “emerging horizon for self-assembly of nanoparticles”.¹⁴³ Silica particles,^{144, 145} latex particles,¹⁴⁶⁻¹⁴⁸ gold-,^{143, 149-151} cadmium selenide-,^{139, 140} iron oxide-,^{143, 149} and other, sometimes rather exotic nanoparticles, such as polymer microrods,^{152, 153} carbon nanotubes,¹⁵⁴ hydroxy apatite nanoparticles,¹⁵⁵ clay particles,¹⁵⁶ spore particles¹⁵⁷ or food colloid particles¹⁵⁸ have been used with various crosslinking

strategies. Modifications of the nanoparticles' surface chemistry is sometimes necessary to enable interfacial assembly.^{143, 149, 150} Silica sols with nanometer-sized particles have been used in surfactant-free synthesis of polystyrene latex particles, which resembles in principle a Pickering emulsion system.¹⁵⁹ In addition, sterically stabilized latexes¹⁶⁰⁻¹⁶² and poly(4-vinyl pyridine)-silica nanocomposite microgels^{163, 164} have been used as stimulus-responsive particulate emulsifiers.

An open question is the contact angle of micro- and nanoparticles at the interface. The contact angle depends on the surface free energies (interfacial tensions) of the involved phase boundaries according to Young's equation:

$$\cos \theta = \frac{\gamma_{po} - \gamma_{pw}}{\gamma_{ow}} \quad \text{Eq. 1}$$

with γ_{po} , γ_{pw} and γ_{ow} the interfacial tensions at the particle/oil, particle/water and oil/water interface. Hydrophilic particles are preferentially wet by water and the contact angle is $0^\circ \leq \theta \leq 90^\circ$. Hydrophobic particles are preferentially wet by oil and the contact angle is then $90^\circ \leq \theta \leq 180^\circ$. The line tension effect influences the contact angle of small particles which is not considered in the equation above.¹⁶⁵ Optical microscopy can be used to determine the contact angle for larger particles. A technique based on microcontact printing was developed for smaller ones (1-10 μm).¹⁶⁶ The interfacial particle assembly was trapped by a gel ("fossilized") and a PDMS replica was prepared. SEM allowed then to determine the particle's profile and the immersion of the particle at the original interface.^{158, 167} The gel trapping technique has been used for visualization of particle assemblies on colloidosomes¹⁴⁶, for decoration of interfaces¹⁶⁸ and in desymmetrization reactions of nanoparticles.¹⁶⁹ Benkoski and coworkers used a methacrylate that could be flash-cured within one second by UV-light. Although one second means a long time on molecular dimensions, they claimed to obtain snap-shots of particle adsorption states.^{170, 171}

The free energy of detachment from the oil phase reads for a homogeneous particle in general (particle total surface area A_p) and for a spherical (radius r) and rod-like one (aspect ratio a/b) as follows:¹³⁸

$$\Delta G_{do} = \Delta G_{dw} + \gamma_{wo} A_p \cos \theta \quad \text{Eq. 2}$$

$$\Delta G_{do, sphere} = \pi r^2 \gamma_{wo} (1 - |\cos \theta|)^2 \quad \text{Eq. 3}$$

$$\Delta G_{do, rod} = \Delta G_{dw} + 4\pi \gamma_{wo} b^2 \cos \theta (a/b) \quad \text{Eq. 4}$$

The energy well of interfacially trapped spherical particles has a minimum for a contact angle of 90° and increases rapidly with particle size. The same holds true for rod-like particles. The energy of detachment increases with the aspect ratio. It becomes evident that even slight deviations from spherical to rod-like geometry increases the depth of the energy well if the other parameters are held constant.

The lateral organization of particles at liquid-liquid interfaces depends strongly on electrostatic repulsion and on particle hydrophobicity. Repulsion between hydrophilic particles is usually weak and mediated through the water phase. Only for hydrophobic particle monolayers where the electrostatic repulsion is strong and mediated through the oil phase, highly ordered two-dimensional surface crystals can be found.¹³⁸ The direct visualization of particles at liquid-liquid interfaces is restricted to micrometer-sized objects that can be observed with conventional light microscopy. Confocal laser scanning microscopy rendered inhomogeneous coating of oil-droplets with charge-stabilized latexes. Adsorbed particles formed extended patches with dense packing but also large free areas have been observed.¹⁷² The observed structures have been proposed to be due to diffusion-limited cluster aggregation (DLCA).¹⁷³ However, if the fine-balanced equilibrium structure is not disturbed by external forces, regular patterns are observed in which particles occupy equilibrium positions with maximum distance.¹⁷⁴ The lateral mobility of single interfacially trapped particles and particle clusters has been found to strongly depend on the viscosity of the oil phase.¹⁷³⁻¹⁷⁵ The thickness of the nanoparticle layer at the interface and lateral order can be evaluated with AFM and TEM and from cross sections.¹⁷⁶ The kinetics of the adsorption process can be conveniently followed by pendant drop tensiometry.^{142, 151}

Moreover, the assembly of nanoparticles at liquid-liquid interfaces was also extended to polymer interfaces. Nanoparticles segregated preferentially at the interfaces in microphase separated block copolymers^{177, 178} and at polymer-liquid interfaces^{179, 180}.

1.2.2 Protein Adsorption at liquid-liquid Interfaces

The recent reports on the use of proteins and bionanoparticles to construct capsules are particularly interesting. Capsules from CPMV-stabilized Pickering emulsions have been prepared and characterized in detail.¹⁸¹ Stable capsules of BSA at the water/chloroform interface formed and detached from the capillary;^{182, 183} casein films were enzymatically crosslinked,¹⁸⁴ the interfacial behaviour of BSA and glycosylated derivatives was investigated at the air-water interface.¹⁸⁵ Self-assembled hydrophobin protein films at the air-water interface were structurally analysed and revealed a two-dimensional order after pick-up on a graphite substrate and characterization with AFM.¹⁸⁶ Microcapsules fabricated from recombinantly produced spider silk were prepared and their mechanical and permeability properties characterized.^{187, 188} BSA microcapsules were also prepared on sacrificial scaffolds.¹⁸⁹

The proteins and protein cages used in this work are termed “bionanoparticles” which reflects the ability to image them directly (at least the protein cages) at the interfaces by microscopic techniques. On the other hand, it seems more appropriate to treat the adsorption phenomena within the theoretical framework of protein adsorption which considers the flexible and highly hydrophilic nature of them, i. e. the observation of surface denaturation.

1.2.3 Quantitative Modelling of Protein Adsorption at liquid-liquid Interfaces

Protein adsorption at liquid interfaces has been a topic in colloid science for decades.¹³² A challenging problem was the quantitative description of surface tension isotherms and the kinetic modelling of protein adsorption. In the recent years significant progress was made: The developed equations allow the quantitative dynamic and static description of protein adsorption at fluid interfaces as well as the adsorption of nanoparticles with minor modifications.^{190, 191} Detailed derivations will be presented in chapter 2.1. The final equations and the procedure how to model protein adsorption data are introduced in the next paragraph to not lose them in the in-depth derivation. Some comments on the peculiarities of protein adsorption are given first.

1.2.3.1 Surface Tension of Protein Solutions

It is a technically difficult task to measure the protein adsorption directly at fluid interfaces. The classical Wilhelmy plate method,¹⁹² X-ray^{193, 194} or neutron reflectivity,¹⁹⁵⁻¹⁹⁸ the radiotracer technique¹⁹⁹ or ellipsometry^{200, 201} can be employed.²⁰² Nevertheless, extended sets of literature data are rare. Most recent, successful efforts have used axisymmetric drop shape analysis. The shape of pendant drops (pendant drop tensiometry) or buoyant bubbles is analysed according to the equation of Young-Laplace and the corresponding interfacial tension is approximated through fitting algorithms (see chapter 2.2). Dynamic surface tension measurements with pendant drop tensiometry are technically straightforward – in principal, but a relation is needed between the surface tension and the protein adsorption, i. e. an equation of state for the surface layer. Many attempts to model experimental data (see a collection of references in ref.²⁰³) showed, that simple surface state models, for example according to Langmuir-Szyszkowski, Frumkin, reorientation model or aggregation model, are applicable to surfactant layers but are insufficient for protein macromolecules.²⁰⁴ The models are not able to describe the characteristic features of protein adsorption compared to adsorption of common surfactants. These include:²⁰⁵

- surface denaturation, i. e. unfolding of the protein at the interface, especially for low surface pressures
- large partial molar area of proteins that varies with surface pressure
- large non-ideality of the surface layer enthalpy and entropy

The model to develop should reflect the features of a protein adsorption isotherm that can be typically observed in experiments (see Fig. 1):^{199, 203} For low bulk concentration, the adsorption causes almost no measurable increase in surface pressure (region I). After some minimum adsorption, a sharp increase in surface pressure with increasing protein concentration within a narrow concentration regime is observed (region II). Further, the increasing surface pressure leads to interaction between molecules, leading to conformational changes. The thickness of the adsorption layer increases up to ten times for flexible proteins and up to two times for “hard” globular proteins at the same time.²⁰³ The region III is then characterized by an increasing adsorption and adsorption

layer thickness but almost constant surface pressure. Multilayers, interfacial aggregation or interfacial gelation can occur.

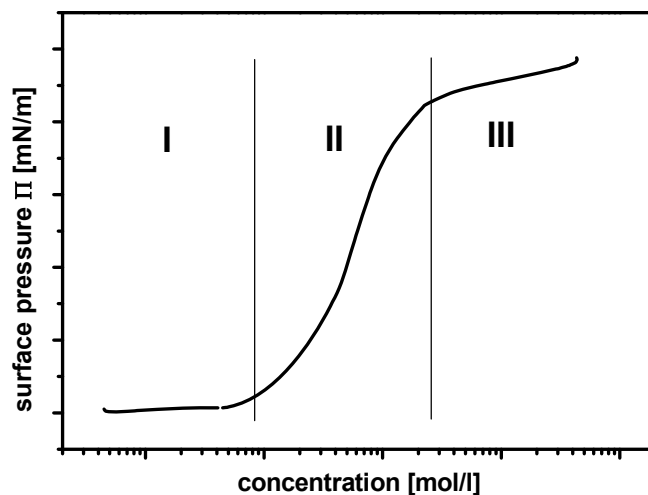


Fig. 1 Typically observed protein adsorption isotherm.

Flexible proteins like β -casein behave differently to “hard” (globular) proteins like BSA or HSA. β -casein shows lower minimum adsorption values for the transition from I to II. Within region II, flexible proteins show a stronger increase in adsorption layer thickness than globular proteins.²⁰³

The categorization into more or less surface active proteins has not led to convincing and clear conclusions,²⁰⁶ moreover, it has been shown, that the amphiphilic diversity of proteins is generally too low to exhibit an effect in their interfacial tensions (although there may be remarkable exceptions).²⁰⁷ These findings contradict somehow the qualitative discussion and conclusions of Beverung et al.²⁰⁸

Considering the dynamic behaviour, it can take tens of hours to achieve adsorption equilibrium. The equilibrium is thermodynamically reversible while desorption is kinetically strongly retarded. This result was obtained by Graham and Philips much earlier and recently confirmed by pendant drop experiments with exchange of the subphase²⁰⁹⁻²¹¹ but questions other reports.^{212, 213} In fact, the possibility to displace adsorbed segments or the whole protein is a topic of ongoing discussion. The quantitative evaluation of the dynamic adsorption curves with the limiting

approximations of the diffusion model of Ward and Tordai results in diffusion coefficients that are several orders of magnitudes higher than would be physically meaningful.²¹⁴ This fact has been attributed to the peculiarities of polymer adsorption, i. e. that the protein enters the interface with many subunits at one time which could obviously mimic a higher diffusion coefficient. Interfacial unfolding can also attribute to a stronger decrease in interfacial tension than predicted by the diffusion model.

The irreversible adsorption of particles at the fluid-fluid interface should not be mixed with the irreversible and localized adsorption (fixed positions!) of particles at solid interfaces. The random sequential adsorption (RSA) model used for the latter is a completely different approach (mainly statistical-thermodynamical) and has been described extensively by Adamczyk.²¹⁵⁻²¹⁷

1.2.3.2 The Concept of Varying Partial Molar Areas of Adsorbed Proteins²¹⁸

The concept of varying partial molar areas is a major breakthrough in the quantitative description and modelling of protein adsorption, in terms of both steady state and dynamic surface tension. Starting point is the concept of the partial molar area as an adjustable parameter during adsorption. No initial guess about a specific molecular model – e. g. flexible polymer chain or hard-core non-interacting particles, etc. – is necessary. The concept of “soft” compressible macromolecular entities would cover all the different conformations for flexible as well as “hard” globular proteins. Indeed, it was shown recently that the model is also suitable to describe adsorption phenomena of micro- and nanosized particles with just minor modifications.^{190, 191}

Joos and Serrien described a system with two different partial molar areas.²¹⁹ As a consequence of their model, the composition and the thickness of the adsorption layer are controlled by the surface pressure. The fraction of molecules with low surface area demand increases with increasing surface pressure i. e. with longer time or increasing bulk concentration. At low surface pressures, the molecules can unfold at the interface (surface denaturation).^{205, 220} The “two-state model” was successfully applied to

polyethylene glycol surfactants which exhibit a reorientation mechanism.^{221, 222} The model of adjustable partial molar surface areas is in agreement with the general physico-chemical principle of Braun-Le Chatelier. The surface pressure controls the composition of the surface layer. At low surface pressures, i. e. at low bulk concentrations or in the beginning of adsorption, an adsorbed macromolecule can occupy a large surface area. With increasing surface pressure, the molecules are compressed and can occupy just a minimum surface area. At the same time, ends or loops are occasionally squeezed out from the surface and the adsorption layer thickness increases (Fig. 2).

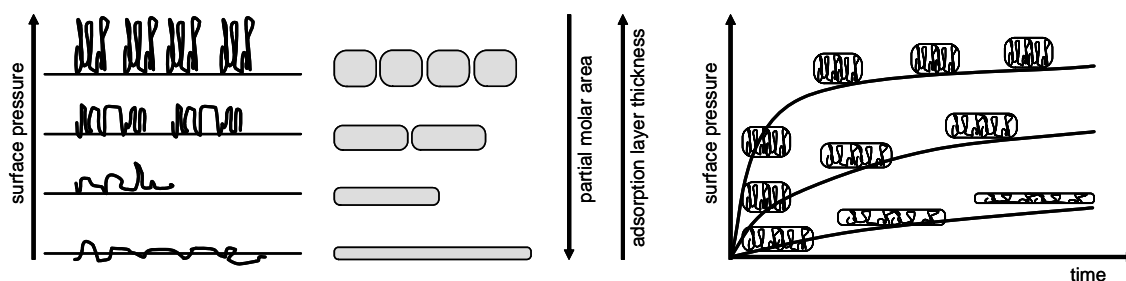


Fig. 2 Schematic drawing of protein adsorption states.²²³

The occupied surface area is expressed as partial molar area ω_i of the respective state i . The model with a discrete number of adsorption states or orientations has been used to model the adsorption of surfactants with different orientation possibilities and surfactant mixtures. The idea was then extended to a multi-state model for proteins that allows the adsorbed molecules to occupy varying partial molar areas.^{203, 218, 224, 225} The partial molar area is a quantification of the size of the protein at the interface, i. e. is also controlled through the degree of surface denaturation. The obtained values allow a quantitative discussion of the adsorption states of different proteins at the same interface (e. g. flexible versus “hard” proteins) or of the same protein at different interfaces (air/liquid versus liquid/liquid). The quantitative description supports nicely the qualitative picture of protein adsorption at interfaces.²⁰⁸

1.2.3.3 Modelling of Protein Adsorption at liquid Interfaces

The model of interfacial thermodynamics put the amount of a substance adsorbed at an interface in correlation to the interfacial tension. In most cases this also holds true for non-equilibrium conditions and is described by the Gibbs fundamental equation:

$$\Gamma(t) = -\frac{1}{RT} \frac{d\gamma(t)}{d \ln c_s(t)} \quad \text{Eq. 5}$$

with the adsorbed amount $\Gamma(t)$ at the interface at the time t , the interfacial tension $\gamma(t)$ and the subsurface concentration $c_s(t)$, that is the bulk phase localized immediately adjacent to the interface. However, this relation is not valid for proteins because of the high non-ideality of the Gibbs free energy. The non-ideal contributions of enthalpy and entropy have been considered in a recently developed surface layer model that is based on the concept of varying partial molar areas as introduced above. The equations describe the equilibrium state of the adsorption layer and correlate the interfacial tension with the adsorbed amount of protein. These are the adsorption isotherm (Eq. 11), the surface layer equation of state (Eq. 10) and the distribution function over the adsorption states differing in their occupied area at the interface (Eq. 12; for derivation and numeration refer to chapter 2.1.1):

$$b_j c_0 = \frac{\omega \Gamma_j}{(1 - \omega \Gamma)^{\omega_j / \omega}} \exp[-2a\omega \Gamma(\omega_j / \omega)] \quad \text{Eq. 11}$$

$$-\frac{\Pi \omega_0}{RT} = \ln(1 - \omega \Gamma) + (\omega - \omega_0) \Gamma + a(\omega \Gamma)^2 \quad \text{Eq. 10}$$

$$\Gamma_j = \Gamma \frac{(1 - \omega \Gamma)^{(\omega_j - \omega_1) / \omega} \exp[-2a\Gamma(\omega_j - \omega_1)]}{\sum_{j=1}^n (1 - \omega \Gamma)^{(\omega_j - \omega_1) / \omega} \exp[-2a\Gamma(\omega_j - \omega_1)]} \quad \text{Eq. 12}$$

The quantitative analysis of protein adsorption starts with modelling of the equilibrium surface pressure isotherm. The partial molar surface area ω serves as adjustable parameter, reflecting the dynamic interfacial conformation of the adsorbed protein. The different behaviour beyond the critical concentration (region III) is modelled with a set of corrected equations; i. e. an additional parameter ε is introduced:

$$-\frac{\Pi\omega_0}{RT} = \frac{1}{\Psi} \ln(1-\omega\Gamma) + (\omega - \omega_0)\Gamma + a(\omega\Gamma)^2 \quad \text{Eq. 13}$$

$$b_j c_0 = \frac{\Gamma_j \omega}{(1-\Gamma\omega)^{\Psi(\omega_j/\omega)}} \exp\left[-2a\Gamma\omega \frac{1}{\Psi}(\omega_j/\omega)\right] \quad \text{Eq. 14}$$

with

$$\Psi = \frac{\Gamma}{\Gamma^*} \exp\left(\varepsilon\omega \frac{\Pi - \Pi^*}{RT}\right) \quad \text{Eq. 15}$$

The Γ_j -distribution over the states of an adsorbed molecule (Eq. 12) is the same in both regimes. The interfacial structure of the adsorbed protein molecules in terms of their partial molar area can then be described through the independent parameters given in Tab. 1 (ε is pertinent to the transcritical region only, D to Ward-Tordai only).

Tab. 1 Independent parameters for modelling static and dynamic protein adsorption according to the model of variable partial molar areas and Ward and Tordai, respectively.

Parameter	Typical values	Description
a	0 ... 1	Frumkin type intermolecular interaction parameter
ω_0	$10^5 \text{ m}^2/\text{mol}$	area per single segment in the adsorption layer
ω_1	$10^6\text{-}10^7 \text{ m}^2/\text{mol}$	minimum occupied surface area per adsorbed molecule
ω_m	$10^8 \text{ m}^2/\text{mol}$	maximum occupied surface area per adsorbed molecule
ε	0 ... 0.2	decrease of molar area due to interfacial condensation (only transcritical branch)
D	$10^{-11} \text{ cm}^2\text{s}^{-1}$	diffusion coefficient (only for Ward-Tordai)

The model isotherm and the specific parameter values can then be used for fitting of the protein adsorption kinetic curves according to the diffusion model of Ward and Tordai.²²⁶

$$\Gamma(t) = 2\sqrt{\frac{D}{\pi}} \left[c_0\sqrt{t} - \int_0^t c_s(t-t')d\sqrt{t'} \right] \quad \text{Eq. 16}$$

Both give insight into protein adsorption kinetics and into the molecular processes at the interface. The power of the model has been proven in a number of studies, among them comparative studies of various proteins at different interfaces (liquid/air²¹⁸ as well as liquid/liquid interfaces²²⁷). The model is continuously refined and expanded to other systems and techniques, e. g. protein/surfactant mixtures^{228, 229} and interfacial dilatational rheology^{230, 231}.

1.3 Bio-Inorganic Composite Materials

Many materials in nature are not composed of soft organic matter only but contain also inorganic, “inanimate” materials. The building of inorganic matter is controlled by biomolecules through molecular recognition processes, templating on the molecular or cellular level and self-assembly. Novel biomolecular methods could contribute to a much clearer understanding of the *in vivo*-formation of inorganic matter into functionally integrated biomolecular hybrid materials. This knowledge is very important for an understanding of interactions between living systems and man-made inorganic and polymeric materials. Tissue engineering and regenerative medicine are particularly important fields in human health and well-being. Recent progress in the production of biomimetic materials resulted in stimulating new ideas for the future progress in these issues.^{232, 233} A successful incorporation of tissue scaffolds, artificial organs and bone substitutes relies on a positive cellular response in the body. Nanochemistry and nanotechnology can deliver solutions for the production of biomimetic materials which meet mechanical and biomedical requirements and additionally incorporate delivery systems with health-regenerating and -supporting or diagnostic properties.²³³

This paragraph gives first a short introduction which highlights a few peculiarities of bioinorganic materials. The next chapter is dedicated to bone tissue engineering; an area that is highly relevant for regenerative medicine but is also of fundamental interest. Much has been learned from cellular responses to man-made materials during the ongoing development of bone substitute materials. Particularly hydroxy apatite materials and coatings have been proven to be advantageous for cell adhesion, growth and proliferation. The chapter 1.4 provides more details about the biomimetic hydroxy apatite mineralization in a simulated body fluid.

1.3.1 Biominerals in Nature

Biomineralization has been attracting an ever increasing interest for the last few years. In living organisms four major groups of biominerals can be found:²³⁴

- silica (opal): sponges, diatoms
- calcium phosphate: metazoa
- calcium carbonates: prokaryota, protozoa, plantae, fungi, metazoa
- iron compounds: restricted primarily to prokaryota

The fascinating and beautiful world of diatoms is one popular example for the astonishing control over the formation of complex bio-inorganic patterns. Its investigation dates back almost two centuries.^{235, 236} Diatoms have become a paradigm how nature controls formation of highly symmetric and diverse structures. It turned out, that the silica skeleton formation is controlled by transcription (i. e. the level of gene expression) or translation (i. e. at the level of protein synthesis or modification). The many stages where control happens make it difficult to determine at the molecular level how a specific pattern emerges. Novel tools of molecular biology and biochemistry allowed progress in many aspects. Polycationic peptides (silaffins in diatoms,^{237, 238} silicateins in sponges^{239, 240}) and polyamines are key components which direct silica biomineralization. Synthetic polymers with similar composition have been used successfully in biomimetic approaches.^{241, 242}

Biomineralization features few peculiarities. First, many materials that exhibit crystalline order are not single crystals but so-called mesocrystals.^{243, 244} Crystallization in nature mostly does not follow the path of atomic, ion or molecule addition to a critical crystal nucleus. Instead, the self-organization of metastable or amorphous nanoscale precursor particles leads to nanoparticulate superstructures (particle-based non-classical crystallization) which can transform to single crystals. They can also remain regularly structured matter with variable morphologies that contains interspaced organic molecules. This process represents a natural bottom-up approach in the best sense and is flexible to produce materials with superior properties and various shapes.

Inorganic matter in nature hardly consists of inorganic matter alone but is accompanied by organic matter, either as protective colloid or as part of the texture. Organic molecules or biomolecules do not only assist non-classical crystallization phenomena but also impart special material and functional properties to the biominerals.^{245, 246} The nacre formation of molluscs shells from calcium carbonate is a well-known example for

this. The shell may best be described as microlaminate composite consisting of crystalline calcium carbonate-platelets which are parallel stacked and separated by thin layers of organic matrix (Fig. 3).²⁴⁷⁻²⁴⁹ Many research efforts have been dedicated to produce artificial materials that mimic the mechanical properties.^{250, 251} Building of such biological and biomimetic nanocomposites relies on the principles of self-assembly to mesocrystal formation.²⁵²

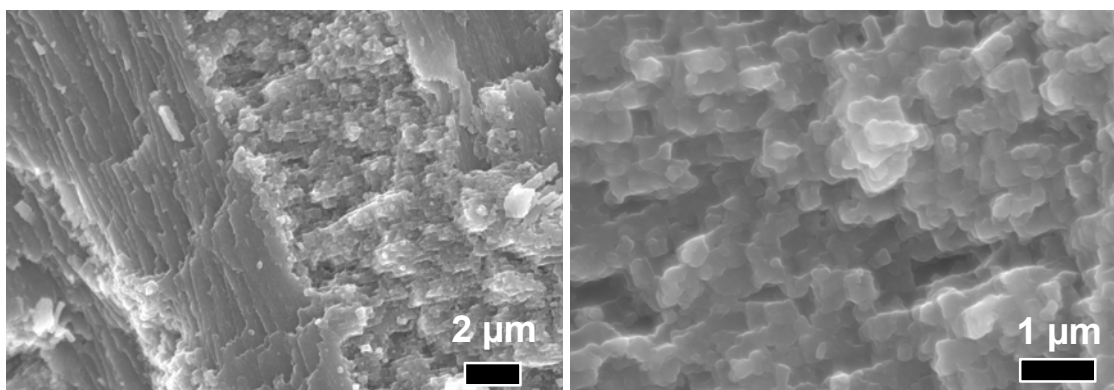


Fig. 3 Hierarchical structuring of a mussel shell: (Left) The shell exhibits a microlaminate structure with perpendicular orientation between different layers; (right) the magnification shows the nanoparticulate mesocrystalline structure of the layers.

1.3.2 Biomimetic Bone Tissues

Hierarchical structuring of mineral phases and soft biomaterials gives many natural materials remarkable mechanical properties, one of the most important material is bone (Fig. 4).^{253, 254} Bone consists of calcium phosphate as hydroxy apatite (HAP). Understanding mineralization processes in the body concerns essential vital functions: bone morphogenesis, formation of teeth but also unwanted pathological calcifications (ectopic calcification, e. g. in arteriosclerosis, end-stage renal disease or cardio-vascular calcifications).²⁵⁵ Clinical treatment as well as the medical development and implant of substitute materials such as artificial hip joints, bone substitutes or heart valves bioprotheses are not only of concern to human well-being but also of high economic interest and triggered large research efforts.²⁵⁵ Bone tissue can be repaired by self-regeneration or self-remodelling if the damaged area is small. If the area is too large (critical defect size), implant materials have to be used. The gold standard regarding

biocompatibility and performance is the autograft, i. e. a piece of bone is transferred from a healthy part of the patient. This approach however suffers from a limited amount of tissue available and damage to another part of the patient's body. If the material is transferred from another person or animals (allograft and xenografts, respectively), rejection reactions and the risk of infections have to be considered. Such materials are often treated with high temperatures to destroy the organic matrix and pathogens but still have to be used with caution. Much research effort has therefore been undertaken to develop biomaterials which overcome the mentioned drawbacks. Bioinert materials (metals, alloys, ceramics etc.) for tissue replacement suffer from a limited lifetime and the focus shifted to new materials which support tissue regeneration by stimulating the body's self-healing mechanisms.

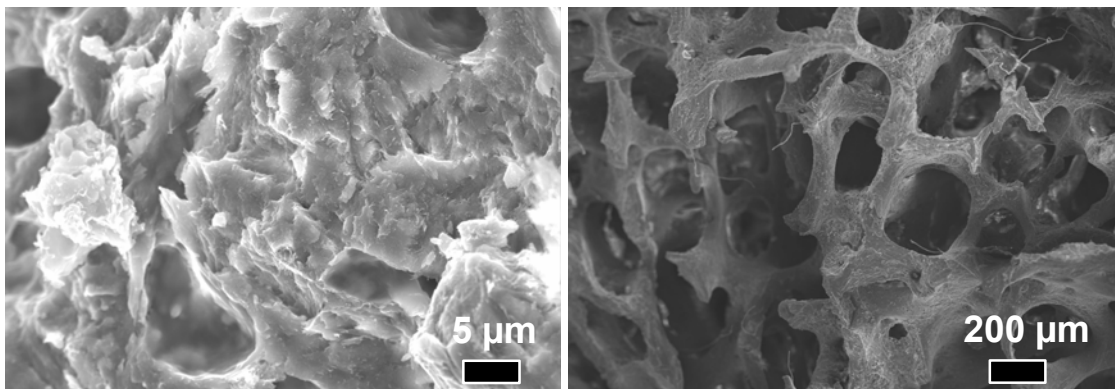


Fig. 4 Hierarchical structuring of bone: The hydroxyapatite/collagen composite (left) forms a macroporous framework (right) which contains soft tissue (here not present anymore).

Bone tissue is a composite of nanosized crystals of hydroxyapatite embedded in collagen protein matrix. Organic-inorganic hybrid materials seem therefore promising as they impart biological functionality as well as a hierarchical structuring which gives mechanical properties similar to natural bone.^{254, 256} For successful bone grafting, the scaffold has to induce bone cell growth (osteinduction) and support bone cell proliferation (osteoconduction).²⁵⁴ Osteoconductive grafts are autogenic and allogenic bone parts, hydroxyapatite and purified collagen. These materials are very likely to be incorporated. A very comprehensive and detailed introduction in the design of biomimetic nanocomposite bone grafts for bone tissue regeneration is given by Murgan and Ramakrishna.²⁵⁴

Composites with nanocrystalline HAP have been proven to yield good results with respect to osteoblast cell adhesion, differentiation and proliferation and integration in new biomineralized tissue.²⁵⁷ Biocompatibility, suitable porosity and biodegradability are further key issues for successful bone remodelling. Many synthetic composites with various biological or biodegradable scaffolds have been produced, among them dextrane,²⁵⁸ collagen,^{259, 260} alginate,²⁶¹ gelatine,²⁶² chitosan,²⁶³ silk protein²⁶⁴ or poly(lactic acid)²⁶⁵. Most of them employ highly alkaline solution conditions and increased temperatures for the formation of hydroxy apatite nanoparticles or use preformed calcium phosphate nanoparticles. Extreme solution conditions might be compatible with few materials but not generally with soft and biological scaffolds and little can be learned about biomineralization from such systems.

It is obviously favourable but at the same time particularly challenging to find suitable biomimetic conditions in the production of nanostructured inorganic materials.²⁶⁶ They allow “green” and cost efficient materials production without the need of more than a beaker. In this work, a simulated body fluid (SBF) has been used to induce hydroxy apatite coatings on biopolymer interfaces. SBF resembles the ionic composition of blood serum without proteins and mimics the highly supersaturated conditions in the body with respect to hydroxy apatite and calcite precipitation.²⁶⁷ SBF mimics successfully the mineralization situation *in vivo*. It has been shown, that results obtained with SBF *in vitro* are directly transferable to *in vivo* systems (see chapter 1.4).²⁶⁷

1.4 Hydroxy Apatite Coating in a Biomimetic Process

The development of glasses in the $\text{Na}_2\text{O-CaO-SiO}_2\text{-P}_2\text{O}_5$ system (generally called Bioglass[®]) by Hench et al. in 1971²⁶⁸ led to the development of many new types of glasses and glass ceramics that become clinically important bone substitutes.²⁶⁹ Moreover, they mark the breaking of the biocompatibility barrier and a milestone in the development of bioactive materials.²⁷⁰ They are not encapsulated by fibrous tissue and are not isolated from the surrounding bone. However, bone has a very complicated hierarchical structure with amazing mechanical properties which are not met by these ceramics.²⁷¹ Different mechanical properties however can lead to significant problems after implantation of artificial bone substitutes. Extended screening of new materials is hampered by the lack of a standard test to assess bone bonding properties and the need of extensive animal testing. It has been proposed that *in vivo* bone building activity can be predicted by the formation of hydroxyl apatite in calcium phosphate solutions.

Initial homogeneous glass of the composition $\text{MgO-CaO-SiO}_2\text{-P}_2\text{O}_5$ (termed glass G) can be subjected to heat treatment to form glass-ceramics.²⁷² In glass-ceramic A-W crystalline oxyfluoroapatite ($\text{Ca}_{10}(\text{PO}_4)_6(\text{O}, \text{F})$) and β -wollastonite ($\text{CaO}\cdot\text{SiO}_2$) particles precipitated homogeneously in a glassy MgO-CaO-SiO_2 matrix.^{273, 274} The 50-100 nm large crystalline parts significantly enhance mechanical strength.²⁷² Similarly to other bioactive materials these glasses and glass-ceramics bond to living bone through an apatite layer that is formed on its surface in the body.^{269, 274} The same type of surface mineralization could be found in an *in vitro* mineralization system. Kokubo and coworkers developed a supersaturated calcium phosphate solution that essentially resembles the ionic composition and concentration of human blood plasma but is devoid of protein (Tab. 1). It is therefore named simulated body fluid (SBF).^{267, 275} This solution became a preferred system for testing hydroxy apatite growth on various substrates. The ability to form apatite on the substrate surface in SBF is correlated with *in vivo* bone building bioactivity of the material.^{267, 269} This has been proven in comparative experiments between *in vivo* tests with rabbits and *in vitro* growth of hydroxy apatite.²⁶⁹ As the surface apatite formed in SBF has a similar composition and structure to bone mineral, osteoblasts might preferentially proliferate and differentiate to produce apatite and collagen on its surface, leading to tight bonding between the

material and living bone. Thus, examining the *in vitro* apatite formation in SBF allows predicting the *in vivo* bone bioactivity as long as the material does not contain substances that induce toxic reactions to cells. The simple *in vitro* conditions substantially improves and speeds up screening for new implant materials. Long duration animal testing with all its uncertainties is not of immediate need and can be remarkably reduced. The validity of the method was shown in a round robin testing and proposed to the International Organization for Standardization as standard testing solution for *in vitro*-measurement of the apatite-forming ability of implant materials.²⁶⁷

Tab. 2 Comparison of nominal ion concentrations in serum, blood plasma and 1.0 SBF.

ion	composition range of serum [mM] ²⁷⁶	blood plasma [mM]	1.0 SBF [mM]
Na ⁺	130-150	142	142
K ⁺	3.6-5.6	5	5
Mg ²⁺	0.74-1.5	1.5	1.5
Ca ²⁺	2.1-2.9	2.5	2.5
Cl ⁻	99-110	103	147.8
HCO ₃ ⁻	8.2-9.3	27	4.2
HPO ₄ ²⁻	0.74-1.5	1	1
SO ₄ ²⁻	0.08-0.12	0.5	0.5
F ⁻	0.01-0.02		
pH		7.2-7.4	7.4

The HAP growth on bioactive glass G and on glass ceramics derived from glass G proceeds via dissolution of small amounts of calcium and silicate ions.^{277, 278} The former increases the local calcium ion concentration and the degree of supersaturation in the surrounding solution with respect to apatite formation.²⁷⁹ Dissolution of silicate ions might provide favorable nucleation sites. Both cooperatively induce hydroxy apatite growth on the surface of the glass ceramic.^{277, 278, 280} Glass G dissolves the highest amounts of calcium ions among the investigated glass ceramics and glasses.²⁷⁷ The formed apatite has a lattice constant similar to bone apatite but is slightly deficient of

calcium. The differences to bone apatite increases if the concentration of the SBF solution is increased from 0.75 fold to 2 fold.²⁷⁹

Based on the proposed mechanism, it was suspected that hydroxy apatite can be grown on virtually any substrate after incubation on bioglass^{279, 281, 282} or bioactive ceramic particles²⁶⁹. Substrates are soaked for two days in 1.0 SBF in contact with grains of glass G. A number of apatite nuclei are formed on the substrate. After removal and further incubation in SBF, a dense and uniform hydroxy apatite layer is formed on the surface. It could be shown, that the mineral layer has bone-like composition and is highly bioactive. Simple immersion in SBF even with occasional addition of additional ions did not lead to surface apatite formation.²⁷⁸ In a systematic investigation with alumina as substrate it was shown that the thickness increased linearly with time if the solution was renewed every 12 h. Higher temperature, higher SBF concentration or shaking the solution increased the growth rate.²⁸² Various inorganic substrates (alumina, titanium, Perioglass[®] and others)^{269, 283, 284}, polymer surfaces (PMMA, PET, PDMS, PTFE, Nylon, etc.)^{269, 279, 281, 283, 285} and fabrics^{281, 283} have been coated. Pretreatment of polymeric substrates with glow-discharge or in alkaline or acidic solutions to enhance the number of polar groups aids the formation of a HAP layer and increases the affinity strength.^{285, 286} More sophisticated materials have been produced by coating of silane/titanium treated polymers.²⁸⁷

Model systems are important tools to isolate certain phenomena from the complex interplay in living systems and to investigate them in dependence of a manageable number of parameters.²⁷⁶ SBF is able to mimic the mineralization conditions in body fluids without the need of biological matter which is an inherent source of error. The preparation of SBF needs great care as it is highly supersaturated with respect to calcium phosphate precipitation.²⁶⁷ To eliminate the instability with respect to calcium carbonate (calcite) formation, the carbonate content was reduced but otherwise the chloride content increased compared to the original composition of blood plasma. The first recipe was adjusted several times and the most recent version is called newly improved SBF (n-SBF), in this work simply called SBF. The refined recipe has been confirmed to lead to stable and reproducible results in many experiments.²⁶⁷

1.5 Bionanoparticles: Plant Viruses, Ferritin and Proteins

1.5.1 Plant Viruses

The first virus isolated was the tobacco mosaic virus (Stanley 1935, Nobel Prize 1946)²⁸⁸, and since then, TMV is connected with many scientific milestones:^{289, 290} first virus to be purified and crystallized (1935), discovery of nucleoprotein nature (1936), first virus seen in electron microscopy (1939), helical structure (1954), discovery of the genome to be RNA (1950s) and the first sequenced viral coat protein (1960), use of cell wall-free protoplasts as *in vitro*-system (1969), transcription of infectious RNA from full-length cDNA clones (1986) and the first isolation of a plant gene conferring resistance to a virus (1994), to name a few. Therefore, understanding the scientific history of TMV, TYMV and CPMV means knowing a main part of the development of biochemistry in general. The development of many techniques in biochemistry and microbiology is closely associated with these viruses. The next chapters introduce the proteins and plant viruses that have been used in this work because their biological structure plays an important role when using them in synthesis, characterization and assembly.

1.5.1.1 Cowpea mosaic virus (CPMV)²⁹¹⁻²⁹⁵

Cowpea mosaic virus (CPMV) is the type species of the genus *Comovirus* (family *Comoviridae*). The crystal structure is refined at 2.8 Å resolution.^{296, 297} It is isometric with pseudo-T = 3 icosahedral symmetry and has a diameter of approximately 30 nm. The 60 small capsid proteins (S, domain A) are arranged as 12 pentamers at the 5-fold axis and the 60 large ones (L, domains B and C) as trimers at the 3-fold axis (Fig. 5). Comoviruses have a bipartite RNA genome consisting of positive-sense ssRNA. The genome of CPMV is fully sequenced. The single open reading frame (ORF) on each RNA is translated into a polyprotein from which the functional proteins are processed by proteolytic cleavage. The viral proteinase and replicase with the RNA-dependent RNA polymerase (RdRp) motive is encoded in RNA1 while the two coat proteins (CP) and the cell-to-cell movement protein are translated from RNA2. Purified preparations

show three centrifugal components: the top component (T) consists of CP only, the middle component (M) and the bottom component (B) differ in their nucleic acid content and contain additionally polyamines. For a successful infection process both RNA-containing particles are necessary. The host range is rather limited and as most comoviruses CPMV is restricted to members of the family *Leguminosae*;²⁹⁸ its name is derived from the symptoms of infected cowpea (*vigna unguiculata*) for which it is the most commonly reported virus disease. High yields of virus can be obtained from infected leaves by means of high-capacity caesium chloride gradient centrifugation.^{296, 299} Typical symptoms on plants are chlorotic mottling and yellow mosaic pattern, distortion, necrosis and growth reduction. Crystalloid cytoplasmic inclusions of virus particles are characteristics of the group.²⁹² While natural transmission occurs mainly by beetles, mechanical transmission is possible as viruses are quite stable in crude sap. The California blackeye is a diagnostic species and suitable propagation host. Inactivation occurs at 55-60 °C after 10 min.

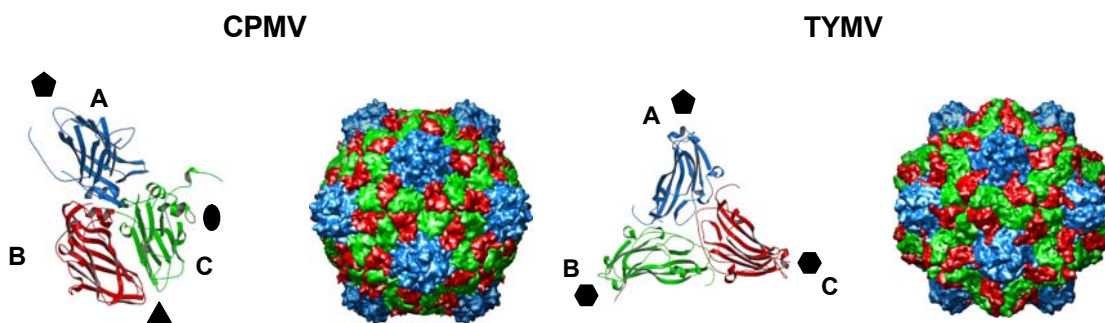


Fig. 5 Ribbon diagram of the coat protein subunits and domains and contour surface plots at 5 Å resolution with corresponding color coding. The locations of the symmetry axes are indicated by the respective symbols. (Left) CPMV: The small subunit forms domain A, the large subunit forms domain B and C. (Right) TYMV: The shell is composed of a single coat protein, each one forming an A, B or C domain.¹⁸

1.5.1.2 Turnip Yellow Mosaic Virus (TYMV)³⁰⁰⁻³⁰⁵

Turnip yellow mosaic virus (TYMV) is the type species of the genus *Tymovirus* (family *Tymoviridae*). Their capsid exhibits T = 3 icosahedral symmetry with a diameter of approximately 30 nm. The in total 180 chemically identical subunits form 32 capsomers (20 hexamers and 12 pentamers) with distinct and clearly visible surface structures

(Fig. 5).³⁰⁶ The protein capsid is specially stabilized through hydrophobic protein-protein interactions. Up to 1 % polyamines neutralize the negatively charged RNA so that the coat proteins are less involved in charge neutralization.³⁰⁶ There are two main sedimenting components, the protein shell with no or little amount of RNA (T-component) and the capsid containing the infectious virus genome (B-component). The known genome is a single (+) ssRNA which is expressed via polyprotein processing and sgRNA synthesis which encodes the CP. The genome contains three overlapping ORFs with motifs for transferase, protease, helicase and RdRp, cell-to-cell movement proteins, and viral CP. A special feature is the so-called “tymo box” at the 3’ terminal part, a 16 nucleotide sequence which is similar in all tymoviruses and functions amongst others as sgRNA promoter. This end of the RNA forms a tRNA like region with pseudoknot structure. Tymoviruses are excellent immunogenes. RNA can be released *in vivo* and *in vitro* through a hole in the capsid by the loss of five to six subunits. Attempts to obtain a non-denatured re-associable form of the TYMV coat protein failed.

The host range is restricted to dicots.³⁰⁵ Chinese cabbage (*Brassica campestris ssp. chinensis* and *ssp. pekinensis*) is found to be a useful host for propagation from which it can be obtained in large amounts and good yields.³⁰⁷ Infected plants show bright yellow mosaic or mottling as a result of severe cytopathic modifications of chloroplasts and mitochondria. The RNA replication and assembly of tymoviruses is thought to take place in characteristic double membrane bound vesicles within the host’s chloroplasts.³⁰⁴ The large portions of empty protein shells can be stained and visualized in light microscopy. Natural transmission occurs via beetles (chrysomelids) in (non-) circulative manner, but mechanical transmission is possible. The robust nature of TYMV made it the virus of choice for many different studies, including AFM-studies of macromolecular crystallization processes. Crude sap is stable for about 10 days; inactivation takes place at approximately 60-65 °C.

1.5.1.3 Tobacco Mosaic Virus (TMV)³⁰⁸⁻³¹⁰

The central role of TMV in many fundamental discoveries in biochemistry and virology in particular has been pointed out above. The tobacco mosaic virus (*tobamovirus*; unassigned genus), is a rod-shaped virus with helical symmetry. The rigid tubes of approximately 18 x 300 nm have a central hollow core of 4 nm. 2100 subunits of a single coat protein enclose the single RNA genome in form of a right-handed helix with a pitch of 2.3 nm. The positive-sense ssRNA is capped at the 5' terminus and has a tRNA-like secondary structure at its 3' end. Four partially overlapping ORFs encode the capsid protein and three non-structural proteins (RdRp, helicase, movement protein) where CP and movement protein are translated from two different sgRNAs. Distinct contacts between each subunit with three nucleotides lead to an *in vivo* and *in vitro* self-assembly of purified coat protein with viral RNA into infectious particles. As most filamentous molecular assemblies, TMV does not crystallize. Today, the structure is resolved to 2.9 Å and 5 Å by fibre X-ray diffraction³¹¹ and electron microscopy³¹², respectively. In combination with novel refinement methods these data are reliable as conventional crystallographically determined structures at comparable resolutions.³¹³ The CP alone assembles into small disks and short helix structures depending on pH, temperature and ionic strength as reviewed by Klug and Lomonosoff.^{314, 315} Starting point for the self-assembly of the nucleoprotein structure is a two-layer disk. RNA containing an “origin of assembly”-sequence will insert into the central hole of the disk and start the bidirectional growth of the disk to an extended rod, pulling up more and more RNA through the hole.³¹⁶ The whole length is determined by the entrapped RNA.

Characteristic cytoplasmic inclusions with hexagonal crystals of layers of viruses can be detected in light microscopy and are diagnostic for tobacco mosaic virus infections. The robust TMV-host system allowed intensive studies of virus replication. The high accumulation and stability make it easy to purify the virus even without the use of an ultracentrifuge but PEG-precipitation.³¹⁷ Heat inactivation occurs at over 90 °C for 10 min. In crude sap or dried materials they remain active over decades, thus TMV is essentially ubiquitous. The isolation of TMV from several rivers has been reported.³¹⁸

While the experimental host range of most tobacco mosaic viruses is broad, in nature few plants have been found susceptible. Infected plants show vein clearing and mosaic,

distortion and blistering. TMV induce necrotic local lesions in inoculated leaves. No true vectors are known and TMV is the type example for mechanical transmission. Transgenic plants which accumulate the coat protein have shown to be protected from severe infection by TMV.³¹⁹

TMV was the first virus vector for expression of foreign genes in plants. High accumulation of the expressed recombinant protein products can build an economical and productive source of therapeutic agents for diseases. Another strategy uses the virus as fusion vector, i. e. the heterologous protein is expressed as part of the virus coat protein.³²⁰

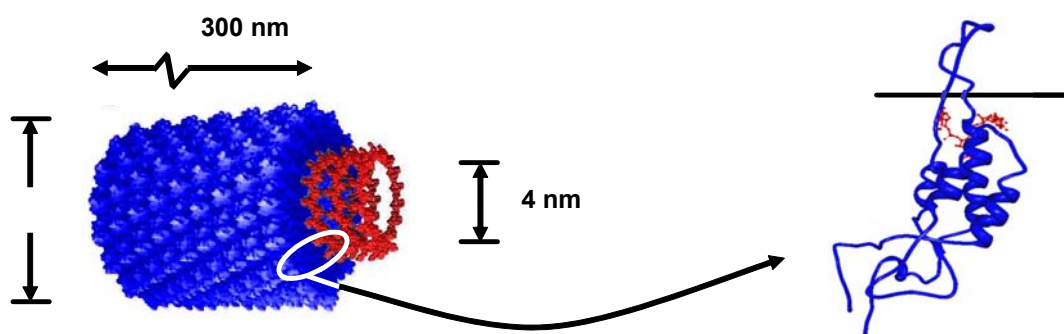


Fig. 6 (Left) Biological molecule and (right) subunits of TMV. TMV is composed of identical subunits (blue) which arrange in helical manner around the DNA (red) in the inner cavity. The subunit contains four helices which make distinct contacts with three RNA nucleotides. The black line indicates the axis of the rod.

1.5.2 Ferritin

Ferritin describes a family of proteins,³²¹ however, in this work, ferritin from horse spleen has been used exclusively. 24 protein subunits self-assemble to form a cage with an outer diameter of approximately 12 nm and an inner cavity of approximately 6 nm that is filled with hydrated ferric oxide (ferrihydrite $\text{Fe}_2\text{O}_3 \cdot n \text{H}_2\text{O}$).³²² Mammalian ferritin consists of a mixture of two different subunits, termed H for heavy and L for light chain, respectively. The ratio varies between organisms as well as between different tissues within an organism. Horse spleen ferritin is little heterogeneous, over 90 % is composed of L chains³²³ with a molecular weight of 19.9 kDa.³²⁴ Each subunit

protein forms a four-helix bundle that arranges in 12 antiparallel pairs to build a roughly rhombic dodecahedron shape.³²⁵ The resulting threefold channels are hydrophilic in nature and considered as the entrance for cations to form the mineral core while the fourfold channels are hydrophobic in nature. Both have a diameter of 0.3 nm. The formation of the mineral core is a multi-step process whose mechanism has been investigated in great detail.³²¹ The L-subunit from horse ferritin was cloned and expressed in *Escherichia coli* to form recombinant ferritin. The subunits self-assemble *in vitro* to a 24-mer shell and can be fully reconstituted with an iron core.^{326, 327} Ferritin preparations from natural sources possess some microheterogeneity, arising firstly from the slightly chemically different capsid proteins (polymorphic forms)³²⁸, secondly from dimers and trimers. This aggregation is accompanied by the loss of a subunit and not reversible through adjusting solution conditions. Further, the iron content can vary from a few Fe-atoms to clusters containing up to 4500 Fe-atoms.

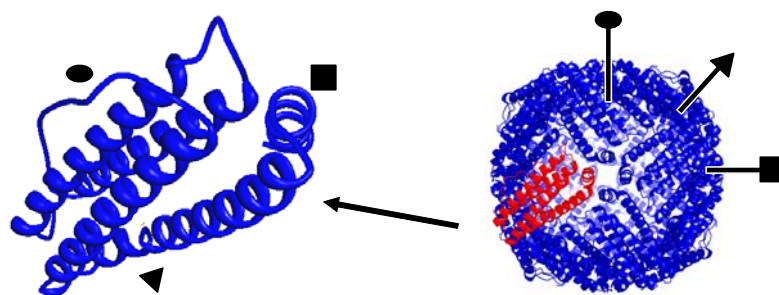


Fig. 7 (Left) Subunit and (right) biological molecule of ferritin. Ferritin is composed of 24 subunits which build a rhombic dodecahedron. One subunit (red) is magnified to show the arrangement of the subunit in four parallel helical segments in more detail. The locations of the symmetry axes are indicated.

Ferritin has been extensively used as a monodisperse model protein in surface science. The possibility to have demineralized empty capsids (apoferritin) and capsids filled with an iron oxide core offers the unique chance to investigate the behavior of topologically identical particles that however differ significantly in weight. This has been used e. g. for investigations of colloidal crystallization.³²⁹ The use of apoferritin as constrained nanoreactor in biomimetic synthesis of inorganic nanoparticles and in the construction of two-dimensional protein arrays is described in chapter 1.1.2.2 and 1.1.2.4.

1.5.3 Bovine/Human Serum Albumin (BSA/HSA)³³⁰⁻³³²

Serum albumin is the most abundant protein in serum, comprising mostly 50 % or more of the total plasma proteins. An average person of 70 kg has an exchangeable albumin pool of 350 g. One more remarkable fact is its lifetime of 27 days during which it makes 15.000 trips around the circulatory system. Albumin makes 80 % of the colloid osmotic pressure because of its high concentration and small molecular weight. Nevertheless, it can be completely replaced by other blood proteins. It is highly soluble (up to 30 % (w/v)) and with an pI of 4.9 the most acidic protein in serum. As one of few secreted proteins it lacks carbohydrate. Serum albumins are the most studied proteins and most popular standards in protein biochemistry. Human serum albumin (HSA) is built of 585 amino acid residues (bovine serum albumin, BSA, 582 amino acids). Its structure is best described by nine loops that group as three semiglobular units with an overall length of 14.1 nm and a diameter of 4.1 nm. The molecule is non-uniformly charged along its structure with a highly negative charged amino terminus and a nearly neutral carboxyl terminus. The protein is stabilized by 17 disulfide bonds, but yet highly flexible through its coil structure. While it is more stable against salt denaturants than many other proteins it changes reversibly at pH = 4-4.5 to a structurally loose and electrophoretically fast moving species (F-state). By this transition 40 titratable carboxyl groups appear that are hidden in the natural state (N-state) which is stable up to pH = 10. As albumins work as carrier for many ligands, commercial preparations typically show some microheterogeneity. This originates from precipitation from its natural source blood serum and is the reason for the slightly yellow colour of commercial preparations. Of special importance are fatty acids that are tightly bound and build the biological entity "serum albumin". The free cysteine that is normally sterically protected can also be the cause for heterogeneity if it carries half-cystine or glutathione in the form of a mixed disulfide. Thus, the molecular weight from physical data is always found higher than expected from its sequence. Further, besides the main monomeric species, dimers, trimers and aggregates are present to a minor part.³³³ Bovine and human serum albumin are essentially indistinguishable in their physical properties.

1.5.4 α_2 -Heremans-Schmid glycoprotein (Ahsg)/fetuin-A³³⁴

Ahsg (human) or fetuin-A (calf) is a plasma protein from the cystatin superfamily of cysteine protease inhibitors with considerable biological importance.³³⁵⁻³³⁷ It has been pointed out that “complete fetuin-A deficiency in humans is probably incompatible with life”.³³⁸ In mammalian blood, the extracellular concentration of mineral solutes is considerably higher than can be expected from their solubility products, but physiological mineralization is restricted to bones and teeth. Besides other factors regulating the complex process of calcification, fetuin-A has been identified in genetic studies with knockout mice as an important systemically acting inhibitor of pathological mineralization in soft tissues and in the extracellular fluid.³³⁹ This study confirms clinical observations that dialysis patients are prone to vascular and valvular calcifications (ectopic calcification), presumably because of their low fetuin-A serum level.^{338, 340} Further studies underlined the key role of fetuin-A in inhibition of vascular calcification, the major risk for cardiovascular events and mortality in atherosclerosis, diabetes and end stage renal disease.³⁴¹ *In vivo* studies revealed that fetuin-A directs the calcification to collagen fibrils; in the absence, mineralization in serum occurs.³⁴² The most abundant serum protein, serum albumin, is a much weaker inhibitor of calcium phosphate precipitation than fetuin-A. Fetuin-A has been shown to form *in vitro* soluble and transient stable colloidal particles of up to 100 nm in diameter in supersaturated solutions of calcium phosphate.³⁴³ The biomineral particle composition and aging properties have been studied in great detail with scattering techniques^{343, 344} and by transmission electron microscopy^{339, 343}. Fetuin-A has a high affinity for hydroxy apatite surfaces and concentrates in the mineral phase of teeth and bones.^{345, 346}

The names Ahsg or fetuin-A are used nowadays interchangeably after they have been found to be species homologues (calf/human) of a plasma glycoprotein. The five oligosaccharide moieties (account for ca. 25 % of the mass) give fetuin-A in SDS-PAGE an apparent molecular weight of 59 kDa compared to 48 kDa from composition.³³⁴ There are no structural data for fetuin-A available yet.³⁴⁷

1.5.5 Physical Properties of Bionanoparticles

Tab. 3: Physical properties of three plant viruses: Cowpea mosaic virus (CPMV), turnip yellow mosaic virus (TYMV), tobacco mosaic virus (TMV)

	CPMV ^{293, 296}	TYMV ³⁰¹⁻³⁰³	TMV ³¹⁰
diameter [nm]	28-30	28-29	18; length: 300
MW coat protein from composition [Da]	41.249 23.708	20.133	17.5
MW whole virus from physical data [MDa]	T: 3.94 M: 5.16 B: 5.98, 5.98	T: 3.6 B: 5.4	39.4
isoelectric point	3.7-4.5	3.75 (4.75 ³⁴⁸)	3.5
number of nucleotides	5889 (RNA1) 3481 (RNA2)	6318 694 (sgRNA)	6395
MW of RNA [MDa]	2.02 (RNA1) 1.22 (RNA2)	2.0	
wt% of RNA in particle	T: 0 M: 24 B _U , B _L : 34	T: 0 B: 35	5
extinction coefficient ϵ [mlmg ⁻¹ cm ⁻¹] at 260 nm	T: 1.28 M: 6.2 B: 10.0 average: 8.1	T: 0.96 B: 9.6 average: 8.6 ³⁴⁹	3.06 ³⁵⁰
optical density (260 nm/280 nm)	T: 0.69 M: 1.57, 1.63 B: 1.69, 1.80 average: 1.64	T: 0.81 B: 1.51	1.19
RI increment dn/dc [cm ³ g ⁻¹] at 578 nm			0.182 ³⁵⁰
sedimentation coefficient [S]	T: 58 M: 98 B: 118	T: 53-54 B: 116-117	194
buoyant density in CsCl [g/cm ³]	T: 1.29 M: 1.40 B: 1.42, 1.47	T: 1.28 B: 1.42	1.325

T, M and B refer to top, middle and bottom component of virus preparations which have been subjected to density gradient centrifugation. Sometimes slightly different values are reported which is expected for different strains and different preparations.

Tab. 4 Physical properties of human serum albumin (HSA), bovine serum albumin (BSA), fetuin-A and horse spleen ferritin.

	HSA ^{330, 351}	BSA ^{330, 351}	fetuin-A	ferritin
MW from composition [kDamol ⁻¹]	66.439	66.267	48 ³³⁴	19.8 ³²⁴
MW from physical data [kDamol ⁻¹]	69.0	66.7	~ 54	18.5
isoelectric point	4.8 defatted: 5.8			4.25-4.50 ³⁵²
extinction coefficient ϵ [ml mg ⁻¹ cm ⁻¹] at given wavelength	5.31 (279 nm)	6.67 (279 nm) 6.61 (280 nm)	4.5 (278 nm) calf serum: 4.1, 5.3 (278 nm) ³⁵³	apoferritin: 8.6-9.7 (280 nm) ³⁵³
RI increment dn/dc [cm ³ g ⁻¹] at given wavelength	1.89 (578 nm)	1.88 (578 nm)		apoferritin: 0.159 ferritin: 0.290 (628 nm)
diffusion coefficient D [10 ¹¹ m ² s ⁻¹]	6.01 ³⁵⁴	5.9 ³⁵⁵		monomer: 3.24

1.6 Outline and Relevance of the Presented Research Work

Bionanoparticles can serve as viable building blocks for the synthesis of well-defined composite materials with high functionality. They are easily accessible materials with precisely defined structure and composition and can conveniently be used in bottom-up approaches to construct novel materials. Of special interest is the development of bioinorganic composite materials which mimic natural materials with their various remarkable structural and functional properties.

In this work, proteins (human and bovine serum albumin, fetuin-A), protein cages (ferritin from horse spleen) and plant viruses (cowpea mosaic virus, turnip yellow mosaic virus and tobacco mosaic virus) are employed to produce functional nanopatterned surfaces and interfaces. Such surfaces and interfaces are employed in biomimetic hydroxy apatite mineralization to produce inorganic biocompatible surfaces and hollow mineral spheres.

The bionanoparticles are characterized in terms of their composition with biomolecular techniques (SEC, SDS-PAGE) and in terms of their structure with physico-chemical techniques (UV-Vis, SLS, DLS, TEM). The intensive characterization is necessary to ensure a qualitative and quantitative basis for reproducible experiments but also to establish different characterization and imaging techniques under conditions suitable for soft and sensible bionanoparticles. The preparation and characterization of fluorescently labelled cowpea mosaic viruses is reported here, too.

Thin protein films and bionanoparticle layers are produced by assembly at liquid-liquid interfaces. The kinetics of the adsorption process is followed by pendant drop tensiometry. Modelling of the surface pressure isotherms allows conclusions about interfacial states of adsorbed molecules. The model parameters are further used for the modelling of the dynamic surface tension.

The liquid oil phase of bionanoparticle-stabilized oil-in-water emulsions is UV-polymerized to allow the characterization of interfacially assembled bionanoparticles with standard AFM and SEM techniques. An acrylate modified poly(dimethyl siloxane)

is used as liquid precursor. The images of the trapped bionanoparticles give insight in the interfacial assembly and structure which can otherwise hardly be accessed. Cross sections from embedded interfaces allow the high-resolution imaging of the bionanoparticle-decorated interfaces in TEM. The adsorption of the structurally very soft proteins cannot be proven by direct imaging but by fluorescence microscopy after reaction with the respective fluorescent antibodies. The adsorption of bionanoparticles at the liquid-liquid interface of perfluoro octane and aqueous buffer is visualized by confocal fluorescence laser scanning microscopy.

Mineralization with hydroxy apatite is conducted with various solutions at room temperature or 37.0 °C and physiological pH = 7.4. The use of a simulated body fluid (SBF) allows the conduction of a biomimetic mineralization which can be related to the *in vivo* performance of the investigated surface. A preincubation step on bioactive glass particles is necessary for SBF with physiological concentrations to induce hydroxy apatite growth on surfaces. For technical applications, simplified aqueous solutions are used but extreme pH and temperatures are avoided. The development of hydroxy apatite coatings on poly(ethylene terephthalate) as model substrate is followed with time. PDMS-surfaces with different immobilized proteins are used to mimic bio-related interfaces. The induction and growth of hydroxy apatite is compared for surfaces with different immobilized proteins and for different mineralization solutions. Extensive structural characterization with SEM as well as compositional characterization with EDX is shown for the mineralized surfaces.

Finally, true bionanoparticle Pickering emulsions (i.e. liquid-liquid interfaces) are used to produce mineralized capsules. Different mineralization solutions are tested and the formation of compact mineral shells is investigated after different incubation times and exchange of the mineralization solution.

The presented work can be summarized as follows: After characterization of the bionanoparticles (chapter 4), the adsorption kinetics at liquid-liquid interfaces is investigated (chapter 5) and the surface or interface of bionanoparticle Pickering emulsions is structurally characterized (chapter 6). After identification of the parameters for the mineralization of solid surfaces, liquid-liquid interfaces are mineralized with

hydroxy apatite to obtain biocompatible interfaces and mineral capsules (chapter 7). In depth theoretical background of the kinetic modelling and a detailed description of applied analytical methods is given in chapter 2.

Each part implies significant importance to applied and technological aspects. Protein adsorption phenomena³⁵⁶ and protein³⁵⁷ and particle stabilized emulsions³⁵⁸ play an important role in food technology^{359, 360} and cosmetics³⁶¹. The investigation of the adsorption of well-defined large protein particles at liquid-liquid interfaces contributes to the understanding of complex compositions of natural colloids and colloid assemblies or cosmetic formulations containing biomolecules.

SBF has been used in many research works as testing solution to predict biocompatibility, i. e. support of cell adhesion and growth. Development of artificial bone tissues with improved properties and all related medical aspects are expected to have such a tremendous impact on human quality of life in future that the World Health Organization declared 2000-2010 as the “Bone and Joint Decade”.³⁶² But biomineralization experiments in SBF are not only used for testing the biocompatibility of bone substitute materials^{256, 281, 282} or other implants such as semiconductor nanostructures for therapeutic and diagnostic devices.^{363, 364} Biocompatible hydroxy apatite coatings can also enhance mediation of cell differentiation³⁶⁵ or as transporter for the controlled release of pharmaceuticals.³⁶⁶ Knowledge of cell-substrate interaction is the basis for the development of novel devices employing guided cell structures, e. g. in lab-on-a-chip applications, neuronal cell integration etc.^{367, 368}

The biomineralization of Pickering emulsions is reported for the first time as a novel way to produce hierarchically structured composite materials. This principle is not restricted to hydroxy apatite or certain proteins and solution phases. The rich variety of possible systems allows envisaging many applications in the field of cell encapsulation, drug delivery, porous scaffolds for tissue engineering etc. The principle reminds of tenside and polymer phase templated sol-gel synthesis of inorganic materials which had a great impact on the field of regularly structured porous materials.^{369, 370}

2 Theoretical Background and Methods

2.1 Modelling Protein Adsorption at liquid-liquid Interfaces

2.1.1 Quantitative Description of Equilibrium Surface Tension of Protein Solutions²⁰³

2.1.1.1 Adsorption at Low Protein Concentrations

The following derivation is adequate for the description of mixtures of different components as well as for a surface mixture of different states of one component. As the aim of the following chapter is the development of a surface equation of state for proteins, the text is formulated based on the latter system.

The partial molar surface area of an adsorbed protein can vary between a maximum value ω_{\max} and a minimum value ω_{\min} which reflect the proteins' geometrical dimensions but not necessarily that of their native conformation. "Neighbouring" conformations differ by a constant incremental value $\Delta\omega$ that can be chosen equal to the molar area of a solvent molecule or the area occupied by a protein segment, e. g. amino acid, and is much smaller than ω_{\min} . With the total number n of possible states of the protein, it follows $\omega_{\max} = \omega_1 + (n-1)\Delta\omega$ and $\omega_i = \omega_1 + (i-1)\Delta\omega$ with $1 \leq i \leq n$ and $\omega_{\min} = \omega_1$. The actual value of ω reflects how much the protein at the interface is unfolded. It has been shown that the degree of unfolding depends on the specific protein due to its molecular structure and on the interaction with the non-polar phase.

The total protein adsorption Γ is given as sum over all adsorptions Γ_i of the protein in

the different states i : $\Gamma = \sum_{i=1}^n \Gamma_i$. The total surface coverage results in $\theta = \omega\Gamma = \sum_{i=1}^n \omega_i \Gamma_i$.

Obviously, ω is the mean weighted molar area average over all n states of the protein in the interfacial layer.^{218, 227}

The derivation starts with the generalized Butler's equation³⁷¹ for the chemical potential of each component in the bulk phase (superscript α) and surface (superscript s):^{203, 224}

$$\begin{aligned}\mu_i^s &= \mu_i^{0s} - RT \ln f_i^s x_i^s - \gamma \omega_i \\ \mu_i^\alpha &= \mu_i^{0\alpha} - RT \ln f_i^\alpha x_i^\alpha\end{aligned}\quad \text{Eq. 6}$$

μ_i represents the chemical potential of each component i . Superscript 0 denotes the state in standard conditions, f_i are the activity coefficients, $x_i = N_i / \sum N_i$ are the molar fractions with N_i and N_0 the number of moles of state i and solvent, respectively, γ is the surface tension and ω_i the partial molar area of the component i . Partial molar areas depend on the way how the surface is defined. The dividing surface is chosen such that the total surface area is given by $A = \sum_{i=0}^n \omega_i N_i^s$. The following convention

$\omega_0 \neq \omega = \sum_{i=1}^n \omega_i \Gamma_i / \sum_{i=1}^n \Gamma_i$ satisfies this condition. It assigns a positive (however not necessarily physical meaningful) value for the partial molar area of the solvent and an average value for the adsorption state of the adsorbed molecules. The total surface excess is then given by $\sum_{i=0}^n \Gamma_i = 1/\omega_0 + (1 - \omega/\omega_0) \sum_{i=1}^n \Gamma_i$.²⁰³ By this equation a Gibbs

dividing surface is defined in a different way than the usual Gibbs convention where the excess of solvent Γ_0 has a zero value. Then, a general surface equation of state and adsorption isotherm for each surface active component i in an ideal diluted bulk solution can be obtained:^{203, 224}

$$\begin{aligned}\ln \left(\frac{f_0^s x_0^s}{f_0^\alpha x_0^\alpha} \right) &= -\frac{\Pi \omega_0}{RT} \\ \ln \frac{f_i^s x_i^s / f_{i0}^s}{K_i f_i^\alpha x_i^\alpha / f_{i0}^\alpha} &= -\frac{\Pi \omega_i}{RT}\end{aligned}\quad \text{Eq. 7}$$

$\Pi = \gamma_0 - \gamma$ represents the surface pressure with γ_0 as the surface tension of the pure solvents. $K_i = (x_i^s / x_i^\alpha)$ is the distribution constant at infinite dilution ($x_i^\alpha \rightarrow 0$ or $\Pi \rightarrow 0$). Additionally, in this equation activity coefficients at conditions for infinite

dilutions of the surface active components (subscript 0) have been introduced because they are experimentally better accessible than the pure state that is defined as the standard condition²²⁴. The values of the molar fractions x_i^s are expressed in terms of the surface area fractions (coverages) $\omega_i\Gamma_i$ with ω_i the partial molar surface area through $x_k^s = \omega_k\Gamma_k / n_k \sum_{i \geq 0} (\omega_i\Gamma_i/n_i)$ where $n_i = \omega_i/\omega_0$.^{203, 372} The activity coefficients f_i^s are also expressed in terms of coverages.

The non-ideality in Gibbs-free energy due to intermolecular interaction and varying partial molar areas has to be included into the activity coefficients f_i^s .²⁰³ The enthalpic contribution to non-ideality is determined by intermolecular interactions and can be estimated by a first-order model. For a binary surface mixture of equal-area molecules, this would result in a Frumkin equation of state. The enthalpic part has been derived as²⁰³

$$\ln f_0^{sH} = a\omega^2\Gamma^2, \quad \ln f_i^{sH} = an_i\omega_0^2\Gamma_0^2 \quad \text{Eq. 8}$$

A first order Flory-type model was employed to account for the entropic contribution to non-ideality and derived as²⁰³

$$\ln f_j^{sE} = 1 - n_j \sum_{i \geq 0} (\omega_i\Gamma_i/n_i) + \ln \left[n_j \sum_{i \geq 0} (\omega_i\Gamma_i/n_i) \right] \quad \text{Eq. 9}$$

As final result a surface layer equation of state is obtained:

$$-\frac{\Pi\omega_0}{RT} = \ln(1 - \omega\Gamma) + (\omega - \omega_0)\Gamma + a(\omega\Gamma)^2 \quad \text{Eq. 10}$$

Π is the surface pressure, a is a Frumkin-type intermolecular interaction parameter and ω , ω_0 and Γ are partial molar areas and the adsorption, respectively, as defined above. Compared with earlier models, this equation generalizes the model in ref.³⁷² Further, it expands and corrects the equations that were derived by Miller, Fainerman and coworkers earlier^{223-225, 229, 373, 374} and were used in a few studies.^{202, 375, 376} The

entropic contribution was not considered properly there due to a different choice of the Gibbs dividing interface. The contribution of non-ideality was summarized in a constant that has been mainly characterized as an electrostatic interaction.

The adsorption isotherm for each state j of the adsorbed protein reads²⁰³

$$b_j c_0 = \frac{\omega \Gamma_j}{(1 - \omega \Gamma)^{\omega_j / \omega}} \exp[-2a\omega \Gamma (\omega_j / \omega)] \quad \text{Eq. 11}$$

where c_0 is the bulk protein concentration (assumed to be constant) and b_j is the adsorption equilibrium constants for the j th state. It will be assumed that b_j is constant over all n states, i. e. $\sum b_j = n b_j$.²⁰³ The distribution function for the adsorption of the j th state of a protein molecule can then be expressed as a function of the total adsorption:²⁰³

$$\Gamma_j = \Gamma \frac{(1 - \omega \Gamma)^{(\omega_j - \omega_1) / \omega} \exp[-2a\Gamma (\omega_j - \omega_1)]}{\sum_{j=1}^n (1 - \omega \Gamma)^{(\omega_j - \omega_1) / \omega} \exp[-2a\Gamma (\omega_j - \omega_1)]} \quad \text{Eq. 12}$$

In Eq. 12 is the fact contained that at high surface coverage the adsorbed molecule favours states with small partial molar areas.^{219, 227, 372} At very low surface pressures all adsorption states are equally probable.

Further, the implicitly contained Gibbs equation is omitted in Eq. 11 and Eq. 12 by substitution of ω_0 with an average defined by $\omega = \sum_{i=1}^n \omega_i \Gamma_i / \Gamma$. This leads to much better agreement of the model to experimental values.²⁰³ This means that in Eq. 10 ω_0 is chosen corresponding to real molecular sizes for the calculation of the solvent activity coefficient while for the definition of the Gibbs dividing surface and Eq. 11 a much larger value for ω_0 is used. Therefore, also the partial molar areas in these equations differ, but are constant.

With this set of equations, the first part (region I and II in Fig. 1) of the surface pressure isotherm can be well modelled, where an increase of the bulk concentration leads to an increase in surface pressure.^{203, 227}

2.1.1.2 Adsorption at High Protein Concentrations

Equations Eq. 10 - Eq. 12 have been used to model successfully the adsorption at low protein concentrations. However, above a certain critical concentration c^* , the respective adsorption Γ^* seems to be independent of the surface pressure Π^* . It is experimentally found that with increasing concentration the adsorption increases further at almost constant surface pressure (region III, Fig. 1).^{199, 205} The corrected model for region III has to consider two-dimensional condensation within the protein layer. The aggregates are assumed to have an average molar area ω_a that is much larger than that of any other state i : $\omega_a \gg \omega_i$. However, the area per molecule in the aggregate is assumed to be equal to that of non-associated molecules. With $\Gamma_a \ll \Gamma_i$ and $\sum_{i=1}^n \Gamma_i \equiv \text{const.} = \Gamma^*$ we obtain $\omega^* \approx \omega \Gamma / \Gamma^* = \omega \Psi$. The equation of state and the adsorption isotherm for the post-critical regime $c > c^*$ transform to²⁰³

$$-\frac{\Pi \omega_0}{RT} = \frac{1}{\Psi} \ln(1 - \omega \Gamma) + (\omega - \omega_0) \Gamma + a(\omega \Gamma)^2 \quad \text{Eq. 13}$$

$$b_j c_0 = \frac{\Gamma_j \omega}{(1 - \Gamma \omega)^{\Psi(\omega_j/\omega)}} \exp\left[-2a \Gamma \omega \frac{1}{\Psi} (\omega_j/\omega)\right] \quad \text{Eq. 14}$$

where

$$\Psi = \frac{\Gamma}{\Gamma^*} \exp\left(\varepsilon \omega \frac{\Pi - \Pi^*}{RT}\right) \quad \text{Eq. 15}$$

ε is a parameter in the range between 0 and 0.2 which accounts for the decrease in partial molar area due to condensation in the interfacial layer. Thus, for the post-critical regime III a single additional parameter Γ^* , calculated via Eq. 10 and Eq. 11 for the

given Π^* is needed. Note that at the critical point $\Psi = 1$ and the two branches coincide.

The phenomena in regime III have been interpreted as formation of bi- or multilayers and interfacial condensation. The adsorption isotherm for the second layer has been described with a Langmuir adsorption model with an adsorption equilibrium constant b_{II} for the second layer (with $b_{II} \ll b$) and a coverage of the second layer proportional to the coverage of the first layer.²⁰² This approach can explain twice as high adsorptions at constant surface pressure for saturated interfaces.²⁰³

2.1.2 Quantitative Description of Dynamic Surface Tensions

The adsorption kinetics of proteins follow different steps: First, the molecule diffuses from the bulk solution to the subsurface (the bulk solution immediately adjacent to the interface), followed by adsorption from the subsurface to the interface with more or less unfolding (surface denaturation).²⁰⁸ This step can be hindered by an adsorption barrier. However, in the course of the following derivation, it will be assumed, that diffusion is the rate determining step and adsorption from the subsurface to the interface is instantaneous. A third step would be interfacial changes of the adsorption layer, e. g. aggregation or multilayer formation. Depending on protein, interface and protein concentration, an induction time is observed at the beginning of adsorption. The surface tension starts to decrease measurable only when a certain minimum surface coverage is reached.²²³

The equation for dynamic surface tensions based on diffusion only has been developed by Ward and Tordai for fresh and non-deformed surfaces:^{223, 226, 377}

$$\Gamma(t) = 2\sqrt{\frac{D}{\pi}} \left[c_0 \sqrt{t} - \int_0^{\sqrt{t}} c_s(t-t') d\sqrt{t'} \right] \text{ or} \quad \text{Eq. 16}$$

$$c(x,t) = c_0 - \frac{2}{\sqrt{D\pi}} \int_0^{\sqrt{t}} \frac{d\Gamma(t-t')}{dt} d\sqrt{t'}$$

In this equation c_0 is the protein bulk concentration, $c_s(t)$ is the subsurface concentration, t the time and t' a dummy integration variable. One boundary condition is Fick's first law at the surface ($x = 0$):

$$\frac{\partial \Gamma}{\partial t} = j = D \frac{\partial c}{\partial x} \quad t > 0 \quad \text{Eq. 17}$$

The second boundary condition is the assumption of an infinite bulk phase:

$$\lim_{x \rightarrow \infty} c(x, t) = c_0 \quad t > 0 \quad \text{Eq. 18}$$

The initial conditions are a homogeneous concentration distribution, a freshly formed interface and zero adsorption:

$$c(x, t = 0) = c_0 \quad \text{and} \quad \Gamma(t = 0) = 0 \quad \text{Eq. 19}$$

With Eq. 16 the surface concentration or the diffusion coefficient can be calculated if one of it is known. However, the problem is that the subsurface concentration $c_s(t)$ is not explicitly known. If the interfacial tension $\gamma(t)$ is determined by the concentration of the solute in the surface $\Gamma(t)$, this holds also true for equilibrium conditions (γ_{eq}, Γ_{eq}). Further, if we assume no activation barrier in the adsorption process and an instantaneous equilibrium between the surface and the subsurface, $\Gamma(t)$ will depend only on the subsurface concentration $c_s(t)$. Under equilibrium conditions when the net-adsorption has ceased, the subsurface concentration equals the bulk concentration: $c_s(t) = c_0$. Therefore the relationship between γ and $c_s(t)$ can be obtained from observations under equilibrium conditions (γ_{eq}, c_0) and no assumption for the surface concentration has to be made. This relationship is the surface pressure isotherm. The isotherms Eq. 11 and Eq. 14 are used and serve additionally as boundary condition.

It is important to point out, that the key for the equation of Ward and Tordai is the assumption that the diffusion from the bulk solution to the subsurface is the rate

determining step. The subsurface is very fast depleted, i. e. it is assumed, that the equilibrium between subsurface and surface is quickly established and no barrier is involved. Comparison with experimental data would help to decide about the existence of an adsorption barrier and help to explain sometimes very slow adsorption processes.²²⁶ If the diffusion coefficients that are calculated from Eq. 16 (named here D_s) are much smaller than the conventionally obtained diffusion coefficient D of that system, the adsorption process is obviously hindered by an activation barrier. Besides that, the value of D_s would have no physical meaning as Eq. 16 has been derived under the assumption of instantaneous equilibrium which has been invalidated now. If D_s is of the same order of magnitude as D , the diffusion process to the interface is the rate determining step.²²⁶ Under no means, D_s should become larger than D .

As the equation proposed by Ward and Tordai has been derived for flat interfaces, an additional term has to be introduced to account for the surface curvature in case of bubbles or drops.³⁷⁸

$$\Gamma(t) = 2\sqrt{\frac{D}{\pi}} \left[c_0\sqrt{t} - \int_0^{\sqrt{t}} c(0, t-t') d\sqrt{t'} \right] \pm \frac{c_0 D}{r} t \quad \text{Eq. 20}$$

where r means the radius of curvature. The additional term has to be added for a bubble and subtracted for a drop. The adsorption at the surface of a drop is slower while the adsorption at the surface of a bubble is faster compared to a flat interface.

The application of the equation in combination with the above obtained surface equation of state to experimental data shows good agreement for the initial time of adsorption or low concentrations, where the diffusion stage is longer.²²⁷ This reflects that the equation of Ward and Tordai is just valid in the diffusion regime; however, at long adsorption times, other mechanisms can contribute to the interfacial changes as well that are not considered in the model.

The simple diffusion penetration model allows an estimation of the time until which the diffusion process is completed. This is the case, if the thickness of the diffusion layer $\delta = \sqrt{D\pi t}$ equals the drop radius.

2.1.3 Approximate Solutions for Dynamic Surface Tensions³⁷⁹

To handle Eq. 16, approximate solutions applicable to certain time intervals have been developed. Hansen derived for $t \rightarrow 0$ (i. e. assuming $c_s(t) = 0$):³⁸⁰

$$\Gamma = 2c_0 \left(\frac{Dt}{\pi} \right)^{1/2} \quad \text{Eq. 21}$$

Usually, this approximation holds widely true for short adsorption times or low concentrations.³⁸¹ For the differences between the adsorption at bubbles and drops, the factor cDt/r has to be added or subtracted, respectively,²²³ the factor becomes important for e. g. β -casein at times > 1000 s.³⁷⁸ With the Gibbs adsorption equation

$$d\sigma = -RT\Gamma d \ln c \quad \text{Eq. 22}$$

one obtains for the short time approximation

$$\Delta\sigma_{t \rightarrow 0} = \sigma - \sigma_0 = -2RTc_0 \left(\frac{Dt}{\pi} \right)^{1/2} \quad \text{Eq. 23}$$

$$\left(\frac{d\sigma}{dt^{-1/2}} \right)_{t \rightarrow 0} = -2RTc_0 \left(\frac{D_{eff}}{\pi} \right)^{1/2} \quad \text{Eq. 24}$$

In case of the presence of an adsorption barrier, the diffusion coefficient resembles an effective diffusion coefficient in which the adsorption rate constant β is contained:³⁷⁹

$D_{eff} = D \left[1 + 2(D/\pi t)^{1/2} / \beta \right]^{-2}$. For the long time approximation one obtains similarly:

$$\Delta\sigma_{t \rightarrow \infty} = \sigma - \sigma_{eq} = \frac{RT\Gamma^2}{c_0} \left(\frac{1}{\pi Dt} \right)^{1/2} \quad \text{Eq. 25}$$

When setting $c_s(t-t') = c_0$, Eq. 16 can be directly integrated and one obtains.³⁷⁹

$$\Delta\sigma_{t \rightarrow \infty} = \sigma - \sigma_{eq} = \frac{RT\Gamma^2}{2c_0} \left(\frac{\pi}{Dt} \right)^{1/2} + \frac{RT\Gamma^2}{2c_0\beta t} \quad \text{Eq. 26}$$

This result was first obtained by Rillaerts and Joos³⁸² and is the basis for the extrapolation of equilibrium surface tensions via $\sigma_{eq} = \sigma(t^{-1/2})_{t \rightarrow \infty}$. The second term on the right hand side considers the case of an adsorption barrier. The slope of Eq. 25 and Eq. 26 differ by a factor of $2/\pi$.

At long times (i. e. in equilibrium $\Gamma = \Gamma_0$) the slope of the plot σ vs. $t^{-1/2}$ for the Hansen-approximation and Joos-approximation (Eq. 25 and Eq. 26, respectively) is

$$\frac{d\sigma}{dt^{-1/2}} = \frac{RT\Gamma_0^2}{c_0} \left(\frac{1}{\pi D} \right)^{1/2} \quad \text{Eq. 27}$$

$$\frac{d\sigma}{dt^{-1/2}} = \frac{RT\Gamma_0^2}{2c_0} \left(\frac{\pi}{D} \right)^{1/2} + \frac{RT\Gamma^2}{c_0\beta t^{1/2}} \quad \text{Eq. 28}$$

Thus, a linear dependence of $\sigma(t^{-1/2})$ should be expected for diffusion controlled adsorption at long times with the slope given by the right hand side of Eq. 27 and Eq. 28, respectively.³⁷⁹ The term originating from the adsorption barrier would vanish in this case. It has been pointed out that the coincidence of the experimental curve with the purely mathematically correct derivation cannot be a proof of a diffusion mechanism but serve as a criterion for surfactant purity.³⁷⁹

An analysis of these results and comparison to experimental curves show, that Eq. 27 is useful only for $t \gg 50t_d$ (with the characteristic time of a diffusion-controlled adsorption process $t_d = \Gamma_0^2/c_0^2D$) and for low surface coverage.³⁸³ The problem is that for low surface coverage surface active impurities may adsorb in this time interval and

induce significant errors. On the other hand, for short adsorption times, no contribution of impurities is observed, but here the adsorption barrier does not vanish.³⁷⁹ Eq. 28 describes a linear part of the curve in the time range $50 \geq t/t_d \geq 1$, also just for small surface coverages. For longer times, an error results, which is, however, smaller than the one arising from possible surfactant impurities. With increasing impurity concentration, the time at which the impurity becomes effective, is shifted to shorter times. The curves deviate significantly to larger slopes and therefore towards lower σ_∞ . As conclusion, Eq. 28 has been recommended as approximation for the slope for intermediate time intervals. Extrapolation to infinite times yields values that are typically smaller than the real equilibrium surface tensions.³⁸³ Eq. 27 suffers from the need for low surface activity compounds (low surface coverages) and equilibrium conditions where surface impurities may come into play. A simple linear extrapolation of the data curve may yield the best fit in this case.

Equilibrium surface tension values of surfactants can be obtained from Eq. 27 and Eq. 28. For proteins, Wüstneck proposed to use an extrapolation of $d\gamma/dt^{-1}$ rather than an extrapolation of $d\gamma/dt^{-1/2}$.³⁸⁴ Starting from Eq. 28 and after simplification, one obtains:³⁷⁹

$$\frac{d\sigma}{dt^{-1}} = \frac{RT\Gamma^2}{2c_0\beta} \quad \text{Eq. 29}$$

Eq. 29 reflects the presence of an adsorption barrier at large times. Such obtained values are in better agreement with experimental data.²²⁹

2.1.4 Depletion of Droplets

Droplets can be significantly depleted during the course of adsorption of protein, especially at concentrations lower than 10^{-7} mol. The usually much larger reservoir of solution surrounding a bubble is assumed to keep a constant concentration.³⁷⁸ Thus, if experiments are performed to yield the same final surface pressure, the protein adsorption can be calculated in principle through^{223, 385}

$$\Gamma = \frac{V}{S} (c_D - c_B)_{\pi=const.} \quad \text{Eq. 30}$$

where V and S are the volume and surface area of the drop and c_D and c_B are the initial protein concentrations in the drop and the bubble, respectively. Any method, in which the volume- to surface-ratio is large enough can be used instead of the bubble method with the approximation in Eq. 30.³⁸⁶

The differences between bubble and drop experiments are significant. While adsorptions in bubble experiments correspond well to independently obtained data by other methods, the drop method does not allow one to obtain a correct surface tension isotherm for low concentrations.^{386, 387} The isotherm is shifted to higher concentrations. For low concentrations the observed differences in the surface pressure can be attributed to the significant redistribution of protein between the bulk and surface of drops. For high protein concentrations the slower adsorption rate for drops (see Eq. 20) allows the proteins to unfold to a greater extent. The compression and refolding on the drop surface take then a longer time and the (pseudo-) equilibrium surface tension is higher than in the case of adsorption to bubbles.^{223, 378, 387}

2.2 Determination of Interfacial Tension by Axisymmetric Drop Shape Analysis

Several methods are available to measure surface or interfacial tensions of systems out of adsorption equilibrium.^{388, 389} Each of them has a characteristic time window and certain experimental limitations. While improvement of the existing techniques to time ranges below 100 microseconds seems difficult (currently only achievable with growing drop or bubble or maximum bubble pressure methods^{390, 391}), drop shape analysis techniques extend the long time range to hours and days.³⁸⁵ This allows the observation of equilibrium states of adsorption layers that are reached just after long times.

The pendant drop technique is especially suited for the study of liquid-fluid interfaces under dynamic conditions and for extreme experimental conditions, e. g. high temperatures or pressures and viscous liquids. Interfacial tensions of liquid-vapor or liquid-fluid interfaces and contact angles from the shape of sessile and pendant drops and captive bubbles can be obtained contactless. Advanced dosing systems allow the controlled change of the drop volume and experiments to investigate the dilational rheology³⁹²⁻³⁹⁴ and surface relaxation phenomena of adsorption layers.^{395, 396} More importantly, they can be used to keep the drop volume constant.³⁹⁷ The exchange of the bulk solution can be achieved with a coaxial double-capillary allowing the study of relaxation and desorption phenomena.²¹¹ Layer-by-layer assembly on drop surfaces can be prepared with repeated exchanges of the bulk solution, too.³⁹⁸

The physical basis for the determination of interfacial tensions by the analysis of the drop shape³⁹⁹⁻⁴⁰² is the Laplace-Young equation of capillary. It describes the shape of axisymmetric bubbles and drops with the interfacial tension γ and their principal radii of curvature R_1 and R_2 in relation to the pressure difference Δp across the curved interface:

$$\Delta p = \gamma \left(\frac{1}{R_1} + \frac{1}{R_2} \right) \quad \text{Eq. 31}$$

The curvature b at the apex (i. e. the origin) is given by

$$\frac{1}{R_1} = \frac{1}{R_2} = \frac{1}{R_0} = b \quad \text{Eq. 32}$$

Eq. 31 yields for the pressure at the apex $\Delta p_0 = 2b\gamma$ due to the axial symmetry of the interface. In the absence of any other external forces than gravity, Eq. 31 develops to

$$\gamma \left(\frac{1}{R_1} + \frac{1}{R_2} \right) = 2\gamma b - \Delta\rho g z \quad \text{Eq. 33}$$

$\Delta\rho$ is the density difference between the drop phase and the surrounding medium. While surface tension tends to make the drop spherical, gravitation tends to elongate the drop. Both forces balance each other and give the resultant drop shape. Mathematically, the integration of Eq. 33 is straightforward only for cylindrical menisci (i. e. with one $1/R = 0$) but numerical methods can be applied for the special case of axisymmetric drops which is not a significant restriction. The geometrical relations of the drop profile are specified in Fig. 8.

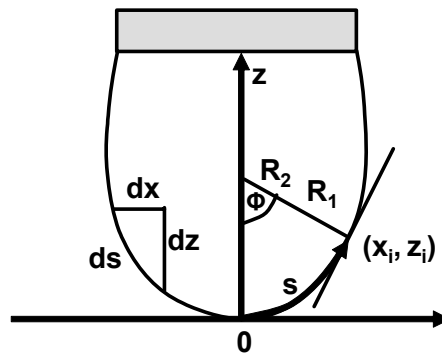


Fig. 8 Geometry of the drop profile.

With

$$\frac{1}{R_1} = \frac{d\phi}{ds} \quad \text{Eq. 34}$$

$$\frac{1}{R_2} = \frac{\sin \phi}{x} \quad \text{Eq. 35}$$

Eq. 36 is obtained:

$$\frac{d\phi}{ds} = 2b + cz - \frac{\sin \phi}{x} \quad \text{Eq. 36}$$

where $c = \Delta\rho g/\gamma$ is the capillary constant and has positive values for sessile drops and negative values for pendant drops. Eq. 36 and the geometrical relations

$$\frac{dx}{ds} = \cos \phi \quad \text{Eq. 37}$$

$$\frac{dz}{ds} = \sin \phi \quad \text{Eq. 38}$$

form a set of first order differential equations for x , z and ϕ as functions of the arc length s . The boundary conditions at the drop apex ($s = 0$) are $x(0) = z(0) = \phi(0) = 0$ and $d\phi/ds = b$. The points $p(x, z, b, c)$ of a theoretical Laplacian axisymmetric liquid-fluid interface curve can be obtained by simultaneous integration over the set of equations for given values of b and c .

The pendant drop tensiometer in its basic version consists of a diffuse light source which illuminates the drop from behind. A CCD-camera and a microscope are used to obtain a magnified image of the drop. The determination of surface or interfacial tension follows two steps. After the acquisition of a drop image and determination of the profile coordinates from the digitized image via edge detection algorithms, a series of theoretical Laplacian profiles are fitted to the experimental coordinates with the interfacial tension γ as adjustable parameter. While in principle a simple method, evaluation of instrumental design, experimental conditions and algorithm development have been proposed just recently. A comprehensive discussion of various possibilities to improve measurements and a detailed analysis of typical errors are given in ref. ³⁹⁹⁻⁴⁰¹.

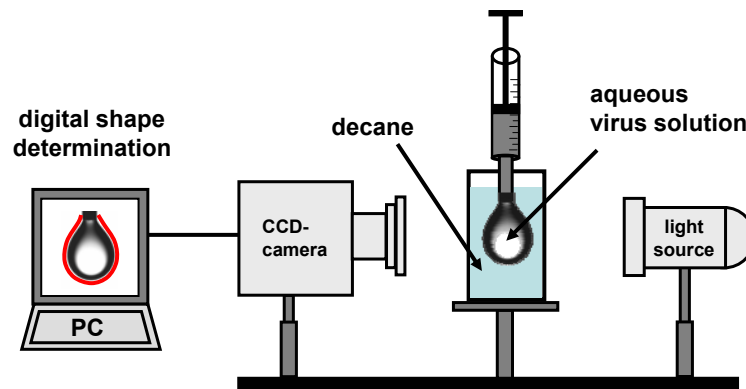


Fig. 9 Schematic experimental setup for pendant drop tensiometry

2.3 Light Scattering Techniques

Light scattering techniques are divided into static light scattering (SLS) and dynamic light scattering (DLS; also termed photon correlation spectroscopy or quasi-elastic light scattering). While the first technique measures a time-averaged total intensity as a function of the scattering angle, the latter records temporal variations in the intensity of the scattered light, usually at a fixed angle of 90° . SLS gives access to the weight average molecular weight M_w , the z-average of the mean-square radius of gyration R_g^2 , and the second virial coefficient A_2 . DLS allows the determination of diffusion coefficients D , hydrodynamic radii R_h and size distributions. In any case multiple scattering (interparticle interference) has to be avoided and thus the measurements are performed in dilute systems. Both light scattering techniques have been applied extensively in colloid chemistry⁴⁰³ and protein characterization.⁴⁰⁴⁻⁴⁰⁶

2.3.1 Static Light Scattering⁴⁰⁷

In this work SLS is used as a detector in size exclusion chromatography, giving access to absolute molecular weights and sizes of the separated fractions. This is of importance as the complex solution structures of proteins do not allow a meaningful calibration. In static light scattering the time-average scattered intensity i_s is measured:

$$\frac{i_s}{I_0} = R_\theta \frac{1 + \cos^2 \theta}{r^2} \quad \text{Eq. 39}$$

The scattered intensity depends on the intensity of the incident light I_0 , the scattering angle θ (unscattered light passes at 0°) and the position r of the scatterer distant from the detector. By using vertically polarized light, no angular dependence of the scattered light in the xy-plane (detection plane) is observed and $1 + \cos^2 \theta = 2$. The Rayleigh ratio R_θ sums up some constants (λ : wavelength of the incident light, n and dn/dc : refractive index of the solvent and refractive index increment of the solution, respectively) and contains the weight average molecular weight M_w of the scatterer and

the second virial coefficient A_2 of the solution and reads for incident vertically polarized light

$$R_\theta = \frac{4\pi^2}{\lambda_0^4 N_A} \frac{(n \, dn/dc)^2 c}{(1/M_w + 2A_2c)} \quad \text{Eq. 40}$$

The equation can then be written in a linear form as

$$\frac{Kc}{R_\theta} = \frac{1}{M} + 2A_2c \quad \text{with} \quad K = \frac{4\pi^2 (n \, dn/dc)^2}{\lambda_0^4 N_A} \quad \text{Eq. 41}$$

These equations are valid for small particles (diameter $< \lambda/20$; Rayleigh scattering) in infinitely diluted systems. For small proteins, e. g. BSA with a radius of approximately 3.5 nm, the scattering is independent of the detection angle.

In light scattering of larger particles ($\leq \lambda/20$) intramolecular interference due to scattering from centres on the same particle can occur (Debye-scattering). From the angular dependent scattering the shape and size of the molecule can be obtained. A form factor $P(q)$ is introduced that considers the geometry and the structure of the particle.⁴⁰⁸ The expansion yields

$$P(q) = \frac{i_{s,q}}{i_{s,q=0}} = 1 - \frac{q^2}{3} \langle R_g^2 \rangle + \dots \quad \text{Eq. 42}$$

$q = 4\pi/\lambda \sin(\theta/2)$ is the scattering vector with wavelength λ of the incident light and the scattering angle θ . Solid spheres, rigid-rod particles or Gaussian coils have different form factors, which, however, do not significantly differ in the q -range relevant for light scattering. Information extracted from a comparison of experimental particle scattering curves with calculated $P(q)$ are hardly reliable if light scattering only is concerned.⁴⁰⁷ In the limiting case of small angles, the form factor approaches the value

given by the right hand side of Eq. 42 precisely, independent of the particle shape. After insertion of Eq. 42 into Eq. 41 and simplification the Zimm-Equation is obtained.^{407, 409}

$$\frac{Kc}{R_\theta} = \frac{1}{M_w P(\theta)} + 2A_2c = \frac{1}{M_w} + \frac{q^2 \langle R_g^2 \rangle_z}{3M_w} + 2A_2c \quad \text{Eq. 43}$$

The weight average molecular weight M_w can be obtained from the intercept of a plot of Kc/R_θ versus $q^2 + kc$ (Zimm-plot, k is an arbitrary weighting factor). The mean square radius (also radius of gyration, z-average) $\langle R_g^2 \rangle_z$ and the second virial coefficient A_2 can be evaluated from the two extrapolations $q \rightarrow 0$ (interference free limit) and $c \rightarrow 0$ (interaction free limit), respectively.⁴⁰⁷ Other plots (R_θ/Kc or $\sqrt{Kc/R_\theta}$ vs. q^2 , Debye or Berry method, respectively) can be used interchangeably for small molecules.

The theory described above holds true for the Rayleigh-Gans-Debye (or Born) approximation with the criteria $|n/n_0 - 1| \ll 1$ and $(4\pi na/\lambda_0)n/n_0 \ll 1$ (n and n_0 are the refractive index of the solution and the pure solvent, respectively, λ_0 is the incident wavelength and a the maximum dimension of the particle). The first equation states that the amount of light that is scattered by the particle is negligible compared to the incident beam (diluted conditions); the second states that the total phase change of the wave passing through the particles is negligible compared to a wave passing through the pure solvent only.

In this work, static light scattering is used as a detector in size exclusion chromatography. The concentration in chromatography is already very low and the approximation $c \rightarrow 0$ is valid; thus we get immediately the mean square radius from the slope and the molecular mass from the intercept of the measurement at different angles. It should be remembered, that SLS is applicable just for larger polymers, i. e. usually for proteins larger than 50 kDa.

2.3.2 Dynamic Light Scattering^{410, 411}

The physical background for the fluctuations in the intensity of the scattered light is the thermal movement of the scattering centres in solution (Brownian motion) causing a Doppler shift in the frequency of the scattered light and thus a band broadening. The correlation between the scattered intensity I at time t and after a delayed time $t + \tau$ is mathematically expressed by an autocorrelation function^{411, 412}

$$C(\tau) = \langle I(t)I(t+\tau) \rangle = \lim_{t_n \rightarrow \infty} \frac{1}{t_n} \int_t^{t+t_n} I(t')I(t'+\tau) dt' \quad \text{Eq. 44}$$

where the brackets indicate the temporal average. For time-invariant random processes, the autocorrelation function is independent of t and it can be shown that

$$\begin{aligned} C(\tau) &\rightarrow \langle I(t)^2 \rangle && \text{for } \tau \rightarrow 0 \\ C(\tau) &\rightarrow \langle I(t) \rangle^2 && \text{for } \tau \rightarrow \infty \end{aligned} \quad \text{Eq. 45}$$

The asymptotic value for large delay times τ equals the square of the arithmetic time average, i. e. the intensities of scattering events with long time intervals become independent and are not correlated anymore. For nonperiodic $I(t)$, $C(\tau)$ decreases monotonically from $\langle I(t)^2 \rangle$ to $\langle I(t) \rangle^2$ and the ratio of the autocorrelation function to its asymptotic value gives the normalized intensity autocorrelation function $g_2(\tau)$:

$$\frac{C(\tau)}{\langle I(t) \rangle^2} = \frac{\langle I(t)I(t+\tau) \rangle}{\langle I(t) \rangle^2} = g_2(\tau) \quad \text{Eq. 46}$$

Standard instruments measure the intensity of the scattered light by photon counting which gives a proportional intensity signal (homodyne mode) and thus directly $g_2(\tau)$. However, for further analysis the normalized electric field autocorrelation function $g_1(\tau)$ is the key function. The necessary relation is the Siegert equation:^{412, 413}

$$g_2(\tau) = A \left(1 + B |g_1(\tau)|^2 \right) \quad \text{Eq. 47}$$

where A and B are the background and a coherence factor, respectively. For dilute and non-interacting dispersions the intensity fluctuations are caused by single-particle motion. For monosized, hard spherical particles, $g_1(\tau)$ resembles an single exponential decay curve

$$g_1(\tau) = e^{-\Gamma\tau} \quad \text{Eq. 48}$$

and with the scattering vector $q = 4\pi n/\lambda \sin(\theta/2)$ (λ : wavelength of incident light; n : refractive index of the medium; θ : scattering angle) we obtain the translational self-diffusion coefficient D_0 of the unhindered Brownian motion through^{410, 411}

$$\Gamma = D_0 q^2 \quad \text{Eq. 49}$$

With the well-known Stokes-Einstein relation

$$D_0 = \frac{k_B T}{6\pi\eta R_H} \quad \text{Eq. 50}$$

(η : viscosity of the medium) we obtain the hydrodynamic radius R_h which means the radius of a sphere with the same hydrodynamic properties as the particle under investigation.

A degree of polydispersity can lead to deviations from single exponential behaviour. In this case the decay of the autocorrelation function is a superposition of the single exponential decays from the respective monodisperse fractions of the sample and can mathematically expressed by

$$g_1(\tau) = \int_0^{\infty} G(\Gamma) e^{-\Gamma\tau} d\Gamma \quad \text{Eq. 51}$$

where $G(\Gamma)d\Gamma$ represents the fraction of the scattered intensity from particles with decay rates from Γ to $\Gamma + d\Gamma$. To obtain $G(\Gamma)$ from $g_1(\tau)$, mainly two methods are used today: CONTIN analysis uses a modified Laplace transformation of $g_1(\tau)$.⁴¹⁴⁻⁴¹⁶ In order to limit the number of possible solutions, a regularization is applied (thus also called regularization fit). CONTIN is especially useful for broad and multimodal distributions but is sensitive to artefacts from the integration process.⁴¹⁷ For a successful application of CONTIN, two species should differ in their respective hydrodynamic radii at least by a factor of two and the measurement should have a good signal to noise-ratio. The cumulant method is a polynomial fitting procedure by $\ln g_1(\tau) = \ln A - \mu_1\tau + 1/2!\mu_2\tau^2 - 1/3!\mu_3\tau^3 + \dots$ (μ_1, μ_2, \dots : cumulants).⁴¹⁸ The initial slope μ_1 (first cumulant) can be interpreted as an average decay rate $\langle\Gamma\rangle$ from which the average hydrodynamic radius $\langle R_h \rangle_z$ can be obtained. $\mu_2 = \langle(\Gamma - \langle\Gamma\rangle)^2\rangle$ is the variance of the distribution. Hence, μ_2/μ_1^2 characterizes the relative variance of the particle size distribution, commonly referred to as the polydispersity index. Both methods, CONTIN and cumulant analysis, give z-averages of the decay rate and the hydrodynamic radius, respectively.⁴⁰⁴

The obtained diffusion coefficients are apparent values that have to be corrected to zero angle and concentration by $D = D_0(1 + k_d c)$ (D apparent or perturbed diffusion coefficient).^{355, 419} The parameter k_d is connected with the thermodynamic solution properties of the particles through $k_d = 2A_2M_w - k_f - 2\nu$ where k_f is the frictional coefficient and ν is the partial specific molar volume of the solute.⁴⁰⁴

Rotational motions and internal dynamics, e. g. segment relaxations in large macromolecules, can lead to additional intensity fluctuations and have to be considered. Extrapolation to zero angle eliminates these contributions. The rotational diffusion coefficient can be measured with depolarized dynamic light-scattering (DDLS). The

decay Γ_{vH} of the time-dependent depolarized scattered intensity (vertically polarized incident light) is attributed to both, translational and rotational motion, with their respective diffusion coefficients:⁴²⁰

$$\Gamma_{vH} = D_t q^2 + 6D_r \quad \text{Eq. 52}$$

The rotational diffusion coefficient D_r is connected through rather complicated expressions with the dimensions of the scattering object.^{420, 421} Since the depolarized scattering intensity is weak, special instrumentation is needed and few examples can be found in literature employing this method.⁴²¹ The pioneering experiments on DDLS have been performed with tobacco mosaic virus.⁴²²⁻⁴²⁴

From a combination of SLS and DLS measurements the ratio R_g/R_h can be obtained which is sensitive to the shape of particles. For rodlike particles a value larger than two is expected.⁴⁰⁴

2.4 Size Exclusion Chromatography

Liquid chromatography is one of the most widespread analytical techniques in laboratories. In biochemistry, quite a few variants with different separation mechanisms are commonly in use.⁴²⁵ RP-HPLC (reversed-phase high-performance liquid chromatography; hydrophobicity), IEC (ion exchange chromatography; ionic interactions), HIC (hydrophobic interaction chromatography; hydrophobic interactions), IMAC (immobilized metal ion affinity chromatography; metal-chelate mediated interactions) and SEC^{333, 426, 427} (size exclusion chromatography, also gel permeation chromatography, GPC; hydrodynamic volume) are the most important to mention. The detection of the analyte with UV, RI or conductivity detectors allow more or less just to monitor the separation process but yield no direct further physical information. Laser light scattering (LS) detection in liquid chromatography has some advantages as it allows the on-line evaluation of the mass and size of proteins. Especially in biotechnology industry and pharmacological formulations the molecular weight is not

the only parameter of interest but also particle size, reflecting their conformation and related biological functions. Aggregation states, complexation with macromolecules or conjugation with ligands need a contact-less, non-destructing method for investigation. Protein molecular weights can be measured conveniently with gel electrophoresis under denaturing conditions (SDS-PAGE) or through mass spectrometry techniques, particularly by matrix-assisted laser desorption/ionisation (MALDI) and electrospray ionisation (ESI), techniques, that allow the mild desorption and ionisation of even large proteins.^{428, 429} However, both techniques destroy the three-dimensional structure of the sample molecules. Analytical ultracentrifugation is a valuable method for the analysis of proteins in their native conformation but is still a cumbersome and moreover quite slow technique (runtimes few hours to days).⁴³⁰⁻⁴³³ Light scattering techniques on the other hand are non-invasive, non-destructive and a fast technique that allow absolute determination of the molecular mass and structure, covering a broader range of these values than any other technique.

The coupling of size exclusion chromatography with on-line multi-angle laser light scattering (MALLS) allows simultaneous separation and analysis of polydisperse samples with low sample amount.⁴³⁴ Absolute molecular weight detection is especially important for protein chromatography. For globular, compact “standard” proteins a calibration curve can be established,⁴³⁵ but for a different conformation the molecular weight is not generally correlated to the size of the molecule and thus not to the elution volume, too.⁴³⁶ A general calibration with protein standards is not feasible. With LS detection the absolute size and molecular weight can be determined independent of the elution volume. Any separation mechanism can be used and column-solute interactions have not to be accounted for.⁴³⁴ Field flow fractionation (FFF) became due to recent technological improvements a reliable separation method, too, in which light scattering detection can be employed. The advantage is the significant larger size range which can be separated in FFF.⁴³⁷ In combination with on-line dynamic light scattering the hydrodynamic radius can be obtained.^{438, 439} Knowing both radii allow a conclusion of the conformation of the molecule or complex. The same information can be obtained from quadruple detection with an additional viscosity detector.⁴⁴⁰

The relation for the molecular weight determination with light scattering is Eq. 43:

$$\frac{Kc}{R_\theta} = \frac{1}{M_w P(\theta)} + 2A_2c \quad \text{Eq. 43}$$

In each elution slice, the concentration is determined with a concentration detector, either RI or UV. Further, A_2 and dn/dc must be known. The A_2 -term can be usually ignored as the concentration in chromatographic runs is very low.^{333, 434} For small molecules the scattering shows no angular dependence. $P(\theta)$ approaches unity for small particles and/or small angles and can be set approximately so for proteins with $\langle R_g^2 \rangle^{1/2} \leq 15$ nm.⁴²⁶ Eq. 43 simplifies to $Kc/R(\theta) = 1/M_w$ and the molecular weight can be obtained from the measurement at one angle (known also as “low angle laser light scattering”, LALLS).^{434, 441-443}

The output of the LS detector can be expressed with a calibration constant K_{LS} including the other constants: $(LS) = K_{LS}cM_w (dn/dc)^2$. Similarly, the refractive index (RI) signal can be expressed as $(RI) = K_{RI}cM_w (dn/dc)$ where K_{RI} is the RI instrument calibration constant. With both equations, the molecular mass can then be calculated according to (two-detector method):^{333, 426, 427}

$$M_w = \frac{K_{RI}}{K_{LS}} \left(\frac{dn}{dc} \right) \frac{(LS)}{(RI)} \quad \text{Eq. 53}$$

The molecular weight thus obtained is not based on a “true” light scattering measurement; rather, the factor $(K_{RI}/K_{LS})dn/dc$ is measured through a protein standard, e. g. BSA.

For molecules that are “homo“-polypeptides, an average value $dn/dc = 0.187$ can be usually assumed. A drawback is the limited sensitivity of the concentration detectors (RI or UV) in the case of high molecular weight analytes with low concentrations. In cases where dn/dc is not known or constant, the refractive index increment has to be

determined separately. The tabulated values for a given wavelength (mostly mercury lines) have to be corrected as dn/dc depends non-linearly on λ :

$$\left(\frac{\partial n}{\partial c}\right)_{\lambda} = \left(A + \frac{B}{\lambda^2}\right) \left(\frac{\partial n}{\partial c}\right)_{546\text{nm}} \quad \text{Eq. 54}$$

The factor is 0.99 for proteins for the correction from 546 nm to 620 nm.⁴⁴⁴⁻⁴⁴⁶ Further, the value depends sensitively and non-linear on solution properties (buffer type, ionic strength, temperature).⁴⁴⁶⁻⁴⁴⁸

Generally, for most viruses, dn/dc is not known. It cannot be calculated like for proteins with incremental values for the amino acids as a significant part of the virus consists of polynucleic acid. Besides that, signal intensities are very low compared to the UV signal. The concentration is therefore determined by the UV-detector (three detector method):^{333, 427}

$$M_w = \frac{K_{RI}^2}{K_{LS} K_{UV}} \frac{1}{\varepsilon} \frac{(LS)(UV)}{(RI)^2} \quad \text{Eq. 55}$$

$(UV) = K_{UV} c \varepsilon$ is the signal output of the UV-detector. The extinction coefficient ε is usually determined experimentally and available as concentrations of any biomolecular samples are routinely estimated through absorption spectroscopy. It is clear, that in return ε can be determined from the signal intensities of the UV and RI detector, if dn/dc is known.⁴²⁷ It must be emphasized that dn/dc must be exactly known or measured with an exact calibrated RI detector and UV detector. The three-detector approach allows the measurement of the mass of the polypeptide component in conjugated proteins as ε can be calculated for the pure polypeptide content and dn/dc can be set to 0.187.^{333, 427, 449}

With the ASTRA-software⁴⁵⁰ scattering from multi-angle detection can be fitted according to the Zimm, Debye, Berry or random-coil method. According to Eq. 43 the

absolute weight average molecular weight M_w and mean square radius $\langle R_g^2 \rangle$ is calculated. All methods give similar results for small molecules.^{426, 427}

2.5 Transmission Electron Microscopy

In transmission electron microscopy electrons are allowed to transmit the thin (≤ 150 nm) specimen. The image is originating from electrons scattered by the sample. According to Abbe, the resolution g is restricted by the wavelength according to $g = 0.61\lambda/n\sin\alpha$ with λ : vacuum wavelength, n : refractive index and α : aperture half angle of the objective lens (typically $1-2^\circ$). For electrons, much lower wavelengths (according to de Broglie: $\lambda = h/mv$, λ : wavelength, m , v mass and velocity of electrons) can be achieved than are used in optical microscopy. The wavelength of the electrons depends on the acceleration voltage of the electron gun, which is typically 80 kV and higher. This explains the much higher theoretical spatial resolution (0.1-0.2 nm) of transmission electron microscopes compared to optical microscopes. The practically achievable resolution is determined by the electron optical system (spherical and chromatic aberration) and the sample (thickness, radiation damage). According to the rule of Cosslet, resolution cannot be better than 1/10 of the sample thickness.

Electrons that are emitted from an electron gun pass through the condenser lens which focuses the beam onto the sample. Tungsten hairpin cathodes or LaB₆-cathodes are used as electron guns, the later having stronger brightness. The electron gun is usually built as a triode (Wehnelt configuration) with a cylinder hole cathode at a more negative potential than the hairpin cathode and a hole anode. The Wehnelt configuration has a focusing action producing a crossover between the Wehnelt cylinder and the anode which is demagnified by the electron optics onto the specimen to yield the final beam size. The electrons that are shining through the specimen are magnified by the objective and projector lenses onto a fluorescent screen or a CCD-camera. Lenses can be built as magnetic, electrostatic or compound lenses to focus the beam. Additional coils are used to correct the spherical aberration.

The electron beam can interact with the sample in different ways (Fig. 10). Inelastically scattered electrons produce a diffuse contrast-reducing background and have to be eliminated by apertures and energy filtering. Energy filtering can be achieved e. g. by a combination of magnetic and electric fields in omega-shaped energy filters. Elastically scattered electrons keep their energy and produce the scattering absorption contrast and phase contrast image when interfering with another or the unscattered beam. Many instruments offer three modes of imaging, elastic and inelastic dark field imaging (“imaging with the scattered electrons”) and bright field imaging (“imaging with the directly transmitted electrons”).

In cryo-transmission electron microscopy (cryo-TEM) the sample is flash-frozen and the molecules are embedded in vitreous ice. As the contrast between protein and solvent is usually very low, high resolution images have to rely on image reconstruction procedures. Cryo-TEM resolution can reach 1 nm and below. In scanning transmission electron microscopy (STEM), an electron beam with a diameter of only a few Å or nm is used to scan the sample area. Recent significant technological improvements allow sub-nm resolution.

The sample is either thinly spread on a filmed grid or cut into thin sections. In the first case, carbon sputtered or poly(vinylacetate)-coated (Formvar, Pioloform) grids are available. For thin sectioning, ultrasharp diamond knives in an ultramicrotome are used that allow the consistent semi-automatic preparation of sections with a typical thickness of 50-70 nm. The phase contrast at high resolutions is often quite weak, especially in microbiology where the samples usually do not contain atoms of high weight that scatter electrons a lot. To enhance the contrast, negative staining has been developed.⁴⁵¹⁻⁴⁵³ The sample is surrounded by electron-dense material, usually a salt from a heavy metal (e. g. uranyl acetate or phosphotungstic acid). The object under investigation appears bright against the darker background, thus the term negative staining. Negative staining tolerates various additives and can aid resolution down to 1-2 nm.⁴⁵⁴ Other methods include gas phase staining with RuO₄ or OsO₄ which is mainly used for polymeric thin films.

2.6 Scanning Electron Microscopy

The great advantage of scanning electron microscopy (SEM) is founded in its much larger depth of field, brilliant image contrast and the extremely wide range of magnification, ranging from 10 to over 100000 fold. A finely focused electron beam is scanned with deflection coils line by line over the sample. The long focal length allows a large working distance (distance between sample surface and lower pole piece of the electron optics) which is needed to collect sufficient signal intensity with the detectors that are placed above the sample. If electrons hit the sample, different interactions can occur, resulting in a different yield of secondary electrons which are converted to a grey-level image. Other signals, generated by the interaction of the electron beam with the sample, carry different information and can be mixed to obtain images with multidimensional information.

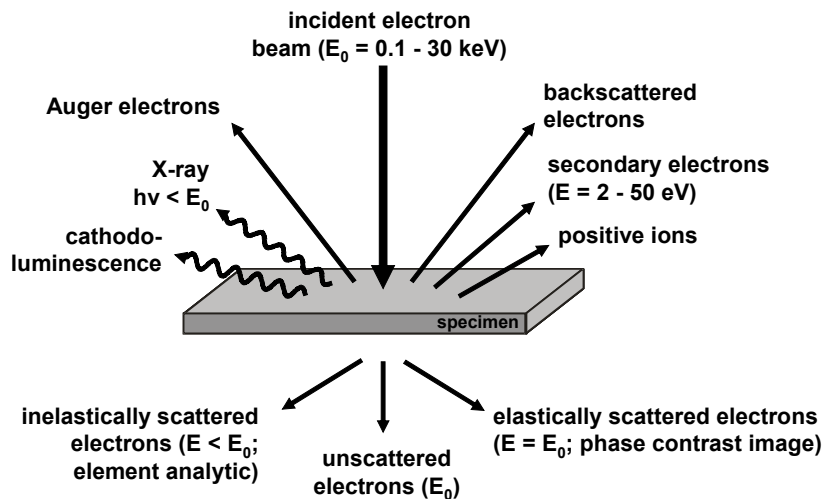


Fig. 10 Interaction of an incident electron beam with a thin sample

The electron beam can interact with the sample through elastic scattering, giving rise to backscattered electrons (BSE) or through inelastic scattering, causing secondary electrons (SE), Auger electrons, cathodoluminescence and X-rays (Fig. 10, Fig. 11). Usually, the image in SEM is acquired through secondary or backscattered electrons. Secondary electrons emerge from a depth of 5-50 nm. The escape depth depends on the atomic number and material composition as well as electronic properties of the sample. The yield of SE increases with the atomic number but is above a certain threshold independent of beam electron energy. SE are collected through an electric field and

detected by an Everhart-Thornley detector which is based on scintillation detection and signal amplification by a photomultiplier. For high resolution, the working distance has to be reduced to a minimum and the sample comes very close to or is even moved inside the lower pole piece. Thus, the sample is immersed into the field of the objective lens of the lower pole piece. Secondary electrons are caught on a spiral path upwards in the magnetic field of the lens and are detected on an electrostatic detector of annular type above the objective lens. This combination is known under the trade name “Gemini lens”. In-lens detection is advantageous for low-voltage SEM because it combines excellent image resolution with high collection efficiency at low electron energies.

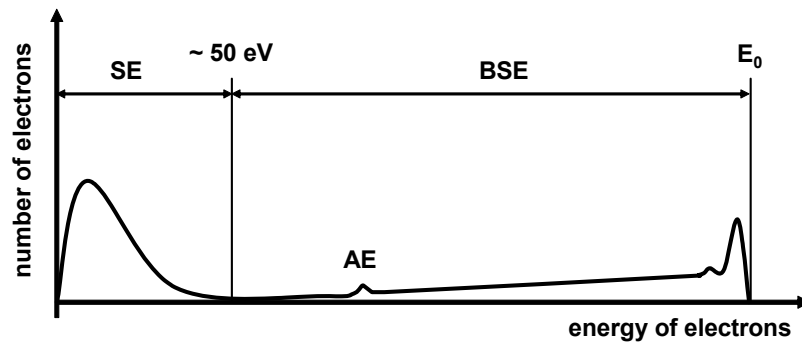


Fig. 11 Schematic energy distribution of electrons emitted upon interaction with the fast electrons of the primary beam. SE: secondary electrons; BSE: backscattered electrons; AE: Auger electrons; E_0 : incident electron beam energy.

Backscattered electrons (BSE) probe depths up to some microns and their yield is independent of atomic weight for heavier elements but depend on incident beam energy and detector position. For BSE detection microchannel plate detectors are used because Everhart-Thornley detectors show very low collection efficiency for high energy electrons. Cathodoluminescence (CL) is the emission of photons which are emitted during recombination of excited electrons and holes that have been generated by the electron beam. CL is often encountered with insulators and semiconductors. The spectrum of X-rays in SEM is composed of a continuum superimposed with an X-ray spectrum. X-rays are generated either from deceleration of electrons (continuum or bremsstrahlung) or from element characteristic electron transitions which can be used for element microanalysis (see below).

Contrast and resolution in SEM depends in a complex manner on instrument technology (beam energy, beam diameter, sample bias, signal detection, amplification and processing) and the electron-sample interaction (material contrast, surface charge distribution, magnetic contrast, crystal orientation). The secondary electron yield depends on the angle of incidence of the electron beam at the surface and the orientation of the surface related to the Everhart-Thornley detector. Edges and protruding surface features give larger SE yields because diffusely scattered electrons can pass through them. Charging artefacts of insulating objects can cause overbrightening, too. The contrast in BSE detection depends significantly on the detector orientation because only electrons with a straight sample-detector trajectory are detected and a pronounced shadow effect for protruding objects is observed.

An important technical improvement was the development of scanning electron microscopes with field emission electron guns. Their small beam diameter of 1 nm or less and low acceleration voltages allow high resolution imaging. Field emission electron guns can be divided into cold field emission guns (CFE) or thermal field emission guns (TFE), the first having a smaller energy spread and allow higher resolutions at low acceleration voltages. Both need excellent gun vacuum conditions.

Resolution of the SEM is basically limited by the diameter of the electron beam but SE and BSE emerge from an interaction volume and surface area significantly larger than the beam diameter (Fig. 12). If the field of view at the sample surface approaches the lateral size of the excitation volume, SE and BSE which emerge from bulk atom interactions (SE2 and BSE2) will not change to smaller surface features but the SE1 and BSE1-yields which arise from direct interactions with the topmost atomic layers will depend sensitively on local features as small as the beam diameter. High resolution imaging is therefore essentially restricted to SE1 and BSE1. In low energy SEM, SE2 and BSE2 fall together with SE1 and BSE1 due to the much lower penetration depth. SE are generated near the surface and can escape more easily, the SE yield increases up to one and the specimen current becomes zero. For low energy electrons, inelastic scattering is reduced and radiation damage also, a clear advantage in soft matter science. Biological specimens often contain no or few atoms of high weight and a significantly worse signal-to-noise ratio prohibits high resolution imaging. If, however, the samples

are sputter-coated with a thin metal film, SE1 and BSE1 generation is confined to this layer and high resolution imaging conditions can be successfully applied.

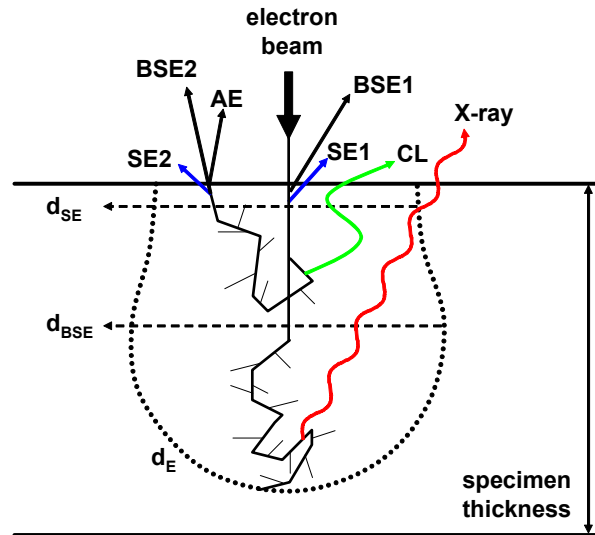


Fig. 12 Schematic illustration of signal generation in a thick specimen upon interaction with an electron beam. SE: secondary electrons; BSE: backscattered electrons; AE: Auger electrons; CL: cathodoluminescence; d_{SE} and d_{BSE} : escape depth for SE and BSE, respectively; d_E : electron interaction range (dotted line).

The interaction of the incident electrons with the sample can be used for analytical purposes.⁴⁵⁵ If a primary electron excites a bound electron in the shell of a sample atom, a hole is created which can be filled by electrons from higher energy levels. The energy can be released as X-ray photons or through the emission of secondary electrons (Auger-electrons). The former are analysed in energy dispersive X-ray spectroscopy (EDX).

The emitted X-ray photons have typically energies in the range of few hundred to some thousand electronvolts. Each element produces a characteristic series of peaks from the quantum-mechanically allowed transitions. Spectroscopic information cannot be obtained due to the high energies of the incident electrons involved. The peaks are superimposed by a continuum non-characteristic background (Fig. 13). Non-characteristic contributions to signal intensity arise from X-rays generated from back-scattered and stray electrons hitting microscope components. The maximum possible energy is given by the incident electron energy (Duane-Hunt limit).

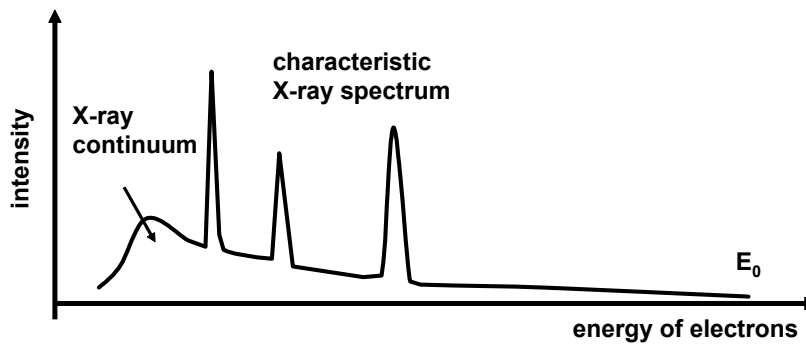


Fig. 13 Schematic X-ray spectrum emitted from a specimen upon interaction with fast electrons of the primary beam (E_0 : Duane-Hunt limit).

To quantify the element concentrations, the spectrum has to be corrected for different cross sections, fluorescence and absorption in the sample and detector. The technique is not suitable for detection of trace elements and accuracy is limited to a few percent. Compared to X-ray photoelectron spectroscopy (XPS) which probes just the topmost few atomic layers, EDX is a “bulk” analysis technique since the interaction volume of the primary electrons is quite extended which sets also the practical limit for the obtainable lateral resolution ($\sim 1 \mu\text{m}$). The increased probe size due to the larger working distance and higher probe current do not count in this respect. X-ray detection is based on the photoelectric effect. X-rays imping on a Li-doped silicon layer and create electron-hole pairs (one pair/3.8 eV). A bias is applied between gold electrodes on the front and back of the silicon layer and the current is amplified by a field emission transistor (FET). The detector is cooled with liquid nitrogen to prevent Li-diffusion into the electric field and to reduce the detector noise. The FET must be reset to avoid saturation of the signals if the integrated signal reaches a threshold level. Low processing speed results in more accurate determination of the X-ray energy but implies a detector dead time during which the detector is not able to process more incoming photons. Nevertheless, modern instruments allow dead times up to 60 % up to which the output count rate remains linear with the input count rates.

2.7 Atomic Force Microscopy (AFM)

Surface probe microscopy techniques use probes that are approached to a few nm to the sample surface where they experience a surface force field. In atomic force microscopy

(AFM), a sharp probe tip is approached.³ It experiences long range attractive forces (van-der-Waals forces, electrostatic or magnetic forces) which are overcome at very short distances by repulsive interatomic forces.⁴⁵⁶ The cantilever, onto which lower side the probe tip is mounted, experiences a deflection down- or upwards that is amplified by a reflected laser beam which points to a position-sensitive split photodiode. Piezoelectric scanners move either the sample or the probe head with the cantilever and the tip, respectively, to scan the sample surface area.

In contact mode, the probe tip is in continuous contact with the sample. If the distance between tip and sample reference surface is kept constant, the cantilever is deflected when scanned over a surface feature. Excellent height resolutions and high scan rates are possible but just for samples with low surface roughness otherwise the tip can be easily damaged, collect material or may damage the sample. In constant force mode, the height image is generated from the vertical movement of the z-piezo that is necessary to keep the deflection constant. The height thus depends on the tip-surface interaction.

In dynamic force mode, the tip is in “no” contact⁴⁵⁶ or intermittent contact (also termed tapping mode)⁴⁵⁷ with the sample. The cantilever is excited with a piezo to an oscillation near its resonance frequency. In non-contact mode, the measurement is done at attractive interactions (measurement frequency larger than resonance frequency). In tapping mode, the setpoint is chosen a little bit lower than resonance frequency. The height image is generated in both cases from the z-piezo movement that is necessary to keep the amplitude at the chosen setpoint. In case of repulsive interaction, a phase shift is registered additionally to the amplitude damping that is related to the viscoelastic properties of the sample and hence gives a material contrast.^{458, 459} For hard tapping conditions, the soft material shows a larger phase shift while for soft tapping conditions attractive forces dominate the interaction and no straightforward interpretation is possible. This last case is observed particularly for biological samples which are always covered by a hydrophilic aqueous film in the humid laboratory environment. Tapping mode is the preferred operation mode for soft biological specimens. The sample is just at the lower turning point of the oscillation movement of the cantilever in contact with the tip and interaction is minimized. No lateral force is applied to the sample.

The sharpness and apex shape of the tip are of high importance for high-resolution imaging. Commercial tips fabricated from Si or Si₃N₄ have typical radii of curvatures of some ten nanometers. The resulting image is a convolution of the AFM probe shape with that of the particle. On the other hand, the height gives mostly highly accurate values. Particle sizes can therefore just be deduced from vertical measurements.^{59, 460} Si-probes are sharper but also stiffer which precludes their successful use in high-resolution imaging in fluids. Oxide sharpened Si₃N₄ tips give superior results in imaging of the relative rough structures of virus assemblies or thinly spread viruses. The development of other types of sharp tips (polymeric tips⁴⁶¹, carbon nanotube tips⁴⁶², ...) for high resolution imaging of soft surfaces is an ongoing process.

AFM has emerged during recent years as a new high-resolution imaging technique for soft biological samples.^{463, 464} The progress in structural virology is a nice example.⁴⁶⁵ Tapping mode and low scan rates are the preferred imaging conditions for high resolution. Fourier filtering of surface crystals allows reconstructions to further improve images, similarly to electron microscopy.⁴⁶⁶ AFM can be performed in physiological fluids (in-situ imaging) and no effects of dehydration or staining distort the image as it is currently observed in electron microscopy.⁴⁵⁷ Under proper conditions, AFM does not perturb the surface under study and the imaging process can be done over long times to record dynamic processes. Further, the exchange of the liquid allows the observation of the specimen under different conditions.

A series of publications by McPherson and coworkers nicely show the power of high resolution AFM imaging in structural virology.^{465, 467, 468} They developed robust imaging conditions that allowed the in-situ imaging of virus crystal growth over periods of several days (investigations with TYMV see ref.^{469, 470})^{471, 472}. AFM has recently been integrated in an immunosensor assay (“ViriChip”) for the detection and identification of virus particles.⁴⁷³

Applications of AFM in biochemistry go beyond pure imaging of biological molecules and interfaces.^{474, 475} Recognition and binding sites⁴⁷⁶ and conformational strengths of single biomolecules⁴⁷⁷ can be probed with functionalized tips.⁴⁶⁴ AFM can be used to

investigate the elastic and viscoelastic properties of samples.⁴⁷⁸ In dip-pen lithography the tip is used to deposit material and to pattern surfaces with high precision.^{479, 480}

A typical problem in biological AFM is the weak affinity of the sample to the substrate. Loosely bound molecules may move or contaminate the tip.⁴⁸¹ This is especially observed during in-situ imaging in fluids. Typical results are poor resolution and flat surface images or double pictures from twin tips. Damage or deformations of the soft material can mainly be overcome by using tapping mode AFM.^{457, 463}

2.8 UV-Vis Spectroscopy

As plant viruses consist of both nucleic acid (mostly RNA) and protein, their absorption spectrum consists of a superposition of the absorbance of nucleic acid (minimum at 230 nm; maximum 260 nm) and protein (minimum at 250 nm, maximum at 280 nm).⁴⁸² Nucleic acid absorbs much stronger than protein. The peak maximum of a virus preparation is therefore typically at 260 nm and shifts to higher wavelengths with higher protein/nucleic acid ratio. The ratio A_{260nm}/A_{280nm} of the absorbances at the two wavelengths characterizes the protein content (empty capsids or capsids with RNA) and is a measure of the purity of the preparation (presence of plant protein contamination). The protein content is calculated according to Lambert-Beer with $E_\lambda = \varepsilon_\lambda cd$ with E_λ : absorbance or extinction, ε_λ : extinction coefficient, c : concentration and d : optical path length. Larger virus particles, especially elongated ones, can aggregate and absorption has to be corrected for light scattering. Significant readings above 315 nm are an indication as protein does not absorb in this region. Estimate correction values are tabulated.⁴⁸² For small proteins the corrections negligible.⁴⁴⁵

3 Experimental Section

3.1 Chemicals

Salts for the preparation of buffers were obtained from Sigma-Aldrich or Fluka in the quality p. a. and prepared with ultrapure water (Arium 611 DI, Sartorius, Goettingen, Germany). The solvents which have been used for pendant drop tensiometry and the salts for the preparation of the mineralization solutions and glass A are listed in the following. The sources of the proteins and ferritin is given, too.

di-ammonium hydrogen phosphate	Fluka	≥ 99%
calcium carbonate	Sigma-Aldrich	99+%
calcium chloride dihydrate	Fluka	≥99%
calcium fluoride	Sigma-Aldrich	99.9%
calcium nitrate tetrahydrate	Fluka	≥99%
calcium phosphate dibasic dehydrate	Sigma-Aldrich	98 %
citric acid	Roth	99,5%
decane	Sigma-Aldrich	99+%
magnesium chloride hexahydrate	Fluka	≥ 99,0%
magnesium oxide	Sigma-Aldrich	98 %
perfluorooctane	Fluorochem	98 %
potassium chloride	Fluka	≥ 99,5%
potassium phosphate dibasic anhydrous	Fluka	≥ 99,0%
sodium bicarbonate	Fluka	≥ 99,7%
sodium chloride	Fluka	≥ 99,5%
sodium dodecyl sulfate	Fluka	≥ 99,0%
sodium sulfate anhydrous	Fluka	≥ 99,0%
tris(hydroxymethyl)aminomethane	Sigma-Aldrich	99,9%
albumin, bovine serum	Sigma-Aldrich	96 %
albumin, human	Sigma-Aldrich	30 wt% in 0.85 wt% NaCl/0.1 wt% NaN ₃
fetuin, from fetal calf serum	Sigma-Aldrich	

ferritin, from horse spleen	Fluka	50-150 mg/ml in 150 mM NaCl solution
-----------------------------	-------	--------------------------------------

Poly(ethylene terephthalate) (PET; film, thickness 0.25 mm, biaxial orientation) for mineralization experiments was obtained from GoodFellow, Cambridge, England. The acrylate modified poly(dimethyl siloxane) (in this work simply called PDMS) was ZipconeTM UA from Gelest/ABCR, Karlsruhe, Germany.

3.2 Virus Preparation

Some suspensions of CPMV were prepared and characterized during a research stay in the laboratory of Prof. Qian Wang, University of South Carolina, Columbia, USA. Some batches of CPMV and all suspensions of TYMV and TMV were obtained as purified preparations from his group. The virus solutions have been characterized before use with UV-Vis spectroscopy, SEC and DLS. The purification of cowpea mosaic virus from infected leaves of chinese cabbage is described in the following section.⁴⁸²⁻⁴⁸⁴

The leaves were collected and directly frozen in at certain stages of plant development. Different parts of an infected plant contain different amounts of virus and the right time of harvesting is a key factor to obtain high yields of virus. The frozen leaves can be worked up any time later if needed.

The infected leaves (appr. 100 g) were mechanically pulverized and mixed with 400 ml of chilled (4 °C) 0.1 M potassium phosphate buffer (pH = 7.0). 1 ml β -mercaptoethanol was added and the whole soup homogenized with a kitchen blender. The mixture was filtrated through two layers of cheesecloth. During the procedure which should be done rapidly, it was ensured that the temperature remained below 10 °C. The filtrate was centrifuged for 20 min at 10500 rpm and the supernatant was filtrated through four layers of tissue towel. An equal volume of chloroform and n-butanol (1/1 v/v) was added and for 30 min stirred in cold. Foaming has to be avoided. The two-phase mixture was centrifuged at 6000 rpm for 10 min before the aqueous phase was collected and 6.4 g NaCl and 8.8 g PEG (6 kDa or 8 kDa) added to 0.2 M and 8 % (w/v) respectively. Again, the solution was stirred for 30 min in cold and

additionally stored for 1 h in the refrigerator before it was centrifuged at 15000 rpm for 15 min. The pellet was resuspended in 50 ml of 0.1 M potassium phosphate buffer (pH = 7.0). For the work-up of the cysteine-mutant the buffer contained 10 mM TCEP to avoid particle aggregation and precipitation through oxidative disulfide-bridging. Protein was removed at 9500 rpm for 15 min before the virus was centrifuged down at 42000 rpm for 2.5 h (Beckman Ultra 50.2 Ti rotor) at 4 °C. The supernatant was discarded and the virus, visible as faint white precipitate, was resuspended with 0.01 M potassium phosphate buffer (pH = 7.0). The purity of the batches was checked by FPLC and the concentration was determined by UV-Vis-spectroscopy. In this preparation, 20.68 mg virus was obtained but the yield typically reaches 100 mg/100 g leaves.

The same procedure can in principle be used for purification of TYMV. The extraction buffer is 0.1 M potassium phosphate at pH = 7.8, for storage diluted 10fold. For tobacco mosaic viruses many methods are established.^{482, 483} If high purity of the virus is needed, density gradient centrifugation can be used which further separates the particles by their size or shape (sucrose cushion) or their buoyant density (CsCl gradients).⁴⁸²

3.3 Conjugation Reactions to CPMV

The preactivated dye was conjugated according to standard procedures.^{48, 52} Since a maximum dye-loading was intended, 1000 equivalents of dye per protein subunit were used. A maximum of up to 200-240 aminogroups per subunit can then be addressed.⁴⁸ The reaction was done in 0.1 M potassium phosphate buffer at pH = 7.0 containing 20 % DMSO at a virus concentration of 1 mg/ml. The excess dye was removed by gel filtration⁴²⁵ with Bio-Gel P100 (Biorad, Munich, Germany) according to the manufacturers protocol.

3.4 Preparation of Pickering Emulsions

The oil phase was added to the buffered bionanoparticle or protein solutions (1/10 v/v) followed by vigorous shaking by hand. The concentrations were 5 mg/ml for ferritin

and the proteins and 1 mg/ml for the viruses. The adsorption process was done for 3 h at room temperature with occasional tilting of the tubes to swirl and mix the droplets with the supernatant solution. If the bionanoparticles should be crosslinked, the supernatant was removed and ten volumes of aqueous glutaraldehyde solution (1.0 wt%) were added to the droplet suspension and the reaction proceeded for 30 min. Pickering emulsions with crosslinkable PDMS precursor oil were then exposed for 5-10 min to UV-light (Heraeus Noblelight, TQ 150-56001725). Finally, the droplets were washed five to six times with ten volumes of deionized water.

3.5 Preparation of glass A

The glass A was prepared from MgO, CaCO₃, SiO₂, CaHPO₄ × 2 H₂O and CaF₂.^{272, 273} The mixture had the nominal composition (wt%) MgO 4.6, CaO 44.7, SiO₂ 34, P₂O₅ 16.2 and CaF₂ 0.5. The finely grinded powder was heated slowly over 30 min to 1450 °C in a glassy carbon crucible, hold for 5 min at that temperature and then cooled down to room temperature with an air stream. The glass bead was pulverized with a steel ball mill (S1, Retsch, Haan, Germany) and sieved (Analysette 3, Fritsch, Idar-Oberstein, Germany) to yield two fractions with particles of diameters < 90 μm and 90-250 μm.

3.6 Preparation of SBF

The preparation of SBF was done as suggested by Kokubo with minor modifications:²⁶⁷ 900 ml of purified water were placed in a 1000 ml polycarbonate Erlenmeyer flask. The flask had been rinsed with diluted HNO₃ to remove remaining impurities, especially from previous SBF preparations, that might work as nucleation sites. Care has been taken that the container had no scratches and the stirring bar was clean and not scratching the bottom. Glass containers should be avoided for obvious reasons. A crystal clear flask is advantageous that any even faint precipitation during preparation can be detected immediately. The pH-electrode was also rinsed with diluted HNO₃ and rinsed with copious amounts of purified water. It was then calibrated at 20 °C with

standard solutions at pH = 4.01 and pH = 10.01. The calibration was further verified with a pH = 7.0 standard solution at 20 °C and 37 °C. The recalibration was done immediately before every preparation. The flask was immersed in a water bath and the temperature set to 37.0 °C and monitored accurately with a thermometer. The reagents 1-8 listed in Tab. 5 were dissolved one by one in the given order.

Tab. 5 Reagents for the preparation of SBF.²⁶⁷

order	reagent	molecular weight [g/mol]	amount [g], [l] for 1.0 SBF	amount [g], [l] for 1.5 SBF
1	NaCl	58.44	8.035	12.053
2	NaHCO ₃	84.01	0.355	0.533
3	KCl	74.55	0.225	0.338
4	K ₂ HPO ₄	174.18	0.176	0.265
5	MgCl ₂ × 6 H ₂ O	203.031	0.311	0.466
6	1.0 M HCl		0.039	0.059
7	CaCl ₂ × 2 H ₂ O	110.98	0.387	0.580
8	Na ₂ SO ₄	147.01	0.072	0.108
9	tris	142.04	6.118	9.177
	1.0 M HCl		0-0.005	0-0.0075

The 1.0 M HCl was applied with a large volume Eppendorf pipette. CaCl₂ × 2 H₂O has to be dissolved grainwise little by little. The volume of the solution was then adjusted to approximately 980 ml. The pH-electrode was immersed (pH = 1.1) and tris was added in small amounts, little by little, and dissolved slowly. After each addition, the gradual increase in pH was controlled. When pH was above 7.00, the temperature was monitored to be exactly at 37.0 °C and the solution carefully checked for precipitation after each addition. Further tris was added until pH was below 7.45. 1.0 M HCl was added dropwise (appr. 1 ml) to lower the pH to 7.42, followed by addition of the remaining tris until pH < 7.45. Finally, the solution was adjusted with few drops 1.0 M HCl to exactly pH = 7.40 at exactly 37.0 °C. SBF with the listed concentrations (named 1.0 SBF) had a conductivity of 16.17 mS/cm and SBF with 1.5 fold concentration (named hereafter 1.5 SBF) had a conductivity of 23.3 mS/cm, both at pH = 7.40 and

37.0 °C. The solution was cooled down to room temperature in the water bath and the volume was readjusted to exactly 1000 ml. The pH at room temperature is quite higher (both pH = 7.81), the conductivity changes only slightly (16.42 mS/cm and 23.6 mS/cm, respectively).

To prepare SBF with citrate (named 1.5 SBF/cit), 1.5 SBF was heated to 37.0 °C and citric acid was slowly dissolved to a final concentration of 1.0 mM. The pH of the solution was readjusted with tris to exactly pH = 7.40. Final conductivity was 23.5 mS/cm.

3.7 Preparation of Supersaturated Calcium Phosphate Solution Containing Citrate (Ca/P/cit)

500 ml of a 5 mM ammonium phosphate solution was added to 500 ml of a 10 mM calcium nitrate solution containing 2.5 mmol citrate (added as citric acid). The solution was adjusted to pH = 7.40 with small amounts of concentrated ammonium hydroxide solution. Precipitation is observed when reaching pH = 7.0. The solution was allowed to settle for about 30 min, then filtrated with a 0.22 µm nylon syringe filter and immediately used. Initial pH was pH = 7.40 and conductivity was around 1430 µS/cm at room temperature.

3.8 Profile Analysis Tensiometry

For pendant drop tensiometry an OCA 20 instrument (Dataphysics, Stuttgart, Germany) was used. It enables the automated acquisition of images with a video camera and subsequent fitting of the drop profile with the accompanying software (vers. 2.1.9). The temperature was monitored with a Pt-100 temperature sensor and found to be constant at 20.0 ± 0.2 °C. The drop was created at the end of a blunt-end cannula (Braun Sterican, Melsungen, Germany) attached to a disposable plastic syringe. The outer diameter of the needle was precisely measured with a calibrated microscope. The first one or two drops were detached into the solution to create a fresh drop surface. Manual

feed via a micrometer screw was faster and more convenient than using the automated dosing system. Fast video acquisition at the beginning was not used, as an initial time interval of 3-5 seconds is characterized by errors anyway, as it is inherently associated with the method of blowing up the drop and the resulting vibrations. The buffered protein stock solution and the buffer for dilutions were filtrated with a 0.22 μm nylon syringe filter (Roth, Karlsruhe, Germany). The decane solution in the glass cuvette (110-OS, Helma, Müllheim, Germany) was saturated by shaking with purified water. The whole setup was placed on a pressured-air damped table, however, no significant effect on the curves within the experimental error was found, as has been also pointed out in ref⁴⁸⁵. The camera and the needle were aligned horizontally and vertically, respectively with the aid of a water bubble level and visual inspection. Any deviation from the symmetry requirement which is one of the theoretical basis in the equations above (chapter 2.2) will consequently affect the accuracy of the calculation method.⁴⁰¹ Besides these precautions no further efforts have been undertaken to improve the setup and measurements.⁴⁸⁵ The interfacial tension of purified decane vs. water was reported to be 53.2 mN/m⁴⁸⁶. The proposed purification of decane did not result in measurable effects. The surface tension of the pure solvent and buffer solution, respectively, was always decreasing for long measurement times. Obviously, the buffer salts contained some surface active contaminations which could not be avoided. Further, the virus suspensions are prepared from natural material with the aid of various surfactants and despite purification by centrifugation, still some surfactants might be dragged with. Another source of surface active components is the virus itself. A considerable amount (for CPMV up to 1 wt%) can be polyamines. Upon surface denaturation or from disassembled viruses in solution these non-ionic surfactants can be freed from the capsid's interior and compete with virus adsorption. This effect is pronounced at long adsorption times. In the quantitative analysis, these influences were not considered.

3.9 Size Exclusion Chromatography

SEC of viruses and proteins were performed in aqueous buffer (0.15 M NaCl, 25 mM potassium phosphate, 0.01 wt% NaN_3 ; pH = 7.0) with an Agilent 1200 series HPLC-system (Agilent Technologies, Waldbronn, Germany) consisting of a micro-vacuum

degasser, an isocratic pump, a manual injector (Rheodyne 7725(i), Rheodyne Europe, Alsbach a.d. Bergstrasse, Germany), a variable wavelength UV-detector, a light scattering (LS-) detector (miniDAWN TREOS, 658 nm, Wyatt Technology Europe, Dernbach, Germany) and a refractive index (RI-) detector. The instrument was controlled by the accompanying HPLC control module or through the Wyatt software. Data acquisition and evaluation was done with the Wyatt software ASTRA V (version 5.3.2.15). The elution buffer was filtrated through a 0.22 μm nylon filter (Roth, Karlsruhe, Germany). The column was protected by an in-line filter before the injector (Wyatt; 0.1 μm Durapore VVLP membrane filter, Millipore, Eschborn, Germany). The sensitivity of the light scattering detector demands an additional in-line filter (0.22 μm Durapore GV, Millipore) after the column. Column bleeding would give rise to many spikes and an increased background noise in the LS detector signal. The separating column was a Superose 6 10/300 GL prepacked agarose gel column (Amersham Biosciences Europe, Freiburg, Germany). Its large separation range from 5 kDa to 5 MDa for globular proteins with an exclusion limit of 40 MDa allows the size-selective separation of whole viruses.⁴²⁵ Flow was kept at 0.25 ml/min as a large backpressure arising from the three detectors prevents higher flow rates with respect to column stability. The samples – usually a 50 μl -loop and 60 μl of sample solution were used – were directly filtrated through a home-made needle in-line filter (0.22 μm Durapore GV, Millipore) during injection. This device based upon the NanoFilter from Wyatt allows filtration of small sample volumes with minimal sample hold back (< 3 μl). The UV-detector was calibrated with BSA-solutions of different concentrations, the LS detector with toluene and the RI-detector with BSA or NaCl-solutions.⁴⁴⁹ System alignment and LS detector normalization was done with a BSA-run (10 mg/ml in elution buffer; remember that for small molecules the scattering is independent of the angle).

3.10 Dynamic Light Scattering

Dynamic light scattering measurements were done with a DynaPro Titan quasi-elastic light scattering instrument (Wyatt Technology Europe, Dernbach, Germany). The samples were filtrated through 0.22 μm or 0.45 μm nylon syringe filters (Roth,

Karlsruhe, Germany) directly in microcuvettes (UVette, Eppendorf, Hamburg, Germany or micro glass cuvettes, Wyatt). The laser (60 mW) had a wavelength of 828.68 nm and the laser power was adjusted to obtain a count rate of 0.7-1 MHz. The scattering angle was 90°. The cuvettes were thermostatted to 20 °C. Data acquisition and manipulation was done with the software Dynamics (version 6.9.1.15, Wyatt). Usually, five acquisitions of each 5 s were averaged to one measurement; 10-20 such measurements were averaged. The values presented are usually the average over different batches.

3.11 UV-Vis Spectroscopy

UV-Vis measurements were done with an Evolution 300 spectrophotometer (ThermoFisher Scientific, Dreieich, Germany). Micro quartz cuvettes with a light path of 10 mm (105.201-QS, Hellma, Müllheim, Germany) were used. Background subtraction was usually done with water or buffer solution. The used buffers had no adsorption at 260 nm and above.

3.12 SDS-Polyacrylamide Gel Electrophoresis (SDS-PAGE)

SDS-polyacrylamide gel electrophoresis⁴⁸⁷ followed standard procedures.⁴⁸⁴ The samples were mixed with 5 x sample buffer (4/1, v/v) and heated for 5 min to 95 °C. The sample buffer consisted of 62.5 mM tris buffer (pH = 6.8), 10 % (v/v) glycerol, 2 % (w/v) SDS, 5 % (v/v) thioethanol and 0.125 % (w/v) bromophenol blue (final concentrations). After cooling down, the samples were spun down for 60 s at 10 krpm with a microcentrifuge. 20 µl of the denatured sample was then applied to the gel. For molecular weight determination a molecular weight ladder (BenchMark Protein Ladder; Invitrogen, Karlsruhe, Germany) was run in one lane. The precast gels (Ready Gel Tris-HCl, 10 % or 4-15 %, Bio-Rad, Munich, Germany) were prepared and installed in the electrophoresis chamber (Mini-PROTEAN Tetra Cell, Bio-Rad) as described in the manual. Electrophoresis was run in tris-buffer (25 mM tris, 192 mM glycine, 0.1 % (w/v) SDS; final pH approx. 8.3) for 5 min at 100 V and then for 45 min at 150 V. The gels were stained with Coomassie (0.1 % (w/v) Coomassie Brilliant Blue

R250, 450 ml methanol, 450 ml water and 100 ml acetic acid) for 15 min at room temperature, washed and destained with a mixture of 10 % (v/v) methanol, 10 % (v/v) acetic acid and 80 % (v/v) water for 15-20 h at room temperature. The gels were photographed with a digital camera or an Intas gel documentation system (Intas, Göttingen, Germany; white light or UV light of 312 nm).

3.13 MALDI-TOF Mass Spectrometry

Matrix-assisted laser desorption ionization-time of flight (MALDI-TOF) mass spectrometry has been performed on non-digested virus suspensions with a standard protocol for proteins (saturated aqueous solution of sinapic acid). A Bruker Reflex III equipped with a 337 nm N₂-laser was used. The measurements were done in linear mode with 20 kV acceleration voltage and external calibration with proteins of known molecular weight. It should be mentioned that mass spectrometry on whole, intact viruses is possible with electrospray ionization (ESI) and charge-detection⁴⁸⁸ and virus even keeps its viability.⁴⁸⁹

3.14 Confocal Fluorescence Laser Scanning Microscopy

A commercial confocal fluorescence laser scanning microscope (Zeiss LSM 510 META/Confocor2) equipped with the following laser lines: 405, 458, 477, 488, 514, 543 and 633 nm, was used to obtain fluorescence micrographs. The appropriate excitation wavelength for each dye and the corresponding filter set with standard settings was chosen. A 63 x C-Apochromat oil immersion objective was used. The droplets were settled in 8-well glass bottom chambers (Nunc, Wiesbaden, Germany) without further fixation. The 3-dimensional pictures were assembled from typically 200 confocal images with a slice thickness of 0.44 μm .

3.15 Transmission Electron Microscopy and Sample Preparation

A Zeiss CEM 902 transmission electron microscope (Carl Zeiss SMT AG, Oberkochen, Germany) with an acceleration voltage of 80 kV was used for TEM-measurements in bright-field mode. Pictures were gathered with a CCD camera (MegaView3, Olympus Soft Imaging Solutions, Münster, Germany) and the software iTEM (Olympus Soft Imaging Solutions).

Samples were usually prepared as thinly spread specimens on filmed grids or embedded in epoxy resin (EPO-TEK 301 1LB Kit, Epoxy Technology, Polytec, Waldbronn, Germany). The hardened blocks were then cut with a microtome (Ultracut E, Reichert-Jung; today Leica Biosystems, Nussloch, Germany) equipped with a diamond knife (Diatome, Biel, Switzerland). Usable cuts with a thickness of 60 nm (judged from the interference colour of the floating film) could be prepared consistently which finally were picked with a 400 mesh copper or gold grid (Athene Old 400, Plano, Wetzlar, Germany).

“Whole mount”-views of viruses were prepared by spreading diluted virus solutions on pioloform coated copper or carbon coated gold grids (Plano). After 2 min adsorption, the excess solution was blotted off with a tissue paper, and negatively stained with uranyl acetate (UA) or phosphotungstic acid (PTA) for 10 min.^{490, 491} The stain was blotted off with a tissue paper and the grid washed with one drop of water. The grid was allowed to air dry.

3.16 Scanning Electron Microscopy and Sample Preparation

For SEM imaging a LEO 1530 Gemini instrument (Zeiss SMT, Oberkochen, Germany) equipped with a field emission cathode was used. Acceleration voltage was usually set to 3 kV. An in-lens detector and a working distance of 2 mm were used. The lateral resolution limit was estimated to 2 nm. Samples were mounted on steel stubs with conducting double adhesive tabs and eventually further fixed with silver paste or Scotch conducting tape. Biopolymer samples were sputter-coated with a thin platinum layer (approximately 1 nm). Hydroxy apatite samples were coated with a conducting carbon

layer. EDX measurements were made with an Oxford INCA-System (detector EDS6901; Oxford Instruments GmbH, Wiesbaden, Germany). The working distance was set to 9 mm and the acceleration voltage to 10 keV. Detector dead times of 5-10 % were reached. Spectra at three different points at three different sample sites were measured and averaged.

3.17 Atomic Force Microscopy

AFM measurements were performed with a Dimension 3100 (Veeco Instruments Inc., Santa Barbara, California) in tapping mode. Si₃N₄-tips (Olympus OMCL-AC160TS-W2, AtomicForce F & E, Mannheim, Germany) with a typical spring constant of 40 N/m and a resonance frequency of 200-300 kHz were used throughout the work. The samples were mounted on steel taps with double sided adhesive stripes. The images were processed with smooth and plane-fit routines that were implemented in the software NanoScope 7.10 (Veeco Instruments).

3.18 X-ray Diffraction

Diffraction patterns were measured with a PANalytical X'Pert Pro X-ray diffractometer system (PANalytical GmbH, Kassel-Waldau, Germany), equipped with an X'Celerator semiconductor detector in reflection geometry. Cu-K α radiation with a wavelength of 0.154 nm was used. The sample was mounted on a silicon zero-background holder and measured under rotation.

3.19 Further Instruments

pH and conductivity measurements were done with a WTW inoLab pH/Cond 720 instrument. SenTix 81 and SenTix Mic were the pH-electrodes, calibrated at pH = 4.01 and 10.01 and TetraCon 325 was the conductivity probe, calibrated with 3 M KCl.

4 Characterization of Viruses

Protein characterization in solution can be done with many different techniques, such as size exclusion chromatography (SEC) and other liquid chromatography techniques, fluorescence spectroscopy, nuclear magnetic resonance spectroscopy (NMR; including pulsed-field gradient techniques, PFG-NMR), circular dichroism (CD), Fourier transform infrared spectroscopy (FT-IR), UV-Vis spectroscopy, membrane osmometry, analytical ultracentrifugation (AUC), mass spectrometry in all its variants, gel electrophoresis etc. to name the most common. These essentially contactless methods (except the latter two) are especially suited to obtain information on the conformational complexity of biological materials, including their size, shape, aggregates and complex formation.

Routine batch characterization has been done to ensure a constant sample quality and composition. This is especially necessary for materials which are obtained from natural resources (applies to all materials used in this work). Proteins and ferritin have been fractionated and characterized and only the monomer fractions have been used in the preparation of Pickering emulsions and protein-coated PDMS surfaces.

4.1 Characterization of Viruses and Proteins with Aqueous SEC and Light Scattering Detection

Proteins and viruses were analysed with size exclusion chromatography to find out about the presence of aggregates and impurities in the solutions. The static light scattering detector allowed the on-line evaluation of absolute molecular weights and radii if a concentration detector is additionally used. In all SEC measurements, the traces from RI-detection as well as UV-detection were recorded; both can be used as concentration detector. As has been described above, in any case, the refractive index increment dn/dc at the laser light scattering wavelength must be known for the analysis according to the Zimm-equation. If UV-detection is employed, the absorption coefficient at the measurement wavelength must be known, too. RI-detection of proteins in buffer solutions suffers from much less sensitivity compared to UV-detection.

Moreover, dn/dc is hardly known but the absorption coefficient mostly is because absorption measurements are a routine task to determine solute concentrations. Therefore, RI and UV have been routinely used to prove the correct calibration and instrument setup with measurements of BSA-solutions. But throughout the SEC spectra that will be shown, the UV-detector was employed as concentration detector which yielded more consistent and reliable results with low concentrations, too. The values that were particularly used can be found in the virus and protein properties table in chapter 1.5.5. For LS-analysis, dn/dc was set to 0.187 ml/g for all proteins and viruses, conscious of possibly arising errors from that. Ferritin was the only exception because no reasonable absorption coefficient could be found but dn/dc was measured recently.³²⁹

Bovine serum albumin (BSA) is a standard protein for many applications and has therefore been investigated in great detail. It is well known that besides the main monomeric fraction also dimers and trimers as well as higher, unspecified aggregates can be found.^{333, 426} The exact composition depends on solution conditions but mostly on different sources. The SEC run of a commercial preparation of BSA is shown in Fig. 14 with the traces from light scattering (LS), UV-Vis (UV) and refractive index (RI) detection. The highest peak of each trace was normalized and the traces were shifted for clarity. The molecular weights and root mean square (rms) radii for the three most intensive peaks are shown. The main fraction of BSA was the monomeric peak, corresponding to a molecular weight of 66.6 kDa, while the earlier eluting peaks at 61.5 min and 57.5 min corresponded to dimers and trimers with a molecular weight of 126.3 kDa and 180.5 kDa, respectively. The software principally calculated an rms radius, but the BSA monomer is actually too small to show an angular dependence of the scattering. The calculated values were rather arising from scattering fluctuations relative to normalization. The values for the aggregates showed low signal-to-noise ratio because of the low intensity of the concentration signal. The displayed part of the chromatogram covers the whole separation range, starting from the elution of the void volume at 27.5 min and ending with the elution of the total volume at 78 min.

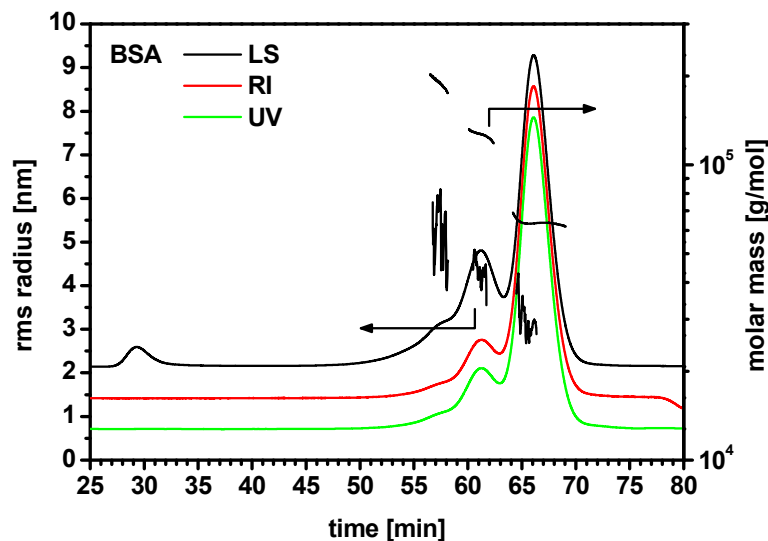


Fig. 14 SEC of bovine serum albumin with LS, RI and UV trace and molecular weights and rms radii.

Similar aggregation behaviour in solution has been reported for ferritin (Fig. 15). Commercial preparations contained small amounts of large aggregates that eluted at 30 min with the void volume. UV and LS signal indicated a broad distribution of eluting aggregates until 44.5 min when a first defined fraction started to elute, followed by dimers (50.0 min; MW = 1.59 MDa, rms radius 13.6 nm) and the main monomeric fraction (57.0 min; MW = 692 kDa, rms radius 6.8 nm). Both radii were in agreement with the expected values and the measured hydrodynamic radii. The monomer peak suffered from a large error which arised from the small size which is close to the limits of the technique.

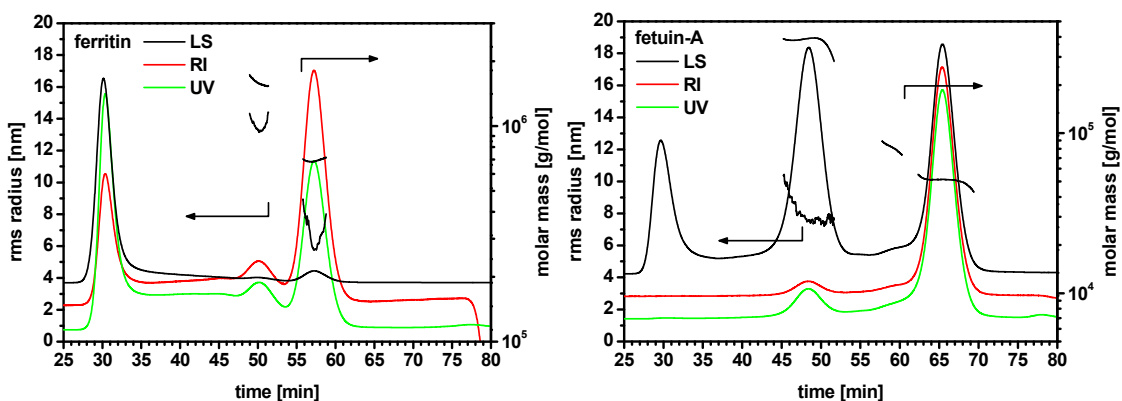


Fig. 15 SEC of horse spleen ferritin and fetuin-A with LS, RI and UV trace as well as molecular weights and rms radii for the resolved peaks.

Ferritin contains varying amounts of ferrihydrite, depending on batch and source which influences the absorption and refractive index.^{321, 492} This heterogeneity influenced the molecular weight determination. The values for the molecular mass were reasonable and have been obtained quite consistently with different batches of horse spleen ferritin from one manufacturer.

Fetuin-A from calf serum was also subjected to size exclusion chromatography (Fig. 15). At 58.5 min a peak with a molar mass of 381 kDa eluted. This was obviously an impurity as this peak could not be ascribed to some defined aggregate. The impurity made up approximately 15 wt% compared to the main monomeric fraction of fetuin-A as calculated from the absorption (based on the assumption of equal absorption coefficients for both solutes). The peak at 59.0 min corresponded to the dimer (MW = 80.9 kDa) and the main peak at 65.5 min corresponded to the monomer (MW = 51.1 kDa). Fetuin-A is even smaller than BSA (rms radius 3.2 nm³⁴⁴) and no rms radius could be reliably obtained with static light scattering here.

CPMV and TYMV behaved like ideal model colloids. The preparations were devoid of aggregation and the viruses eluted in a single broad peak (Fig. 16, left; Fig. 17, left). A three-angle light scattering detector was sufficient to determine the molecular weight as well as the rms radius reliably (Fig. 16, right).

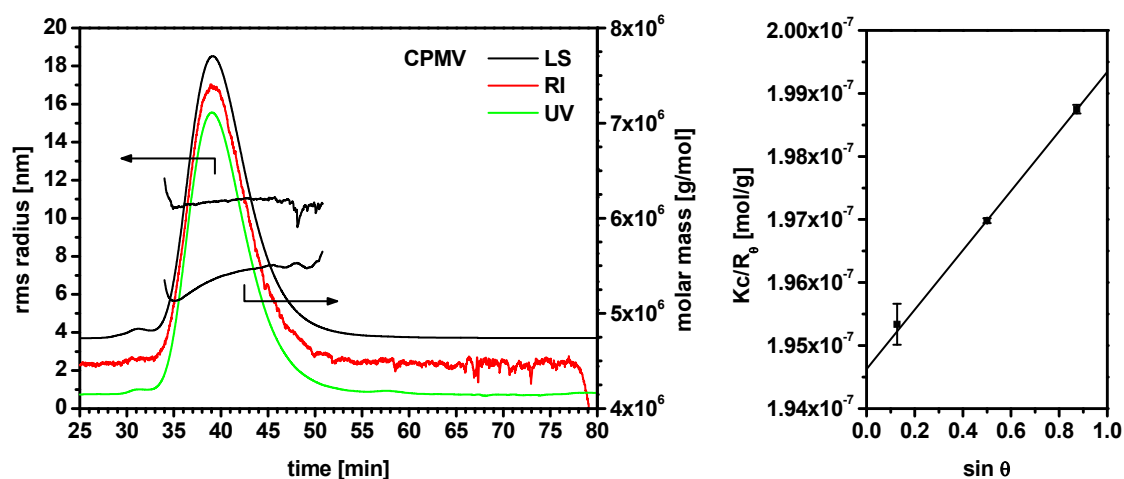


Fig. 16 (right) SEC of CPMV with LS, RI and UV trace and molecular weight and rms radius; (left) Zimm plot from the three-angle LS detector.

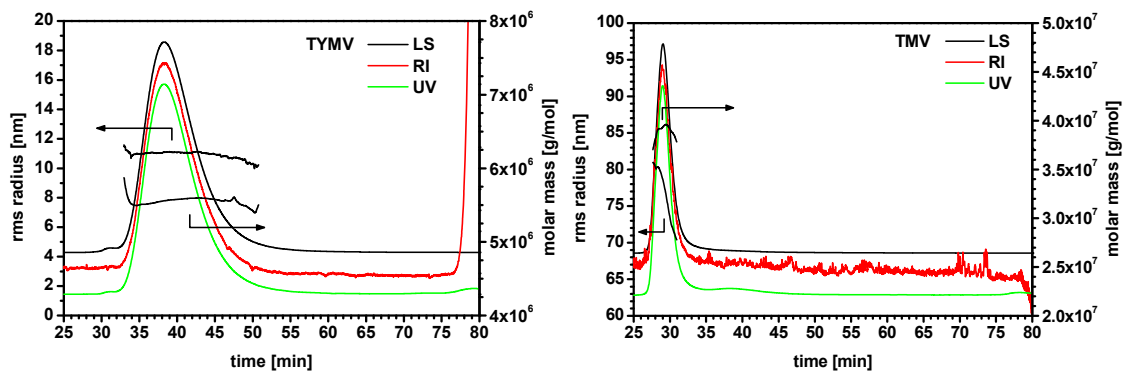


Fig. 17 SEC of TYMV and TMV with LS, RI and UV trace and molecular weight and rms radius.

The molecular weight and radius were nearly constant over the whole peak for both icosahedral viruses. The deviations at the edges of the peaks were caused by an inaccurate determination of the concentration by the low intensity of the UV-detector signal. Molecular weights that were determined with the RI detector as concentration source were typically 5-10 % smaller than those obtained with UV detection. TMV eluted with the void volume and no separation took place, indicated by the very narrow peak although the decreasing rms radius within the peak suggested that smaller rods eluted at the trailing edge (Fig. 17, right). The radii of the viruses are all about 5-10 % smaller than expected from the size of the viruses. The masses and radii of the viruses from light scattering detection in SEC are collected in Tab. 6.

Tab. 6 Molecular weights and rms radii from size exclusion chromatography with LS detection for three different plant viruses.

	CPMV	TYMV	TMV
molar mass [MDa]	5.4	5.6	38.9
rms radius [nm]	10.9	11.0	77.1

4.2 Characterization of Viruses and Proteins with Dynamic Light Scattering

Dynamic light scattering (DLS) has become a standard tool to investigate size and weight of biological solutes of all kind.^{493, 494} The scattered intensity is proportional to

the sixth power of particle size and thus very sensitive to the presence of large dust particles. The dilute virus solutions have therefore been clarified by filtration with a 0.22 μm nylon filter. Tobacco mosaic virus was filtered through 0.45 μm . Using smaller pore sizes leads to substantial loss of material on the filter and a selection towards a size distribution with shorter rods. Further, filtration should not be done too often on the same solution. Shear forces seemed to break the rods partially into smaller pieces when squeezed through the filter.

In DLS quasi-spherical plant viruses can be adequately described by a single exponential term in the intensity autocorrelation function.^{495, 496} Here, the concentration of virus solution was very low (usually 0.01-0.1 mg/ml) and no extrapolation to zero concentration had to be done.³⁴⁸ Also, the effect of ionic strength or pH is negligible for the viruses investigated within the usually employed solution conditions.⁴⁹⁶ The values obtained for CPMV, TYMV and TMV are given in Tab. 7. The size distribution plots (CONTIN) are shown in Fig. 18.

Tab. 7 Hydrodynamic radii and diffusion coefficients of three different plant viruses.

	CPMV	TYMV	TMV
r_h [nm]	14.9 ± 0.3	15.1 ± 0.1	55.3 ± 0.1
$10^7 \times D$ [cm^2s^{-1}]	1.431 ± 0.076	1.395 ± 0.007	0.381 ± 0.007

Cowpea mosaic viruses as well as turnip yellow mosaic viruses have an icosahedral shape. As dispersed moving objects they behave like isotropic spheres. Dynamic light scattering at 90° gave a hydrodynamic radius of 14.9 nm for CPMV and 15.1 nm for TYMV. The curves indicated very good monodispersity. The size of both viruses has been determined before and the literature values correspond well to the measured hydrodynamic radii and diffusion coefficients, respectively.^{50, 348}

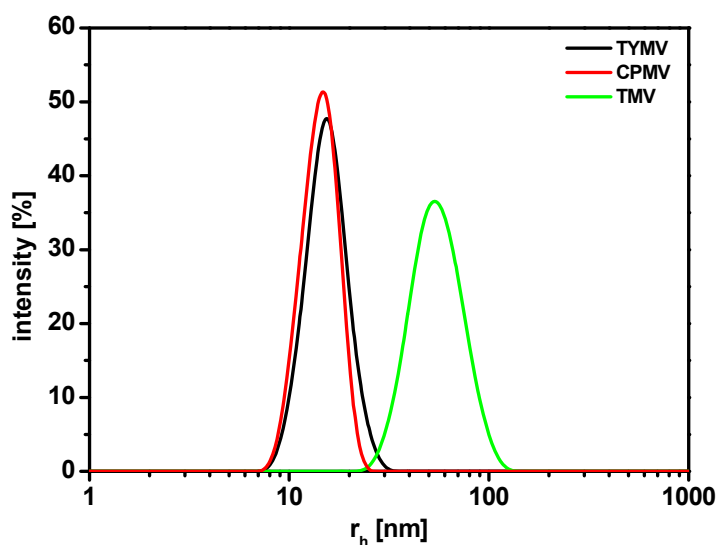


Fig. 18 CONTIN-plot of three different plant viruses.

Tobacco mosaic viruses are rod shaped with a size of 300 x 18 nm. Until recent years, before methods for the synthesis of near-monodisperse nanorods have been established, they have been almost exclusively the source for monodisperse rigid rods. For various scattering techniques they have been working as model objects in pioneering research works, also in DLS and DDLS. The decay curve of diluted TMV suspensions can be sufficiently described with a single exponential, too, and the obtained apparent diffusion coefficient equals the translational diffusion coefficient. Strictly, this is applicable for TMV only at low scattering angles ($\theta < 30^\circ$). With increasing scattering angle, the rotational contribution has to be considered; however, at 90° , both contributions are of similar magnitude and the separation of the correlation decay into two exponential terms is not easy and allows no accuracy in the calculated D_r .⁴⁹⁷

The apparent diffusion coefficient obtained here was deduced from CONTIN analysis, however, for monomodal narrow dispersed samples, a cumulant fit yields very similar values. In our measurements consistently a mean value of $3.8 \times 10^{-8} \text{ cm}^2 \text{ s}^{-1}$ was obtained for TMV. The concentration of the virus solution was 0.1 mg/ml or below and thus far beyond the overlap concentration of 2.45 mg/ml.⁴²¹ In literature, the values for the translational diffusion coefficient of TMV spread widely. Commonly, values of $3.2 - 4.3 \times 10^{-8} \text{ cm}^2 \text{ s}^{-1}$ have been reported.⁴⁹⁸⁻⁵⁰⁰ From the TMV sedimentation coefficient and the known molecular weight⁵⁰¹ a value of $D_{20}^0 = 4.24 \times 10^{-8} \text{ cm}^2 \text{ s}^{-1}$ has

been calculated.⁴⁹⁸ Calculations according to Broersma's relationship and others give a similar value, $4.0 \times 10^{-8} \text{ cm}^2 \text{ s}^{-1}$.⁴²¹ Considering the concentration dependence of the true translational diffusion coefficient and correcting it to water at 20 °C, a value of $D_{20}^0 = 4.27 \cdot 10^{-8} \text{ cm}^2 \text{ s}^{-1}$ has been reported.⁴⁹⁷ This value is in exact agreement with the calculated D_t according to Doi and Edwards for rigid rods with the dimensions of TMV.

Lehner et al. found that screening the surfaces charges of TMV through salt addition changed the translational diffusion coefficient from 3.61×10^{-8} to $4.05 \times 10^{-8} \text{ cm}^2 \text{ s}^{-1}$, a value, that has also been found by Wilcoxon and Schurr.⁴²¹ Up to now, only the work of Wilcoxon and Schurr employed a virus preparation that has been rigorously purified to a strictly monodisperse fraction devoid of any aggregated or broken particles by means of ultracentrifugation and filtration.⁴⁹⁸ There have been efforts to sort the virus according to the length since the first method of purification of TMV.⁵⁰² Solution conditions under which end-on or side-on aggregation can be avoided, are contradictory.^{497, 500} Aggregation and smaller fragments in normal preparations lead to a considerable spread in the values for the hydrodynamic radius and diffusion coefficient. A clean purification and stock maintenance was beyond the aim and capabilities within this work. TMV preparations were therefore used as received from standard work-up. The light scattering data of the employed virus preparations could not be subjected to a detailed analysis. The obtained apparent values represented rather typical average values of unfractionated TMV preparations with some length distribution of rods.⁴⁹⁹

BSA is a compact protein at and near its isoelectric point ($pI = 4.8$). Numerous investigations showed that it does not change its configuration or conformation in a pH-range of 4.5-10.5, however, at low pH and high pH expansion of the molecule occurs. At physiological pH, the diffusion coefficient with $D_0 = (6.01 \pm 0.04) \times 10^{-7} \text{ cm}^2 \text{ s}^{-1}$ is found to be largely independent of ionic strength, protein concentration and buffer type within meaningful ranges but depends on all of this parameters below the isoelectric point.^{354, 355} Complications for BSA arise from its tendency to aggregate in solution. BSA was therefore separated by preparative size exclusion chromatography in its fractions (see chapter 4.1). The values for the hydrodynamic radius and diffusion

coefficient given in Tab. 8 are obtained off-line by DLS on the separated fractions. For comparison, the values of an unfractionated sample are given, too. Similarly, fetuin-A was fractionated with size exclusion chromatography and off-line DLS measurements were performed on the monomer fraction. The obtained value agreed well with the reported hydrodynamic radius of 4.2 nm.³⁴³

Tab. 8 Hydrodynamic radii and diffusion coefficients of BSA and fetuin-A.

	monomeric BSA	unfractionated BSA	monomeric fetuin	unfractionated fetuin (bimodal)
r_h [nm]	3.51 ± 0.28	3.94 ± 0.24	3.90 ± 0.30	5.43 ± 0.47
				67.4 ± 6.2
$10^7 \times D$ [cm ² s ⁻¹]	6.01 ± 0.45	5.28 ± 0.48	5.47 ± 0.46	3.90 ± 0.31
				0.31 ± 0.03

The aggregation behaviour of ferritin has been discussed above (chapter 4.1). The fractions obtained from preparative SEC were subjected off-line to DLS. In Tab. 9, the hydrodynamic radii and diffusion coefficients are compared to the values obtained from apoferritin by Petsev et al.⁵⁰³ Since apoferritin differs from ferritin just in its molecular weight but not in the hydrodynamic size, the same diffusion coefficients can be expected. This fact has been supported by the identical second virial coefficient A_2 of both molecules. A_2 characterizes the pair interaction which is determined by the identical surfaces of ferritin and apoferritin. The last fraction collected from SEC corresponded to ferritin monomers. The previous fraction could be ascribed to dimers. The diffusion coefficient agreed with the calculated diffusion coefficient of a prolate spheroid with one ferritin monomer diameter and a double ferritin monomer length. The third last fraction seemed to consist of an average of 3-5 ferritin particles. The diluted unfractionated batch gives a broad monomodal peak in DLS (Fig. 19). The value is of less significance as it is subject to the batch heterogeneity which can strongly vary.

Petsev et al. argued that the presence of aggregate impurities is not a merely aggregation but accompanied by a structural change during which the involved ferritin cages

partially denature.^{503, 504} This explained why a purified and fractionated solution which was maintained properly, kept its “monomeric” properties for some weeks without detectable aggregation.⁵⁰⁴

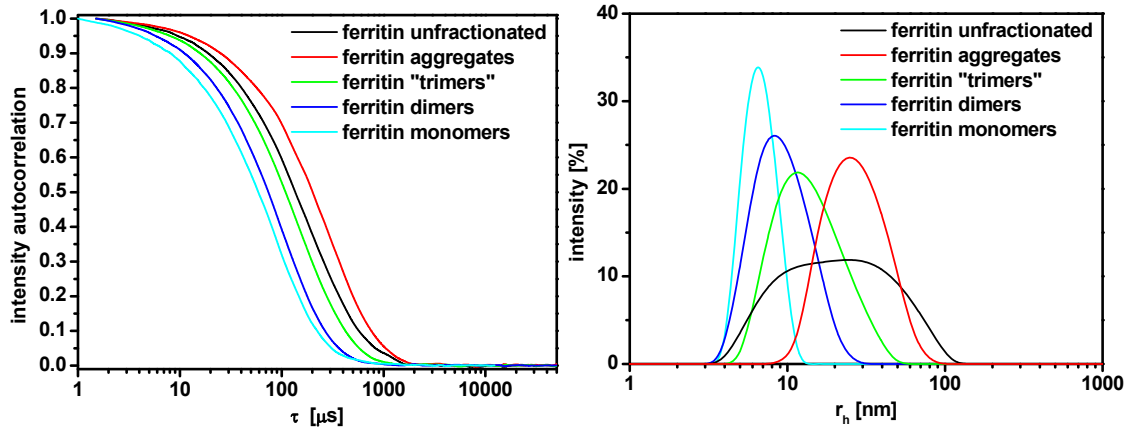


Fig. 19 Autocorrelation curves and CONTIN-plots of an unfractionated ferritin solution and of fractions from SEC.

Tab. 9 Hydrodynamic radii and diffusion coefficients of ferritin fractions.

	monomers	dimers	“trimers”	unfractionated
r_h [nm]	6.83 ± 0.16	9.30 ± 0.16	13.81 ± 0.22	17.95 ± 0.29
$10^7 \times D$ [cm ² s ⁻¹]	3.08 ± 0.07	2.26 ± 0.04	1.52 ± 0.02	1.17 ± 0.02
r_h [nm] ⁵⁰³	6.35	9.20	13.38	
$10^7 \times D$ [cm ² s ⁻¹] ⁵⁰³	3.19	2.21	1.48	

4.3 Bionanoparticle Characterization with SDS-PAGE

In sodium dodecyl polyacrylamide gel electrophoresis (SDS-PAGE), proteins are denatured and reduced in a heating step with SDS and 2-mercaptoethanol, respectively. This is necessary because only fully denatured proteins behave like simple coil-like macromolecules which hydrodynamic properties do not depend upon their specific three-dimensional conformation anymore. SDS binds strongly to the uncoiled protein, masks the surface charge and creates a net negative charge. The charge/size ratio is approximately constant for proteins and thus, separation in an electric field takes place

according to their size and their weight, respectively. Smaller molecules move faster than larger ones. The molecular weights are compared to the bands from a mixture of protein standards that is applied to a separate lane. The considerable amount of RNA which is contained in the virus precipitates during the denaturing step. It is not applied to the lanes of the gel and is not interfering during the sample preparation and the separation process.

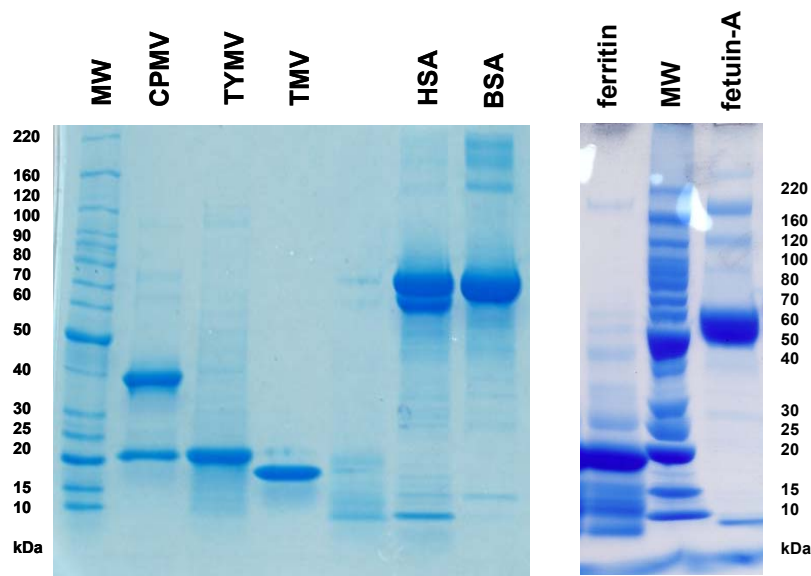


Fig. 20 SDS-PAGE of viruses and proteins used in this work (MW: molecular weight ladder).

Cowpea mosaic virus consists of two different coat proteins. 30 copies of a 41.2 kDa protein and 30 copies of a 23.7 kDa protein make the pseudo-symmetric capsid.²⁹⁶ Therefore, in gel electrophoresis two bands could be found. The capsid of the turnip yellow mosaic virus is composed of 60 copies of just one protein. Its molecular weight from composition amounts 20.1 kDa. In the tobacco mosaic virus the genome is enclosed in a helical arrangement of 2130 copies of a single coat protein which weight amounts 17.5 kDa. Also in this case, just one band could be found. The gel electrophoresis of the employed proteins BSA or HSA (both ~ 66 kDa) needs no further comment; the broadened bands or the occasionally found double band was ascribed to the mentioned microheterogeneity of serum albumins. Fetuin-A is a heavily glycosylated protein and appeared therefore in SDS-PAGE at higher molecular weight (54 kDa) than expected from composition (48 kDa). Ferritin has been reported as notoriously stable against usual denaturants.⁵⁰⁵ The employed sample buffer in combination with a

prolonged denaturing step of 10 min at 100 °C however cracked the assembly into the 24 subunits. The slightly different molecular weights of the L- and H-chains could not be resolved with the gel that was used. In horse spleen ferritin 90 % are L-chains with a molecular weight of 19.9 kDa.^{323, 506} The gels with all viruses and proteins are shown in Fig. 20. The molecular weight ladder and the corresponding molecular weights are depicted, too. Within the resolution limits of the gel the reported molecular weights were confirmed.

SDS-PAGE can be used as a cheap and fast method to evaluate protein conjugation with tags, dyes or polymers. In chapter 4.5 the characterization of dye-labelled CPMV with SDS-PAGE is presented.

4.4 Bionanoparticle Characterization with Transmission Electron Microscopy

The development of transmission electron microscopy and sample preparation techniques are closely connected with virology. The monodisperse, highly symmetric and structurally identical particles have been and are still be used as model specimens for the development of electron microscopy techniques.^{312, 507} Viruses are transparent to electrons and the contrast has usually to be enhanced with electron-dense materials.^{452, 453} During negative staining, the heavy metal stain surrounds the objects but does not penetrate it. The sample becomes brightly visible against a dark background. Commonly used negative stains are salts of phosphotungstic acid and uranyl acetate.

Pioloform and carbon grids were treated with a short glow discharge to improve hydrophilicity of the polymer films and enhance virus binding. First, CPMV was used to evaluate the adsorption and imaging characteristics on the two different films on the grids. Carbon is generally hydrophobic but glow-discharge treatment rendered a film surface which was sufficiently hydrophilic to enable homogenous spreading of single virus particles. On pioloform grids on the other hand, CPMV tended to form two-

dimensional crystalline patches. This often seemed to be triggered by dewetting processes during drying of the stained specimen.

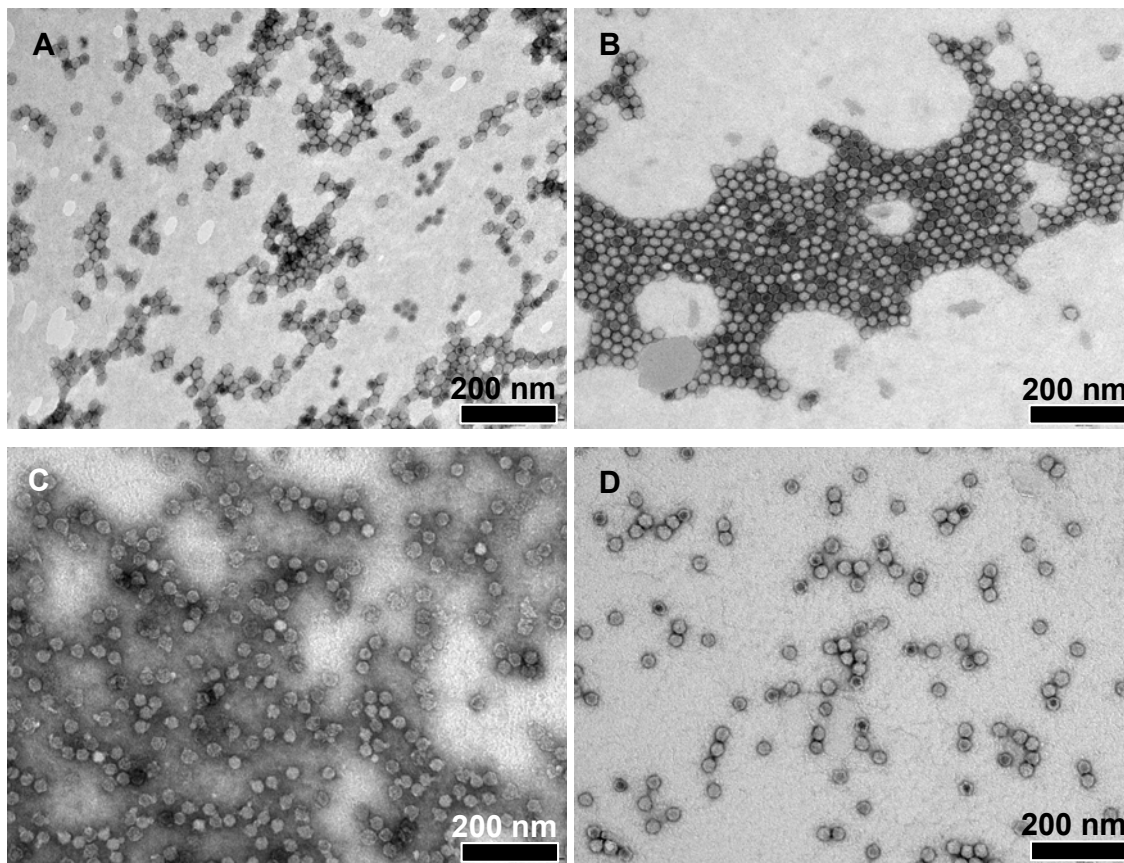


Fig. 21 TEM of negatively stained CPMV: (A) Uranyl acetate, pioloform; (B) phosphotungstic acid, pioloform; (C) uranyl acetate, carbon; (D) phosphotungstic acid, carbon.

Two different stains were used to account for probable incompatibility of some stains to the sample and buffer conditions. Uranyl acetate showed a strong influence on particle morphology. Virus particles appeared distorted or even degraded (Fig. 21, A, C). Further, the strong background staining led to high sensitivity to the electron beam. The films were easily destroyed and imaging became difficult. On the other hand, phosphotungstic acid stain concentrated around the sample. Virus particles kept their morphology and seemed not to be influenced by the stain. The specimen was stable under even high beam dose at highest magnifications. Overall, the best images were obtained from viruses spread on pioloform grids with phosphotungstic acid staining. This protocol was used successfully for TYMV and TMV, too.

CPMV formed large two-dimensional crystalline patches. As mentioned above, this might not only have been caused by interaction of the virus particles with each other but also by surface tension forces during dewetting. Compact hexagonal arrays were formed with occasional imperfections (Fig. 22, A). CPMV particles are icosahedral and appeared as distinctly shaped hexagons. A closer inspection of the specimen revealed that many particles appeared dark in the interior. These particles were empty capsids which were nicely seen as bright edges. The stain could penetrate the empty capsid and led to an electron dense core which appeared dark (Fig. 22, B).

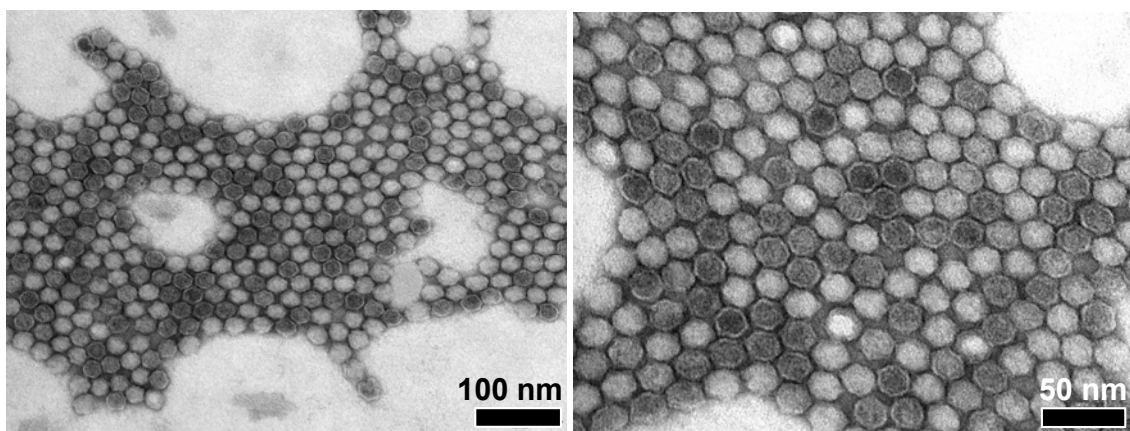


Fig. 22 TEM of negatively stained CPMV on pioloform.

TYMV specimens were prepared similarly to CPMV. Both stains, uranyl acetate and phosphotungstic acid, gave nice images (Fig. 23). The microstructure of the virus surface was better revealed with uranyl acetate staining (Fig. 23, A).

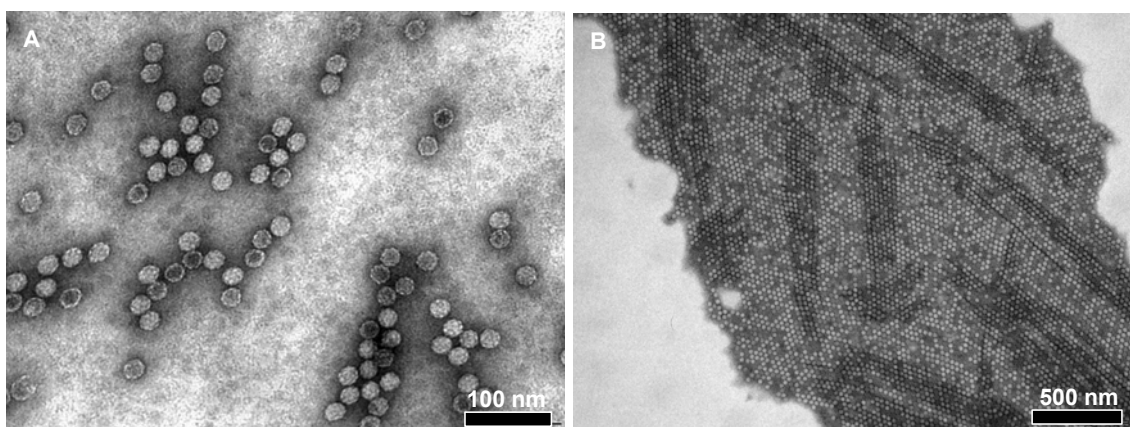


Fig. 23 TEM of negatively stained TYMV on pioloform: (A) Uranyl acetate; (B) phosphotungstic acid.

The icosahedral capsid ($T = 3$ -symmetry) is composed of 180 identical copies of one single coat protein. They appear on the exterior of the capsid as twelve capsomers with five-fold symmetry while another twenty capsomers show quasi six-fold symmetry (see also Fig. 5). At these symmetry axes the virus exhibits protrusions. The distance to the lowest depressions in the capsid at the quasi three-fold axes amounts approximately 4 nm.³⁰⁶ The raspberry-like surface morphology could be clearly discerned in the TEM images. High resolution imaging in AFM is able to resolve the surface morphology of single TYMV particles, too.^{465, 470} Similarly to CPMV, empty capsids could be found. Spread TYMV particles could assemble to different surface morphologies (Fig. 24, A). Mostly compact hexagonal arrays were formed, obviously due to the surface pressure arising from drying and dewetting (Fig. 24, C). This could even lead to the formation of double layers (Fig. 24, D). Where particles were more thinly spread and – obvious from the dark background – the sample dried in homogenously, also square crystals could be found (Fig. 24, B).

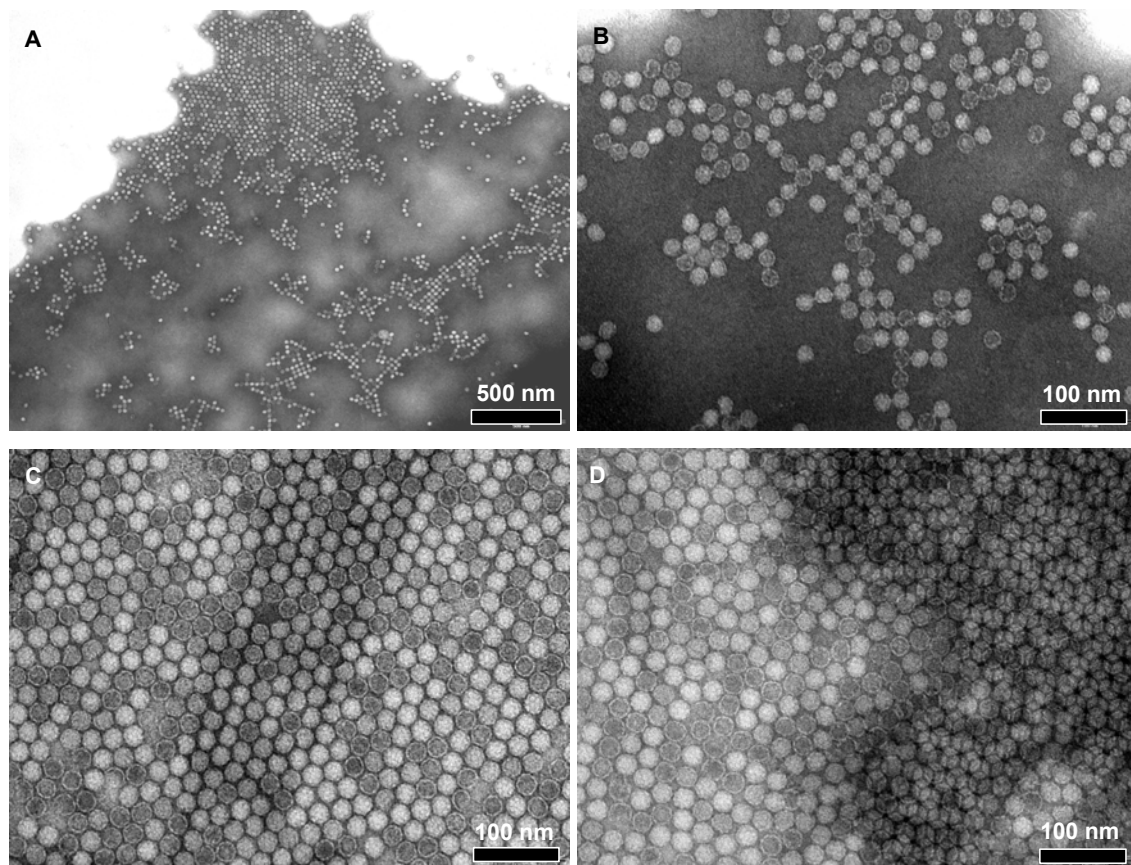


Fig. 24 TEM of negatively stained TYMV on pioloform. Different surface crystal structures: (A) overview, (B) square crystalline areas, (C) hexagonal surface crystal, (D) double layer.

TMV formed long end-on aggregates when stained with uranyl acetate (Fig. 25, A). The rods were well-separated and no preferential side-on aggregation could be seen, rather, the TMV rods were lying across each other. Sometimes they were unusually bent. The rigid nature of the TMV particles was well preserved during negative staining with phosphotungstic acid. In high resolution images, the inner channel could be seen which was accessible to the heavy metal stain (Fig. 25, B). Occasionally, small discs could be found, too. Such discs act as precursors from which the TMV assembly starts if RNA is present.³¹⁴ Strong side-on aggregation to TMV-bundles could be observed (Fig. 25, C) but also thinly spread, well separated viruses which aggregate end-on to long rigid rods could be seen (Fig. 25, D). The precise conditions for the observed aggregation phenomena were elucidated. Both aggregations were found on the same grid.

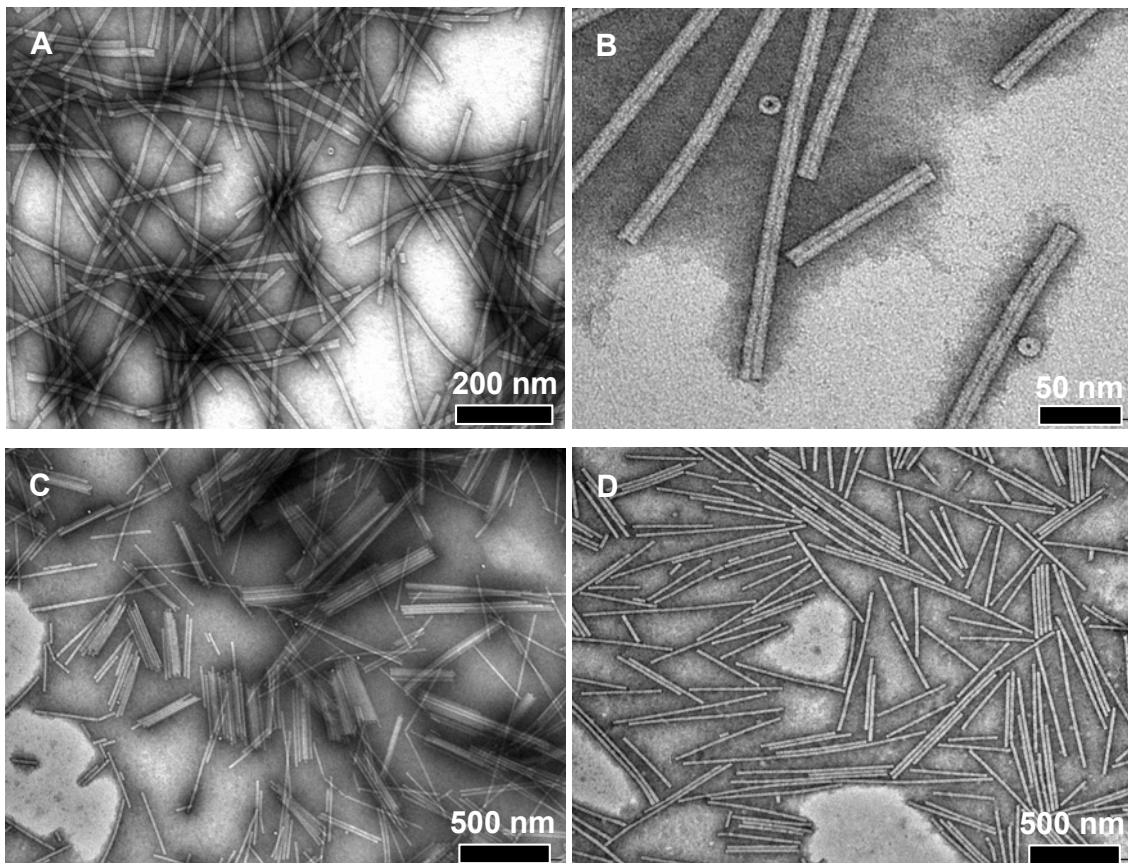


Fig. 25 TEM of negatively stained TMV on pioloform: (A) Uranyl acetate, (B)-(D) phosphotungstic acid.

4.5 Dye-labelled Cowpea Mosaic Virus

(Confocal) fluorescence microscopy allows the convenient visualization of fluorescently labelled biological structures and has rendered astonishingly beautiful and detailed pictures of cellular components and processes.^{508, 509} (Bio-) nanoparticle coated oil droplets and freely suspended membranes have been visualized with this technique, too.^{139, 181} The pictures give a good impression of the confinement of the particles at the interface (see chapter 6.1).

Generally, proteins or RNA show just weak fluorescence. Cowpea mosaic virus was therefore labelled with fluorescent dyes, fluorescein and tetramethylrhodamine, according to standard procedures (Fig. 26). The dyes were activated as *N*-hydroxy succinimide esters and conjugated to the virus capsid. A mixture of buffer/DMSO was used to enhance dye solubility. After reaction for 20 h at 8 °C, excess dye was removed by three cycles of gel filtration.

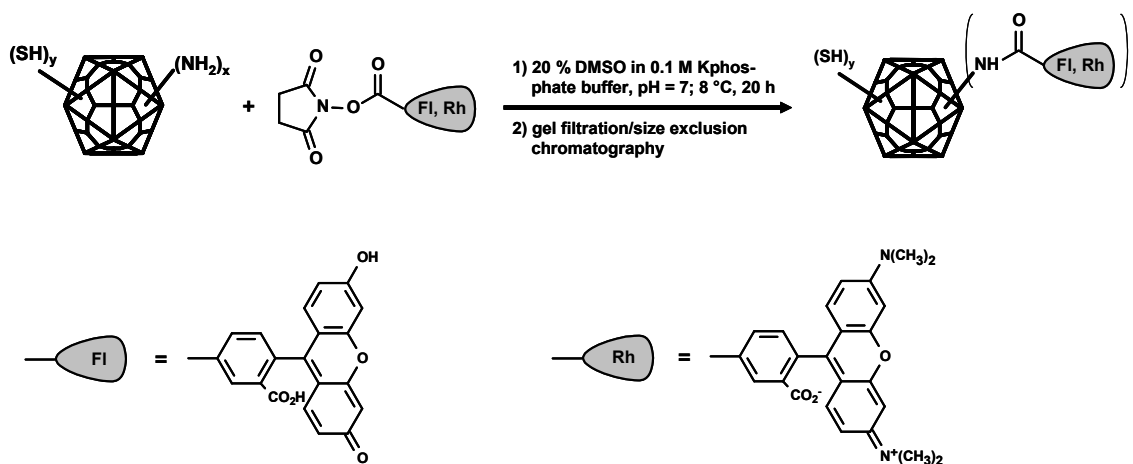


Fig. 26 Conjugation of fluorescein (Fl) and tetramethylrhodamine (Rh) to wild-type CPMV.

The dye-labelled viruses were characterized by SEC (Fig. 27). The molecular weight of the attached dyes was too less to be seen in the laser light scattering within the experimental error. The elution volume remained unaffected, too. DLS gave similar values as the native virus. SEC and light scattering just proved that the particles remained intact during the conjugation reaction.

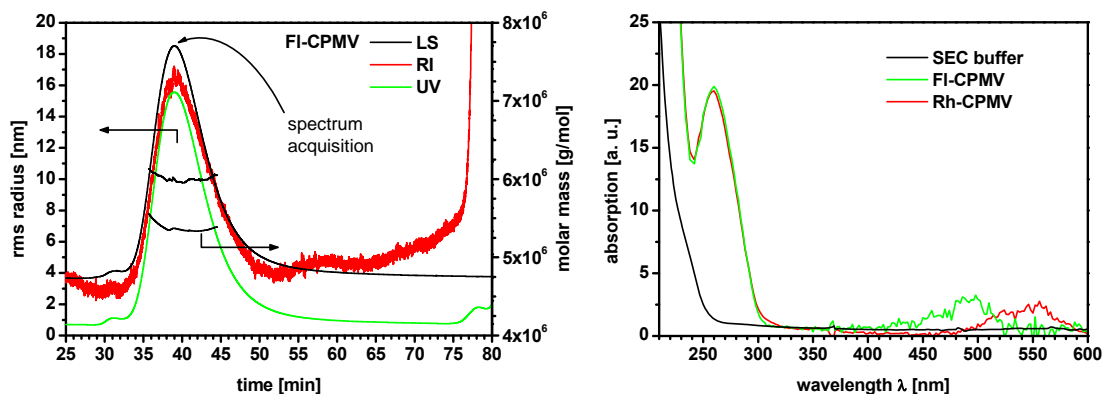


Fig. 27 (Left) Analytical SEC of fluorescein-labelled CPMV. (Right) UV-Vis adsorption spectra of fluorescein- and tetramethyl rhodamine-labelled CPMV at the elution time of 39.0 min.

At the elution of CPMV at 39.0 min, a spectral run was performed while continuous flow. Since the peak was broad and the spectral run took less than 30 seconds, no significant change in the concentration occurred. Although the absorption spectra showed significant noise at larger wavelengths, the typical absorption maxima for fluorescein at 495 nm and for tetramethyl rhodamine at 546 nm could be seen.

Since the dye absorbs just weakly at 260 nm, the ratio of CPMV/dye could be determined from the ratio of the absorption at 260 nm and the characteristic absorption of the dye in the visible range. Under the assumption, that conjugation did not change the absorption coefficient of 5- (and 6-) carboxyfluorescein succinimidyl ester (mixed isomers: $\epsilon = 74000 \text{ cm}^{-1}\text{mol}^{-1}$ at 495 nm) and 5- (and 6-) carboxytetramethyl rhodamine succinimidyl ester (mixed isomers: $\epsilon = 95000 \text{ cm}^{-1}\text{mol}^{-1}$ at 546 nm)⁵⁰⁸, an average of 107 fluorescein molecules and 66 rhodamine molecules had reacted with the capsid of one virus. Under the conditions of the experiment, an average of 200-240 fluorescein dyes should be attached per capsid.^{48, 52} The much lower loading achieved here could be explained with a slow degradation of the targeted functional groups of the virus capsid during prolonged storage of the batch.

In a systematic investigation of the reactivity of the accessible amino groups in the capsid of CPMV, the lysine residue 38 on the small subunit proved to be most reactive.⁴⁸ Overall, two amino groups on the small subunit and additional three amino groups on the large subunit are solvent-exposed but just four of them were accessible under forcing but non-denaturing conditions.⁴⁸ The selectivity depended on the

activation of the dye: isothiocyanate-activated dyes show specificity towards the lysine residue 38 of the small subunit but *N*-hydroxy-succinimid activated dyes were rather non-selective and labelling of the small and the large subunits occurred.^{48, 52} This could be seen in SDS-PAGE where both subunits were separated. In Fig. 28 the unstained gel was illuminated with UV-light and the fluorescence of the dyes indicated that both subunits were labelled. No fluorescence could be observed for the bands of wt-CPMV. On the right, the same gel is shown after Coomassie staining. The appearance of a double band for the small subunit could be explained by the partial cleavage of a short peptide from the carboxy-terminal end of the small subunit of CPMV.⁵¹⁰

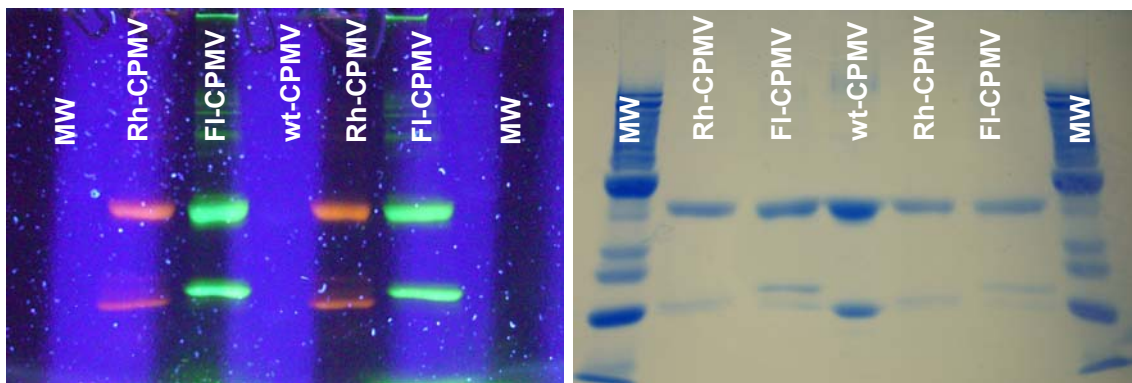


Fig. 28 SDS-PAGE of dye-labelled CPMV. (Left) UV-illumination, unstained gel. (Right) Coomassie stained gel (MW: molecular weight ladder).

Conjugated proteins can be conveniently characterized by mass spectrometry. Mild ionization methods like MALDI-TOF and ESI allow the measurement of high molecular weight peptides and polymers. Further, after tryptic digestion, smaller protein fragments can be analysed with high mass resolution. Here, the virus was not digested but the intact particles were subjected to MALDI-TOF mass spectrometry (Fig. 29). Simple standard conditions for protein mass spectrometry with sinapic acid as matrix were employed. Both subunits gave peaks with high intensity; additionally, the peak at 10 kDa could be ascribed to the double charged small subunit, the double charged large subunit fell together with the peak of the small subunit at 20 kDa. The peaks at 64 kDa and 85 kDa were single charged aggregates. The broad peak did not allow identifying the mass increase of 400-500 Da on both subunits; however, the increased intensity (especially of the 40 kDa peak) may be a hint for stronger absorption and ionization efficiency of the dye-conjugated subunits.⁴⁵ Also the appearance of the aggregates in

case of the fluorescein-labelled CPMV pointed to that, although, such argumentation has to be done with precaution.

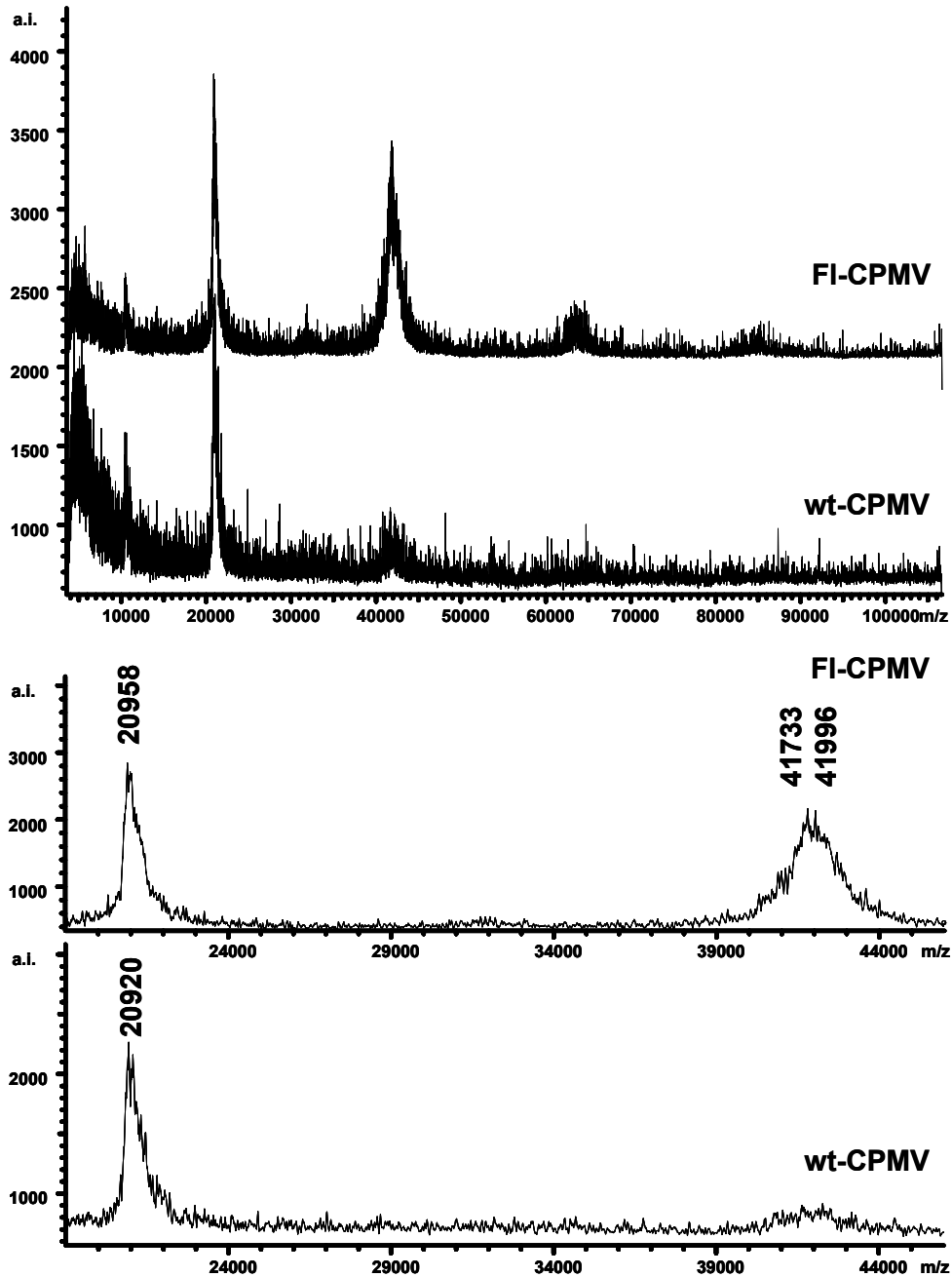


Fig. 29 MALDI-TOF mass spectrometry of wild-type CPMV (wt-CPMV) and fluorescein-labelled CPMV (FI-CPMV). (Top) overview; (bottom) magnification of the spectrum part with both subunits.

5 Protein Adsorption at liquid-liquid Interfaces

In contrast to simple surfactants, protein adsorption at liquid interfaces includes further dynamic processes at the interface. Proteins can unfold or be compressed after adsorption, depending on the bulk concentration and time. Large non-ideal entropic and enthalpic contributions do not allow the application of the basic Gibbs adsorption equation. The concept of varying partial molar areas has been a key to a quantitative description of the adsorption of proteins in very good agreement with experimental data and in accordance with the established qualitative picture. Moreover, the interaction of proteins with different non-polar phases (air or oil) can be quantified in terms of the partial molar area, too, and support qualitative descriptions and observations. The underlying interfacial dynamics can explain the sometimes very long times to achieve quasi-equilibrium.

In this work HSA, BSA and fetuin-A have been used as model proteins to establish the method and to prove the setup for interfacial tension measurements. Recent instrumental and methodological progress will certainly help to make pendant drop tensiometer measurements more a routine than a sometimes intricate and tedious task. Some of the difficulties that were encountered and their influence on the experiment will be addressed and discussed in the following, too. After it is ensured that the experimental and theoretical methods are in accordance with what is known from literature, the static and dynamic interfacial tensions of ferritin, CPMV and TYMV solutions at the decane/buffer solution interface will be presented and discussed.

5.1 Surface Tension Measurements of Proteins at liquid-liquid Interfaces

Protein solutions were diluted from the stock solutions with buffer. The drop with the protein solution was created at the end of a blunt cannula which was immersed in decane. The pendant drop measurements were immediately started but vibrations etc. from the drop formation did not allow to access measurement times shorter than 4-7 seconds. The dynamic interfacial tension curves for different concentrations for the

three proteins are shown in Fig. 30 and Fig. 31. Please note that corresponding colours do not mean the same concentration in the plots of different proteins except the orange curves which are the blank measurements (decane/buffer solution) in each graph.

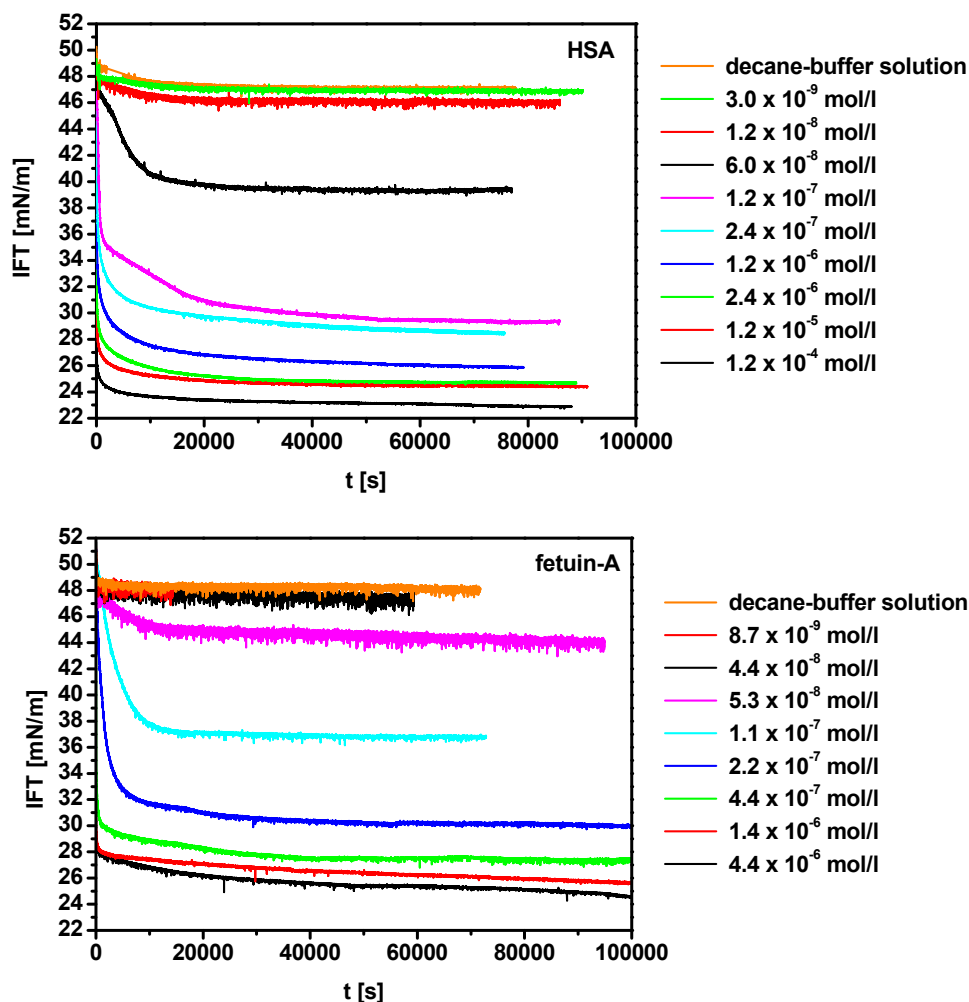


Fig. 30 (Top) Dynamic interfacial tension measurements of HSA and (bottom) fetuin-A at the decane/buffer solution interface.

A plot of the interfacial tension versus the reciprocal time allowed the determination of the interfacial tension in equilibrium state from the extrapolation $1/t \rightarrow 0$ as suggested by Wüstneck et al. and Fainerman et al.^{379, 384} (Fig. 31, bottom). This extrapolation considers the presence of an adsorption barrier in spite of the extrapolation $1/\sqrt{t} \rightarrow 0$. Both extrapolations have different assumptions, and for this reason it seemed not appropriate to use an average of the values as has been done previously, although both values were quite similar.²²⁷

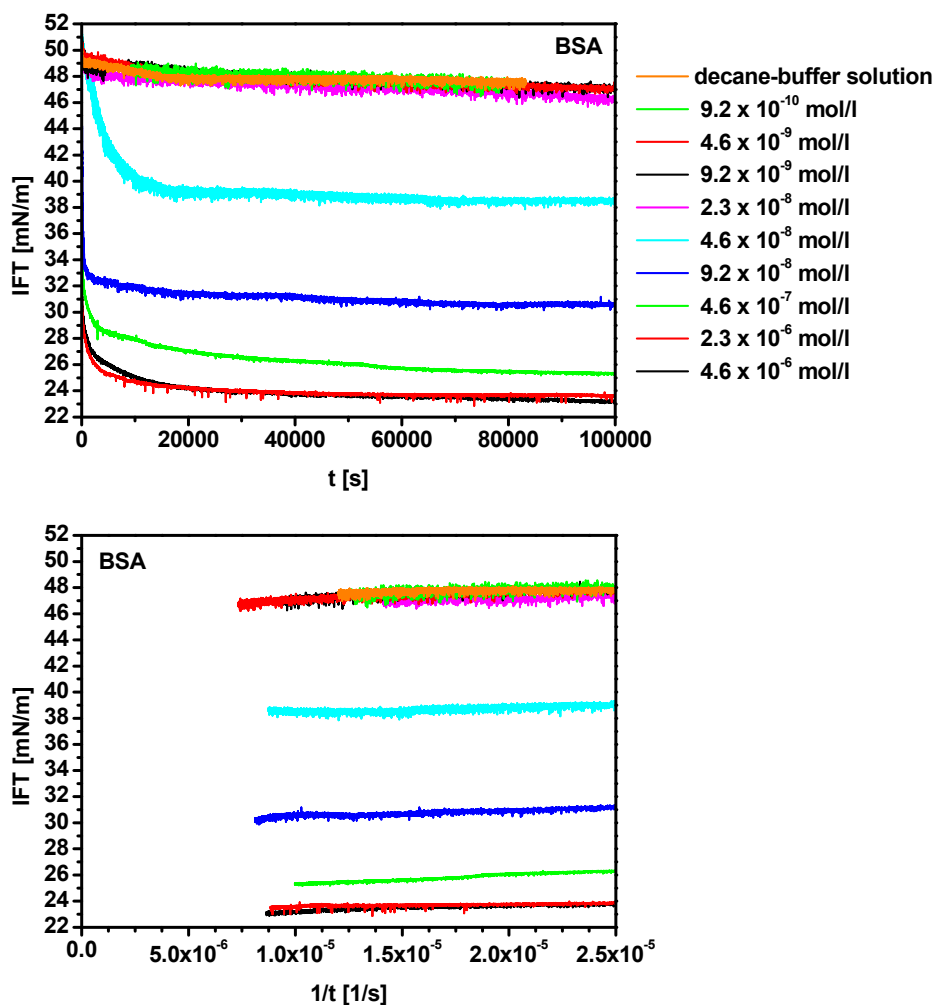


Fig. 31 (Top) Dynamic interfacial tension measurements of BSA at the decane/buffer solution interface and (bottom) the plot of the interfacial tension versus reciprocal time (same colour coding)

Measurements were done mostly for more than 24 h to achieve equilibrium conditions and values starting from 50000 s were usually used for extrapolation. In fact, extrapolated values were close to the measured final surface tension values. The interfacial tension of water versus pure decane was reported in literature to be 53.2 mN/m.⁴⁸⁶ Various batches of decane and purification cycles were tried in this work but this value was never really reached. All measurements with pure solvents and solutions of low concentration gave starting values of 52 ± 1 mN/m but were decreasing slightly after long times. One explanation might be small amounts of surface active contaminations in the buffer salts which could not be removed and come into play at long adsorption times. Further, BSA and fetuin-A samples were monomeric

fractions obtained from SEC which might also be a source of contaminations. Consequently, the buffer that was used for the dilutions of BSA and fetuin-A was also obtained after elution from the SEC and not separately prepared. Strictly speaking, the contaminations were huge but no better purification could be accomplished in this work.

The surface pressure isotherm was therefore always calculated from the extrapolation of the measured equilibrium surface tension of the actually employed pure solvent and buffer solution via $\Pi = \gamma_{0,t \rightarrow 0} - \gamma_{1,t \rightarrow 0}$. This procedure does not change the surface pressure isotherm if we assume that the surface pressure of the contaminants somehow add to the surface pressure caused by the protein which is approximately true for low protein concentrations.^{511, 512} In Fig. 32 the surface pressure isotherms for buffered solutions of HSA, BSA and fetuin-A versus decane are shown. The curves for HSA and BSA should be very similar but deviate at higher surface pressures. A possible reason might be that HSA was not separated to its monomer fraction but used as received. The fetuin-A isotherm is quite similar to the BSA-isotherm but shifted slightly to larger concentrations.

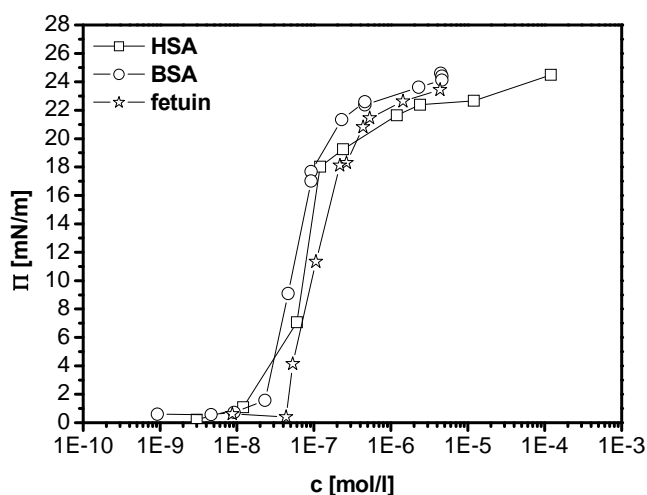


Fig. 32 Interfacial pressure isotherms of human serum albumin (HSA), bovine serum albumin (BSA) and fetuin-A at the decane/buffer solution interface.

As described in chapter 2.1.4, significant depletion of the initial bulk concentration occurs during the pendant drop measurements. Therefore, the plot of interfacial tension versus initial bulk concentration (as in Fig. 32) is shifted to higher concentrations compared to the curve plotted with the true equilibrium bulk concentration.

Unfortunately, there is no way to measure the very low bulk concentrations in the drop at adsorption equilibrium. A possibility is the correction of the initial bulk concentration for the adsorbed amount of protein (Eq. 30). The difficulty is that also the protein surface concentration at the drop interface cannot be determined easily. To the best of our knowledge, only Graham and Phillips reported independent curves of protein surface concentration (ellipsometry, radio tracer technique) and surface pressure (Wilhelmy plate method) versus true equilibrium bulk concentration, respectively, for lysozyme, β -casein and HSA at the decane/solution interface.¹⁹⁹ Makievski et al. recorded a surface pressure isotherm of HSA at the decane/solution interface with pendant drop tensiometry.³⁷⁵ They used the $\Gamma - \Pi$ -isotherm from Graham and Phillips to correct their surface pressure isotherm according to $c = c_0 - \Gamma(S/V)$ and found good agreement of their surface pressure isotherm with that of Graham and Phillips for low surface pressures.

For several reasons, this procedure was not followed here. The isotherm of Graham and Phillips had a maximum surface pressure of ~ 18 mN/m, a much lower value than was found by Makievski et al. and in this work where the maximum surface pressure was 27 mN/m and 24 mN/m, respectively. This difference in the range of Π precluded the meaningful use of the $\Gamma - \Pi$ isotherm of Graham and Phillips for other isotherms. The good agreement of the corrected surface pressure isotherm of Makievski et al. with those of Graham and Phillips might be a coincidental result.

Recently, the use of different surface tension techniques was proposed to correct the depletion of drops, particularly the combination of bubble and drop techniques, although any surface tension technique which has a significantly different surface-to-volume-ratio can be used.³⁸⁷ But another difficulty arises from the fact that different techniques imply different adsorption velocities. According to Eq. 20, the adsorption on a bubble is faster than on a drop if the same protein concentration is used. On the other hand, to obey the mass balance Eq. 30, the surrounding solution of a bubble must have a lower concentration to achieve the same equilibrium surface tension as a drop. This implies slower adsorption kinetics. However, the velocity of the adsorption process has an influence on the adsorbed amount of protein. This was shown by the detailed

investigation of the dynamic adsorption behaviour of β -casein at drop and bubble interfaces by Makievski et al.³⁷⁸ The authors found significant differences of the equilibrium surface tension between drop and bubble experiments. The surface tension of drop experiments was always significantly higher, for low as well as high initial bulk concentrations. The former observation could be ascribed to depletion of the drop solution but the latter must have been ascribed to an effect due to different adsorption kinetics. At high initial bulk concentrations, the equilibrium surface tension of bubbles was achieved much faster than in the case of drops while for lower initial bulk concentration the situation was reverse. The different adsorption kinetics could be explained in terms of the multiple state model of proteins at interfaces. Slower adsorption kinetics allowed the protein to unfold at the interface and to occupy a large partial molar area. For high bulk concentrations, the increasing surface pressure forced the adsorbed protein to occupy smaller partial molar areas but at low bulk concentration and lower surface pressures, the protein could not be refolded in finite times. Miller et al. suggested stirring of the solutions to achieve the same adsorption velocities.³⁸⁷ However, this seems not practical for small solution volumes. Finally, the peculiarities of protein adsorption where interfacial kinetics play an important role prevent a simple comparison or even convertibility of different adsorption experiments. It has to be mentioned that the proposed correction however worked well for highly surface active surfactants.³⁸⁶

Despite hard efforts no meaningful correction of the presented data sets for HSA and BSA could be achieved using already published data. Further, the drop volume under consideration may have to include the volume of the capillary and/or the syringe, too, as large diameter cannulas were employed and the measurements were run for long adsorption times. Finally, fetuin-A and the bionanoparticles were measured for the first time and data for comparison and/or correction were not available. The data of Graham and Philips for the adsorption of lysozyme, β -casein and HSA at the air/solution and oil/solution interface advise caution: each protein exhibited a peculiar Γ - Π -isotherm which could not be used for any other protein. Thus, for the following discussion one has to be aware that the surface pressure isotherms are all shifted towards higher apparent equilibrium bulk protein concentrations than the true equilibrium bulk concentration. Considering all points discussed above, the most appropriate approach to

overcome the problem would be to measure each data set with at least two drops of different size.³⁸⁷ The mass balance equation can be applied with reasonable accuracy for droplets which diameter differs at least by a factor of two. The experimental setup must be thoroughly revised then since parameters like drop size, cannula diameter, density of the employed solution etc. influence the drop shape and the accuracy of the interfacial tension measurement (see for a detailed investigation ref.^{399, 485}). Each isotherm must contain enough data points to allow interpolation of data points with the same final surface pressure as required by Eq. 30: $\Gamma = V/S(c_D - c_B)_{\pi=const.}$. All together, these efforts could not be achieved in the course of this work. Rather, we will explain in the modelling chapter how the shift of the surface pressure isotherm was reflected in the model parameters and how this influenced the modelling of the dynamic surface tension curve.

Finally, one has to state that surprisingly few data sets have been measured and presented throughout the last decades despite the recent good success in theoretical modelling of protein adsorption. Few of them comprise sufficient data points to achieve reasonably robust curves which allow meaningful comparison. Additionally, different systems (air/solution, oil/solution), oil phases, proteins and techniques (bubble shape, pendant drop, ellipsometry, Langmuir trough, Wilhelmy plate, radio tracer etc.) have been used. Each of them has peculiarities but they also complement each other. There is the feeling that a consistent series of good experiments with different techniques for a few but well-defined systems might be valuable for a further good progress in the field.

5.2 Modelling of Protein Surface Pressure Isotherms

Aksenenko published a set of programs which made the application of adsorption theory to experimental data amenable to a wider scientific public.⁵¹³ Own experimental data can be loaded and modelled according to several different adsorption isotherms, among them Langmuir, Frumkin and reorientation models. The programs are continuously refined and some of them can be freely accessed through the web.⁵¹⁴ Here, we used the program “ProteinM” which allows modelling of surface pressure isotherms according to the variable state model. Aksenenko kindly provided the program and

support.⁵¹⁴ The modelling procedure and the relevant equations are summarized in chapter 1.2.3.3 and are explained in detail in chapter 2.1.1. The reader is referred to these chapters for the theoretical background and the derivation of the equations.

The program was extensively used by Miller, Fainerman and coworkers in many research works. BSA and β -casein have usually been employed as model proteins in most of the works and some data sets were reported. The values for the modelling of the adsorption isotherm of BSA at the water/air interface in Tab. 10 were taken from a previous investigation of Berthold et al.¹⁸⁵ To the best of our knowledge, no results for modelling of the surface pressure isotherm of BSA at the oil/water interface were reported using the latest version of the protein adsorption model. A preliminary comparative study of HSA at the air/water and oil/water interface and modelling using a previous version of the theoretical model was presented in ref.^{223, 375} but cannot be compared well to our work. Parameter values for the β -casein adsorption at the air/water and oil/water interface from literature are also included in Tab. 10. They will help in the following discussion to work out differences of the adsorption at the air/water and oil/water interface.

Tab. 10 Parameter values in model calculations; the values for BSA at the decane/water interface are values obtained in this work.

	ω_0	ω_{\min}	ω_{\max}	a	b_p	ε	Π^*
	[m ² /mol]	[m ² /mol]	[m ² /mol]		[m ³ /mol]		[mN/m]
(a) BSA ²⁰³ (air/water)	2.5×10^5	2.5×10^7	7.5×10^7	1	3.0×10^2	0.05- 0.1	16-17
(b) BSA (decane/water)	2.15×10^4	3.5×10^7	7.5×10^7	0.75	3.0×10^2	0.05	21.5
β -casein ²²⁷ (air/water)	2.5×10^5	4.5×10^6	4.5×10^7	1	3.5×10^3	0.2	22
β -casein ²²⁷ (tetradecane/ water)	4.0×10^5	4.5×10^6	1.0×10^8	0.5	1.0×10^5	0.2	32

In Fig. 33, the experimental surface pressure isotherm of BSA at the decane/buffer solution interface is presented along with the calculated curve based on the model of varying partial molar areas (green: parameter set (b) for oil/buffer solution interface). The parameter values that have been used are included in Tab. 10.

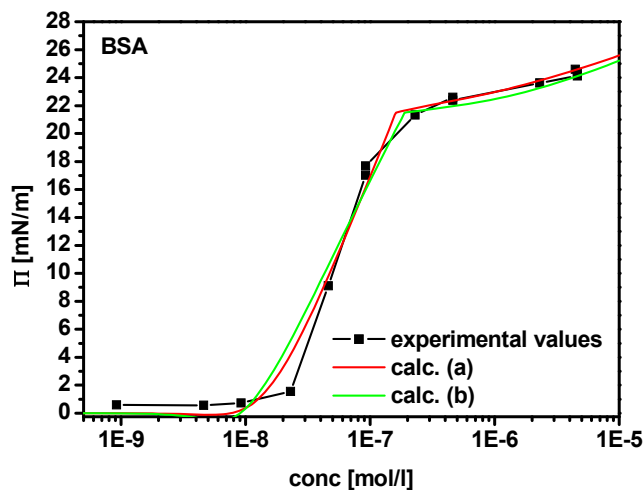


Fig. 33 Interfacial pressure isotherm of BSA at the decane/buffer solution interface and calculated curves according to the model of varying partial molar areas with the parameter values for the (a) air/water and (b) oil/buffer solution interface (see entries in first and second line, Tab. 10).

The parameter values for BSA at the air/water interface which were known from literature were used as an initial good guess in the modelling procedure. Then, the interaction parameter a was first screened for a meaningful value and that the calculated curve fits roughly the shape of the experimental curve. The value b was used to shift the calculated curve over the data points. Next, the different ω s were screened over a large range to yield progressively better fits. Π^* and ε were varied in a last step since they did not affect the precritical part of the curve. Any fitting procedure has the inherent (and mathematically proven) problem that no unambiguous result can be obtained. Even for “well-defined” functions (which is not the case here) that depend on more than one parameter, there is no finite algorithm which ensures the localisation of the global minimum. Thus, a rather different set of parameters may yield curves which fit the experimental values equally good. Some physical rationality must be used to identify reasonable parameters. BSA is known to be a “hard” protein which is less prone to denaturation and less flexible than others. It was assumed, that the structure of BSA was similar at the air/water and the oil/water interface. Thus, the parameter values for

the air/water interface could be a good starting point. Indeed, the parameter values that were determined for the oil/water interface were in the end quite similar to the starting values. The parameters could be changed in any order and direction but the parameters for a best fit remained the same. Pure mathematically, it cannot be ensured that the found solution is the global minimum; however, the found minimum made good sense as it coincides with physico-chemical interpretations (see below).

The parameter values for the adsorption of BSA, HSA or fetuin-A were pretty the same. The values are summarized in Tab. 11. One has to consider that the data basis for the presented surface pressure isotherms is relatively poor; in the steeply increasing part of the curve only very few data points have been measured. It is just sufficient to model and accept the calculated curve as reasonable but does not allow to discuss possible differences or to interpret the obtained values in too tiny details. If we look at the parameter values of BSA at the air/water and the oil/water interface, they almost did not change, moreover they can be considered as equal. The fitting curve calculated with the parameter values for the air/water interface is also included in Fig. 33 (parameter set (a), red curve). It is very obvious that not only the mathematically defined best fit (parameter set (b), green curve) but also parameter set (a) would be well acceptable.

Tab. 11 Parameter values for the calculated interfacial tension isotherms of BSA, HSA and fetuin-A at the decane/buffer solution interface.

	ω_0 (m ² /mol)	ω_{\min} (m ² /mol)	ω_{\max} (m ² /mol)	a	b_p (m ³ /mol)	ε	Π^* (mN/m)
BSA	2.2×10^5	3.5×10^7	7.5×10^7	0.75	3.0×10^2	0.05	21.5
HSA	2.2×10^5	3.5×10^7	7.5×10^7	0.75	2.0×10^2	0.063	20.0
fetuin-A	2.2×10^5	3.8×10^7	7.6×10^7	0.75	1.5×10^2	0.043	21.0

The quantification of the adsorption state in terms of the interfacial partial molar area allows discerning differences for the adsorption of proteins at different interfaces. We first summarize some observations and conclusions for β -casein from the literature and then turn to the discussion of the parameter values for BSA. The β -casein adsorption at the air/water and the oil/water interface has been comprehensively studied and

modelled.^{203, 227} β -casein is considered to be a flexible protein and its conformation at the interface is very dependent on its interaction with the adjacent oil phase. The area ω_0 of an adsorbed protein segment and the maximum occupied area ω_{\max} were determined as approximately double at the tetradecane/solution interface but the minimum area ω_{\min} was kept the same. The Frumkin interaction parameter a and the adsorption constant b were then used as fitting parameters, taking values that provided the best fitting. The lower value of a at the oil/water interface compared to the air/water interface was explained by the solvation power of the organic phase for hydrophobic protein segments which led to weaker interaction between protein segments at the interface. Both findings – the change of the interfacial partial molar areas and the lower interaction parameter - were interpreted in terms of a stronger interaction of the protein with the oil phase than with the non-polar air phase which gave rise to a stronger unfolding at the oil/solution interphase.³⁷⁶ The analysis of the interfacial elasticity confirmed these observations and provided further details on the interfacial conformations and unfolding of the protein.⁵¹⁵

The identical parameter values for the adsorption of BSA at both interfaces could be explained by the “hard” nature of the globular protein. It is less flexible than β -casein and less prone to conformational changes at the interface. This explained also the later onset of the interfacial pressure increase for BSA (at around 1 mg/m², see Fig. 34) compared to β -casein (0.5 mg/m²).²⁰³ The less unfolding was further reflected in the average occupied molar area (Fig. 34). BSA was only slightly compressed from 5.5×10^7 to 3.5×10^7 m²/mol with increasing surface pressure, i. e. approximately 1.5fold. On the other hand, β -casein was compressed tenfold for the transition from the diluted to the saturated surface layer.²⁰³ The more compact and rigid conformation of BSA is finally the explanation for the very similar behaviour at the oil/water and the air/water interface. BSA was chosen for the discussion because the surface pressure isotherm contained most data points of the three proteins investigated here. However, HSA is (physico-) chemically very similar to BSA; the discussion for the adsorption of BSA could be given equally for HSA and in fact, they have sometimes been mixed in the discussions and interpretations in literature.

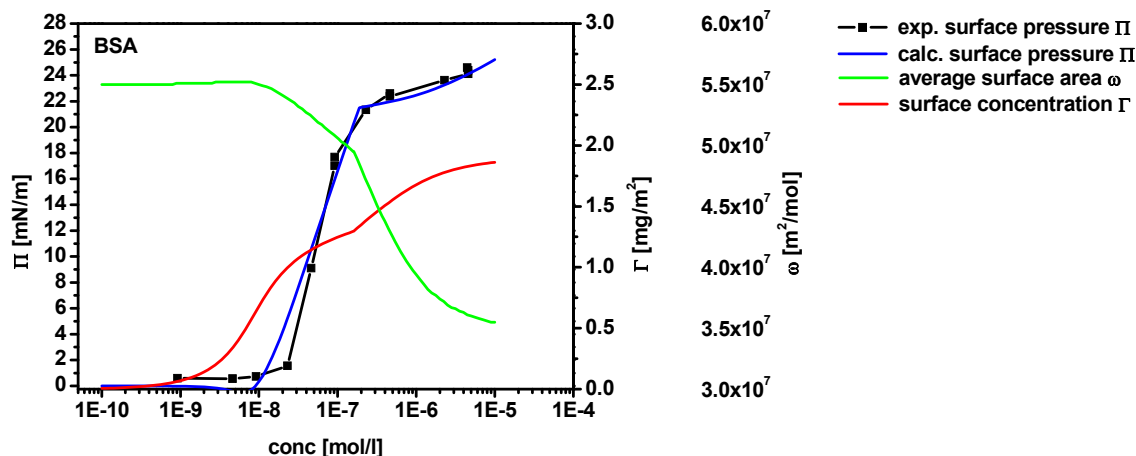


Fig. 34 Experimental and modelled (parameter set b) interfacial pressure isotherm, the calculated surface concentration Γ and the average occupied molar area ω of BSA at the decane/buffer solution interface.

As already mentioned, the surface pressure isotherm of fetuin-A was very similar to those of BSA/HSA (Fig. 32) which was also reflected in the very similar model parameter values (Tab. 12) and the similar curves of the average surface area and surface concentration (Fig. 35).

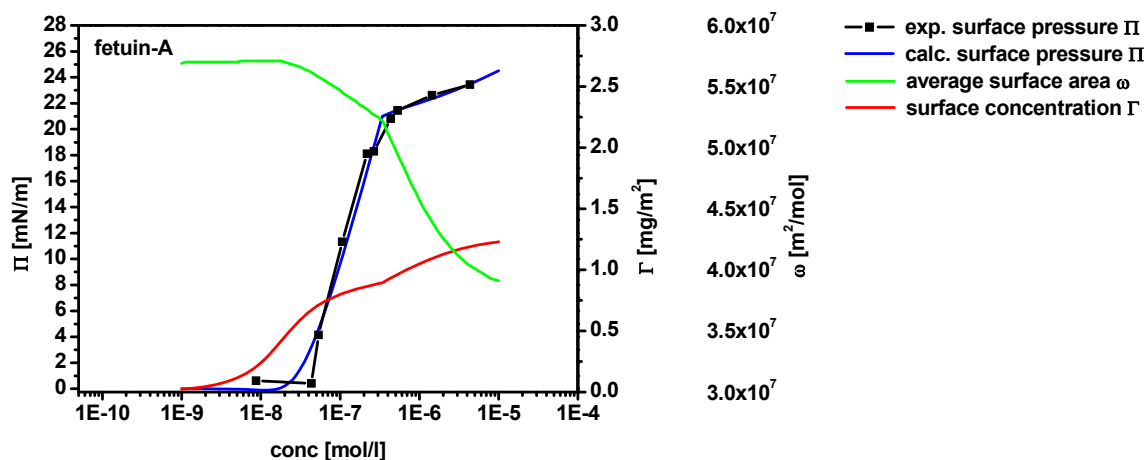


Fig. 35 Experimental and modelled interfacial pressure isotherm, the calculated surface concentration Γ and the average occupied molar area ω of fetuin-A at the decane/buffer solution interface.

Most probably fetuin-A has very similar physico-chemical behaviour like the “hard” BSA or HSA molecules. The lower mass surface concentration and slightly higher unfolding at the interface as seen from the average occupied surface area is a consequence of the slightly lower molecular weight (Fig. 35). A detailed discussion seems – given the poor data basis and the lack of literature data – not justified at the

moment. A more detailed investigation would however be of interest as fetuin-A contains – differently to all the other investigated proteins – a significant amount of carbohydrate.

It has already been pointed out above that the interfacial pressure isotherms were not corrected for depletion of the drop solution. This directly affects the value of the equilibrium constant b . As seen in Eq. 11, b does not enter the surface pressure isotherm but actually shifts the whole curve as it scales the concentration via bc_0 , i. e. b had only the meaning of a fitting parameter. For this reason, the obtained value of b is an apparent one and cannot be compared or discussed with literature values. It might be different for up to two orders of magnitude in different experiments. Further, the corrected curve would be flattened to lower concentrations because depletion and correction is stronger at low concentrations. However, this effect is minor and the parameter values would not be altered much. Finally, both effects do not invalidate the discussion above.

5.3 Modelling Dynamic Interfacial Tension Curves of Proteins

The parameter values obtained from the equilibrium surface or interfacial pressure isotherm and additionally the diffusion coefficients (see Tab. 7, Tab. 8, Tab. 9) were then used to model the dynamic adsorption curves according to Ward and Tordai.²¹⁸ We used the program “QProtein” which was developed and kindly provided by Aksenenko.⁵¹⁴ It used an iterative procedure to obtain the solution for the equation of Ward and Tordai which is based on diffusion only. The modelling of β -casein has been described in literature and satisfactory agreement between theory and experiment was found for the initial stages and low bulk concentrations.²¹⁸ Other interfacial processes which are not reflected in the purely diffusional model of Ward and Tordai come into play at times close to equilibrium and at high bulk concentrations and are mostly the limiting factors of the applicability of the equation of Ward and Tordai. The effective diffusion coefficient was found to be slightly higher for the adsorption at the oil/buffer solution interface, a fact that has not yet been satisfactorily addressed with an explanation. It must be mentioned, that the agreement between model and experimental

dynamic adsorption curves could be significantly improved if the maximum occupied area of a protein molecule was allowed to change during the fitting procedure. As remarkable result the maximum occupied area changes with the initial bulk concentration in excellent agreement with the concept of varying partial molar areas.²²⁷

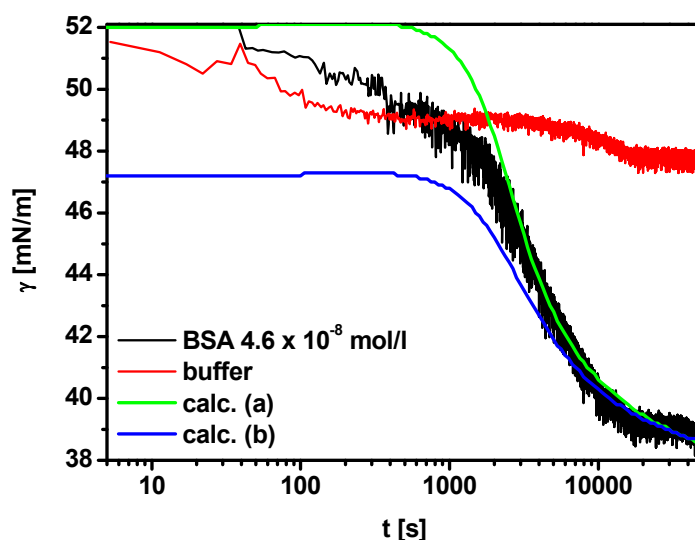


Fig. 36 Dynamic interfacial tension of BSA at the decane/buffer solution interface ($c = 4.6 \times 10^{-8} \text{ mol/l}$) and of the pure decane/buffer solution. The two calculated curves refer to different parameter sets (see Tab. 11, first line), with (a) $\gamma_0 = 52 \text{ mN/m}$, $b = 5.2 \times 10^2 \text{ m}^3/\text{mol}$ and (b) $\gamma_0 = 47.17 \text{ mN/m}$, $b = 3.0 \times 10^2 \text{ m}^3/\text{mol}$.

The dynamic interfacial tension curve for BSA ($c = 4.6 \times 10^{-8} \text{ mol/l}$) is plotted against the logarithmic time in Fig. 36. Here the effect of the insufficiently pure solvents and buffer solutions became dramatically obvious. After an initial strong drop of the interfacial tension we found another decrease after long times which led to a final equilibrium surface tension value of 47.17 mN/m rather than the literature value of $53 \pm 0.2 \text{ mN/m}$ for the pure solvents. The crucial point was that the fitting parameters of the surface pressure isotherm insert into the fitting procedure for the dynamic surface tension, i. e. the starting value γ_0 was 47.17 mN/m rather than the initial value of 52 mN/m . The direct consequence is that the calculated curve starts at 47.17 mN/m and consequently, there was insufficient agreement between the calculated curve and the experimental data points. Satisfactorily agreement could be found if $\gamma_0 = 52 \text{ mN/m}$ is chosen and the parameter b is adjusted to larger values (from $3 \times 10^2 \text{ m}^3/\text{mol}$ to

$5.2 \times 10^{-2} \text{ m}^3/\text{mol}$). Again, we used b as a fitting parameter because this value was not well defined in our data set anyway. The poor agreement between the calculated and the experimental curve for up to 2000 s must be ascribed to the impurities which were also seen in the measurement of the interfacial tension of the pure decane/buffer solution interface; further, the decrease of the interfacial tension at very long adsorption times (seen at approximately 30000 s) could be ascribed to the presence of impurities as well. There was the suggestion to treat the adsorption phenomena in our experiments as two separate adsorptions, one of the pure protein solution and one of a “contaminant” solution, in a simple additive way.^{511, 512} However, this procedure did not alleviate the differences for the early times much but would have introduced some new assumptions for the contaminants which seemed too speculative.

As already mentioned, the purely diffusional model of Ward and Tordai has its limitations at high concentrations and at times close to equilibrium. Both cases can be found in Fig. 37 in which the experimental and corresponding calculated curves for different concentrations are presented.

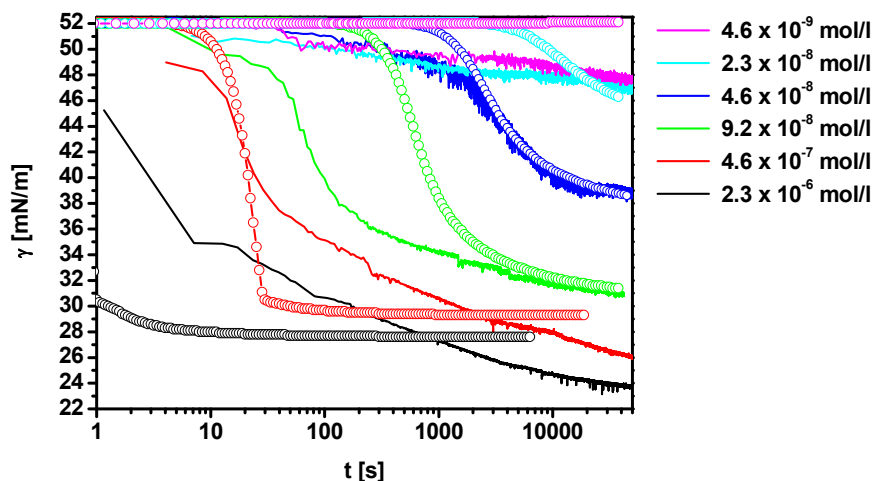


Fig. 37 Dynamic interfacial tension curves of BSA at the decane/buffer solution interface for different concentrations. Solid lines: experimental values; open symbols: corresponding calculated values according to Ward and Tordai and the model of varying partial molar areas with the parameter values given in Tab. 11.

We found only good agreement for $c = 4.6 \times 10^{-8} \text{ mol/l}$, which was a point in the middle of the steeply increasing part of the interfacial pressure isotherm. Progressively less agreement could be found for higher as well as lower concentrations. The latter must be

clearly ascribed to the impurities in our measurement. Of course, the model would predict for sufficiently low concentrations (i. e. for Γ smaller than the minimum adsorption) no change of the interfacial tension but in our case, the contaminants were responsible for a significant change at any low concentration (see e. g. $c = 4.6 \times 10^{-9}$ mol/l). The disagreement for high concentrations was typically observed for any protein solution and has been well described in literature.²¹⁸ In the beginning of the experiment the process developed slower than predicted by the theory. This could be explained by the initial unfolding of the protein at the interface for lower surface pressures. The slow transition rate between different states in the following was responsible for the less strong decrease of the interfacial tension. It was shown that the incorporation of reformation kinetics in the modelling improved the agreement between theory and experiment.⁵¹⁶ For long adsorption times at high bulk concentrations multilayer adsorption etc. occurred. The interfacial tension is determined by interfacial processes which were not included in the diffusional model of Ward and Tordai. The interfacial kinetics are very slow and adsorption equilibrium was not achieved within a reasonable time frame (see e. g. $c = 2.3 \times 10^{-6}$ mol/l).

To give a conclusion, the use of insufficient pure solvents was seriously interfering with the adsorption of protein during the experiment. Although we could identify this influence we could only discuss it qualitatively. While the overall observations are in excellent agreement with other investigations and reports in literature, the obtained values should still be treated with care. No conclusion should be drawn from tiny differences in the obtained values when comparing to other reports or other systems. However, the aim to prove and establish the methodology in this work must be still considered as highly successful.

The proposed limiting approximations of the equation from Ward and Tordai for short adsorption times to calculate the diffusion coefficient resulted in values which are several orders of magnitude too high, a result that is well-known and was already reported earlier.²¹⁴ This was found for the proteins and especially for the bionanoparticles in the investigations here, too. The much too high diffusion coefficient has been explained as the simultaneous adsorption of multiple segments of the protein which could obviously mimic a larger diffusion coefficient. Further, pendant drop

tensiometry is not suitable for short time ranges and affected by comparatively large errors, thus by no means the short time approximation can be applied. Modelling the whole curve with the available programs provided a much more valid approach.

5.4 Bionanoparticle Adsorption at liquid-liquid Interfaces

There was a preliminary report on the use of pendant drop tensiometry to investigate the adsorption kinetics of cowpea mosaic virus at the perfluoro octane (PFO)/buffer solution interface.¹⁸¹ The experiments have been repeated with much extended adsorption times to achieve true adsorption equilibrium but it turned out that PFO tended to wet the metal capillary. Strongly varying interfacial tension curves with accidental strong decreases and even increases were observed and data could not be reproduced reliably. Further, it seemed more useful to stick to the liquid/liquid system used throughout the investigations with the proteins and therefore ferritin and the virus solutions have been measured at the decane/buffer solution interface, too.

The interfacial tension measurements of ferritin and virus solutions require some comments on the reproducibility of the experiments. The production of the virus suspensions from plant leaves exhibits the risk of contamination with other biomolecules. Strict purifications with density gradient centrifugation and extensive dialysis would have been necessary and even then, during the different steps further surface active contaminants could be introduced. The solutions that have been used here could not be subjected to a rigorous purification procedure because of limited sample amount and access to technical equipment. The samples have just been clarified by filtration with 0.22 μm filters before measurement. It turned out, that within a batch but also between different batches the measurements for a certain concentration can vary within 1-2 mN/m. The measurements were generally stronger affected by artefacts than the measurements of the proteins and reasonable curves had to be selected. The dynamic interfacial tension for solutions of different concentrations of CPMV, TYMV and ferritin are shown in Fig. 38 and Fig. 39.

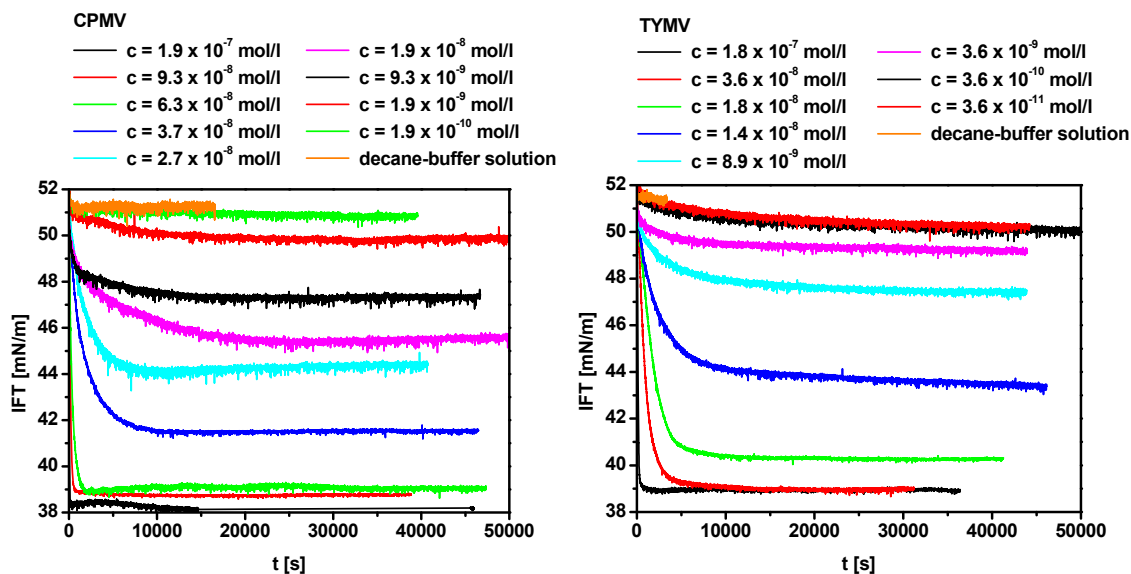


Fig. 38 Dynamic interfacial tension measurements of (left) cowpea mosaic virus (CPMV) and (right) turnip yellow mosaic virus (TYMV) suspensions at the decane/buffer solution interface.

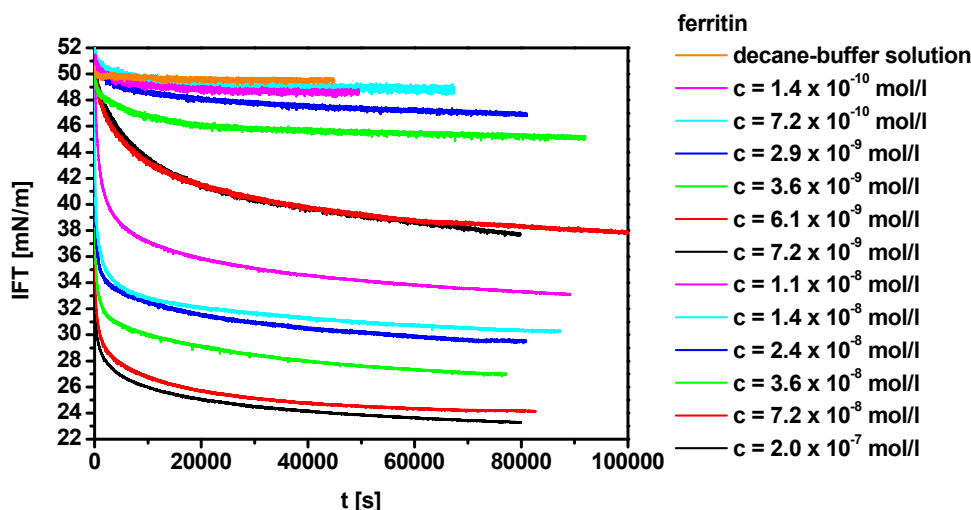


Fig. 39 Dynamic interfacial tension measurements of ferritin suspensions at the decane/buffer solution interface.

The equilibrium interfacial tension values have been determined in the same way as for BSA from the $1/t \rightarrow 0$ extrapolation of a plot of the interfacial tension γ versus reciprocal time. The thus obtained surface pressure isotherms for the bionanoparticle suspensions are presented in Fig. 40.

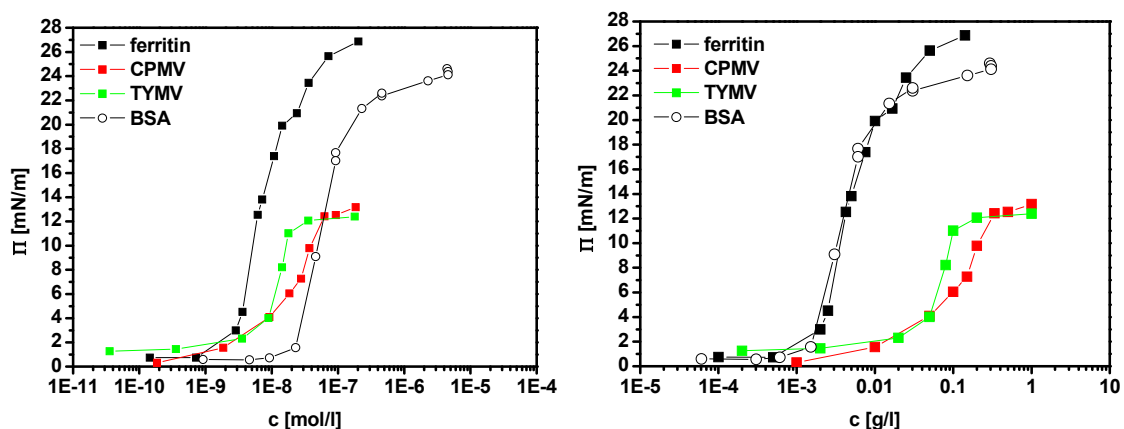


Fig. 40 Interfacial pressure isotherm of TYMV, CPMV and ferritin at the decane/buffer solution interface, plotted vs. (left) molar concentrations and (right) mass concentration. For comparison, the isotherm of BSA is included, too.

A significant shift of the curves for ferritin and the two icosahedral plant viruses could be observed compared to BSA which isotherm is included in Fig. 40 for comparison, too. However, given the compact shape and very different molecular weight of ferritin and the viruses, respectively, it would be more appropriate to compare the different bionanoparticles according to their weight concentration. Then we found that the interfacial pressure curve of ferritin fell together with that of BSA while the curves for the plant viruses are significantly shifted towards higher concentrations. That meant, that the virus particles were much less efficient in stabilizing the interface at the same given protein mass concentration. Further, they were much less surface active than ordinary proteins or ferritin as seen from the much lower maximum surface pressure. That both viruses behaved more or less identical was not surprising; both viruses have the same size (radius 15 nm), shape (icosahedral) and structure (pseudo-T3). As already mentioned, proteins of average compositions do not exhibit significant differences in the interfacial tension.

The modelling of the ferritin surface pressure isotherm has been performed with the program “ProteinM” similarly to the modelling of the proteins BSA and fetuin-A. As we knew from images of the adsorbed ferritin at the interface, it built a dense monolayer (see chapter 6.2). For a hexagonal crystalline assembly, an average surface area of $1.4 \times 10^7 \text{ m}^2/\text{mol}$ was calculated. This value was used with a slightly lower and slightly higher number as starting values for the minimum and the maximum occupied surface

area ω_{\min} and ω_{\max} , respectively. The surface area of an adsorbed protein segment was kept the same as for the proteins, also the Frumkin-like interaction parameter a . Parameter b was used again only as fitting parameter to achieve an overlay of the calculated curve with the experimental curve.

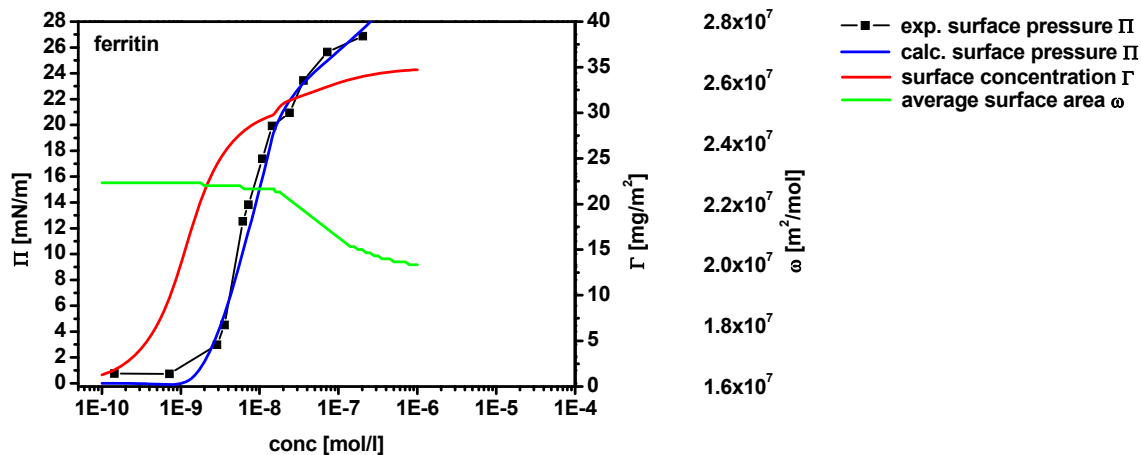


Fig. 41 Experimental and modelled interfacial pressure isotherm, the calculated surface concentration Γ and the average occupied molar area ω of ferritin at the decane/buffer solution interface.

The dynamic surface tension curves already indicated the tendency of ferritin solutions to hardly reach equilibrium. We see in chapter 6.3 that the particles remained largely intact upon adsorption, i. e. obviously only the side which was adsorbed at the oil interface was denatured, but this did not destroy the protein shell. It could therefore be assumed that the interfacial dynamics were not dominated by refolding processes but rather reordering processes at the interface from liquid-like to more ordered and denser surface assemblies. About the formation of multilayers we can only speculate as long as no measurement of the surface layer thickness is available. Moreover, the observation that ferritin was not denatured at the interface – which is supported by the well-known stability of the ferritin cage – was also proven by the parameter values from the isotherm fitting (Tab. 12). The ferritin isotherm had sufficient data points to yield a stable and convincing fitting curve. The minimum and maximum occupied molar surface areas were nearly the same and amounted $2.0\text{-}2.5 \times 10^7$ m²/mol. Consequently, the average surface area of an adsorbed ferritin particle did not change for the transition from a diluted to a dense surface layer (Fig. 41, green curve). This result proved nicely the universal power of the concept of varying partial molar areas. It includes soft

macromolecules which can undergo significant conformational changes (e. g. β -casein), “hard” globular proteins (e. g. BSA) which undergo only minor conformational changes and it is also able to correctly model the adsorption of large macromolecular assemblies. The similar (i. e. here even identical) interaction parameter a makes sense in the way that it is a not well-defined constant summarizing intermolecular interactions which are similar for different proteins.

Tab. 12 Parameter values for the calculated interfacial tension isotherms of ferritin at the decane/buffer solution interface; the different parameter sets (a) and (b) for CPMV and TYMV are explained in the text.

	ω_0 (m ² /mol)	ω_{\min} (m ² /mol)	ω_{\max} (m ² /mol)	a	b_p (m ³ /mol)	ε	Π^* (mN/m)
ferritin	2.1×10^5	2.0×10^7	2.5×10^7	0.75	1.5×10^4	0.04	19.5
(a) CPMV, TYMV	2.5×10^5	1.3×10^7	1.1×10^8	0.5	4.0×10^2 , 9.0×10^2	0.5	12.5 12.0
(b) CPMV, TYMV	2.2×10^5	3.5×10^7	7.5×10^7	0.75	4.0×10^2 , 9.0×10^2	0.2	12.5 12.0

The modelling of the dynamic interfacial tension curves of ferritin according to Ward and Tordai with the program “QProtein” failed. The program did not calculate any increase of surface pressure with the given parameters, even for the highest ferritin concentrations. The overlay of the fitting curve with the experimental interfacial pressure isotherm could only be achieved if the concentration was scaled with a large value for the adsorption constant b . However, a further adjustment of b in the fitting procedure of the dynamic interfacial tension curve did not improve the discrepancy significantly. The problem could be that the more efficient decrease of the surface pressure at low concentrations could not be solved by simply adjusting the adsorption constant b but rather a different mechanism or model isotherm has to be considered. The purely diffusional model of Ward and Tordai is definitely limited but the absolute failure of applicability is a sign that a different model isotherm or adsorption mechanism might be necessary. It is possible that protein complexes with their considerable dimensions must be treated by including their occupied surface area in a different way. Possible starting points for a new set of equations can give the recently

reported description of the surface pressure isotherms from particulate monolayers in Langmuir troughs.^{190, 191, 517}

The interfacial pressure isotherms of the plant virus solutions were unfortunately only insufficiently determined. The virus solutions were prone to erroneous measurements and not all measurements could be identified as reasonable and included into the isotherms. The establishment of a more robust isotherm would have required very intensive efforts which finally could not be accomplished here. Model curves which have been calculated according to two different sets of parameter values are included in each of the plots of the two isotherms (Fig. 42). The parameter set (a) (red curves) was obtained for both virus isotherms as similar mathematically best fit. It barely describes the experimental isotherm of CPMV and only insufficiently the isotherm of TYMV. The parameter set (b) (green curves) was used from the modelling of BSA as kind of model protein parameter set. Pure mathematically, parameter set (a) would have been the one of choice. But it is very obvious that the minimization of the error is not the only argument for the validity of the curve; in fact, which curve would be better seemed to depend only on one or two data points. Thus, we did not trust to go further on with the evaluation as long as no better isotherms were available.

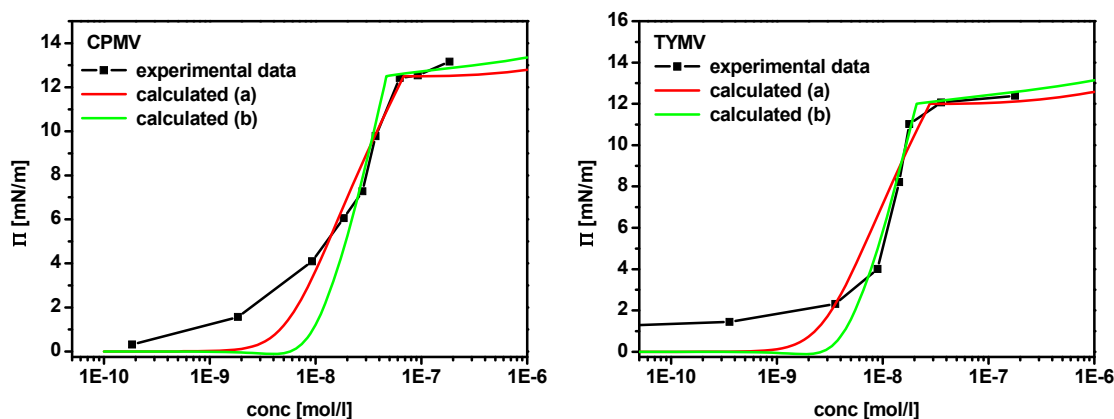


Fig. 42 Experimental and calculated interfacial pressure isotherms for CPMV and TYMV at the decane/buffer solution interface for two different parameter sets (see Tab. 12).

6 Investigation of Bionanoparticle Assemblies at Interfaces

The protein cage of ferritin and the viruses have sizes which are accessible to many different surface analytical techniques. The experiments in this chapter aim to prove the presence of the bionanoparticles at the interface and to image the assembly to find out about the two-dimensional surface structures. The liquid interface itself is difficult to access analytically. Horizontal pick-up of interfacially assembled nanoparticles has been routinely used to transfer the assembly to solid interfaces, however, surface tension and dewetting effects can lead to significant re-ordering during drying which may lead to erroneous conclusions. Therefore, we cross-linked the bionanoparticle assemblies with glutaraldehyde before drying or we used a liquid precursor oil phase which could be cross-linked by UV-light. The bionanoparticles are fixed together at the interface and the surface of the dried capsules or of the solid Pickering droplets can be investigated under dry or solution conditions with SEM or AFM.

6.1 Bionanoparticles at liquid-liquid Interfaces

Pickering emulsions were prepared by adding the oil phase to the buffered bionanoparticle solutions (maximum 1/10 v/v) followed by vigorous shaking by hand. The droplets had typical diameters of some ten micrometers and were quite polydispers. Excessive creaming was observed if ultrasound or mechanical stirring was used. Since the dispersity and size of the droplets was not of primary interest here, no efforts were undertaken to obtain different emulsions by other dispersion techniques. The suspensions of oil droplets prepared from the proteins and ferritin were stable for several months without coalescence, even if the droplets had been extensively washed with pure buffer or water or were heated to 37 °C for several weeks. However, in some cases of Pickering emulsions that were prepared from plant virus solutions, coalescence was observed within 2-3 hours although the droplets were crosslinked.

The droplets had sizes which made them amenable to investigations with optical microscopy but the thickness of the bionanoparticle layer is certainly too small to be seen. This problem could be circumvented if fluorescently labelled particles were used.

CPMV that was labelled with fluorescein or tetramethylrhodamine (see chapter 4.5) was used to prepare a Pickering emulsion with perfluorooctane as oil phase. After assembly, the droplets were extensively washed with buffer. The droplets were then imaged with a confocal laser scanning fluorescence microscope using standard conditions for fluorescein and rhodamine excitation and image acquisition, respectively. In fluorescence microscopy with a confocal configuration the image is generated just from the emitted light in a horizontal plane with a finite thickness. The pictures resemble horizontal cross-sections. One such horizontal cut through several droplets is shown in Fig. 43, A. The bright fluorescence at the interface showed the preferential adsorption and trapping of the CPMV particles at the perfluorooctane/buffer solution interface. The interior oil phase was completely dark and no particles were dissolved in the oil phase. The surrounding aqueous phase showed some negligible residual background fluorescence. Many pictures along the z-axis were acquired and an overlay of all planes was merged to give a three-dimensional image reconstruction (Fig. 43, B). The images visualized nicely the confinement of the bionanoparticles at the interface.

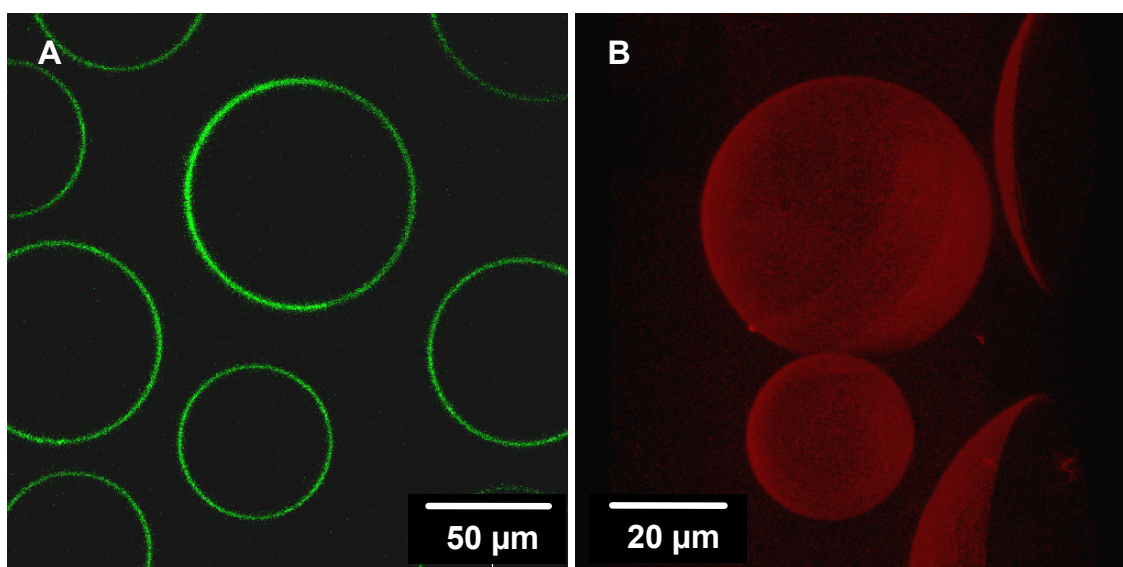


Fig. 43 (A) Z-section from confocal laser scanning fluorescence microscopy of a Pickering emulsion prepared with fluorescein-labelled CPMV and (B) three-dimensional reconstruction of a Pickering emulsion prepared with tetramethylrhodamine-labelled CPMV.

The technique of fluorescence recovery after photobleaching (FRAP) was tried to investigate the mobility of virus particles. The movement is confined to lateral diffusion since the virus is trapped at the interface. CPMV-Pickering emulsions were used which

have been cross-linked with glutaraldehyde solution for 30 min before washing or which have not been cross-linked. In the first case, no fluorescence recovery should be found after photobleaching of a small area with the scanning laser because the virus particles should be fixed to their neighbours. In the case of not cross-linked virus particles, a slow recovery of the fluorescence should be observed because not bleached viruses can diffuse from the surrounding to the bleached area. The results were not conclusive, for example, no photobleaching was observed for the not cross-linked particles which would have meant an instantaneous recovery which would have been quite unrealistic. Nevertheless, these experiments would contribute a lot to the understanding of the interfacial assembly of proteins and nanoparticles at liquid interfaces and there is a certain need for repetition. Fluorescence correlation spectroscopy would be another tool to investigate lateral diffusion dynamics of single molecules at membranes and interfaces.⁵¹⁸⁻⁵²⁰

6.2 Bionanoparticle Membranes

Bionanoparticles at liquid-liquid interfaces formed stable capsules and membranes. If they were deposited and dried on a flat substrate they folded similarly like a deflated football and could be imaged by optical or electron microscopy (Fig. 44).

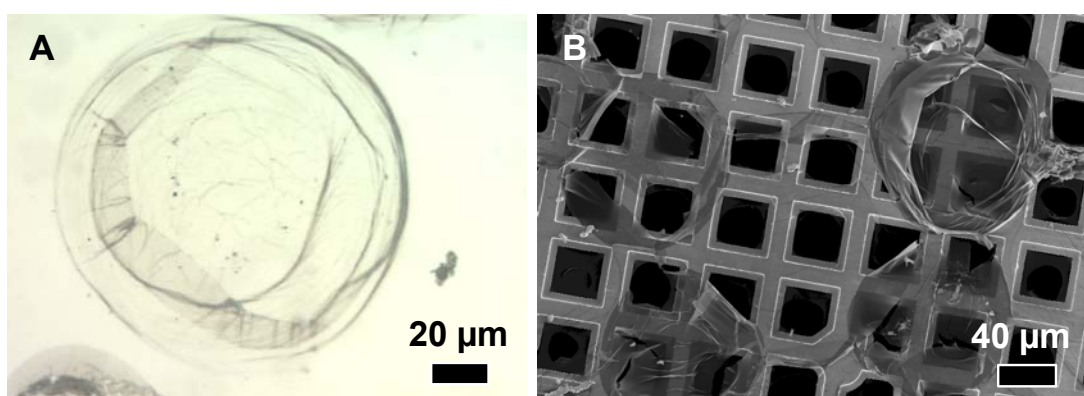


Fig. 44 Dried capsules prepared from a ferritin stabilized perfluorooctane/buffer solution Pickering emulsion: (A) optical microscopy; (B) scanning electron microscopy.

Droplets of bionanoparticle Pickering emulsions were dried on TEM grids (Fig. 44, B) and investigated by transmission electron microscopy (Fig. 45). Ferritin was employed

as stabilizing particle of the perfluoro octane/buffer solution interface and crosslinked with 1 % glutaraldehyde (v/v) before washing. The organic oil phase destroyed the support film on the grid and the capsules spanned freely over the holes of the grid. A capsule is shown in Fig. 45 which was burst and only one layer is seen. In the upper part, typical wrinkles of the folded capsule shell can be seen. The ferritin layer ripped during imaging in the TEM and the left part was folded back. The image was not stained and the black dots represent the iron oxide cores of ferritin. We found a dense and compact layer but closer inspection revealed that the layer did not exhibit two-dimensional crystalline order. This could not be ascribed to the presence of ferritin dimers or aggregates since the monomer fraction was employed; further, this could not be ascribed to the heterogeneity of the ferritin core as well since the outer protein coat is identical and independent of the size of the inorganic core. In fact, ferritin and apoferritin (ferritin devoid of the iron oxide core) have identical pair interactions.^{329, 503}

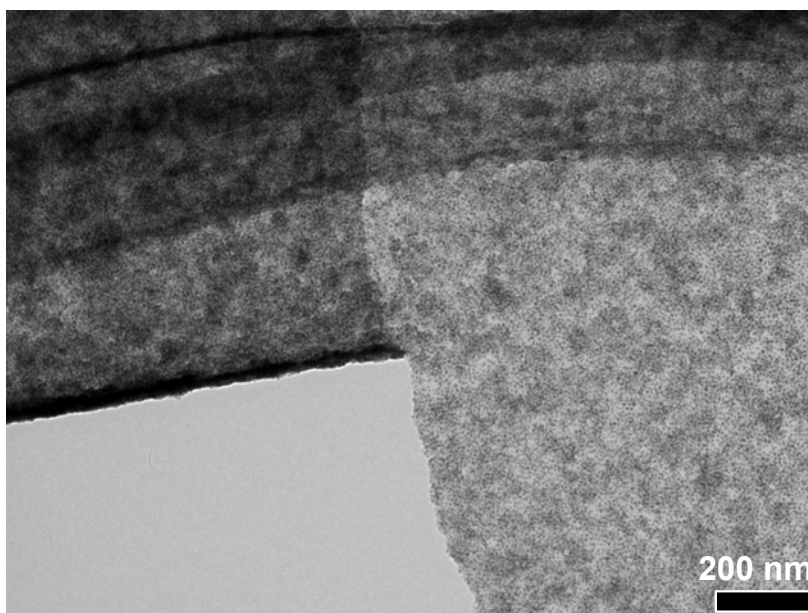


Fig. 45 TEM of a membrane from a ferritin stabilized Pickering emulsion droplet which spans over the hole of the grid.

The assembly of ferritin at various interfaces was reported several times in literature. Similarly dense but not well-ordered arrays of ferritin were reported if ferritin was simply deposited on substrates from evaporated droplets.^{116, 117} Good quality surface crystalline assemblies were just obtained from interfacially assembled ferritin particles and if some additives in the aqueous buffer or organic phase were additionally present

which directed a regular self-assembly.¹¹⁵ Such additives were e. g. poly(1-benzyl-*L*-histidine)¹¹⁵, dehydroabietylamine¹¹¹ or CdSO₄^{110, 521}. We believe that we see a realistic image of the surface structure of assembled ferritin and suppose that the surface morphology can be influenced if certain additives will be added. A general guideline of favourable conditions for two-dimensional surface crystallization of proteins and protein particles has not been developed yet. In fact, it might be difficult to find conditions which go beyond protein and interface specific protocols. The bionanoparticles might experience different degrees of surface denaturation upon contact with the oil phase which influences the self-assembly process as well. Indeed, it was mostly assumed that the additives were modifying the interface and thus the interaction of the assembled proteins. Modification of the surface interaction of interfacially assembled ferritin particles was not accomplished here since the investigation of the surfaces should relate to the adsorption kinetics of chapter 5.4 for which additives were not desirable.

Despite hard efforts we could not accomplish a similar approach for the plant viruses, too.¹⁸¹ If droplets were similarly let for adsorption, cross-linked with glutaraldehyde, washed and immediately deposited on silicon wafers or TEM grids, we found no dried and folded capsules after drying in vacuum. Instead, we observed free round areas, close together and unspecific and structure-less protein debris between them. We concluded that during drying the droplets disintegrated. Unlike the protein or ferritin capsules, the cross-linking was not sufficient to keep the assembled viruses together. An increased concentration of glutaraldehyde did not solve this problem. For the particular case of TMV no dense assembly was observed on solid PDMS surfaces onto which the rods had been interfacially trapped (see chapter 6.3). This was most likely the reason why it was impossible to obtain a stable capsule shell from TMV, too.

We wanted to investigate the thickness of the adsorption layer in an as much undisturbed state as possible. Washing and drying of the capsules on a surface might have removed further adsorbed multilayers. Scattering techniques were considered as ideal alternative because they can be used to probe Pickering emulsions contactless and without the need of washing, crosslinking etc. The scattering of the membrane has to be separated from the scattering contribution of the liquid phases arising from the different

scattering crosssections of the employed oil and buffer.^{522, 523} This can be done in neutron scattering with the contrast variation technique.⁵²⁴ The scattering contrast of the buffer can be adjusted with heavy water (deuterium oxide) to match the scattering contrast of the oil phase and the scattering due to the shell remains.^{525, 526} We performed a set of experiments to extend the previous investigations on the determination of the shell thickness of CPMV stabilized Pickering emulsions.¹⁸¹ However, it was not possible to evaluate the experiments, presumably because of an erroneous contrast matching. The experiments are also in light of the determination of protein adsorption at liquid-liquid interfaces of high relevance and will be repeated in future.

6.3 Bionanoparticles Trapped at PDMS-Surfaces

The liquid-liquid interface is difficult to investigate. Relatively easier is the analytical access to solid interfaces, either in solution or in air. We envisaged a technique to trap the bionanoparticles at a liquid-liquid interface where the oil phase could be solidified after the assembly process. A precursor oil was used which can be crosslinked by UV-light. This had the great advantage that the system was not disturbed at any moment. An acrylate modified poly(dimethyl siloxane) precursor was chosen because it was sufficiently hydrophobic, not too viscous at ambient temperatures or below and gave stable emulsions which were not creaming. The crosslinking was done for 5-10 min with a Hg-halogenide lamp, although the surface was solidified after less than 1 min. The aim was not to take snapshots of intermediate stages of the assembly and the actual crosslinking time was not critical. The technique is used in some variants now by few other researchers and has been named “gel trapping technique”^{146, 169}, “fossilized assemblies”¹⁷¹ etc.

6.3.1 Investigation of the Surface Structure with SEM

Scanning electron microscopy with a field emission gun is especially well suited for soft and sensitive surfaces. FE-SEM in combination with in-lens detection allows imaging with very low acceleration voltages but very high resolutions as it was described in

detail in the theoretical background in chapter 2.6. The necessary short working distance allows however no large depth of field and only a certain plane is sharply in focus. The preparation of the samples was not as delicate as suspected. The Pickering emulsions could be dried and the droplets fixed with freshly applied conductive silver paste on a stub. Small droplets were sufficiently immobilized by simply drying on a conductive double side adhesive tab, especially if a lot of them were deposited in a kind of disordered colloidal crystal. The samples were sputter-coated with platinum to yield a conductive surface and to enhance the surface contrast. At low magnifications significant charging was observed, however, at high magnifications good imaging conditions were prevailing. Although the imaging conditions were as gentle as possible, the sample area under investigation was damaged after a few scans. In Fig. 46, an overview over the surfaces of solid PDMS Pickering emulsion droplets prepared from BSA, ferritin, CPMV, TYMV and TMV is shown as obtained from FE-SEM. The surface of BSA stabilized droplets showed no specific surface pattern (Fig. 46, A). The protein formed a featureless macromolecular layer and no single entities could be distinguished. The quite rough surface structure could be explained with the presence of protein aggregates. In this particular preparation, a non-fractionated BSA sample was used. If the monomer fraction of BSA was employed, the surface was absolutely featureless and no precise focussing was possible. The surface structure of ferritin stabilized Pickering emulsions is presented in Fig. 46, B; here, the droplets were prepared from a non-fractionated ferritin solution, too. We could identify many single ferritin particles on the droplet surface besides large aggregates. The necessity to fractionate bionanoparticle preparations became obvious; otherwise no homogeneous assembly could be achieved. Both spherical plant viruses, CPMV and TYMV, could be imaged with good quality (Fig. 46, C, D). We found a dense assembly but similarly to the ferritin assembly, no two-dimensional order was observed. The physical control of the surface adsorption of plant viruses was investigated in some recent research works. It was found that inter-virus interactions could be controlled to some extent by addition of poly(ethylene glycol) or by changing the electrostatic interactions through the salinity and pH of the virus solution.^{120, 125} These reports dealt with systems at solid interfaces and implied the use of modified surfaces and directed virus binding through ligands. Thus, these reports do not directly apply to our system with a liquid-liquid interface.

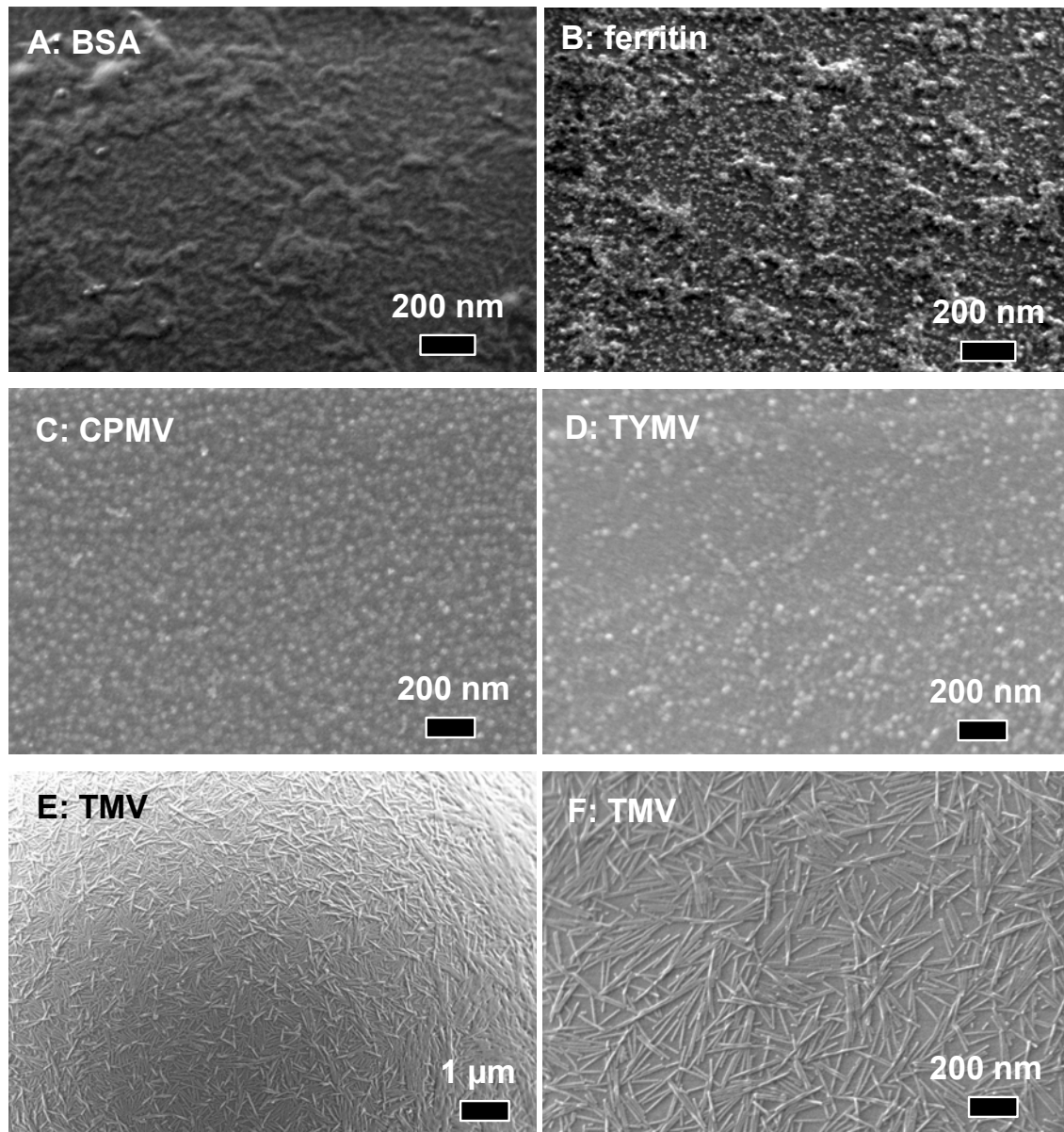


Fig. 46 SEM of Pickering emulsions prepared with different bionanoparticle solutions and a cross-linkable PDMS precursor oil.

Suci et al. found that differently “hard” amino-functionalized surfaces (prepared from either aminosilane- or poly(*L*-lysine)-coating) had an influence on the local order of the virus which was explained by a different mobility of the virus at the polymer surface compared to the aminosilane functionalized surface.¹²⁰ We suppose that by applying suitable solution conditions to modify inter-viral interactions a dense and regular assembly of viruses could be obtained similarly as it was reported for the production of surface crystalline ferritin assemblies.

The solid Pickering emulsions which were prepared with solutions of tobacco mosaic viruses rendered particularly impressive pictures. The stabilization of bionanoparticle Pickering emulsions was achieved without a dense and regular assembly of rods. In fact, a lot of free areas were observed. Further, the viruses were often lying across each other. However, this was not the result of a tendency to build multilayers. A closer inspection revealed that all viruses had at least at one point contact with the surface. Most of them were bridging other viruses and had contact with the surface at more than one point. At the crossing point, the viruses showed distinct inflections. This could be explained by a strong interaction of the viruses with the oil phase. Viruses were strongly attracted by the free PDMS oil/buffer solution interface which forced the virus to bend unusually if it comes about crossing another TMV rod. It could not be figured out to which extend the other virus rod was forced to submerge into the oil phase. TMV was always considered as rigid rod if it was investigated in solution. This property was confirmed also if the rod was deposited on solid surfaces from aqueous solutions. No such strong bending of the virus could be observed e. g. if deposited on TEM grids (see chapter 4.4, Fig. 25). Thus we attributed the observed bending not only to strong attraction forces but also to a weakening of the viral nucleo-protein assembly by surface denaturing upon contact with the oil phase.

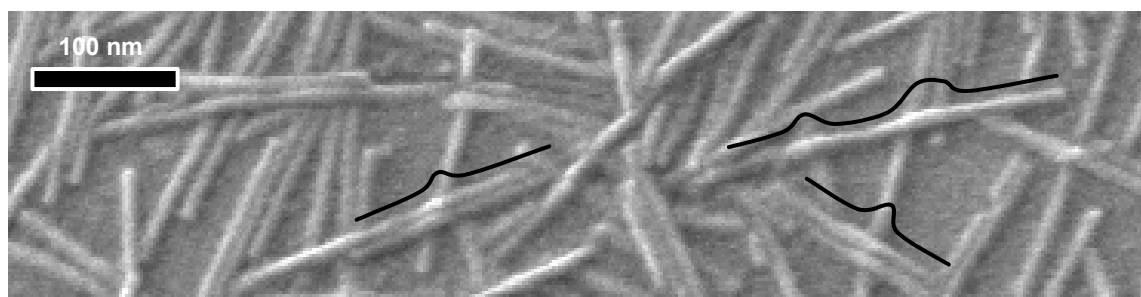


Fig. 47 SEM of TMV rods adsorbed on a PDMS Pickering emulsion. Black lines should guide the eye.

6.3.2 Investigation of the Surface Structure with AFM

Very similar information as with SEM on the surface structure can be obtained in principle from AFM, too, but the measurements can be conducted at dry conditions as well as in liquid solution, e. g. physiological conditions, which would require

considerable technical complexity in case of the SEM. Further, AFM is the surface analytical tool of choice for highest resolutions for height as well as lateral dimensions.

The direct imaging of bionanoparticle covered liquid-liquid interfaces was not accomplished successfully in an AFM equipped with a liquid cell. Wetting phenomena of the oil and the buffer solution made it impossible to obtain a useful signal when the cantilever contacted the interface. The already introduced particle trapping technique with a cross-linkable PDMS precursor oil was therefore used but the imaging of Pickering droplets was also not accomplished successfully. The limited accuracy with which the cantilever could be positioned on a predetermined spot on the surface made it very hard to successfully approach and to measure the curved surface of a droplet. Finally, flat surfaces were prepared for the AFM measurements. The same materials were used, but the PDMS was first filled into a trough which had been placed in another trough. Then the bionanoparticle solution was filled into the outer trough until it drowns the inner trough and the oil phase. Similarly to the preparation of the Pickering emulsions, the assembly process was allowed to proceed for at least three hours before the oil phase was crosslinked with UV-light and the surfaces were gently washed by dipping into water and dried with a soft stream of nitrogen.

In Fig. 48, a collection of images for different bionanoparticle coated PDMS surfaces is shown. No specific surface pattern was observed for BSA covered surfaces. As already mentioned, small proteins were expected to adopt a more or less featureless coil structure at the interface (Fig. 48, A). Compared to surfaces which were prepared from pure buffer solution (Fig. 48, I) we found however a slightly increased surface roughness. The surface assemblies of the icosahedral plant viruses CPMV and TYMV (Fig. 48, B and C, respectively) and of ferritin (Fig. 48, D-F) could be successfully imaged. TYMV has been used as model colloid in crystallization experiments followed by AFM. McPherson, Kuznetsov and coworkers could present images of highly ordered virus assemblies with very good resolution.⁴⁶⁰ Even single capsomers could be distinguished. This was true for virus particles as part of large crystalline areas but viruses that were adsorbed on mica and randomly distributed could only render images with much lower resolution and intricate surface structures of single viruses could not be revealed anymore.⁴⁶⁰ As we were more interested in the investigation of the gross

assembly, standard conditions and tips were used which did not allow high resolution imaging. Further, as already mentioned, irregular assemblies are very difficult to image with high resolution and the samples were not suitable for such investigations.

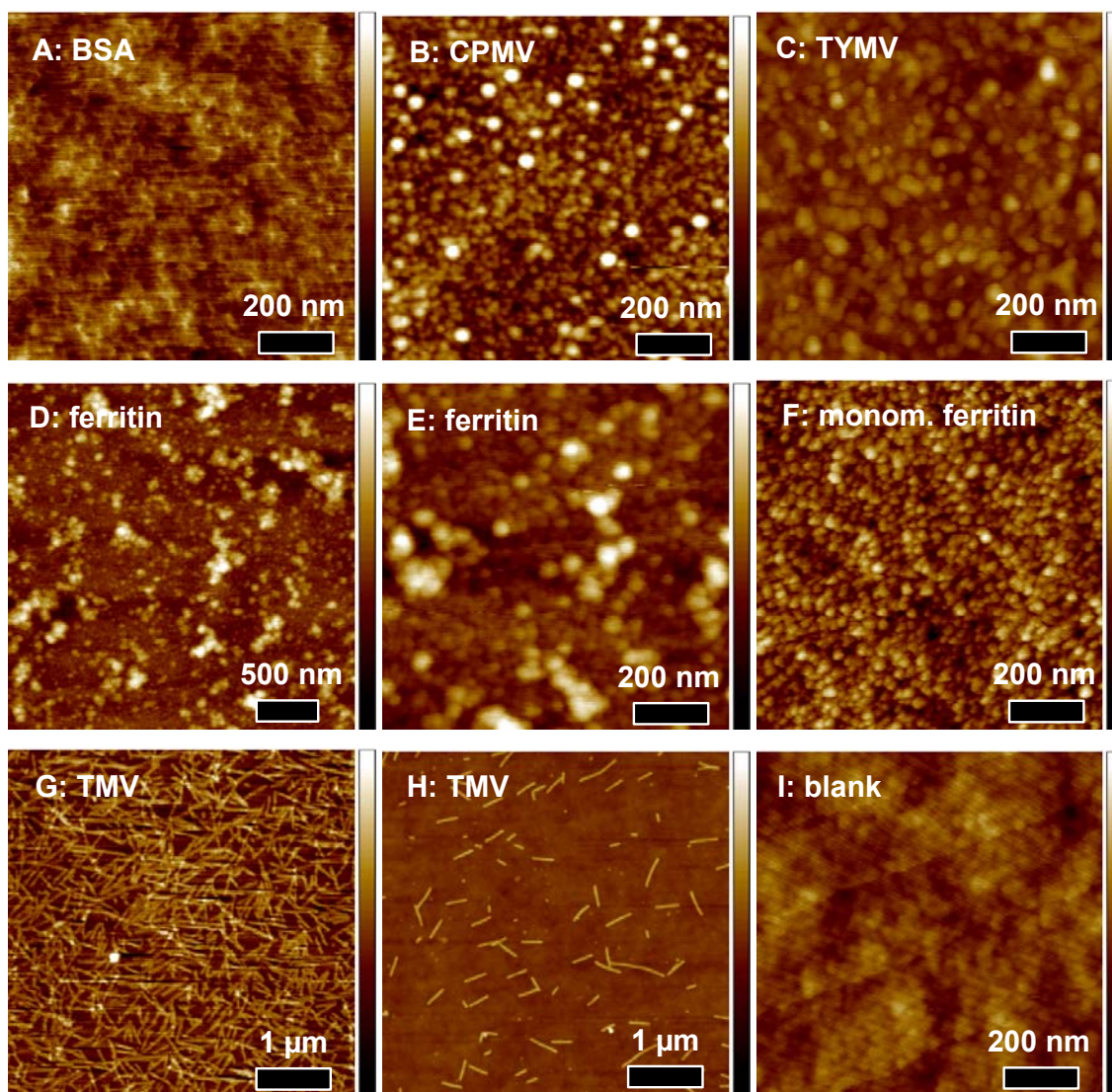


Fig. 48 AFM height images of bionanoparticle-coated and a blank PDMS surface (full height bar: (A) 10 nm; (B), (C) 20 nm, (D) 50 nm), (E) 30 nm, (F) 10 nm, (G) 50 nm, (H) 50 nm, (I) 10 nm)

The three images that are shown for the surfaces which were covered with ferritin illustrate once more the difference between heterogeneous ferritin solutions which were taken directly from stock batches and the fractionated ferritin monomer solutions. In Fig. 48, D and its magnification E, we find similar large aggregates that were observed in SEM. However, they were better resolved and it could be seen that they consisted of

distinguishable, single ferritin particles. The surface that was covered with ferritin from the monomer fraction was free of aggregates. A dense assembly of ferritin particles could be observed which however did not show long-range order (see discussion above for the assembly visualized with TEM, Fig. 45). The TMV showed the same surface structure as in SEM (Fig. 48, G vs. Fig. 46, F) and we want to refer to the discussion there, too. As the imaging conditions were not optimum we could unfortunately not investigate the above mentioned softening and bending of TMV in more detail by AFM.

Finally, it is necessary to comment on the two methods, AFM and SEM. Both techniques advanced significantly during the past years as tools to investigate soft biomaterial surfaces. Nevertheless, they still require expert experience. Both techniques were tried here to establish a rapid and robust method to investigate soft bionanoparticle-coated surfaces. AFM offered a much higher resolution and the advantage to work in solution conditions but was very prone to imaging artefacts. The soft and hydrophilic surface attracted always an aqueous surface film in the humid conditions of the laboratory. An increased tapping force was necessary to overcome the attractive forces between tip and sample surface and to work in the repulsive regime under stable conditions. Although the tip was in tapping mode only in intermittent contact with the sample, it collected easily protein material which stuck to the tip and could hardly be removed again. In Fig. 48, F and G we see the effects of this typical problem. A broad tip, resulting from attached material, results typically in blurred surface details (seen to a less extent in Fig. 48, F) or even in twin images. Further, some stripes from withdrawn material can significantly deteriorate the image quality, too (seen to a less extent in Fig. 48, G). Finally, AFM is an intrinsic slow technique. The acquisition of one image with sufficient good quality takes easily 30 minutes. On the other hand, SEM is a very fast technique. It does not mechanically contact the surface but does not let it undisturbed either. Even under mild imaging conditions, i. e. very low acceleration voltages, fast focusing and image acquisition was necessary. After the electron beam was scanned few times over the same area, the surface was significantly damaged and the image deteriorated. Since bionanoparticles do not exhibit heavy elements, a conductive Pt layer has to be applied which enhances the surface contrast to obtain useful images at all. The resolution is not as good as it can be achieved with AFM. Finally, gross assemblies are imaged faster by SEM but for fine details and

quantitative evaluations of the dimensions of surface features the tedious and for our systems sometimes problematic AFM technique had to be used.

In order to assure that the protein particle deposition did not result from a “dip coating”-effect when the surface was removed from the bionanoparticle solutions, we used a flat solid PDMS surface prepared from buffer solution and immersed it for 3 h into a tobacco mosaic virus solution. The sample was treated in the following in the similar way (i. e. UV-illumination, washing) as it was done for the systems with an initially liquid interface. The result is shown in Fig. 48, H. We find indeed some sparsely distributed TMV rods on the surface. However, no dense and irregular network could be observed. The unidirectional orientation of the rods is a direct result of convective deposition during removal of the substrate from the virus solution.

A topic of strong interest in the field of Pickering emulsion research is the question of the “contact angle” of interfacially assembled nanoparticles. Only large micron-sized particles are directly observable with conventional microscopy techniques. Imaging of sub-micron or even nano-sized particles at interfaces has to rely on solid surfaces at which the particles have been immobilized. Then SEM or cryo-SEM techniques can be used to image the surface assembly or the sample can be cut with a microtome and the cross-sections viewed with TEM. We envisaged approaching this question through AFM investigations of TMV on PDMS surfaces. While the lateral resolution of AFM is determined by the convolution of the object size with the tip geometry, vertical dimensions are routinely determined very exactly. We selected a PDMS surface where TMV was adsorbed at the initially liquid surface (e. g. Fig. 48, G) and a sample where TMV was deposited onto an already solid PDMS surface (e. g. Fig. 48, H). The height of many viruses was measured and averaged but there was no significant difference within the determined standard deviation (deposition on solid PDMS: 14.76 ± 0.68 nm; adsorption at the initially liquid precursor interface: 14.85 ± 0.81 nm). In a recently reported detailed investigation on the effects of interfacial interactions on the cross-sectional morphology of TMV with AFM and GISAXS it was found, that on attractive substrates (e. g. silicon wafers) the rod is significantly flattened by a collapse of the inner cavity while on hydrophobic surfaces (e. g. polystyrene films) the rod keeps its round cross-section.⁵²⁷ The reported height of 14.8 nm on a silicon wafer fits our values

for the deposited but also for the adsorbed viruses. It is most likely that the deposited and adsorbed TMV on PDMS collapse in much the same way as reported for hydrophilic substrates. The tobacco mosaic viruses – and most likely the other bionanoparticles similarly, too – were only interacting with the very outermost protein layer with the oil phase; a measurable immersion could be excluded.

We want to add that microtome cross-sections of embedded virus-coated PDMS surfaces could not help to further elucidate the immersion of viruses at the interface. We could find the interface because of the different electron density of the epoxy and PDMS bulk but the viruses could not be distinguished in the epoxy matrix. Many attempts to stain the viruses in the cross-sections failed presumably because the aqueous staining solution did not wet the PDMS/epoxy film efficiently. The surface with the adsorbed viruses was therefore sputter-coated with a thin platinum layer to trace the shape of the virus. We could identify rods which were pointing perpendicular to the cutting plane ((Fig. 49, left, A) and also rods which were lying parallel in the thin section (Fig. 49, left, B). High resolution images were basically supporting the results from AFM, but the surface features were too fuzzy to allow a precise measurement of the immersion depth. Moreover, shrinking effects during infiltration with the embedding resin and compression during cutting would have to be considered, too. Nevertheless, these images illustrated nicely that the virus was indeed rather “lying” on the surface than being measurably immersed.

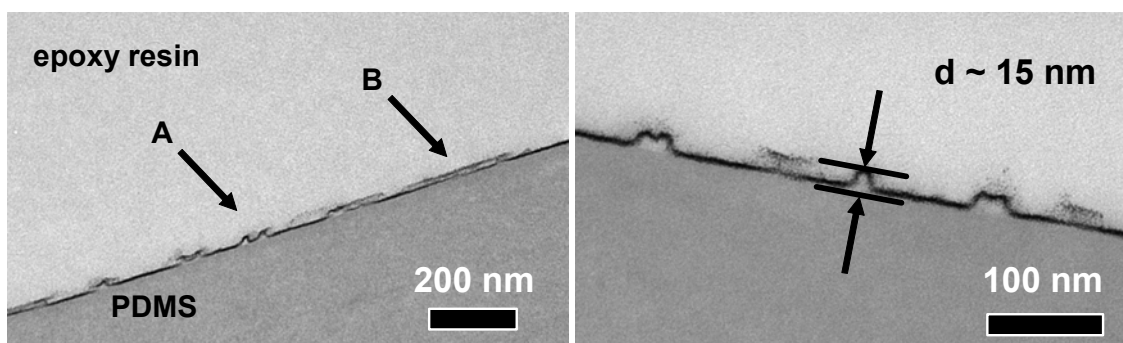


Fig. 49 TEM of cross-sections of an embedded and microtomed TMV-coated PDMS surface.

6.3.3 Fluorescence Microscopy of Antibody-Labelled Bionanoparticle Pickering Emulsions

While the larger protein cages of ferritin and the plant viruses can be directly visualized at the interface with imaging techniques, the proteins HSA, BSA or fetuin-A were too small and too soft to yield useful images. However, the presence can be proven by reaction of the interfacially trapped proteins with the respective fluorescently tagged antibodies. In Fig. 50 fluorescence microscopy images of HSA and ferritin coated PDMS droplets are presented to which the corresponding antibody and in a second experiment also the other antibody was added. Each protein is recognized by the respective antibody but the other antibody is not bound as seen by the missing of fluorescence. Further, neither unspecific binding nor fluorescence from the Pickering droplets itself can be observed. The reaction however does not allow conclusions about the conformation of the protein at the interface. Usually, antibodies recognize a certain sequence of amino acids (epitopes) and the conformation plays a minor role. Attempts to quantify the amount of adsorbed protein on solid Pickering droplets failed. The fluorescence intensity is difficult to quantify anyway and here, the different size of the droplets influences the measured intensity per observation volume additionally.

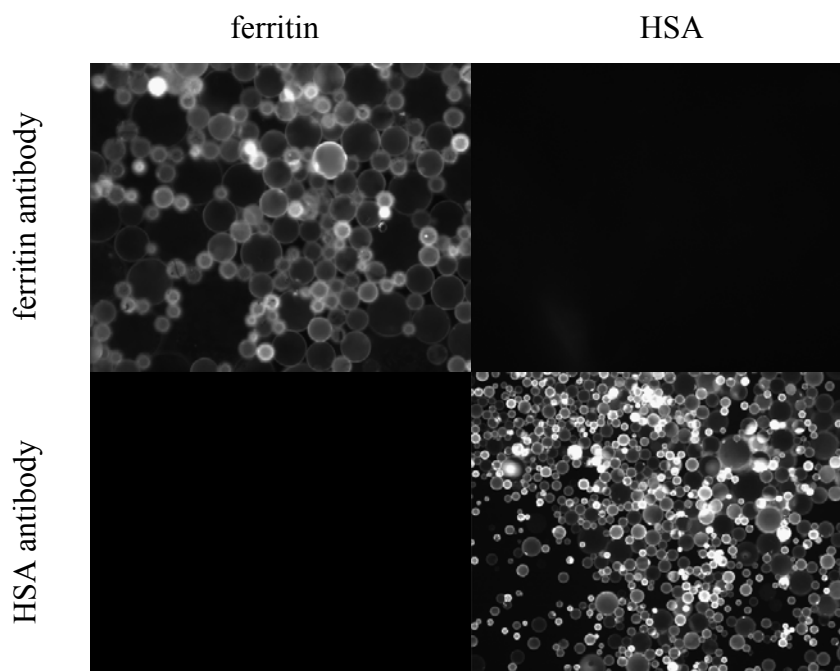


Fig. 50 Fluorescence microscopy images of HSA and ferritin coated PDMS droplets after reaction with the respective antibodies.

7 Hydroxy Apatite Mineralization at Surfaces and Interfaces

Wet chemical synthesis of minerals and mineral coatings at ambient conditions are of considerable technical importance. While hydroxy apatite itself has unfavourable mechanical properties for bone implants, it can serve as very good biocompatible coating on other implant materials.⁵²⁸ Few routes have been reported in the literature for the preparation of hydroxy apatite coatings. Mostly, they contain steps with extreme pH, require high temperature annealing or yield materials with less controlled composition.⁵²⁸⁻⁵³¹ Precisely controlled layers can be achieved with advanced deposition techniques, e. g. ion beam sputtering.⁵³² All these methods have drawbacks regarding their applicability to soft and sensitive surfaces. Further, aqueous solution conditions are inherently more environmentally friendly, safe to handle and do not require expensive and complicated technical equipment.

The production of hydroxy apatite layers with a simulated body fluid (SBF) is among the most important routes employing aqueous solution conditions. SBF deposits hydroxy apatite in a biomimetic fashion. Hydroxy apatite coatings which were prepared via this route were shown to be fully biocompatible. Moreover, the deposition of hydroxy apatite on various materials in SBF is routinely used as a measure of biocompatibility.

The phase of hydroxy apatite is critical for hydroxy apatite based implant materials. Cellular interactions and activities change for different phases of calcium phosphates and calcium phosphate ceramics.^{533, 534} The resorption rate must not be too fast; amorphous material is especially quickly resorbed. The phase of SBF-based calcium phosphate coatings has been shown in many studies to be hydroxy apatite of low crystallinity.^{279, 281}

In the following chapters the mineralization of different surfaces with different mineralization solutions is reported. First, the coating of PET as model substrate with hydroxy apatite is presented. A procedure employing SBF and a prior incubation step of the substrates on bioactive glass particles is introduced. Further, the mineralization with 1.5 SBF containing citrate and with a supersaturated calcium phosphate solution,

containing citrate as well, is described. Then, the same conditions have been used to mineralize protein and bionanoparticle coated solid PDMS surfaces. The observed differences between different mineralization conditions and surfaces are discussed. Finally, fluid interfaces of bionanoparticle stabilized Pickering emulsions are used as scaffolds for hydroxy apatite mineralization to produce hollow capsules.

7.1 Hydroxy Apatite Formation on PET in a Biomimetic Process

7.1.1 Preparation and Characterization of Bioactive Glass A

Kokubo reported the hydroxy apatite formation on surfaces after incubation on bioactive glass particles.^{281, 282} Among the glass ceramics derived from glass G, the parent glass showed the strongest increase of calcium ion concentration in solution and thus has been suspected to induce hydroxy apatite nucleation most efficiently.²⁷⁷ To prepare glass G, a mixture of salts with the final nominal composition MgO 4.6, CaO 44.7, SiO₂ 34, P₂O₅ 16.2 and CaF₂ 0.5 wt% is melted for 2 h at 1450 °C.^{272, 273} This experimental procedure could not be followed as no platinum crucible was available that could withstand this temperature for such prolonged times. Instead, the powder mixture was melted in a glassy carbon crucible up to a temperature of 1450 °C and then cooled down again. Despite the specifications and good inertness of glassy carbon crucibles towards phosphate melts it developed severe smoke and corrosion of the crucible was suspected. Thus, the mixture was kept for just 5 min at 1450 °C and was then slowly cooled down. Energy dispersive X-ray analysis (EDX) confirmed the composition of the final glass (Fig. 51). The signal of carbon arose mainly from the carbon coating of the sample for EDX-analysis, however, the glass product was grey and some carbon impurity from the crucible must be suspected. The EDX-analysis of an industrial sample of bioglass is also included. It contained less silicon and the Ca/P ratio was lower, too.

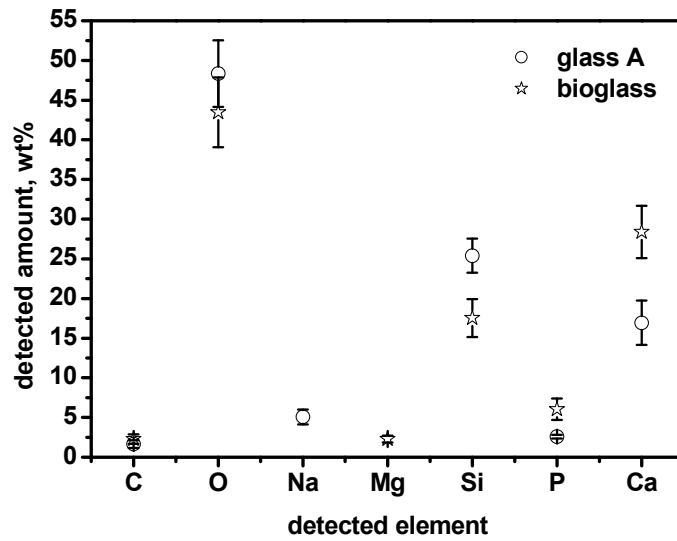


Fig. 51: Elemental composition of the prepared glass A and bioglass from EDX.

Structural investigation of the glasses has been undertaken with X-ray diffraction (Fig. 52). The bioglass was purely amorphous and did not exhibit any structural peaks (not shown). The prepared glass on the other hand showed many peaks which could be assigned to fluoroapatite and the glass has therefore been named glass A.²⁷² A quantification of the crystalline content was not possible.

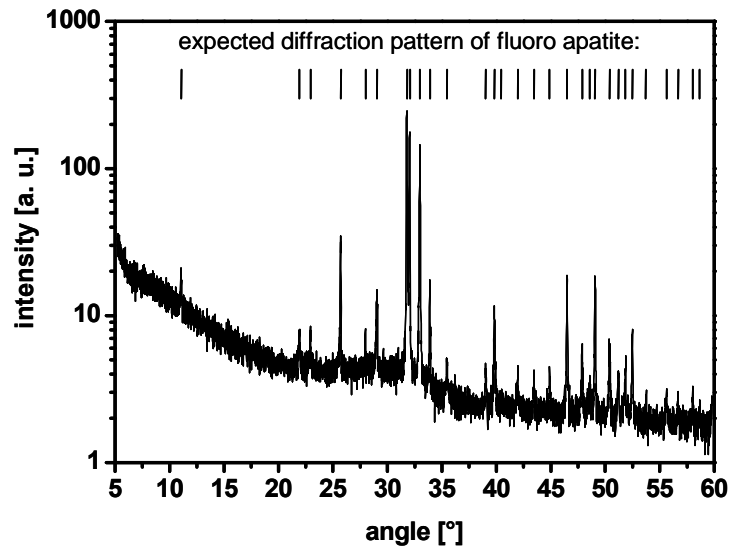


Fig. 52: X-ray diffraction pattern of glass A and expected diffraction pattern of fluoroapatite.

7.1.2 Hydroxy Apatite Formation on Surfaces in SBF Solution

We followed the procedure as it was introduced by Kokubo and coworkers.²⁸¹ Generally, the substrates were first immersed for two days on glass particles in SBF to induce nucleation of hydroxy apatite. The glass particles were suspended in SBF, settled for 15-30 min and the substrates with the surface facing to the bottom laid on them. All experiments were conducted on the prepared glass A, on bioglass and for reference purposes, the experiment was also performed without glass particles. The minimum time for efficient induction of nucleation is varying for different substrates from 6 h for glow-discharged poly(ether sulfone) to 96 h for titanium metal.^{283, 285} Untreated polymer films showed a minimum incubation time of 24 h to reach a thick dense hydroxy apatite layer after the second treatment.²⁸³ Since the aim in this work was the formation of a dense layer, an incubation time of 2 days at 37.0 °C was chosen for all substrates.²⁸³ After this first step, the samples were withdrawn, gently washed by dipping several times in SBF to remove adhering glass particles and immersed in vertical position in fresh SBF solution. The washing step and immersion were done at 37.0 °C, too. The samples were then kept in SBF for 6 days at 37.0 °C while the mineralization solution was exchanged once after 4 days. After that, samples were gently washed with copious amounts of deionized water and blown dry with a stream of nitrogen. This procedure ensured that the deposited minerals did not recrystallize after washing and no residual salt precipitated on the surface of the removed samples. All experiments were done in parallel to minimize effects of possibly slightly varying conditions. In the following text, the procedure employing the two different incubation steps is systematically named by a combination of the first solution which had been used for the incubation on glass particles for 2 days, followed by the solution for the second incubation which has been used for HAP growth for 6 days, e. g. 1.0 SBF/1.0 SBF, 1.0 SBF/1.5 SBF etc. Generally, the results of the experiments with bioglass and glass A were identical in even small details; therefore, only the results of the experiments with glass A will be shown.

7.1.3 Hydroxy Apatite Formation on PET in SBF

PET was used as model substrate because the HAP layer formation on it has been described in literature in detail.^{279, 286} The PET sheets were abraded on one side with sandpaper (grain 400), washed with ethanol and water and dried before they were immersed into mineralization solution. The abraded side was facing downwards to the glass particles. Nucleation occurs often at surface inhomogeneities and one would expect a much more pronounced mineralization on the rough side. Further, the rough side allows a stronger attachment of the mineral layer while on the blank side the brittle layer could peel off. Indeed, for all experiments with PET and different mineralization solutions, the rough side showed increased nucleation but also crystallite overgrowth on protruding surface features. On the blank side, the preferential growth of crystallites on scratches could be observed, especially at the beginning of the mineralization. Some flaking from the blank surfaces was observed for compact and brittle hydroxy apatite layers but only to minor extends. Overall, the same conclusions could be drawn from either of the two sides.

One set of PET substrates was investigated for the reactions during incubation on glass particles in SBF. The polymer sheets were not further immersed in SBF but washed and dried for investigation by SEM (Fig. 53).

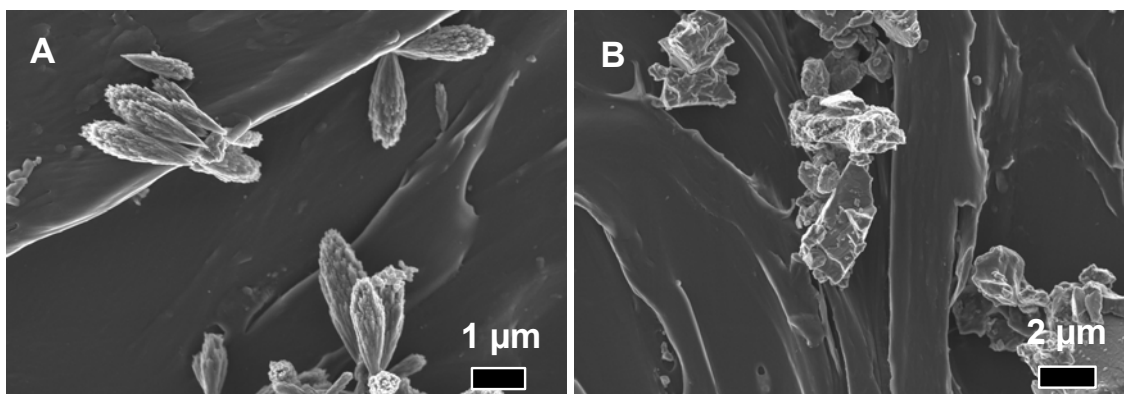


Fig. 53 (A) Calcite crystals and (B) residual mineral deposits on PET after incubation in SBF on glass A.

The sample which was not placed on glass particles did not show any mineral depositions on its surface. For the samples placed on either glass, characteristic

crystallites could be found (Fig. 53, A). EDX showed that these crystallites contained a very small amount of phosphate ($\text{Ca/P} = 26.7 \pm 4.1$) and other elements just in trace amounts except carbon and oxygen. As only reasonable explanation, the depositions must be identified as calcium carbonate crystals. Indeed, SBF is supersaturated to the precipitation of calcite, too.²⁶⁷ Further, irregularly shaped mineral depositions were found on the rough surface of the PET sheets that had been incubated on glass particles (Fig. 53, B). EDX analysis confirmed that these were glass particles that have not been removed during the washing step.

An interesting observation was the formation of mesocrystals. They were found at the edges and on scratches of PET sheets that had been removed from SBF after the incubation on glass particles (Fig. 54). More and better developed mesocrystals could be found after incubation in 1.0 SBF rather than 1.5 SBF. EDX-analysis showed that they had the same composition as the club-shaped crystallites (Fig. 54, C) and the mesocrystals were assumed to consist of calcite, too. High magnification revealed that the mesocrystals were built from small spherical particles of about 50 nm in diameter that grew in trigonal shape (Fig. 54, A, B). They started from a nucleation site and were growing in form of upside down pyramids. The smaller, less regular developed crystallite clubs might have been precursors of the larger mesocrystals. The mesocrystals could be distinguished from dendritic crystals which show smooth surfaces and no particulate fine structure (Fig. 54, D). The deposits on the surface after the first incubation step were usually overgrown by the final hydroxy apatite coating and could not be found after the second incubation step anymore. Nevertheless, they show the influence of the incubation on glass particles on supersaturation which is considered as the prevailing mechanism of induction of hydroxy apatite formation in 1.0 SBF.

The glass particles were collected and dried on a filter paper after the samples had been incubated on them in SBF for two days. Inspection with scanning electron microscopy did not reveal any deposition of hydroxy apatite, so did the composition not change as deduced from EDX. XRD spectra of both glass samples were identical with the material before incubation (data not shown).

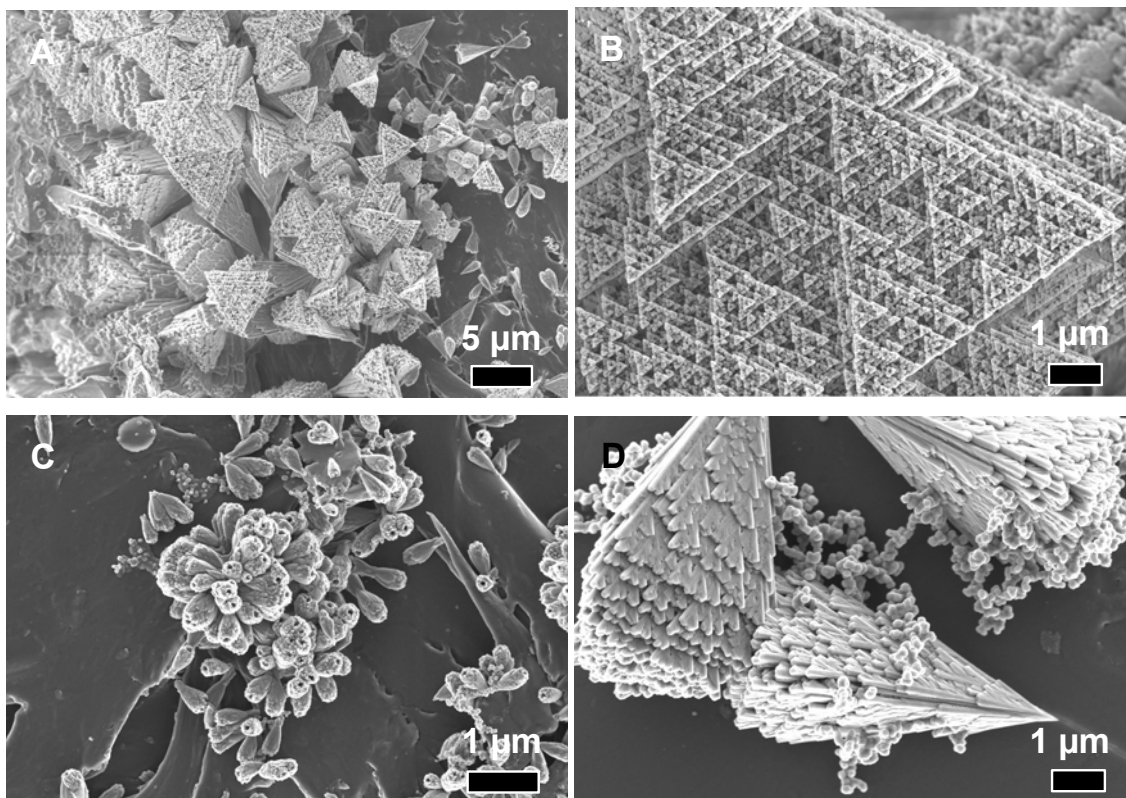


Fig. 54 (A-C) Calcite mesocrystals and (D) dendritic calcite crystals on PET after incubation in SBF.

The SEM images of PET sheets which have been treated with 1.0 SBF/1.0 SBF, 1.0 SBF/1.5 SBF and 1.5 SBF/1.0 SBF, respectively, are shown in comparison in Fig. 55. The coating of the rough surface which was not laid on glass A particles but facing the blank bottom was usually very inhomogeneous when incubated in 1.5 SBF during either the first or the second treatment. There was the crucial question whether the first incubation played the same critical role for HAP growth as for the incubation in 1.0 SBF only (Fig. 55, A, B). The experiments in which the PET sheets were not laid on glass particles were repeated but the sheets were immersed vertically. It turned out, that limited solute exchange between the lower side of the sheet and the flat container bottom might be a reason for inhomogeneous nucleation and growth. Indeed, it was shown that HAP growth is stronger when the solution is stirred.²⁸² Thus, the samples which were not incubated on glass particles during the first step were immersed vertically and results were then consistent for both sides of the PET sheet.

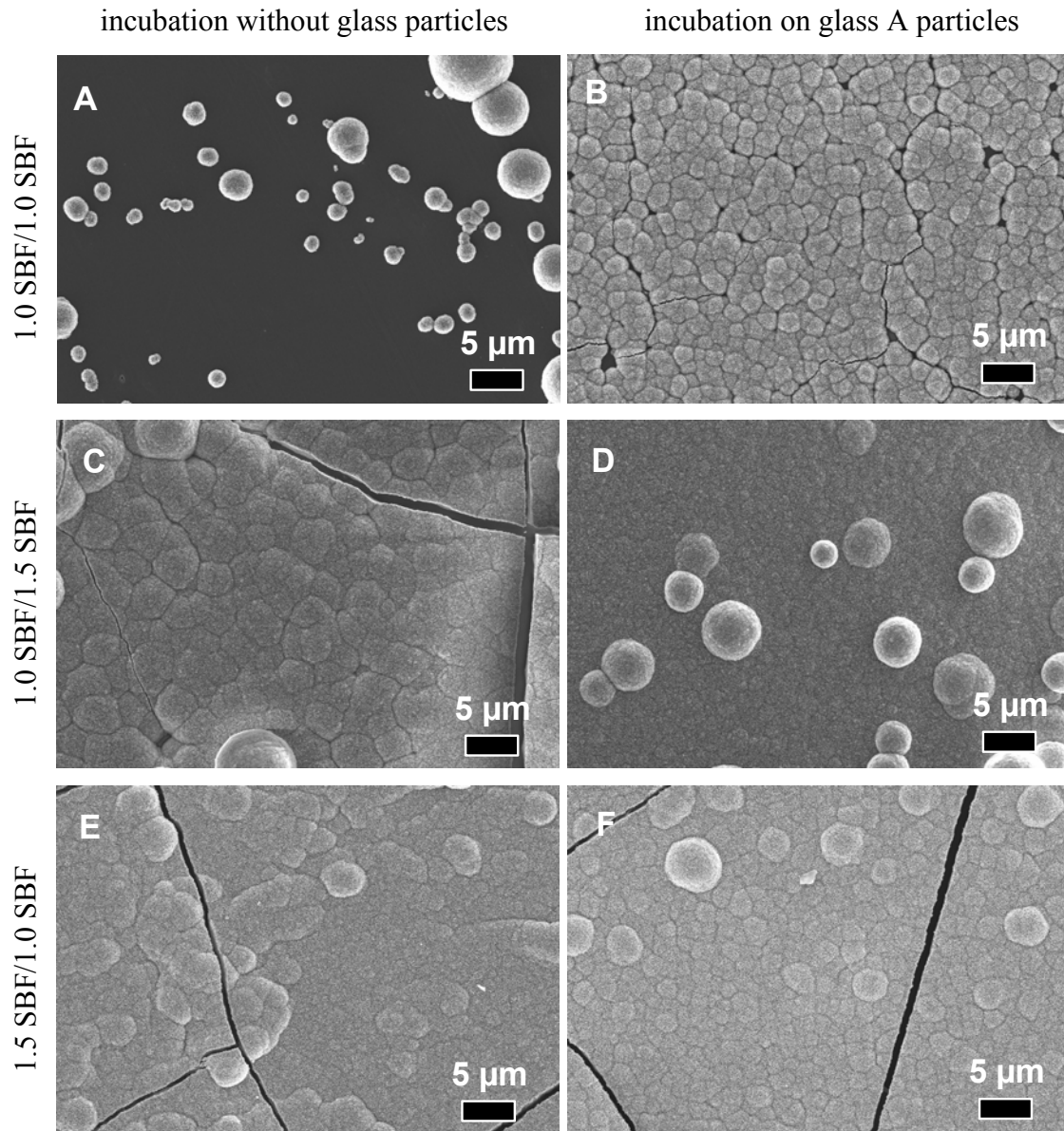


Fig. 55 Hydroxy apatite coating on PET after incubation without and on glass A particles for different SBF concentrations.

For the sample which was not incubated on glass A particles during the sequence 1.0 SBF/1.0 SBF, few nucleation sites and HAP globules could be found (Fig. 55, A). On the other hand, if the prior incubation was conducted on glass A particles, a dense and nearly compact HAP layer was formed on the PET surface (Fig. 55, B). The glass A particles released small amounts of ions into the surrounding solution and led to local supersaturation. Nuclei were formed on the adjacent PET surface which grew to large globules during the second treatment. The mineral layer still revealed the nucleation spots where the HAP globules started to grow. They finally grew together with their

neighbors to form a dense and brittle layer. Only few spots could be revealed where the PET surface was not covered.

A compact HAP layer was formed on PET if in any of the two steps of the procedure 1.5 SBF was used, irrespective whether glass particles were included in the prior incubation step or not (Fig. 55, C-F). 1.5 SBF was much more supersaturated than 1.0 SBF and led inherently to nucleation and mineralization of the surface. However, a closer inspection of the surfaces revealed a more smooth and homogeneous layer of the samples for which glass particles were included in the first treatment. This again supported the proposed function of the glass particles to increase the effective nucleation on the surfaces. Accidental overgrowth of HAP can be found on few surfaces (e. g. in Fig. 55, D).

For the sequence 1.0 SBF/1.5 SBF, Kokubo reported that no HAP coating on poly(ether sulfone) was observed when the first treatment was omitted.^{283, 285, 286} For PET, just a minimum incubation time was reported that was necessary to achieve a certain minimum HAP layer thickness.²⁸³ In subsequent experiments they have always included the incubation step but never reported on a blank experiment.²⁷⁹ It can be concluded from our experiments that hydroxy apatite coating on PET can be achieved if 1.5 SBF is involved and no incubation on bioactive glass particles is necessary. 1.5 SBF is enough supersaturated to promote nucleation and to induce HAP growth on PET. This might be different for other polymers and surfaces but shows the necessity of blind runs to eliminate obviously redundant steps and erroneous conclusions. Finally, it has to be mentioned, that any correlation to *in vivo* bone building activity is lost once 1.5 SBF is involved.

7.2 Hydroxy Apatite Formation on PET in 1.5 SBF with Citrate

The incubation procedure on glass particles might be incompatible with true liquid-liquid Pickering emulsions for which the hydroxy apatite coating should be developed. In order to simplify the process, the time consuming incubation procedure should be overcome. Therefore, a simpler wet chemical coating procedure was sought for. Rhee

and Tanaka reported on the effect of citric acid in SBF and its ability to induce hydroxy apatite growth on bioinert materials.⁵³⁵ Citric acid is an important component of fresh bone which makes up to 1 wt%. At physiological pH, citric acid is completely deprotonated ($pK_3 = 6.4$) and can act as a strong tridentate chelating ligand for calcium ions. Thus, citrate can have an ambiguous role. It can efficiently inhibit calcium phosphate precipitation but can also mediate interactions with the substrate and induce nucleation. Rhee and Tanaka found that citrate in 1.5 SBF had a pronounced effect on the nucleation of hydroxy apatite on a bioinert collagen membrane. Within a concentration range of 0.3-2.0 mM (corresponding to a molar ratio $Ca^{2+}/citric\ acid$ of 12.7-1.9), nucleation and growth of hydroxy apatite was observed. At higher ratios, the very low nucleation rate led to absence of mineralization while at lower ratios the citrate was able to complex all calcium ions and efficiently inhibited calcium phosphate growth.

Citric acid was added to 1.5 SBF (final concentration was 1 mM and molar ratio $Ca^{2+}/citric\ acid$ was 3.75/1) and the pH was readjusted with small amounts of tris. The solution is named in the following 1.5 SBF/cit. Nucleation should be enhanced but hydroxy apatite growth not yet inhibited. First, mineral growth on PET surfaces was investigated to find out more about the kinetics of hydroxy apatite growth. Fig. 56 shows a series of PET samples that were withdrawn after different times of immersion. All samples were vertically immersed in separate containers and kept at 37.0 °C for the indicated times. Nucleation occurred preferentially at surface inhomogeneities. Growth of spherical crystallites of hydroxy apatite was favored along the scratches on the blank site. An increased number of nucleation centers could be found on the rough side but the tendencies and observations were otherwise the same and only the blank side is shown.

After one day (Fig. 56, A), a number of small crystallite nuclei have formed which grew in size for the next four days (Fig. 56, B, C). From then on, the mineralization reaction ceased and no further increase in number or size of the crystallites could be found (Fig. 56, D). Even after very long times (> 300 h) no dense and compact layer had been formed. The exchange of the solution with fresh pre-warmed mineralization solution led to new formation of small nuclei and an increase of the number of HAP crystallites

(Fig. 56, E). The previously formed HAP crystallites did not grow significantly in size. A compact layer started to form (Fig. 56, F) on which accidental growth of single spherical crystallites could be observed. Obviously, multiple exchanges (presumably more than two) are necessary to achieve a dense and compact layer.

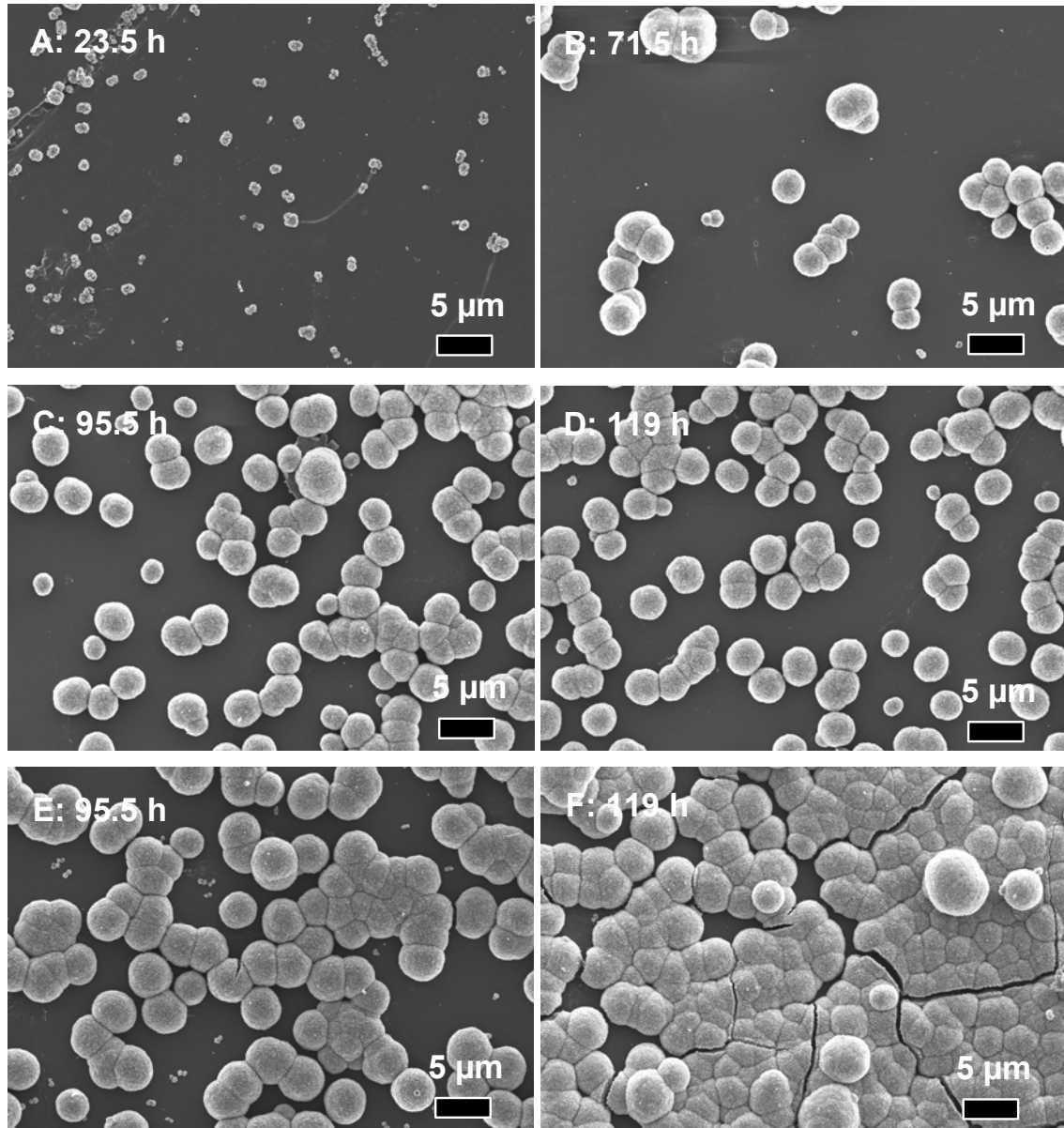


Fig. 56 Nucleation and growth of hydroxy apatite on PET in 1.5 SBF/cit after (A) 23.5 h, (B) 71.5 h, (C) 95.5 h and (D) 119 h and after exchange of the mineralization solution at 71.5 h and removal of the sample at (E) 95.5 h and (F) 119 h.

While SBF has been reported and also proven during this work to remain stable and unchanged in the fridge for weeks, the citrate containing SBF showed some change during storage, leading to faster (within 2-3 days) nucleation and growth.

7.3 Hydroxy Apatite Formation on PET in an Oversaturated Calcium Phosphate Solution

The complex composition of SBF has been proven to be a model for *in vivo* biomineralization of hydroxy apatite. However, the preparation and composition of a simulated body fluid can be too complex from a technical point of view and when considering possible applications. Furthermore, 1.5 SBF tends to precipitation and the results obtained with this solution are not correlated to the *in vivo* behavior anymore anyway. Chung et al. presented the solution phase coating of hydrophilized silicon wafers with a simple oversaturated calcium phosphate solution.⁵³⁶ They used an aqueous solution of calcium nitrate, ammonium phosphate and citrate at pH = 7.4. Unfortunately, the unclear experimental description did not allow a constant and reproducible preparation of hydroxy apatite coatings on hydrophilized wafers according to their report. Coating of PET did not occur at all.

Therefore, the solution composition was reconsidered. An initial composition of 5 mM Ca^{2+} and 2.5 mM phosphate was chosen. Further, 1.25 mM citrate was included into the Ca^{2+} -solution to enhance nucleation and to chelate excess calcium ions at the same time. After addition of the phosphate to the calcium/citrate solution and upon readjustment of the pH to 7.40, a faint precipitate occurred when reaching pH = 7.0 and above. Upon standing for some time, a cloudy precipitate formed and settled. The solution was filtered after standing for about 15-30 min with a 0.22 μm nylon syringe filter and was used immediately. The solution will be named further Ca/P/cit. The change of the solution conditions has been followed by monitoring the pH and conductivity, for the filtrated solutions as well as for the remaining stock solution with the settled precipitate (Fig. 57). The logarithmic scale of the plot was chosen to enlarge the interesting early time span. There is no special meaning to the approximately linear decrease of the pH of the solution.

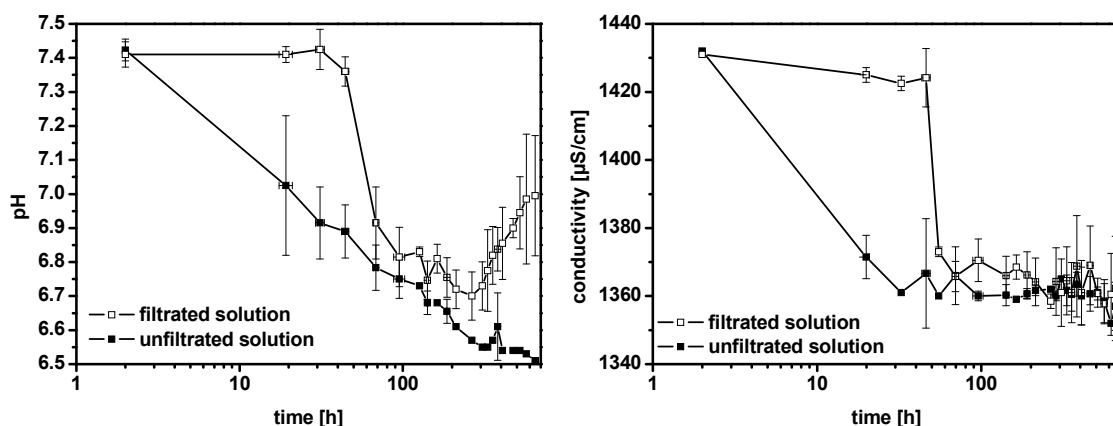


Fig. 57 Change of pH and conductivity of freshly prepared oversaturated calcium phosphate/citrate solutions.

The stock solution aged slowly with continuously decreasing pH. The conductivity decreased first but stayed constant after approximately two days. It can be likely supposed that the precipitate acts as crystallization nuclei which led to a slow depletion of the solution and the observed changes in pH and conductivity. For filtrated solutions a remarkably different behavior was found. A sudden strong decrease of pH and conductivity was observed after an induction period of approximately 50 h. Both filtrated and not filtrated solutions reached the same pH-value and conductivity, but the filtrated solutions showed with longer times a steadily increasing pH-value again while conductivity remains at the same constant value as for the not filtrated stock solutions. Upon long standing, a faint precipitate at the container surface of the filtrated solutions could be observed. The possible solution growth of hydroxy apatite particles in the filtrated solution was followed continuously by DLS over more than 100 h but no considerable change of the scattering intensity could be observed and there was no significant correlation (data not shown). The results were consistently observed for many preparations which are included in the graph in Fig. 57, indicated by the error bars of each data point.

A time series for the mineralization of PET was collected and evaluated with SEM. All samples were immersed vertically in freshly prepared, filtrated Ca/P/cit-solution in separate containers. The mineralization reactions were conducted at room temperature. No nucleation and hydroxy apatite growth could be observed for up to 4 days

(Fig. 58, A). The sample that has been removed from the mineralization solution at 96.5 h showed the beginning of mineral growth (Fig. 58, B). A very sudden change at around 100 h followed, after which a dense layer of hydroxy apatite could be found on the PET surface. The density of the layer stayed the same afterwards even after prolonged time within some sample-to-sample variability (Fig. 58, C; to compare with the sample E, for which the solution was once exchanged, the sample after 285 h was chosen). The layer thickness seemed not to change significantly, too, because at all images taken from the rough or blank side some areas remained uncoated and the overall appearance of the mineralized surface did not change. To achieve a denser and thicker coating, the solution of some samples was once exchanged for freshly prepared Ca/P/cit after 164 h. Within the following 100 h no significant change could be observed. After 121 h (i. e. overall 285 h), some growth on top of the previously very smooth hydroxy apatite layer started to appear, however, a more extended time series has not been conducted (Fig. 58, E). The film looks denser and is compact over the whole surface. The crosssections revealed that the film thickness increased from 0.65 μm to 0.85 μm (Fig. 58, D, F). Similar results were obtained for the mineralization of hydrophilized wafers (Fig. 58, G, H). The HAP layer forms suddenly at around 100 h and remained the same afterwards (again for comparison, the sample after 285 h is chosen rather than the first sample for which a dense layer could be observed). For this substrate, no dense layer was achieved.

Finally, it is puzzling that the sudden surface mineralization does not coincide with the dramatic change in pH and conductivity in the solution. It is an important result that the surface mineralization starts with a certain time lag which does - for certain surfaces - not coincide with the change of the solution properties.

Compared to the mineralization in SBF solutions, the oversaturated Ca/P/cit solution produced a more homogeneous, denser and thinner layer. Regarding the time series, it could be concluded that mineralization was triggered by the aging of the solution and a sudden nucleation and crystallite growth rather than by a slow nucleation process followed by crystallite growth as it was observed for 1.5 SBF/cit.

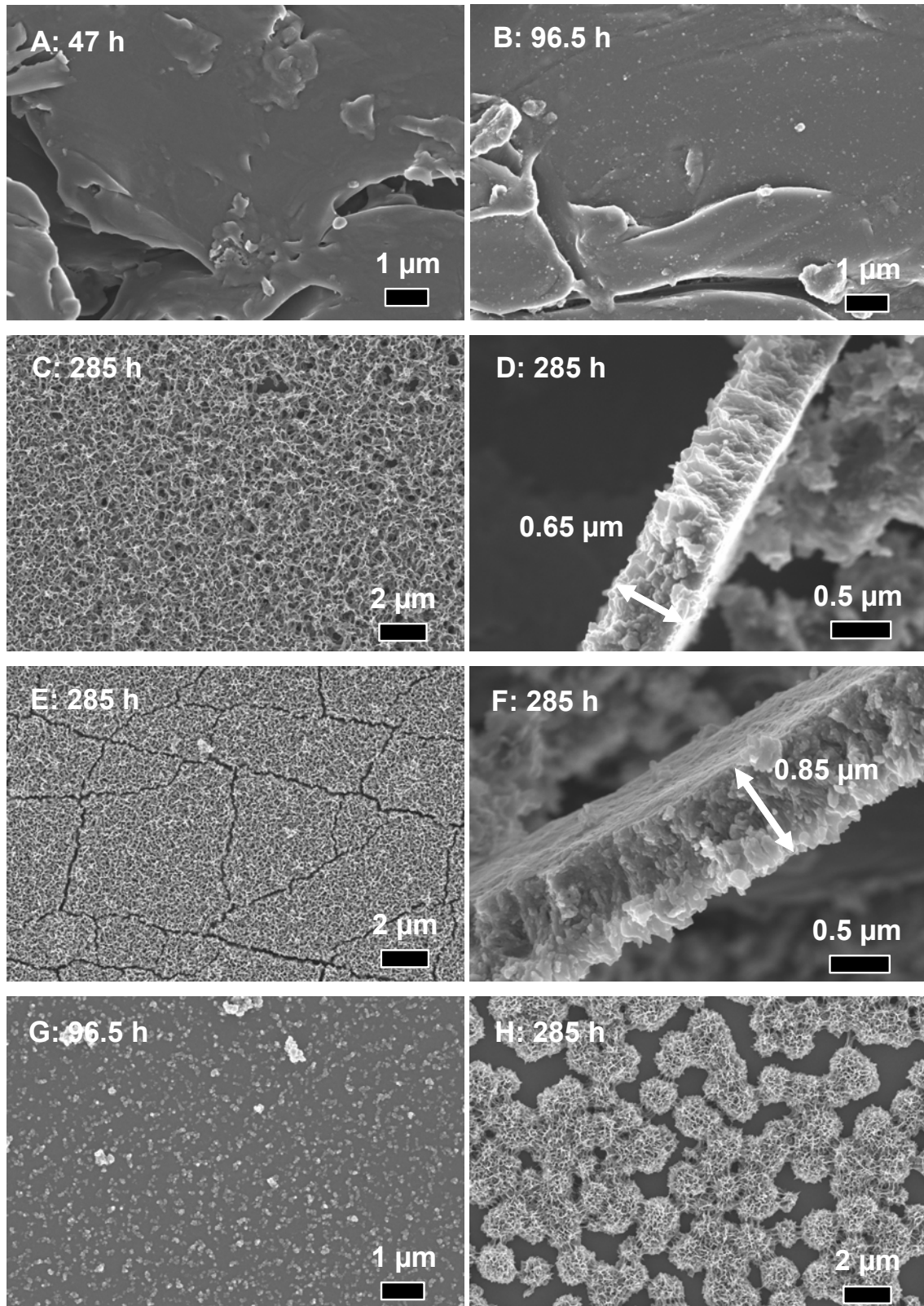


Fig. 58 Nucleation and growth of hydroxy apatite on PET in Ca/P/cit after (A) 47 h, (B) 96.5 h, (C) 285 h; (D) cross-section of the HAP layer of sample (C); (E) 285 h and exchange of the solution after 164 h; (F) cross-section of the HAP layer of sample (E). Nucleation and growth of hydroxy apatite on a Si-wafer in Ca/P/cit after (G) 96.5 h and (H) 285 h.

The closer inspection of the surface revealed the different mechanisms of mineralization further. In citrate containing 1.5 SBF, HAP crystallites grew from few nucleation centres. They formed rather large globules which grew to a certain size and number to finally yield a compact but quite thick layer after multiple immersions. On the other hand, mineralization with Ca/P/cit occurred rapidly but with some delay. A dense layer was formed which was considerably thinner than in the case of 1.5 SBF/cit. No single nucleation spots could be seen but the surface was very smooth and homogeneous.

A comparison of the solution composition of Ca/P/cit with SBF can not be made on a meaningful basis. SBF has a high salinity which influences the supersaturation and the precipitation conditions. Further, the original SBF preparation contains no chelating agent for calcium which further modifies its “real” calcium ion content. The different temperature has an influence on the mineralization conditions, too. SBF is adapted to physiological conditions, i. e. pH = 7.40 at 37.0 °C, but at room temperature, the pH of SBF and its degree of supersaturation is different.

7.4 Mineralization of Bionanoparticle Coated Surfaces

Mineralization processes in nature are controlled by establishing a favourable solution environment in a compartment and by specific interactions with proteins. Liquid-liquid interfaces with trapped proteins may be an interesting option to develop model systems for fluid biological interfaces and to produce novel materials by mimicking natural membranes.

For a first and straightforward analytical access, bionanoparticles have been immobilized on PDMS surfaces. Assembly at the oil/buffer interface and crosslinking the precursor oil is an efficient means to trap the bionanoparticles at the interface and to obtain solid interfaces with self-assembled bionanoparticles (see Fig. 46). The liquid PDMS precursor oil was overlaid with buffer or buffered protein solution and after 3 h adsorption time in darkness at room temperature, the PDMS was solidified by UV-crosslinking for 5-10 min. The surfaces have been gently washed with water and blown dry with a soft stream of nitrogen. Uncoated (i. e. from precursor oil/buffer interface),

BSA-, fetuin-A- and ferritin-coated interfaces were prepared. Additionally, an interface from precursor oil and an aqueous solution of 2 wt% SDS was prepared. The surfaces were 10 x 15 x 1 mm in size and cut into smaller pieces for different mineralization reactions. In this way, multiple experiments with one prepared surface could be performed.

The such prepared surfaces were used for mineralization with hydroxy apatite in the same fashion as it has been described in detail for the model substrate PET in the chapters 7.1-7.3. The procedure with incubation on glass A particles was done for 1.0 SBF/1.0 SBF and 1.0 SBF/1.5 SBF. For reference purposes, also a set of samples was incubated without glass particles. Mineralization reactions were also carried out with 1.5 SBF/cit and with Ca/P/cit.

Although it meant a considerable additional effort, all results were obtained from several overlapping sets of experiments. Separately prepared surfaces were mineralized in parallel with the same prepared mineralization solution. Additionally, the pieces of one prepared surface were mineralized with separately prepared mineralization solutions. Thus, accidental results from a particular prepared surface or mineralization solution could be identified and misinterpretations avoided. Same but separately prepared surfaces and/or same but separately prepared mineralization solutions gave almost always identical results. Among the dozen mineralization series with around 150 investigated samples only three surfaces seemed to have suffered from different conditions or treatment. These results were omitted because they were disproved by results from further experiments which had been in line with the general scheme of observations. We therefore trust that the results of our experiments are highly robust and reproducible.

7.4.1 Biomimetic Hydroxy Apatite Mineralization of Bionanoparticle-Coated Surfaces

Bionanoparticle-coated surfaces were incubated in 1.0 SBF on glass A particles and then in 1.0 SBF and 1.5 SBF, respectively, for the second treatment. Generally, a compact and dense coating on all surfaces was achieved (Fig. 59).

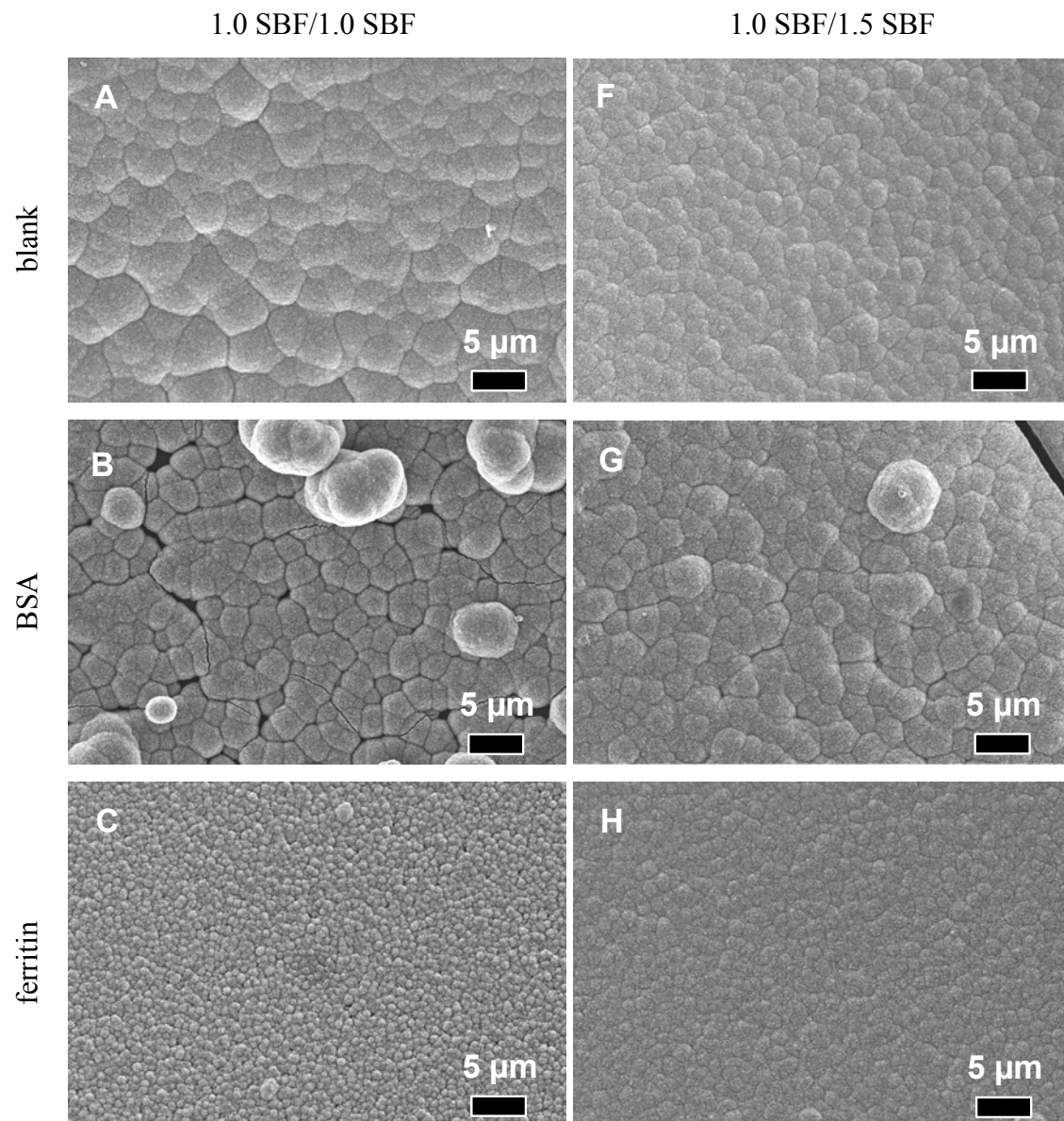


Fig. 59 Hydroxy apatite mineralization of different coated PDMS surfaces with SBF after incubation on glass A particles.

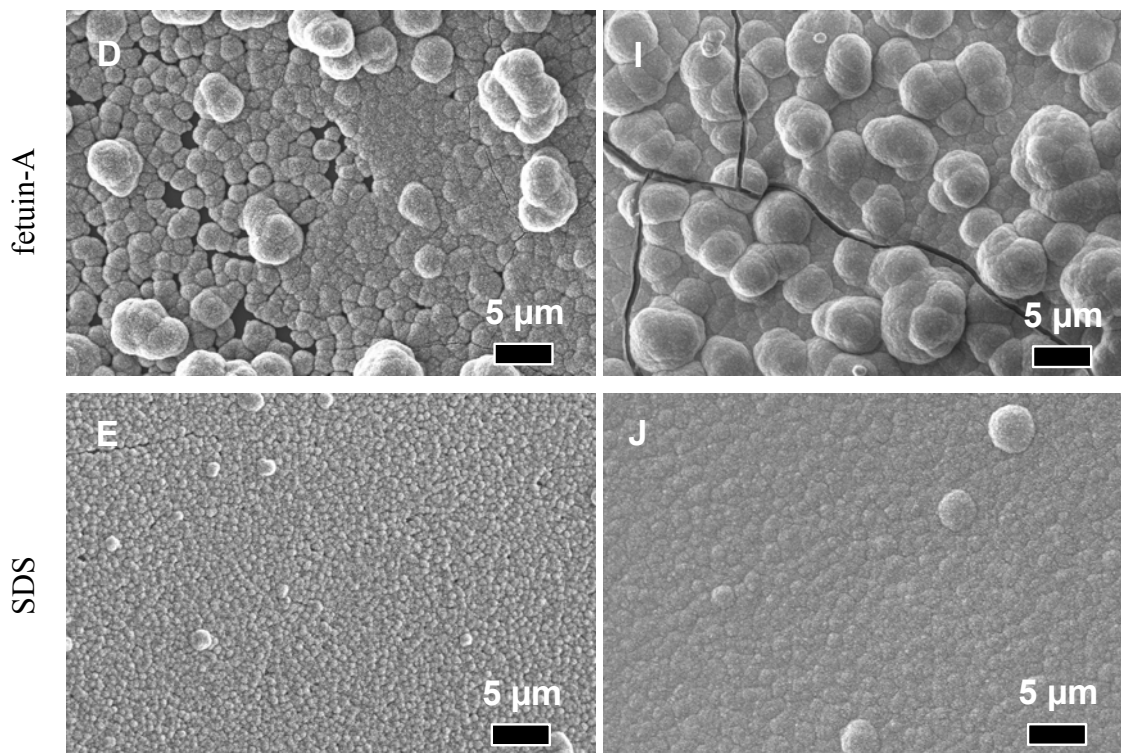


Fig. 59 (cont.) Hydroxy apatite mineralization of different coated PDMS surfaces with SBF after incubation on glass A particles.

A preferential mineralization for protein coated interfaces was not observed. Non-coated PDMS surfaces were mineralized as well as interfaces prepared with SDS-solutions. In the following some details about the surface morphology of the HAP layer on the different coated surfaces are discussed. We would like to highlight again that even distinct details of the surface morphology were reproduced for separately prepared surfaces and mineralization solutions. Generally, the incubation with 1.5 SBF during the second treatment yielded for all sample surfaces a more homogeneous, compact and denser layer (Fig. 59, F-J). The surface was smoother because the thicker layer overcame the initial pattern from the localized nucleation sites. A direct result was that the layers that were produced from 1.0 SBF/1.5 SBF were brittle (see e. g. Fig. 59, I), while the surfaces produced from 1.0 SBF/1.0 SBF remained mainly crack-free. This can be explained by the thicker layers that were grown in 1.5 SBF. In case of the treatment with 1.0 SBF/1.0 SBF the surfaces showed sometimes still free spots (see e. g. Fig. 59, B and D). Occasionally, overgrowth of globules protruding from the mineral layer was observed (see e. g. Fig. 59, D and I). No correlation of this phenomenon to the surface and/or mineralization solution could be identified but it occurred more often

with 1.0 SBF/1.5 SBF, and fetuin-A seemed to be more prone to overgrowth than other surfaces. It was likely that the globules were built on other spots e. g. the container wall and deposited on the surface where they were grown in. Another possibility is the faster heterogeneous nucleation and growth on surface damages and inhomogeneities. The smoothest but also thinnest layers were formed on ferritin coated surfaces and surfaces prepared with SDS (Fig. 59, C, H, E and J). We found a large number of nucleation sites which grew all similar in size to finally cover the whole surface. BSA and fetuin-A on the other hand showed a HAP surface layer very similar to uncoated PDMS (Fig. 59, B, D, G and I vs. A and F). The blank surfaces and the BSA- and fetuin-A-coated surfaces exhibited less nucleation sites which grew later to much larger crystallite globules. These protein coatings have no clearly visible influence on the HAP mineralization. Fetuin-A has been reported to have a strong affinity for hydroxy apatite and to accumulate on bone material. However, it seems that this observation does not allow easy conclusions about a mineralization directing action. A pronounced stronger mineralization of fetuin-A coated surfaces cannot be postulated although on some surfaces strong HAP overgrowth was observed.

From a materials point of view, these observations significantly broaden the applicability of hydroxy apatite coatings to different surfaces. Obviously, the hydroxy apatite coating with SBF seems to be relatively insensitive towards hydrophilic surfaces. On the other hand, a low sensitivity is clearly not advantageous for the development of sophisticated structured materials from e. g. protein arrays. An “all-or-nothing”-effect could be not observed for the investigated surfaces. This would have allowed the production of spatially selective mineralized surfaces which were patterned via micro-contact printing of different proteins.

The possible influence of a prior incubation step on glass particles on the formation of a hydroxy apatite layer is shown in Fig. 60. In the three columns SEM pictures of the different PDMS surfaces are presented which have not been immersed in SBF on glass particles. The result is very similar to the PET-series: as soon as 1.5 SBF is employed in either step (Fig. 60, F-J and K-L), the surface growth of HAP occurred even without prior formation of nuclei from dissolved ions from the glass particles. Only in the case of 1.0 SBF/1.0 SBF a clear effect was found: there was no mineral deposition on the

surface when it had not been incubated on glass particles (Fig. 60, A-E), but a dense and compact layer was formed when it was incubated (compare to Fig. 59, A-E).

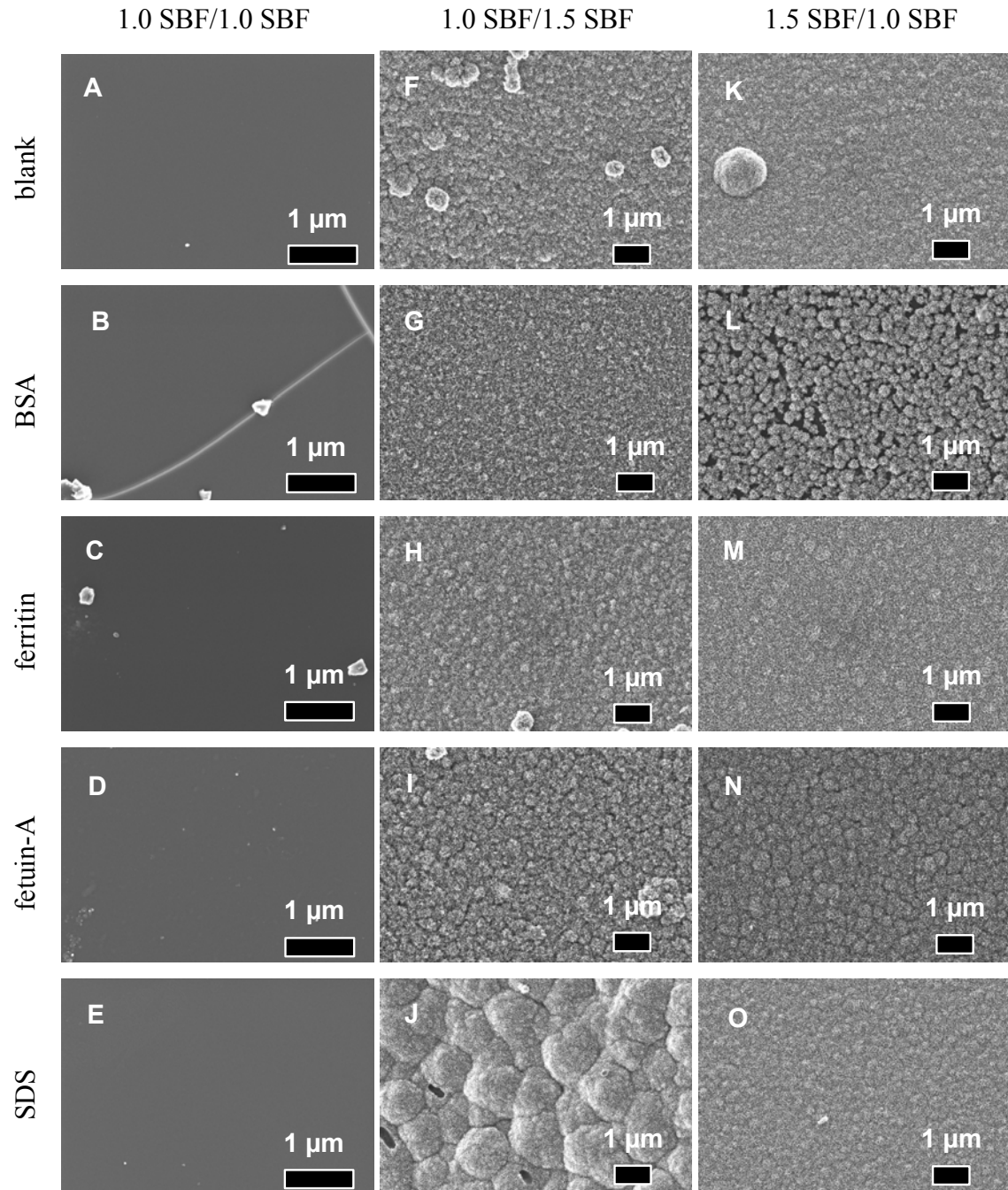


Fig. 60 Hydroxy apatite mineralization of different coated PDMS surfaces with SBF after incubation on no glass particles.

7.4.2 Hydroxy Apatite Mineralization of Bionanoparticle Coated Surfaces in 1.5 SBF with Citrate

The same bionanoparticle coated PDMS surfaces were used for the mineralization with 1.5 SBF/cit. The procedure followed that described for PET in chapter 7.2. The SEM images of the samples are shown in Fig. 61.

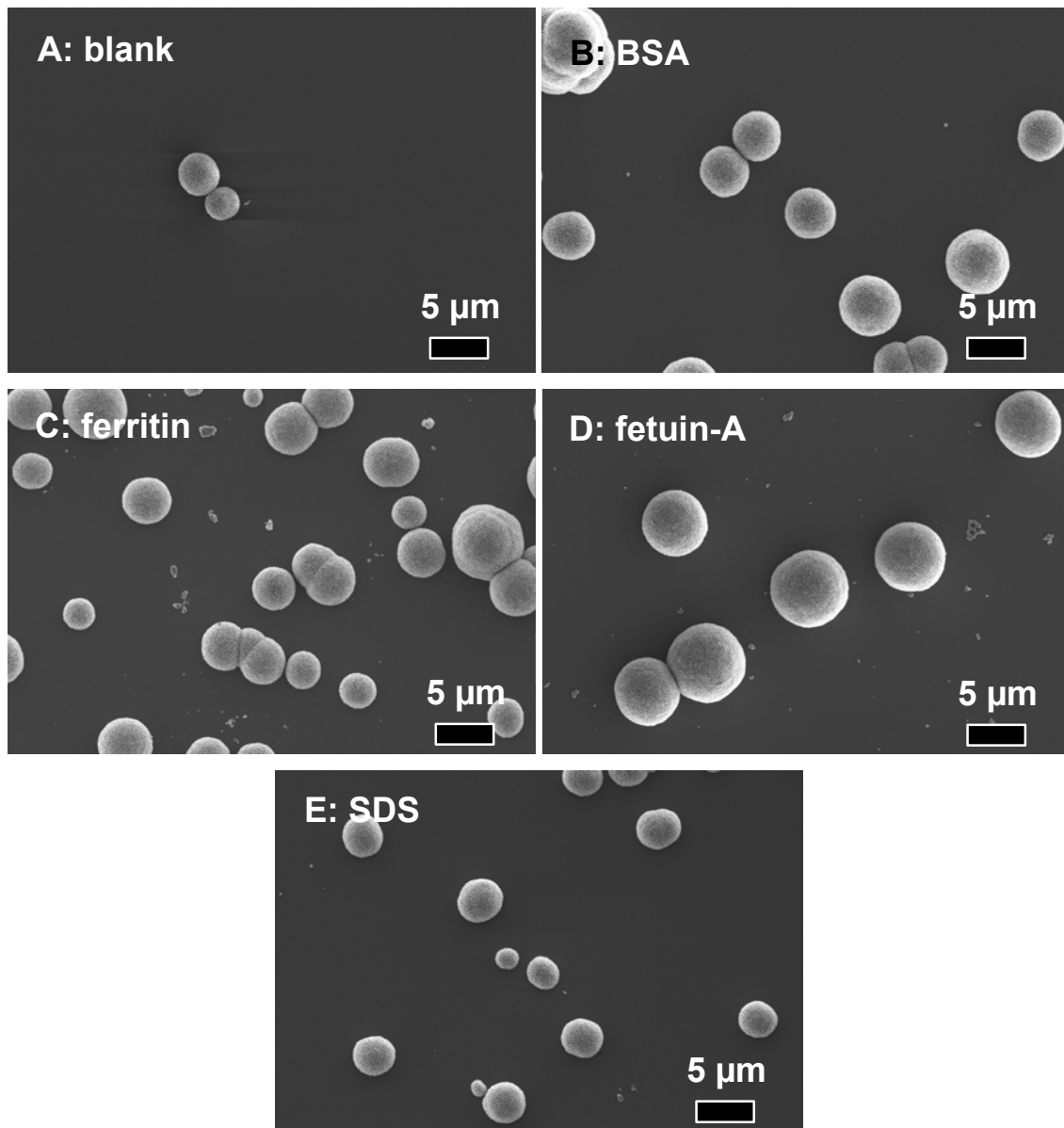


Fig. 61 Hydroxy apatite mineralization of different coated PDMS surfaces with 1.5 SBF/cit after 287 h.

No homogeneous coating but very few and large HAP globes were found which were sparsely distributed over the whole surface. Different bionanoparticle coatings did not

influence the formation of HAP globes. A comparison can be done with the samples that have been mineralized according to Kokubo with immersion in 1.5 SBF during the second treatment and incubation without glass particles (compare Fig. 61, A-E, with Fig. 60, F-J). These samples were densely coated by similar large globes that grew together to build a compact layer. Here, the citrate seemed to mask efficiently calcium ions and to lower the level of supersaturation. It cannot be assumed that a favourable interaction of citrate with the surface bound protein leads to an increased number of nucleation sites on the surface. The model substrate PET was more densely covered by HAP globules but no compact layer was formed either (see e. g. Fig. 56, D).

7.4.3 Hydroxy Apatite Mineralization of Bionanoparticle Coated Surfaces in an Oversaturated Calcium Phosphate Solution

Analogously to the mineralization of PET samples (chapter 7.3), bionanoparticle coated PDMS surfaces have been incubated in an oversaturated calcium phosphate solution (Ca/P/cit) at room temperature. No time series was conducted but the samples were incubated for times much longer than 5 days.

An inspection with SEM revealed a homogeneous coating on all samples (Fig. 62). The mineralization seems to have started from many nucleation sites which quickly grew to a thin and dense layer. The thickness varied with the bionanoparticle surface coating. For ferritin and SDS-coated PDMS samples, the thickness was higher and the very homogeneous mineral layer did not reveal any nucleation sites anymore. On the other hand, fetuin-A coated surfaces built hardly a compact mineral layer, rather, very small crystallites were homogeneously distributed. The blank and the BSA coated surface were quite similar to each other. Many nucleation sites were found from which small crystallite globules grew which finally merged with their neighbours to build a dense and compact layer. Few spots of the bare surface could still be found. Sometimes, hydroxy apatite crystallite globules could be found on the surface (Fig. 62, H) which do not seem to have been grown into the underlying HAP layer. It remains unclear whether they were grown in solution and were not removed during washing or whether they were grown on surface inhomogeneities on top of the first hydroxy apatite layer. This

phenomenon appeared uncorrelated to the PDMS surface coating and mineralization solutions.

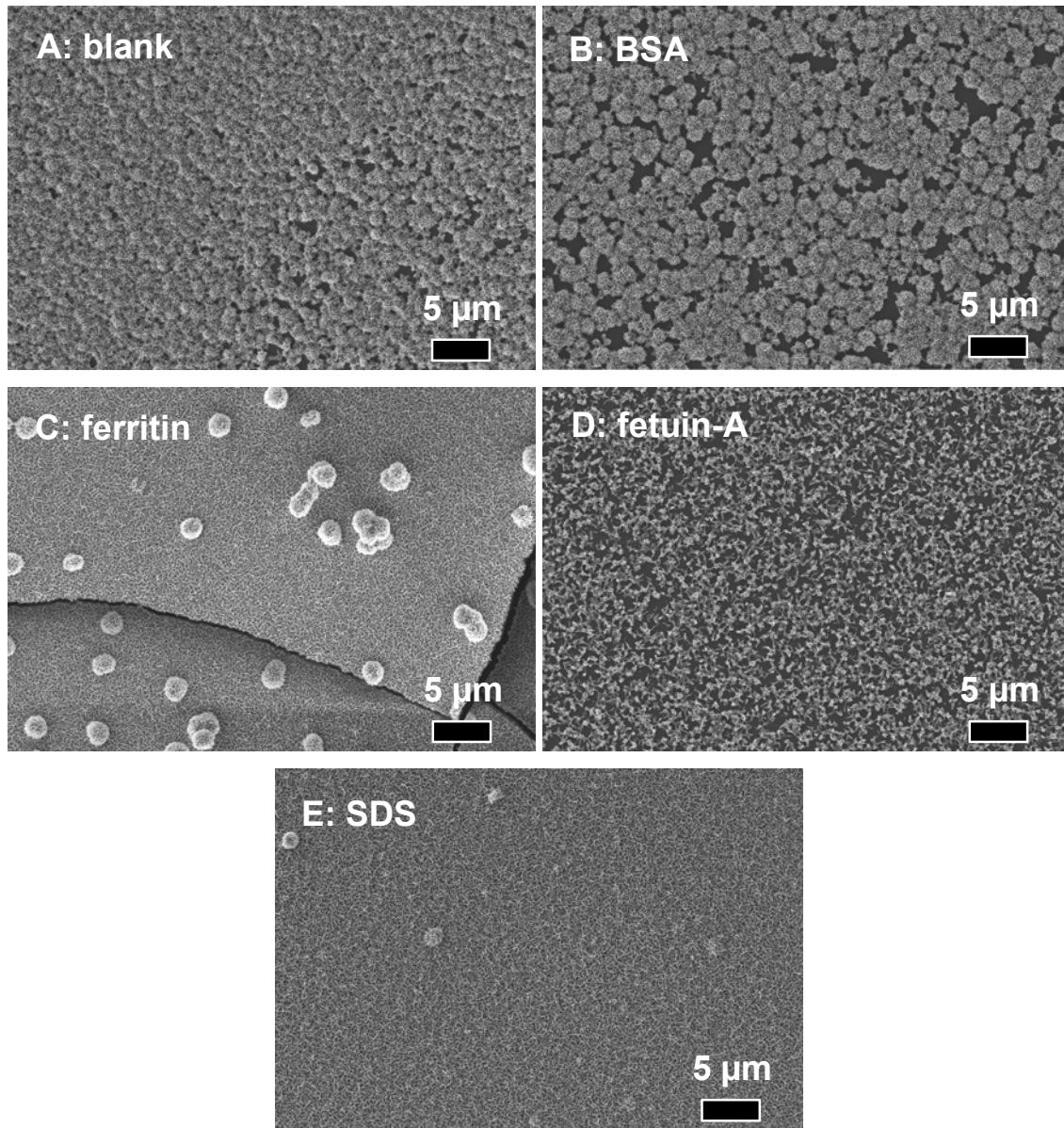


Fig. 62 Hydroxy apatite mineralization of different coated PDMS surfaces with Ca/P/cit after 312 h.

7.5 Investigation of the Hydroxy Apatite Mineral Layer

High resolution images from SEM revealed differences in the structure of the HAP crystallites which have grown in different mineralization solutions. No influence of the substrate could be found which is not unexpected. A possible influence of the underlying protein surface is overcome during the growth of the thick mineral layer. Throughout the text it was assumed, that the HAP layer is crystalline but of low order and thus the depositions were called “crystallites”. This has been confirmed by thin film X-ray diffraction in many different reports on the use of SBF.^{279, 535} The SEM images look very similar and there is no reason to assume that the layer is different to what has been reported, for SBF as well as 1.5 SBF/cit. However, attempts to obtain X-ray diffraction patterns from the HAP layers on PET were not successful up to now. There is the possibility that the layer is indeed amorphous, but also, that the layer is too thin to obtain detectable diffraction signals. Another explanation would be that the peaks are very broad since the possible crystalline domains are very small and finally vanish in the background. Additionally, the biaxial oriented PET sheets exhibit some very broad peaks which might also obscure the weak scattering or broad peaks from the HAP layer. Therefore we cannot give a final conclusion about the phase of the HAP in our experiments yet.

The elemental composition of the HAP layer was investigated by EDX. A typical spectrum of the hydroxy apatite layer is shown in Fig. 63.

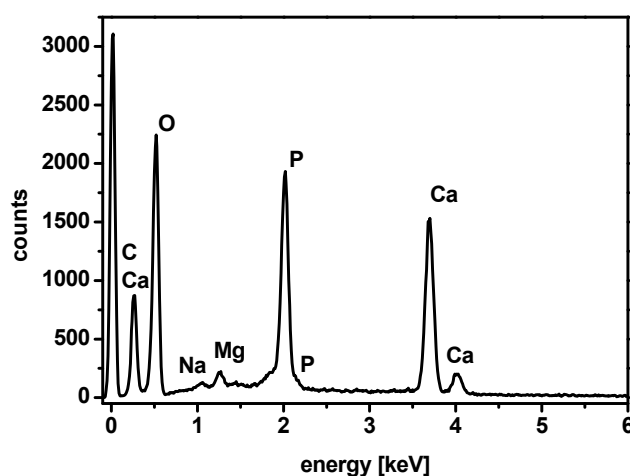


Fig. 63 Typical EDX spectrum of a hydroxy apatite layer (here: HAP on PET, prepared with 1.0 SBF/1.5 SBF). Detected elements (K-lines) are indicated.

Besides calcium and phosphorus, only oxygen and carbon could be generally found. Sodium and magnesium were observed as trace elements when the HAP layer was prepared from SBF but otherwise not. Ratios of elemental contents can be determined quite accurately although EDX has a limited accuracy in the determination of the absolute content. The Ca/P ratio is of special interest (Fig. 64). Natural bone has an average ratio of $\text{Ca/P} = 1.67$ and implant materials should preferentially have a similar value. The HAP layers that were prepared with SBF by the two step procedure according to Kokubo et al. were slightly deficient of calcium. It was reported, that the Ca/P ratio became smaller with increasing SBF concentration; however, the ideal value of 1.67 was not achieved for concentrations even lower than 1.0 SBF.²⁷⁹ Here, the layers prepared with solutions of different concentrations had the same composition within the experimental error. 1.5 SBF/cit had an atomic ratio of 1.65 ± 0.05 which is identical with the Ca/P ratio of 1.67 of natural bone. The mineral layers that were deposited from Ca/P/cit were much richer in calcium than the other samples. The precipitate (Ca/P/cit prec.) that was obtained during the preparation of Ca/P/cit had the same composition as the deposited HAP layers that were prepared with filtrated Ca/P/cit solutions.

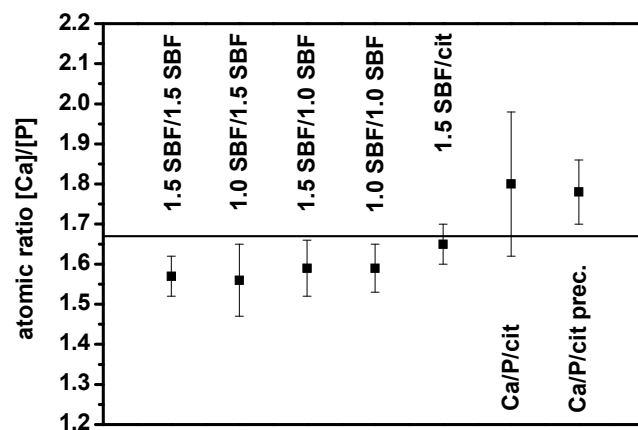


Fig. 64 Ca/P atomic ratio of HAP layers prepared from different mineralization solutions obtained from EDX. The line indicates the Ca/P ratio of natural bone.

The morphology of the HAP layers is shown at high magnifications in the SEM images in Fig. 65. All mineral depositions from SBF exhibited the same morphology, regardless of the involved concentrations and incubation procedures. The layer had a small-scale flaky structure. Irregularly curved plates with a thickness of around 15 nm grew

preferentially perpendicular to the surface. 1.5 SBF/cit exhibited some striking differences to the mineralization in SBF containing no citrate. The structure was not a platelet-like structure but looked more like a sub-microporous sponge. A similar but more open porous structure was observed for Ca/P/cit. It has been reported on the influence of various molecules and particularly also of citrate on the crystal morphology of calcium phosphate minerals.⁵³⁷ However, since the crystallinity for such prepared HAP layers is low (and has still to be proven for the actual sample, respectively), no further discussion is justified at the moment except the statement that citrate significantly alters the structure of the deposited hydroxy apatite.

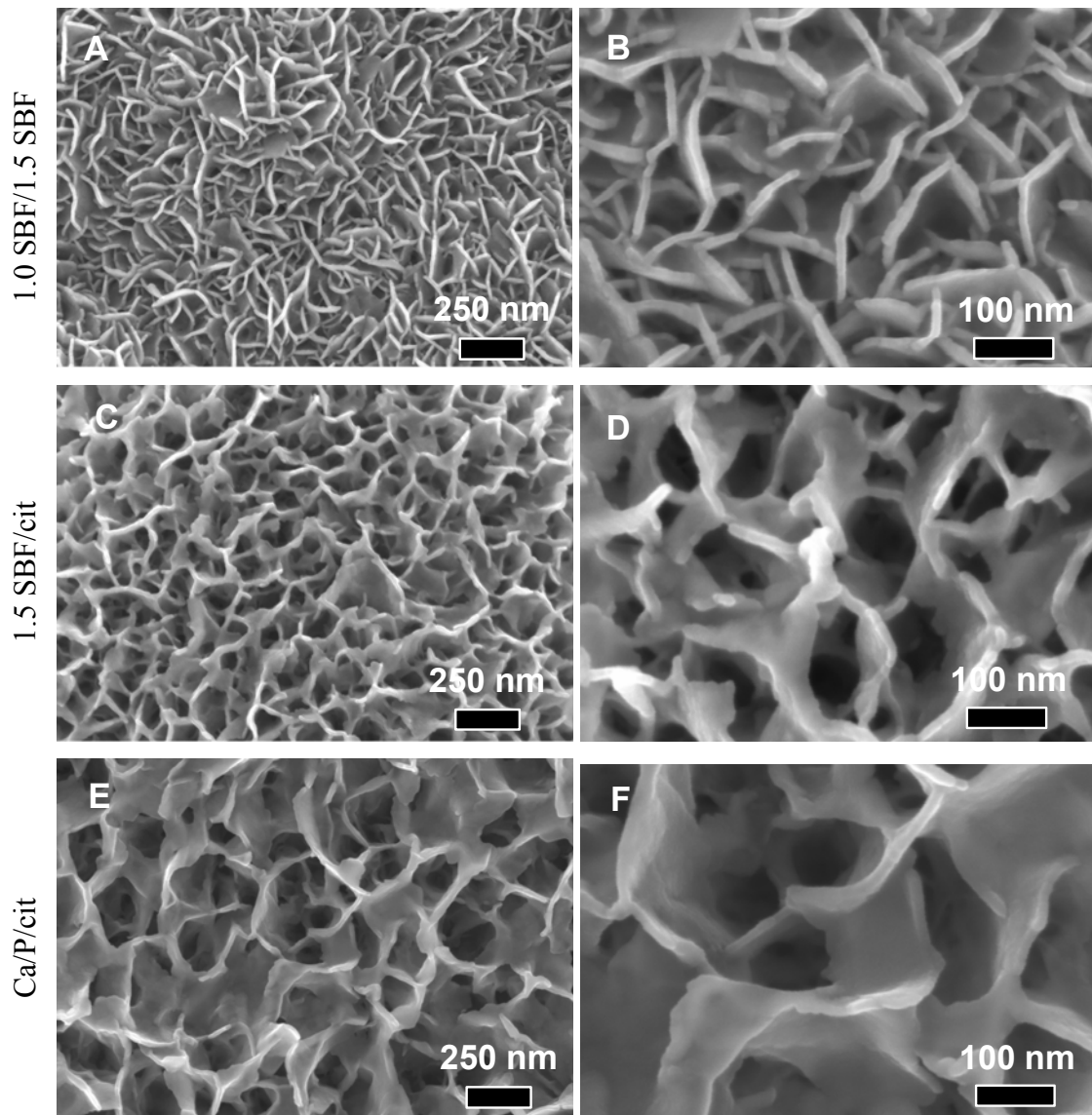


Fig. 65 High resolution SEM images of HAP layers from mineralization with different solutions.

7.6 Comparison of Mineralization Conditions

The growth of hydroxy apatite on PET using different mineralization solutions and conditions is summarized in Tab. 13.

Tab. 13 HAP mineralization on PET.

1.0/1.0 SBF	<ul style="list-style-type: none"> • dense and compact layer after incubation for 2 d/4 + 2 d • coating of samples only after incubation on glass particles
1.0/1.5 SBF	<ul style="list-style-type: none"> • thick and compact layer after incubation for 2 d/4 + 2 d • only minor effect of glass particles
1.5 SBF/cit	<ul style="list-style-type: none"> • no compact layer • slow increase in number and size of HAP crystallites • ceasing after approximately 120 h
Ca/P/cit	<ul style="list-style-type: none"> • dense and compact layer with few small uncoated areas • sudden formation of HAP layer after approximately 100 h • no further growth for longer times

The effect of bionanoparticles immobilized on PDMS and various mineralization conditions on hydroxy apatite growth on PDMS surfaces is summarized in Tab. 14. No time series were conducted; all samples were mineralized for the time indicated.

Tab. 14 HAP mineralization on differently coated (blank, BSA, ferritin, fetuin-A, SDS) PDMS surfaces.

1.0/1.0 SBF	<ul style="list-style-type: none"> • dense and compact layer after incubation for 2 d/4 + 2 d • HAP coating of samples only after incubation on glass particles: <ul style="list-style-type: none"> ○ dense and mostly compact layers for all coatings ○ ferritin, SDS: many nucleation sites, more homogeneous and smoother layer
1.0/1.5 SBF	<ul style="list-style-type: none"> • thick and compact layer after incubation for 2 d/4 + 2 d • HAP coating of samples also for incubation without glass particles: <ul style="list-style-type: none"> ○ dense and compact layers for all coatings ○ similar to 1.0/1.0 SBF but generally smoother layers ○ ferritin, SDS: very smooth, homogeneous and compact
1.5 SBF/cit	<ul style="list-style-type: none"> • thinly spread, big HAP crystallite globes (> 10 d) • no homogeneous and compact coating • no differences for different coated surfaces
Ca/P/cit	<ul style="list-style-type: none"> • dense and homogeneous compact coating (> 10 d) • density and thickness slightly varying with surface coating: <ul style="list-style-type: none"> ○ blank, BSA: dense but not compact ○ fetuin-A: very thin, homogeneous ○ ferritin, SDS: homogeneous, compact

7.7 Mineralization of Pickering Emulsions

Various approaches have been reported in the literature for the production of calcium phosphate capsules or other mineral shells. Most of them exhibit special mechanisms but are not based on a more generally applicable principle. Among them are hollow octacalcium phosphate microspheres by polyelectrolyte mediated crystallization,⁵³⁸ polysaccharide capsules for cell encapsulation mineralized with an amorphous calcium phosphate shell⁵³⁹ etc. In this chapter the mineralization of protein- and bionanoparticle-stabilized Pickering emulsions is presented. We show SEM micrographs of three differently stabilized emulsions. Each of them was mineralized with different calcium phosphate solutions as it has been described above for the solid PDMS surfaces with trapped proteins and bionanoparticles. We find some commonness but also puzzling differences to the mineralization of bionanoparticle-coated solid surfaces and between different Pickering emulsions.

BSA, fetuin-A, and ferritin were used in buffered aqueous solutions at a concentration of 5 mg/ml to prepare Pickering emulsions. The bionanoparticle solutions were vigorously shaken by hand with perfluorooctane (maximum 10 vol% of the final solution). Stable emulsions formed immediately which were allowed to reach adsorption equilibrium for 3 h. The proteins at the interface were crosslinked with an aqueous solution of 1 % glutaraldehyde (v/v) for 30 min at room temperature before the droplets were extensively washed with water. Still no coalescence was observed upon that step. The emulsion droplets were then divided into four containers and the water was exchanged by the respective mineralization solutions, either 1.0 SBF, 1.5 SBF, 1.5 SBF/cit or Ca/P/cit. It was deduced from the time series for the mineralization of PET that mineralization in 1.5 SBF/cit and Ca/P/cit ceased after five days. The incubation in SBF was always conducted for 2 d + 6 d and a dense layer was reached but it is likely that mineralization is completed earlier. Thus, we assumed that 5-7 days are enough time and that the mineralization reactions will not significantly proceed further after that. Certainly, some care must be taken to apply conclusions from the solid surfaces to the liquid interface of Pickering emulsions but nevertheless can be chosen as starting point. The same mineralization time was chosen for all Pickering emulsions because it was considered as more useful to compare the different

mineralization reactions for the different emulsions for the same mineralization time than to stick to the different times that were used for the mineralization of the bionanoparticle coated PDMS surfaces. After each 5-7 days, small samples of the Pickering emulsions were withdrawn and the solution of the remaining emulsion was exchanged for fresh mineralization solution. It was expected that multiple incubations would enhance the formation of a compact and full shell. The tubes were daily tilted to mix the solution and the settled Pickering droplets. The withdrawn samples were extensively washed and dried on a silicon wafer, followed by drying in high vacuum before imaging with SEM. After 16 d, some precipitation on the walls of some containers was observed.

For the emulsions that were incubated in 1.0 SBF, no mineralization of the droplets and no precipitation on the container walls was found (Fig. 66, A). This result was in agreement with the observations at the solid surfaces on which also no mineralization could be observed unless they were incubated on glass particles. 1.0 SBF itself is not enough supersaturated to form efficiently nucleation sites. The mineralization of droplets that was conducted in 1.5 SBF did also not lead to the formation of a compact shell although a dense layer was deposited on bionanoparticle-coated PDMS surfaces, regardless of a previous incubation step on glass particles. After the first and all subsequent exchanges of 1.5 SBF, large crystallite globules could be found on the Pickering droplets (Fig. 66, B). They were very polydisperse and sometimes irregularly grown together but formed hardly a compact shell. The overall very inhomogeneous appearance was observed for all employed bionanoparticles and did not change significantly for subsequent immersion steps. The mineralization seemed not to proceed much further. It was assumed that the supersaturation of SBF was quickly reduced during the nucleation at some spots. Large globules were forming and these may have grown slightly for subsequent exchanges of the solution. However, once these crystallites had formed, they grew preferentially and depleted the solution and no more extra nuclei were formed. Large areas on the droplets remained free and an incomplete shell was formed. Another source of depletion of the mineralization solution could have been the container walls on which after every step of solution exchange stronger mineral precipitates could be found.

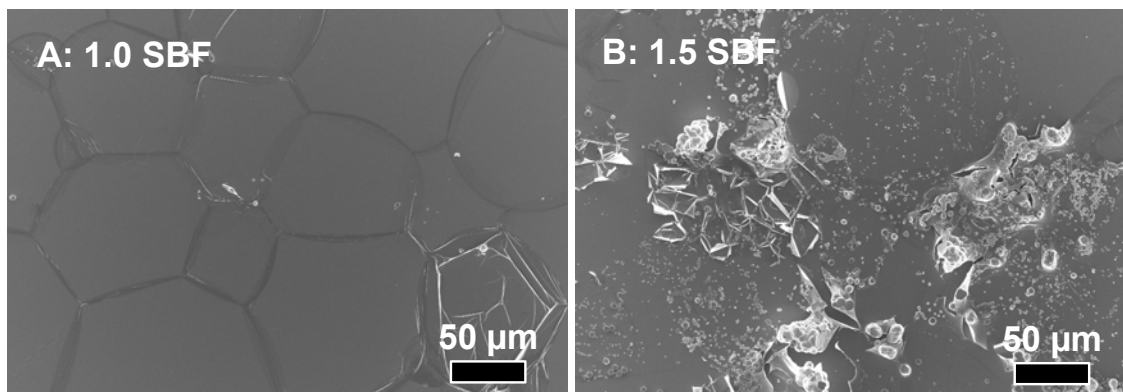


Fig. 66 (A) Mineralization of BSA-stabilized Pickering emulsions (perfluorooctane/buffer solution interface) with 1.0 SBF and (B) 1.5 SBF for 16 days and two exchanges of the solution after 5 and 10 days.

On the other hand, in the case of mineralization with 1.5 SBF containing citrate (1.5 SBF/cit) we found strong mineralization of Pickering emulsions (Fig. 67) even though on all bionanoparticle-coated PDMS surfaces just scarcely distributed HAP globules were produced as shown in chapter 7.4.2 (see Fig. 61). Subsequent exchanges led to increasingly more compact shells (Fig. 67, A vs. B) although the mineralization seemed to slow down (Fig. 67, B vs. C or D). Many droplets with single, separated crystallite globules could still be found even after four exchanges of the solution. Furthermore, nucleation and mineralization did not occur on all spheres evenly. An extreme example is shown in Fig. 67, D, where we found a nearly complete mineral shell but surrounded by droplets which have obviously just been scarcely covered by single separated crystallites. Surprisingly, on ferritin stabilized droplets no HAP at all has been formed during any stage of the immersion procedure (not shown). BSA and fetuin-A stabilized Pickering emulsions were mineralized much the same way and thus only the BSA samples were chosen in Fig. 67.

A closer inspection of the mineral shells revealed the mechanism of the HAP shell formation. Hydroxy apatite nucleated at the surface and the growing crystallites formed globules which were growing together. The nucleation density was relatively weak and in Fig. 68, A, the stabilizing protein membrane which spanned the still free areas could nicely be seen.

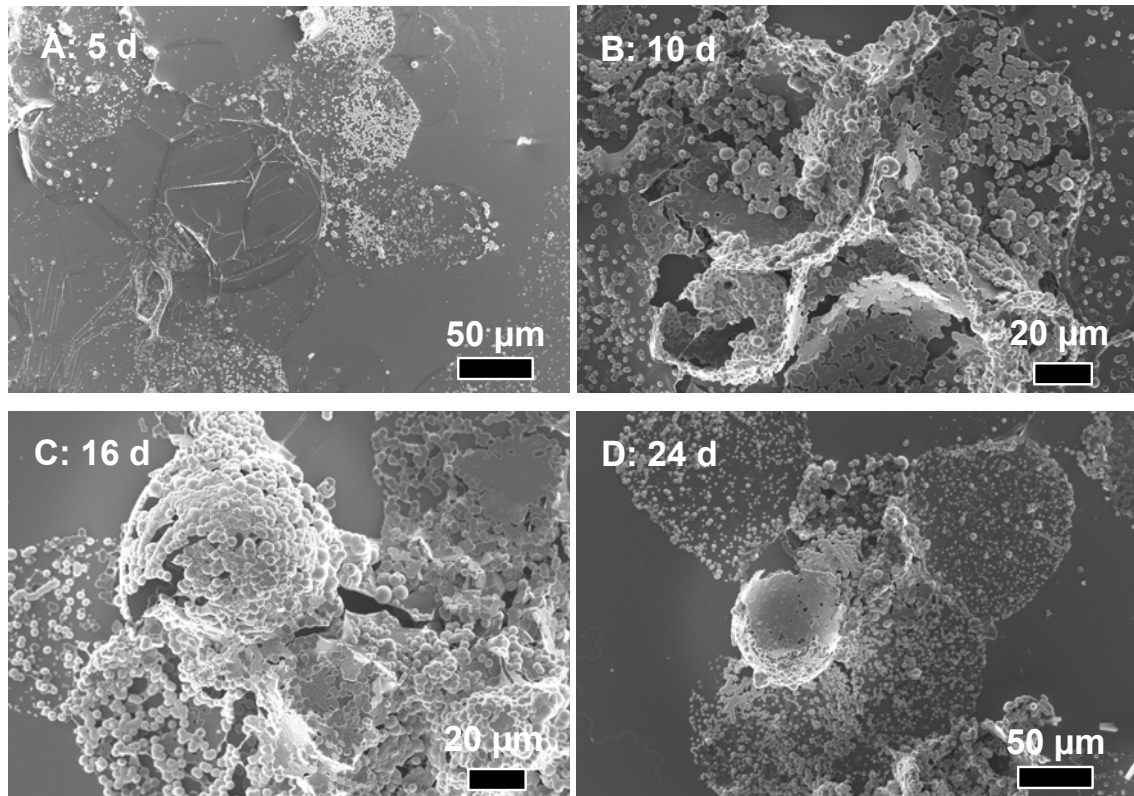


Fig. 67 Mineralization of BSA-stabilized Pickering emulsions (perfluorooctane/buffer solution) with 1.5 SBF/cit for (A) 5 days; (B) 10 days and solution exchange after 5 days; (C) 16 days and solution exchanges after 5 and 10 days; (D) 24 days and solution exchanges after 5, 10 and 16 days.

Fig. 68, B was a view inside a broken droplet. HAP “globules” is in fact not the really correct term because in this image it was seen that the HAP could of course not penetrate the oil phase. The HAP crystallites therefore formed rather half-globes. The side facing the oil phase was flat and smooth.

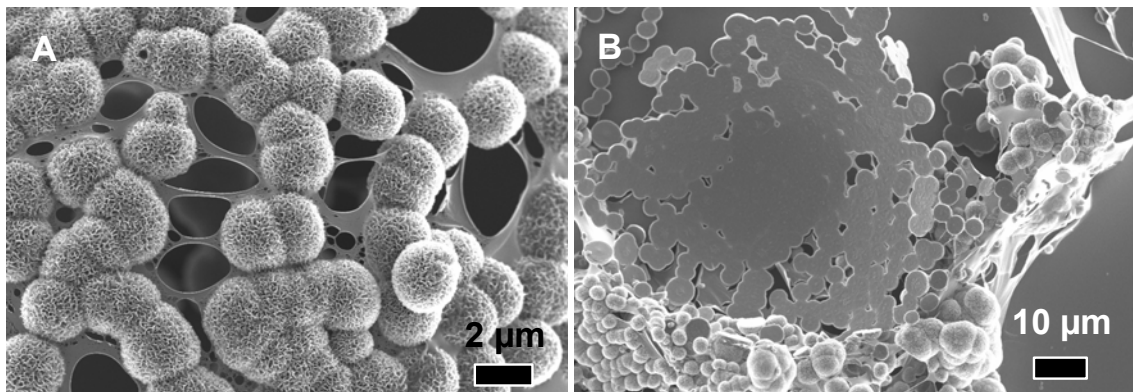


Fig. 68 Mineralization of BSA stabilized Pickering emulsions (perfluorooctane/buffer) with 1.5 SBF/cit.

A shell growth similar to that in 1.5 SBF/cit was observed for BSA and fetuin-A stabilized Pickering emulsions if Ca/P/cit was used in the mineralization reaction. A higher density of HAP crystallites and a more homogeneous coverage could be found. The mineralization seemed to slow down for subsequent multiple exchanges with freshly prepared mineralization solution (Fig. 69, A-D). Though the majority of the Pickering droplets were densely covered by crystallite globules, a compact shell was just formed on few of them. As BSA- and fetuin-A-coated droplets gave similar series and only images of the BSA-samples were selected here.

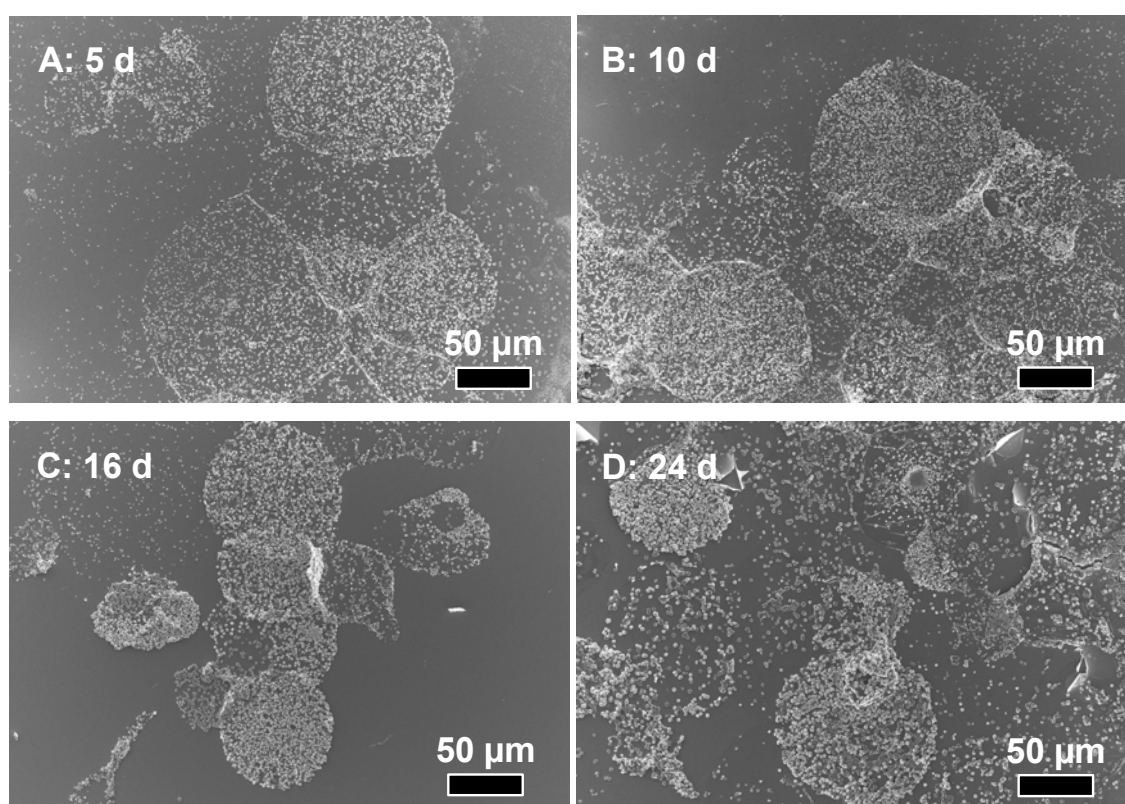


Fig. 69 Mineralization of BSA-stabilized Pickering emulsions (perfluorooctane/buffer) with Ca/P/cit for (A) 5 days; (B) 10 days and solution exchange after 5 days; (C) 16 days and solution exchanges after 5 and 10 days; (D) 24 days and solution exchanges after 5, 10 and 16 days.

Ferritin stabilized emulsion droplets were also more weakly mineralized in Ca/P/cit. A full series of the development of rigid hollow HAP shells is shown in Fig. 70. After the first 5 days in Ca/P/cit, no mineralization could be observed (Fig. 70, A). However, after exchange of the solution and 5 more days, we found that mineralization of the capsules started. The jagged edges of the capsules in Fig. 70, B showed that the capsule

shell was not soft anymore but solid though the thin composite shell was still flexible enough to fold smoothly upon drying. With further time and exchanges of the mineralization solutions (Fig. 70, C: 16 days, two exchanges after 5 and 10 days; Fig. 70, D: 24 days, three exchanges after 5, 10 and 16 days) the shell became thicker and more and more rigid. We finally found many hollow HAP composite capsules which remained intact to a large extent upon drying.

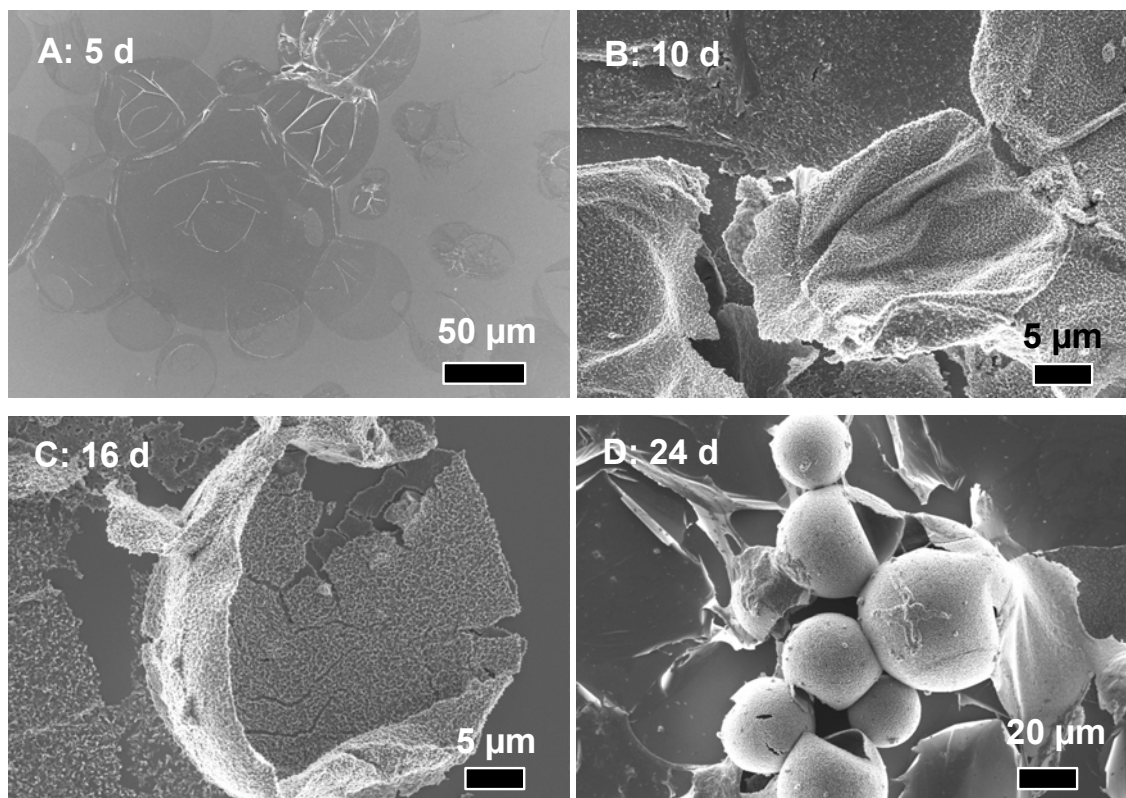


Fig. 70 Mineralization of ferritin-stabilized Pickering emulsions (perfluorooctane/buffer) with Ca/P/cit for (A) 5 days; (B) 10 days and solution exchange after 5 days; (C) 16 days and solution exchanges after 5 and 10 days; (D) 24 days and solution exchanges after 5, 10 and 16 days.

The retarded nucleation and mineralization led to distinct different mineralization characteristics and a much different morphology of the HAP shell (Fig. 71, C) compared to SBF-based mineralization solutions or BSA- or fetuin-A-stabilized Pickering emulsions. No distinct nucleation sites could be revealed; instead a very homogeneous, thin and compact layer is formed on the protein coat onto which very small hydroxy apatite minerals were growing. During the early stages of mineralization, the protein/mineral composite remained very flexible (Fig. 71, A; after 10 days).

Obviously, the composite capsule was held together by the assembled and cross-linked ferritin particles on the shell. Dried capsules showed smooth folds and no cracks. For subsequent incubation steps with fresh mineralization solution, capsules became more rigid and were not folding anymore but breaking (Fig. 71, B; after 24 days). The cross-section of the shell could just be estimated because of the roughness but amounted to approximately 200 nm (Fig. 71, D).

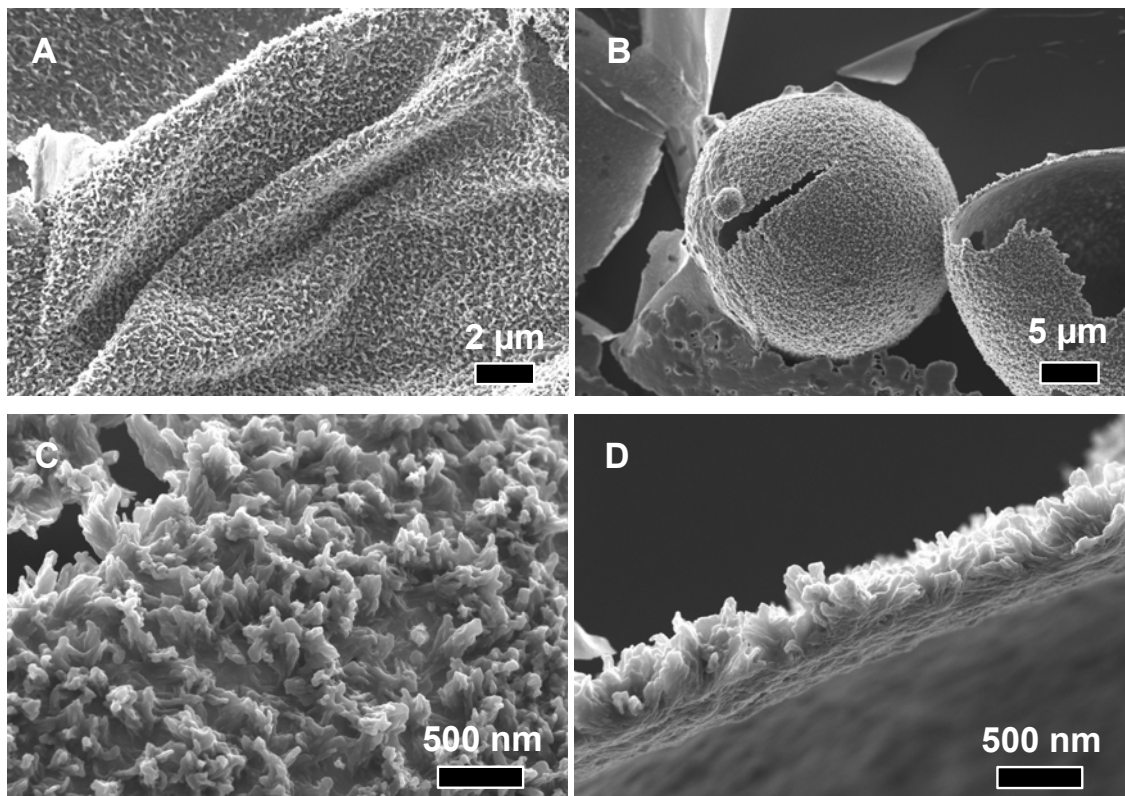


Fig. 71 Mineralization of ferritin-stabilized Pickering emulsions (perfluorooctane/buffer) with Ca/P/cit for (A) 5 days and (B) 24 days and solution exchanges after 5, 10 and 16 days. (C) Magnification and (D) cross-section of the mineral shell of the sample shown in (B).

The observations for the mineralization of bionanoparticle stabilized Pickering emulsions can be summarized as followed: High supersaturation led to the formation of few nuclei which were growing to rather large sizes. As they were depleting the mineralization solution quickly, no further nuclei were formed and compact shells were hardly obtained. This could be seen in the case of 1.5 SBF and 1.5 SBF/cit. Ca/P/cit contains a comparatively large amount of calcium ions which were masked by citrate. The supersaturation was low and nucleation occurred slowly and at many sites. The different density of nucleation sites was also seen for the mineralization of

bionanoparticle coated PDMS surfaces. The slow nucleation and a possibly changing supersaturation might have also been connected with the aging of the solution which was described in chapter 7.3. A dense assembly of HAP crystallites could be found at the interface of BSA- and fetuin-A-stabilized Pickering emulsions, some of them forming compact rigid shells. Ferritin-stabilized Pickering emulsions showed in all cases a very low tendency for HAP mineralization. This meant for Ca/P/cit a very slow but homogeneous growth of a mineral layer on the whole surface. Nucleation sites could not be discerned anymore. With subsequent exchanges of the mineralization solution, the shells were growing evenly in thickness and after four rounds of mineralization, a large number of rigid shell HAP spheres were obtained.

Considering the discussion above, we concluded that a combination of different mineralization steps might be the key to achieve compact shells in a fast mineralization procedure. First a homogeneous HAP layer must have been produced which could work as efficient nucleation site. Then, thick and compact shells could be produced in a second step if highly supersaturated solutions would be used. This is shown in Fig. 72, where ferritin stabilized perfluorooctane/buffer Pickering emulsions were first treated with Ca/P/cit and in following steps with 1.5 SBF/cit. During the first step obviously a scaffold was built which surface served as efficient nucleation site. During the next two rounds of treatment with 1.5 SBF/cit, a rigid mineral shell was forming. HAP crystallites nucleated efficiently at the interface and a compact and thick shell was formed. It should be remembered, that treatment of ferritin-stabilized Pickering emulsions with 1.5 SBF/cit alone did not lead to any mineralization of the interface. Fig. 72 shows droplets, magnifications of the surface and a cross-section. The thickness of the mineral layer here - after three mineralization steps - was approximately four times thicker (~ 800 nm) than for Ca/P/cit mineralization with four solution exchanges (compare Fig. 72, D with Fig. 71, D).

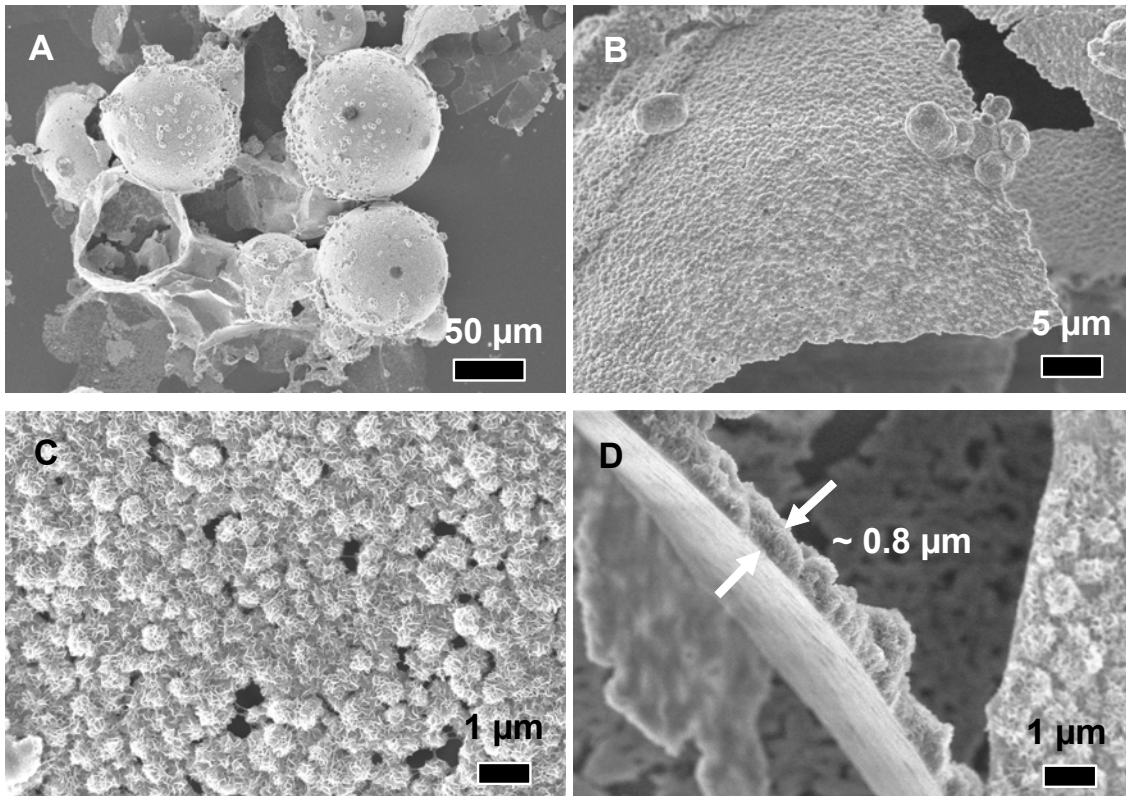


Fig. 72 Mineralization of ferritin stabilized Pickering emulsions (perfluorooctane/buffer) with Ca/P/cit and 1.5 SBF/cit. (B), (C) Magnifications of the mineral shell surface; (D) crosssection of the mineral shell.

Detailed knowledge about the mineralization mechanisms at different interfaces and in different mineralization solutions allowed some rationality in the experimental design to produce capsules with different thickness and surface morphologies. It should be pointed out that despite the observed differences between the three model proteins that were used here, the underlying principle is quite general. Although proteins are excellent foaming agents, this property has hardly been used except in food technology. The experiments presented here are first steps to use proteins also for the production of novel microstructured inorganic materials or ceramics.⁵⁴⁰

8 Summary

Various aspects of mineralized, bionanoparticle-stabilized Pickering emulsions were investigated in this work. Proteins (HSA, BSA, fetuin-A), protein cages (ferritin) and plant viruses (CPMV, TYMV, TMV) were employed to produce functional nanopatterned surfaces and interfaces by means of Pickering emulsions which were employed in biomimetic hydroxy apatite mineralization to produce inorganic biocompatible surfaces and hollow mineral spheres. The work accounts for the emerging interest and significant technological implications of protein and particle stabilized emulsions as well as bio-inorganic nanostructured composite materials.

First, the bionanoparticles and their solutions were characterized with SEC, UV-Vis, SLS, DLS, TEM and SDS-PAGE. Solutions of BSA, fetuin-A and ferritin contained aggregates and had to be fractionated with SEC for the following studies. Structural characterization of the viruses was accomplished by TEM with negative staining. Further, CPMV was labelled with fluorescein and tetramethylrhodamine. The preparation of CPMV-solutions from frozen leaves of cowpea plants is shortly described, too.

Next, kinetic investigations of the adsorption process of the bionanoparticles at the decane/buffer solution interface were performed with pendant drop tensiometry. Interfacial pressure isotherms were recorded for BSA, HSA, fetuin-A, ferritin, CPMV and TYMV. A detailed explanation of the previously developed model of variable surface states of adsorbed proteins and various aspects of protein adsorption experiments were necessary as basis for the discussion and the modelling of the isotherms and the dynamic surface tension. The surface pressure isotherms of BSA and ferritin as well as the dynamic surface tension of BSA could be modelled successfully and were in excellent agreement with previous reports.

Further, oil-in-water Pickering emulsions with perfluorooctane or an UV-crosslinkable PDMS precursor oil were prepared. The liquid-liquid interface could be imaged by confocal laser scanning fluorescence microscopy while the solid interfaces could be accessed with SEM and AFM. The bionanoparticles at the interface formed a dense assembly but the pattern did not show any long-range order. Interestingly, the rods of TMV formed no liquid-crystalline array but an irregular, sparse assembly at the

interface. Height determinations of the adsorbed virus with AFM and TEM of cross-sections from embedded interfaces showed that TMV was not significantly immersed into the oil phase. The adsorption of BSA and ferritin could be further proven by fluorescence microscopy of solid Pickering emulsions that have reacted with fluorescently labelled antibodies.

Finally, mineralization with hydroxy apatite (HAP) was conducted with various solutions under different conditions. The use of a simulated body fluid (SBF) allowed a biomimetic mineralization. A pre-incubation step on bioactive glass particles was necessary to induce HAP growth with SBF at physiological concentrations. Further, 1.5-fold concentrated SBF solution (1.5 SBF/cit) and an oversaturated calcium phosphate solution (Ca/P/cit), both containing citrate, were employed. The development of hydroxy apatite coatings on PET as model substrate was followed with time. PDMS-surfaces with immobilized proteins were used to mimic bio-related interfaces. Extensive structural and compositional characterization was performed with SEM and EDX. The induction and growth of hydroxy apatite was discussed and compared in detail for surfaces with different immobilized bionanoparticles and for different mineralization conditions. Dense coatings were achieved with SBF and Ca/P/cit. Surfaces prepared with ferritin and SDS yielded generally the smoothest and most compact HAP layers. Finally, true bionanoparticle Pickering emulsions (i.e. liquid-liquid interfaces) were used to produce mineral capsule shells. The development of the interfacial mineralization was investigated after various incubation times and exchanges of the mineralization solutions. The observed surface morphologies were explained by different mechanisms of nuclei formation and HAP growth. Particularly, the use of 1.5 SBF/cit or Ca/P/cit led to a dense pattern of single separated nuclei at the interface which tended to grow together to form compact shells. Ferritin-based Pickering emulsions were usually mineralized more weakly than BSA- and fetuin-A-based ones. In the case of Ca/P/cit, the slow mineralization of ferritin-coated oil droplets led to a controlled and very homogeneous formation of thin HAP composite shells. The combination of different mineralization mechanisms allowed the preparation of capsules with various controlled shell thicknesses and surface morphologies. Finally, the work contributes to the basic understanding of protein adsorption at liquid-liquid interfaces and their interfacial structures and shows new ways for the production of composite biomaterials through interfacial templating.

9 Zusammenfassung

In der vorliegenden Arbeit wurden verschiedene Aspekte von mineralisierten, Bionanopartikel-stabilisierten Pickering-Emulsionen untersucht. HSA, BSA, Fetuin-A, Ferritin und Pflanzenviren (CPMV, TYMV und TMV) wurden verwendet, um nanostrukturierte funktionale Ober- und Grenzflächen in Form von Pickering-Emulsionen zu erzeugen. Aus diesen wurden biokompatible, anorganische Oberflächen und Hohlkugeln durch Mineralisierung mit Hydroxyapatit hergestellt. Die Arbeit entstand aus dem Interesse und großen technologischen Relevanz von Protein- und Partikel-stabilisierten Emulsionen und nanostrukturierten Komposit-Materialien.

Die Bionanopartikel und -lösungen wurden mit SEC, UV-Vis, SLS, DLS und SDS-PAGE untersucht. Die Lösungen von BSA, Fetuin-A und Ferritin enthielten aggregierte Teilchen, die für die weiteren Studien mittels SEC abgetrennt wurden. Die Pflanzenviren wurden mittels TEM und negativer Kontrastierung charakterisiert. Weiter wurde CPMV mit Farbstoffen funktionalisiert. Die Isolierung von CPMV aus gefrorenen Blättern von Augenbohnen-Pflanzen wurde ebenfalls beschrieben.

Die Kinetik des Adsorptionsprozesses der Bionanopartikel an die Grenzfläche von Dekan/Puffer wurde mit der Methode des hängenden Tropfens untersucht. Die Isothermen des Grenzflächendruckes wurden für BSA, HSA, Fetuin-A, Ferritin, CPMV und TYMV aufgezeichnet. Das kürzlich entwickelte Model mit veränderlichen Grenzflächenzuständen adsorbierter Proteine und weiterer Aspekte von Protein-Adsorptionsexperimenten wurden detailliert erläutert, um die Adsorptionsexperimente und deren Modellierung kritisch diskutieren zu können. Die Grenzflächenspannungsisothermen von BSA und Ferritin sowie die dynamische Grenzflächenspannung von BSA konnten erfolgreich modelliert werden.

Öl-in-Wasser-Pickering-Emulsionen wurden mit Perfluoroktan oder einem UV-vernetzbaaren PDMS-Öl hergestellt. Die flüssigen Öltröpfchen konnten mittels konfokaler Fluoreszenzmikroskopie abgebildet werden, während die vernetzten, festen PDMS-Tröpfchen mittels REM und AFM untersucht wurden. Die Bionanopartikel an der Grenzfläche bildeten eine dichte Anordnung ohne langreichweitige Ordnung. TMV bedeckte die Grenzfläche in einer dünnen und regellosen Anordnung. Die Messung der Höhe von adsorbierten Viren mittels AFM und TEM von Querschnitten eingebetteter Grenzflächen zeigte, dass TMV nicht in die Ölphase eingetaucht war. Die Adsorption von BSA und Ferritin konnte weiterhin durch Fluoreszenzmikroskopie von Pickering-

Emulsionen gezeigt werden, die mit fluoreszierenden Antikörpern markiert worden waren.

Schließlich wurden Mineralisierungsreaktionen mit Hydroxyapatit in verschiedenen Lösungen und unter verschiedenen Bedingungen durchgeführt. In SBF mit physiologischen Konzentrationen konnte eine biomimetische Mineralisierung erreicht werden, wenn das Substrat zuvor auf bioaktiven Glassteilchen inkubiert wurde. Des Weiteren wurde SBF mit der 1.5-fachen Konzentration (1.5 SBF/cit) und eine übersättigte Calciumphosphat-Lösung (Ca/P/cit) eingesetzt. Die Beschichtung von PET mit Hydroxyapatit wurde zu verschiedenen Zeiten untersucht. PDMS-Oberflächen mit adsorbierten Bionanopartikeln wurden benutzt, um biologisch relevante Oberflächen zu imitieren. Die Charakterisierung der Schichten wurde mit SEM und EDX durchgeführt. Die Induktion und das Wachstum der HAP-Schichten auf den verschiedenen Oberflächen und unter verschiedenen Mineralisierungsbedingungen wurden ausführlich beschrieben und verglichen. In SBF und Ca/P/cit konnten dichte HAP-Schichten erhalten werden. Oberflächen, die mit Ferritin und SDS hergestellt wurden, ergaben meist die glättesten und kompaktesten Schichten. Schließlich wurden tatsächliche Pickering-Emulsionen, d. h. Grenzflächen zwischen Flüssig-Flüssig-Phasen, verwendet, um mineralisierte Kapseln herzustellen. Das Fortschreiten der Mineralisierung an der Grenzfläche wurde nach verschiedenen Inkubationszeiten und Austausch der Mineralisierungslösungen untersucht. Die Oberflächen-Morphologien wurden durch unterschiedliche Mechanismen der Keimbildung und Wachstum der HAP-Schicht erklärt. 1.5 SBF/cit und Ca/P/cit ergaben dichte Anordnungen von einzelnen Keimen an der Grenzfläche, die fortschreitend zu kompakten Schalen zusammenwachsen. Pickering-Emulsionen, die mit Ferritin hergestellt worden waren, wurden meist schwächer mineralisiert als solche, die mit BSA oder Fetuin-A hergestellt wurden. Im Fall von Ca/P/cit führte die langsame Mineralisierung der Ferritin-bedeckten Öltröpfchen zu einem kontrollierten Wachstum einer sehr homogenen HAP-Schicht. Durch die geschickte Kombination von verschiedenen Mineralisierungslösungen bzw. -mechanismen konnte die Bildung von Kapseln mit unterschiedlichen Dicken und Oberflächenmorphologien erzielt werden.

Die Arbeit trägt zum grundlegenden Verständnis der Proteinadsorption an Flüssig-Flüssig-Grenzflächen und deren Struktur bei und zeigt neue Wege zur Herstellung von Komposit-Biomaterialien durch Grenzflächentemplate auf.

References

1. Stöcker, *Taschenbuch der Physik*. Harri Deutsch: Frankfurt am Main, 1998.
2. Binnig, G.; Rohrer, H.; Gerber, C.; Weibel, E. *Applied Physics Letters* **1982**, 40, (2), 178-80.
3. Binnig, G.; Quate, C. F.; Gerber, C. *Physical Review Letters* **1986**, 56, (9), 930-934.
4. Brust, M.; Fink, J.; Bethell, D.; Schiffrin, D. J.; Kiely, C. *Journal of the Chemical Society, Chemical Communications* **1995**, (16), 1655-6.
5. Frens, G. *Nature* **1973**, 241, (105), 20-2.
6. Murray, C. B.; Norris, D. J.; Bawendi, M. G. *Journal of the American Chemical Society* **1993**, 115, (19), 8706-15.
7. Gates, B. D.; Xu, Q.; Stewart, M.; Ryan, D.; Willson, C. G.; Whitesides, G. M. *Chemical Reviews* **2005**, 105, (4), 1171-1196.
8. IBM Research demonstrates path for extending current chip-making technique. http://domino.research.ibm.com/comm/pr.nsf/pages/news.20060220_nemoreleas.html (21.04.2008)
9. Willner, I.; Katz, E., *Bioelectronics*. Wiley-VCH: Weinheim, 2005.
10. Niemeyer, C. M. *Angewandte Chemie, International Edition* **2001**, 40, (22), 4128-4158.
11. Niemeyer, C. M.; Mirkin, C. A., *Nanobiotechnology. Concepts, Applications and Perspectives*. Wiley-VCH: Weinheim, 2004.
12. Niemeyer, C. M.; Mirkin, C. A., *Nanobiotechnology. More Concepts and Applications*. Wiley-VCH: Weinheim, 2007.
13. Steinmetz, N. F.; Evans, D. J. *Organic & Biomolecular Chemistry* **2007**, 5, (18), 2891-2902.
14. Uchida, M.; Klem, M. T.; Allen, M.; Suci, P.; Flenniken, M.; Gillitzer, E.; Varpness, Z.; Liepold, L. O.; Young, M.; Douglas, T. *Advanced Materials* **2007**, 19, (8), 1025-1042.
15. Padilla, J. E.; Yu, T., Self-assembling Symmetric Protein Materials. In *Polyamides and Complex Proteinaceous Materials I*, Fahnstock, S. R.; Steinbüchel, A., Eds. Wiley-VCH: Weinheim, 2003; Vol. 8, pp 261-284.
16. Franklin, R. E. *Nature* **1955**, 175, 379-81.
17. Crick, F. H. C.; Watson, J. D. *Nature* **1956**, 177, 473-5.
18. Reddy, V. S.; Natarajan, P.; Okerberg, B.; Li, K.; Damodaran, K. V.; Morton, R. T.; Brooks, C. L., III; Johnson, J. E. *Journal of Virology* **2001**, 75, (24), 11943-11947.
19. Johnson, J. E.; Speir, J. A. *Journal of Molecular Biology* **1997**, 269, (5), 665-675.
20. Rux, J. J.; Burnett, R. M. *Current Opinion in Structural Biology* **1998**, 8, (2), 142-149.
21. Ghadiri, M. R.; Granja, J. R.; Milligan, R. A.; McRee, D. E.; Khazanovich, N. *Nature* **1993**, 366, (6453), 324-7.
22. Pandya, M. J.; Spooner, G. M.; Sunde, M.; Thorpe, J. R.; Rodger, A.; Woolfson, D. N. *Biochemistry* **2000**, 39, (30), 8728-8734.

23. Padilla, J. E.; Colovos, C.; Yeates, T. O. *Proceedings of the National Academy of Sciences of the United States of America* **2001**, *98*, (5), 2217-2221.
24. Sleytr, U. B.; Sara, M.; Pum, D.; Schuster, B.; Messner, P.; Schäffer, C., Self-Assembly Protein Systems: Microbial S-layers. In *Polyamides and Complex Proteinaceous Materials I*, Fahnstock, S. R.; Steinbüchel, A., Eds. Wiley-VCH: Weinheim, 2003; Vol. 8, pp 285-338.
25. Lee, S.-W.; Mao, C.; Flynn, C. E.; Belcher, A. M. *Science* **2002**, *296*, (5569), 892-895.
26. Tam, J. P.; Lu, Y. A. *Proceedings of the National Academy of Sciences of the United States of America* **1989**, *86*, (23), 9084-8.
27. Tam, J. P.; Profy, A. T. Multiple antigen peptide systems (MAPS) for use as HIV vaccines. WO9303766, 1993.
28. Sadler, K.; Tam, J. P. *Reviews in Molecular Biotechnology* **2002**, *90*, (3-4), 195-229.
29. Tam, J. P.; Lu, Y.-A.; Yang, J.-L. *European Journal of Biochemistry* **2002**, *269*, (3), 923-932.
30. Benito, A.; Mateu, M. G.; Villaverde, A. *Nature Biotechnology* **1995**, *13*, (8), 801-804.
31. Lomonosoff, G. P.; Johnson, J. E. *Current Opinion in Structural Biology* **1996**, *6*, (2), 176-82.
32. Ludwig, C.; Wagner, R. *Current Opinion in Biotechnology* **2007**, *18*, (6), 537-545.
33. Noad, R.; Roy, P. *Trends in Microbiology* **2003**, *11*, (9), 438-444.
34. Colosimo, A.; Goncz, K. K.; Holmes, A. R.; Kunzelmann, K.; Novelli, G.; Malone, R. W.; Bennett, M. J.; Gruenert, D. C. *BioTechniques* **2000**, *29*, (2), 314-316, 318, 320, 321-322, 324, 326-331.
35. Pfeifer, A.; Verma, I. M. *Annual Review of Genomics and Human Genetics* **2001**, *2*, 177-211.
36. Lomonosoff, G. P.; Hamilton, W. D. O. *Current Topics in Microbiology and Immunology* **1999**, *240*, 177-189.
37. Porta, C.; Spall, V. E.; Lin, T.; Johnson, J. E.; Lomonosoff, G. P. *Intervirology* **1996**, *39*, (1-2), 79-84.
38. Lin, T.; Porta, C.; Lomonosoff, G.; Johnson, J. E. *Folding & Design* **1996**, *1*, (3), 179-187.
39. Smith, G. P. *Science* **1985**, *228*, (4705), 1315-7.
40. O'Neil, K. T.; Hoess, R. H. *Current opinion in structural biology* **1995**, *5*, (4), 443-449.
41. Mersich, C.; Jungbauer, A. *Journal of Chromatography, B: Analytical Technologies in the Biomedical and Life Sciences* **2008**, *861*, (2), 160-170.
42. Sergeeva, A.; Kolonin, M. G.; Mollrem, J. J.; Pasqualini, R.; Arap, W. *Advanced Drug Delivery Reviews* **2006**, *58*, (15), 1622-1654.
43. Pinilla, C.; Martin, R.; Gran, B.; Appel, J. R.; Boggiano, C.; Wilson, D. B.; Houghten, R. A. *Current Opinion in Immunology* **1999**, *11*, (2), 193-202.
44. Sen Gupta, S.; Kuzelka, J.; Singh, P.; Lewis, W. G.; Manchester, M.; Finn, M. G. *Bioconjugate Chemistry* **2005**, *16*, (6), 1572-1579.
45. Barnhill, H. N.; Reuther, R.; Ferguson, P. L.; Dreher, T.; Wang, Q. *Bioconjugate Chemistry* **2007**, *18*, (3), 852-859. Ref. in there.
46. Raja, K. S.; Wang, Q.; Finn, M. G. *ChemBioChem* **2003**, *4*, (12), 1348-1351.

47. Wang, Q.; Lin, T.; Tang, L.; Johnson, J. E.; Finn, M. G. *Angewandte Chemie, International Edition* **2002**, 41, (3), 459-462.
48. Wang, Q.; Kaltgrad, E.; Lin, T.; Johnson, J. E.; Finn, M. G. *Chemistry & Biology* **2002**, 9, (7), 805-811.
49. Wang, Q.; Lin, T.; Johnson, J. E.; Finn, M. G. *Chemistry & Biology* **2002**, 9, (7), 813-819.
50. Steinmetz, N. F.; Lomonosoff, G. P.; Evans, D. J. *Langmuir* **2006**, 22, (8), 3488-3490.
51. Blum, A. S.; Soto, C. M.; Wilson, C. D.; Cole, J. D.; Kim, M.; Gnade, B.; Chatterji, A.; Ochoa, W. F.; Lin, T.; Johnson, J. E.; Ratna, B. R. *Nano Letters* **2004**, 4, (5), 867-870.
52. Chatterji, A.; Ochoa, W. F.; Paine, M.; Ratna, B. R.; Johnson, J. E.; Lin, T. *Chemistry & Biology* **2004**, 11, (6), 855-863.
53. Wang, Q.; Raja, K. S.; Janda, K. D.; Lin, T.; Finn, M. G. *Bioconjugate Chemistry* **2003**, 14, (1), 38-43.
54. Meunier, S.; Strable, E.; Finn, M. G. *Chem Biol* **2004**, 11, (3), 319-26.
55. Soto, C. M.; Blum, A. S.; Wilson, C. D.; Lazorcik, J.; Kim, M.; Gnade, B.; Ratna, B. R. *Electrophoresis* **2004**, 25, (17), 2901-2906.
56. Blum, A. S.; Soto, C. M.; Wilson, C. D.; Brower, T. L.; Pollack, S. K.; Schull, T. L.; Chatterji, A.; Lin, T.; Johnson, J. E.; Amsinck, C.; Franzon, P.; Shashidhar, R.; Ratna, B. R. *Small* **2005**, 1, (7), 702-706.
57. Hermanson, G. T., *Bioconjugate Techniques*. Academic Press: San Diego, 1996.
58. Raja, K. S.; Wang, Q.; Gonzalez, M. J.; Manchester, M.; Johnson, J. E.; Finn, M. G. *Biomacromolecules* **2003**, 4, (3), 472-476.
59. Blum, A. S.; Soto, C. M.; Wilson, C. D.; Whitley, J. L.; Moore, M. H.; Sapsford, K. E.; Lin, T.; Chatterji, A.; Johnson, J. E.; Ratna, B. R. *Nanotechnology* **2006**, 17, (20), 5073-5079.
60. Medintz, I. L.; Sapsford, K. E.; Konnert, J. H.; Chatterji, A.; Lin, T.; Johnson, J. E.; Mattoussi, H. *Langmuir* **2005**, 21, (12), 5501-5510.
61. Strable, E.; Johnson, J. E.; Finn, M. G. *Nano Letters* **2004**, 4, (8), 1385-1389.
62. Chatterji, A.; Ochoa, W.; Shamieh, L.; Salakian, S. P.; Wong, S. M.; Clinton, G.; Ghosh, P.; Lin, T.; Johnson, J. E. *Bioconjugate Chemistry* **2004**, 15, (4), 807-813.
63. Rostovtsev, V. V.; Green, L. G.; Fokin, V. V.; Sharpless, K. B. *Angewandte Chemie, International Edition* **2002**, 41, (14), 2596-2599.
64. Sen Gupta, S.; Raja, K. S.; Kaltgrad, E.; Strable, E.; Finn, M. G. *Chemical Communications* **2005**, (34), 4315-4317.
65. Barnhill, H. N.; Reuther, R.; Ferguson, P. L.; Dreher, T.; Wang, Q. *Bioconjugate Chemistry* **2007**, 18, (3), 852-859.
66. Danon, D.; Goldstein, L.; Marikovsky, Y.; Skutelsky, E. *Journal of Ultrastructure Research* **1972**, 38, (5-6), 500-10.
67. Wong, K. K. W.; Colfen, H.; Whilton, N. T.; Douglas, T.; Mann, S. *Journal of Inorganic Biochemistry* **1999**, 76, (3-4), 187-195.
68. Wong, K. K. W.; Whilton, N. T.; Douglas, T.; Mann, S.; Colfen, H. *Chemical Communications* **1998**, (16), 1621-1622.
69. Zeng, Q.; Li, T.; Cash, B.; Li, S.; Xie, F.; Wang, Q. *Chemical Communications* **2007**, (14), 1453-1455.
70. Wetz, K.; Crichton, R. R. *European Journal of Biochemistry* **1976**, 61, (2), 545-50.

71. Lawson, D. M.; Artymiuk, P. J.; Yewdall, S. J.; Smith, J. M. A.; Livingstone, J. C.; Treffry, A.; Luzzago, A.; Levi, S.; Arosio, P.; et al. *Nature* **1991**, 349, (6309), 541-4.
72. Mann, S.; Meldrum, F. *Advanced Materials* **1991**, 3, (6), 316-318.
73. Douglas, T.; Stark, V. T. *Inorganic Chemistry* **2000**, 39, (8), 1828-1830.
74. Douglas, T.; Dickson, D. P. E.; Betteridge, S.; Charnock, J.; Garner, C. D.; Mann, S. *Science* **1995**, 269, (5220), 54-7.
75. Douglas, T.; Strable, E.; Willits, D.; Aitouchen, A.; Libera, M.; Young, M. *Advanced Materials* **2002**, 14, (6), 415-418.
76. Douglas, T.; Young, M. *Nature* **1998**, 393, (6681), 152-155.
77. Douglas, T.; Young, M. *Advanced Materials* **1999**, 11, (8), 679-681.
78. Meldrum, F. C.; Douglas, T.; Levi, S.; Arosio, P.; Mann, S. *Journal of Inorganic Biochemistry* **1995**, 58, (1), 59-68.
79. Mackle, P.; Charnock, J. M.; Garner, C. D.; Meldrum, F. C.; Mann, S. *Journal of the American Chemical Society* **1993**, 115, (18), 8471-2.
80. Wong, K. K. W.; Mann, S. *Advanced Materials* **1996**, 8, (11), 928-932.
81. Aime, S.; Frullano, L.; Geninatti Crich, S. *Angewandte Chemie, International Edition* **2002**, 41, (6), 1017-1019.
82. Kim, I.; Hosein, H.-A.; Strongin, D. R.; Douglas, T. *Chemistry of Materials* **2002**, 14, (11), 4874-4879.
83. Flynn, C. E.; Lee, S.-W.; Peelle, B. R.; Belcher, A. M. *Acta Materialia* **2003**, 51, (19), 5867-5880.
84. Chen, C.; Daniel, M.-C.; Quinkert, Z. T.; De, M.; Stein, B.; Bowman, V. D.; Chipman, P. R.; Rotello, V. M.; Kao, C. C.; Dragnea, B. *Nano Letters* **2006**, 6, (4), 611-615.
85. Kagawa, H. K.; Osipiuk, J.; Maltsev, N.; Overbeek, R.; Quaiter-Randall, E.; Joachimiak, A.; Trent, J. D. *Journal of Molecular Biology* **1995**, 253, (5), 712-25.
86. Koeck, P. J. B.; Kagawa, H. K.; Ellis, M. J.; Hebert, H.; Trent, J. D. *Biochimica et Biophysica Acta, Protein Structure and Molecular Enzymology* **1998**, 1429, (1), 40-44.
87. Trent, J. D. *FEMS Microbiology Reviews* **1996**, 18, (2-3), 249-258.
88. Knez, M.; Kadri, A.; Wege, C.; Goesele, U.; Jeske, H.; Nielsch, K. *Nano Letters* **2006**, 6, (6), 1172-1177.
89. Shenton, W.; Douglas, T.; Young, M.; Stubbs, G.; Mann, S. *Advanced Materials* **1999**, 11, (3), 253-256.
90. Royston, E.; Lee, S.-Y.; Culver, J. N.; Harris, M. T. *Journal of Colloid and Interface Science* **2006**, 298, (2), 706-712.
91. Fonoberov, V. A.; Balandin, A. A. *Nano Letters* **2005**, 5, (10), 1920-1923.
92. Fowler, C. E.; Shenton, W.; Stubbs, G.; Mann, S. *Advanced Materials* **2001**, 13, (16), 1266-1269.
93. Kuncicky, D. M.; Naik, R. R.; Velez, O. D. *Small* **2006**, 2, (12), 1462-1466.
94. Dujardin, E.; Peet, C.; Stubbs, G.; Culver, J. N.; Mann, S. *Nano Letters* **2003**, 3, (3), 413-417.
95. Knez, M.; Bittner, A. M.; Boes, F.; Wege, C.; Jeske, H.; Mai, E.; Kern, K. *Nano Letters* **2003**, 3, (8), 1079-1082.
96. Knez, M.; Sumser, M.; Bittner, A. M.; Wege, C.; Jeske, H.; Martin, T. P.; Kern, K. *Advanced Functional Materials* **2004**, 14, (2), 116-124.

97. Niu, Z.; Bruckman, M. A.; Li, S.; Lee, L. A.; Lee, B.; Pingali, S. V.; Thiyagarajan, P.; Wang, Q. *Langmuir* **2007**, *23*, (12), 6719-6724.
98. Bruckman, M. A.; Niu, Z.; Li, S.; Lee, L. A.; Varazo, K.; Nelson, T. L.; Lavigne, J. J.; Wang, Q. *NanoBiotechnology* **2007**, *3*, (1), 31-39.
99. Niu, Z.; Liu, J.; Lee, L. A.; Bruckman, M. A.; Zhao, D.; Koley, G.; Wang, Q. *Nano Letters* **2007**, *7*, (12), 3729-3733.
100. Niu, Z.; Bruckman, M.; Kotakadi, V. S.; He, J.; Emrick, T.; Russell, T. P.; Yang, L.; Wang, Q. *Chemical Communications* **2006**, (28), 3019-3021.
101. Mao, C.; Solis, D. J.; Reiss, B. D.; Kottmann, S. T.; Sweeney, R. Y.; Hayhurst, A.; Georgiou, G.; Iverson, B.; Belcher, A. M. *Science* **2004**, *303*, (5655), 213-217.
102. Nam, K. T.; Kim, D.-W.; Yoo, P. J.; Chiang, C.-Y.; Meethong, N.; Hammond, P. T.; Chiang, Y.-M.; Belcher, A. M. *Science* **2006**, *312*, (5775), 885-888.
103. Richter, J. *Physica E* **2003**, *16*, (2), 157-173.
104. Braun, E.; Keren, K. *Advances in Physics* **2004**, *53*, (4), 441-496.
105. Braun, E.; Eichen, Y.; Sivan, U.; Ben-Yoseph, G. *Nature* **1998**, *391*, (6669), 775-8.
106. Keren, K.; Krueger, M.; Gilad, R.; Ben-Yoseph, G.; Sivan, U.; Braun, E. *Science* **2002**, *297*, (5578), 72-75.
107. Portney, N. G.; Singh, K.; Chaudhary, S.; Destito, G.; Schneemann, A.; Manchester, M.; Ozkan, M. *Langmuir* **2005**, *21*, (6), 2098-2103.
108. Radloff, C.; Vaia, R. A.; Brunton, J.; Bouwer, G. T.; Ward, V. K. *Nano Letters* **2005**, *5*, (6), 1187-1191.
109. Slocik, J. M.; Naik, R. R.; Stone, M. O.; Wright, D. W. *Journal of Materials Chemistry* **2005**, *15*, (7), 749-753.
110. Yoshimura, H.; Scheybani, T.; Baumeister, W.; Nagayama, K. *Langmuir* **1994**, *10*, (9), 3290-5.
111. Aoyama, K.; Ogawa, K.; Kimura, Y.; Fujiyoshi, Y. *Ultramicroscopy* **1995**, *57*, (4), 345-54.
112. Velev, O. D. *Advances in Biophysics* **1997**, *34*, (Protein Array: An Alternative Biomolecular System), 139-157.
113. Nagayama, K. *Advances in Biophysics* **1997**, *34*, (Protein Array: An Alternative Biomolecular System), 3-23.
114. Yoshimura, H. *Advances in Biophysics* **1997**, *34*, (Protein Array: An Alternative Biomolecular System), 93-107.
115. Yamashita, I. *Thin Solid Films* **2001**, *393*, (1,2), 12-18.
116. Kwon, M.; Choi, H.; Chang, M.; Jo, M.; Jung, S.-J.; Hwang, H. *Applied Physics Letters* **2007**, *90*, (19), 193512/1-193512/3.
117. Miura, A.; Uraoka, Y.; Fuyuki, T.; Kumagai, S.; Yoshii, S.; Matsukawa, N.; Yamashita, I. *Surface Science* **2007**, *601*, (15), L81-L85.
118. Yuan, Z.; Petsev, D. N.; Prevo, B. G.; Velev, O. D.; Atanassov, P. *Langmuir* **2007**, *23*, (10), 5498-5504.
119. Fang, J.; Soto, C. M.; Lin, T.; Johnson, J. E.; Ratna, B. *Langmuir* **2002**, *18*, (2), 308-310.
120. Suci, P. A.; Klem, M. T.; Douglas, T.; Young, M. *Langmuir* **2005**, *21*, (19), 8686-8693.
121. Knez, M.; Sumser, M. P.; Bittner, A. M.; Wege, C.; Jeske, H.; Hoffmann, D. M. P.; Kuhnke, K.; Kern, K. *Langmuir* **2004**, *20*, (2), 441-447.

122. Yoo, P. J.; Nam, K. T.; Qi, J.; Lee, S.-K.; Park, J.; Belcher, A. M.; Hammond, P. T. *Nature Materials* **2006**, 5, (3), 234-240.
123. Klem, M. T.; Willits, D.; Young, M.; Douglas, T. *Journal of the American Chemical Society* **2003**, 125, (36), 10806-10807.
124. Smith, J. C.; Lee, K.-B.; Wang, Q.; Finn, M. G.; Johnson, J. E.; Mrksich, M.; Mirkin, C. A. *Nano Letters* **2003**, 3, (7), 883-886.
125. Cheung, C. L.; Chung, S.-W.; Chatterji, A.; Lin, T.; Johnson, J. E.; Hok, S.; Perkins, J.; De Yoreo, J. J. *Journal of the American Chemical Society* **2006**, 128, (33), 10801-10807.
126. Holmes, T. C. *Trends in Biotechnology* **2002**, 20, (1), 16-21.
127. Hartgerink, J. D.; Beniash, E.; Stupp, S. I. *Science* **2001**, 294, (5547), 1684-1688.
128. Bossmann, S. H., S-Layer Proteins in Bioelectronic Applications. In *Bioelectronics*, Willner, I.; Katz, E., Eds. Wiley-VCH: Weinheim, 2005; pp 395-426.
129. Sleytr, U. B.; Sara, M.; Pum, D.; Schuster, B. *Progress in Surface Science* **2001**, 68, (7-8), 231-278.
130. Ariga, K.; Hill, J. P.; Endo, H. *International Journal of Molecular Sciences* **2007**, 8, (8), 864-883.
131. Binks, B. P. *Current Opinion in Colloid & Interface Science* **2002**, 7, (1,2), 21-41.
132. Möbius, D.; Miller, R., *Proteins at Liquid Interfaces*. Elsevier: Amsterdam, 1998; Vol. 7.
133. Ramsden, W. *Proceedings of the Royal Society of London, Series A: Mathematical, Physical and Engineering Sciences* **1903**, 72, 156-164.
134. Pickering, S. U. *Journal of the Chemical Society, Transactions* **1907**, 91, 2001-21.
135. Dickinson, E.; Leser, M. E., *Food Colloids: Self-Assembly and Material Science*. Royal Society of Chemistry: Cambridge, 2007.
136. Lu, S.; Pugh, R. J.; Forssberg, E., *Interfacial Separation of Particles*. Elsevier: Amsterdam, 2005; Vol. 20.
137. Dinsmore, A. D.; Hsu Ming, F.; Nikolaidis, M. G.; Marquez, M.; Bausch, A. R.; Weitz, D. A. *Science* **2002**, 298, (5595), 1006-9.
138. Binks, B. P.; Horozov, T. S., *Colloidal Particles at Liquid Interfaces*. Cambridge University Press: Cambridge, 2006.
139. Lin, Y.; Skaff, H.; Boker, A.; Dinsmore, A. D.; Emrick, T.; Russell, T. P. *Journal of the American Chemical Society* **2003**, 125, (42), 12690-12691.
140. Skaff, H.; Lin, Y.; Tangirala, R.; Breitenkamp, K.; Boker, A.; Russell, T. P.; Emrick, T. *Advanced Materials* **2005**, 17, (17), 2082-2086.
141. Lin, Y.; Skaff, H.; Emrick, T.; Dinsmore, A. D.; Russell, T. P. *Science* **2003**, 299, (5604), 226-229.
142. Kutuzov, S.; He, J.; Tangirala, R.; Emrick, T.; Russell, T. P.; Boeker, A. *Physical Chemistry Chemical Physics* **2007**, 9, (48), 6351-6358.
143. Wang, D.; Duan, H.; Moehwald, H. *Soft Matter* **2005**, 1, (6), 412-416.
144. Arditty, S.; Schmitt, V.; Giermanska-Kahn, J.; Leal-Calderon, F. *Journal of Colloid and Interface Science* **2004**, 275, (2), 659-664.
145. Giermanska-Kahn, J.; Laine, V.; Arditty, S.; Schmitt, V.; Leal-Calderon, F. *Langmuir* **2005**, 21, (10), 4316-4323.

146. Cayre, O. J.; Noble, P. F.; Paunov, V. N. *Journal of Materials Chemistry* **2004**, 14, (22), 3351-3355.
147. Ashby, N. P.; Binks, B. P.; Paunov, V. N. *Physical Chemistry Chemical Physics* **2004**, 6, (17), 4223-4225.
148. Ashby, N. P.; Binks, B. P.; Paunov, V. N. *Chemical Communications* **2004**, (4), 436-437.
149. Duan, H.; Wang, D.; Kurth, D. G.; Moehwald, H. *Angewandte Chemie, International Edition* **2004**, 43, (42), 5639-5642.
150. Glogowski, E.; He, J.; Russell, T. P.; Emrick, T. *Chemical Communications* **2005**, (32), 4050-4052.
151. Glogowski, E.; Tangirala, R.; He, J.; Russell, T. P.; Emrick, T. *Nano Letters* **2007**, 7, (2), 389-393.
152. Alargova, R. G.; Warhadpande, D. S.; Paunov, V. N.; Velev, O. D. *Langmuir* **2004**, 20, (24), 10371-10374.
153. Noble, P. F.; Cayre, O. J.; Alargova, R. G.; Velev, O. D.; Paunov, V. N. *Journal of the American Chemical Society* **2004**, 126, (26), 8092-8093.
154. Hobbie, E. K.; Bauer, B. J.; Stephens, J.; Becker, M. L.; McGuiggan, P.; Hudson, S. D.; Wang, H. *Langmuir* **2005**, 21, (23), 10284-10287.
155. Fujii, S.; Okada, M.; Furuzono, T. *Journal of Colloid and Interface Science* **2007**, 315, (1), 287-296.
156. Ashby, N. P.; Binks, B. P. *Physical Chemistry Chemical Physics* **2000**, 2, (24), 5640-5646.
157. Binks, B. P.; Clint, J. H.; Mackenzie, G.; Simcock, C.; Whitby, C. P. *Langmuir* **2005**, 21, (18), 8161-8167.
158. Paunov, V. N.; Cayre, O. J.; Noble, P. F.; Stoyanov, S. D.; Velikov, K. P.; Golding, M. *Journal of Colloid and Interface Science* **2007**, 312, (2), 381-389.
159. Schmid, A.; Fujii, S.; Armes, S. P. *Langmuir* **2005**, 21, (18), 8103-8105.
160. Amalvy, J. I.; Armes, S. P.; Binks, B. P.; Rodrigues, J. A.; Unali, G. F. *Chemical Communications* **2003**, (15), 1826-1827.
161. Amalvy, J. I.; Unali, G. F.; Li, Y.; Granger-Bevan, S.; Armes, S. P.; Binks, B. P.; Rodrigues, J. A.; Whitby, C. P. *Langmuir* **2004**, 20, (11), 4345-4354.
162. Read, E. S.; Fujii, S.; Amalvy, J. I.; Randall, D. P.; Armes, S. P. *Langmuir* **2004**, 20, (18), 7422-7429.
163. Fujii, S.; Armes, S. P.; Binks, B. P.; Murakami, R. *Langmuir* **2006**, 22, (16), 6818-6825.
164. Fujii, S.; Read, E. S.; Binks, B. P.; Armes, S. P. *Advanced Materials* **2005**, 17, (8), 1014-1018.
165. Amirfazli, A.; Neumann, A. W. *Advances in Colloid and Interface Science* **2004**, 110, (3), 121-141.
166. Cayre, O.; Paunov, V. N.; Velev, O. D. *Journal of Materials Chemistry* **2003**, 13, (10), 2445-2450.
167. Cayre, O. J.; Paunov, V. N. *Langmuir* **2004**, 20, (22), 9594-9599.
168. Cayre, O. J.; Paunov, V. N. *Journal of Materials Chemistry* **2004**, 14, (22), 3300-3302.
169. Paunov, V. N.; Cayre, O. J. *Advanced Materials* **2004**, 16, (9-10), 788-791.
170. Benkoski, J. J.; Hu, H.; Karim, A. *Macromolecular Rapid Communications* **2006**, 27, (15), 1212-1216.
171. Benkoski, J. J.; Jones, R. L.; Douglas, J. F.; Karim, A. *Langmuir* **2007**, 23, (7), 3530-3537.

172. Tarimala, S.; Dai, L. L. *Langmuir* **2004**, *20*, (9), 3492-3494.
173. Tarimala, S.; Ranabothu, S. R.; Verneti, J. P.; Dai, L. L. *Langmuir* **2004**, *20*, (13), 5171-5173.
174. Tarimala, S.; Wu, C.-y.; Dai, L. L. *Langmuir* **2006**, *22*, (18), 7458-7461.
175. Wu, C.-y.; Tarimala, S.; Dai, L. L. *Langmuir* **2006**, *22*, (5), 2112-2116.
176. Boeker, A.; He, J.; Emrick, T.; Russell, T. P. *Soft Matter* **2007**, *3*, (10), 1231-1248.
177. Glogowski, E.; Tangirala, R.; Russell, T. P.; Emrick, T. *Journal of Polymer Science, Part A: Polymer Chemistry* **2006**, *44*, (17), 5076-5086.
178. Lin, Y.; Boeker, A.; He, J.; Sill, K.; Xiang, H.; Abetz, C.; Li, X.; Wang, J.; Emrick, T.; Long, S.; Wang, Q.; Balazs, A.; Russell, T. P. *Nature* **2005**, *434*, (7029), 55-59.
179. Böker, A.; Lin, Y.; Chiapperini, K.; Horowitz, R.; Thompson, M.; Carreon, V.; Xu, T.; Abetz, C.; Skaff, H.; Dinsmore, A. D.; Emrick, T.; Russell, T. P. *Nature Materials* **2004**, *3*, (5), 302-306.
180. Cheyne, R. B.; Moffitt, M. G. *Langmuir* **2005**, *21*, (23), 10297-10300.
181. Russell, J. T.; Lin, Y.; Boeker, A.; Su, L.; Carl, P.; Zettl, H.; He, J.; Sill, K.; Tangirala, R.; Emrick, T.; Littrell, K.; Thiyagarajan, P.; Cookson, D.; Fery, A.; Wang, Q.; Russell, T. P. *Angewandte Chemie, International Edition* **2005**, *44*, (16), 2420-2426.
182. Lu, G.; An, Z.; Tao, C.; Li, J. *Langmuir* **2004**, *20*, (19), 8401-8403.
183. Lu, G.; Chen, H.; Li, J. *Colloids and Surfaces, A: Physicochemical and Engineering Aspects* **2003**, *215*, (1-3), 25-32.
184. Faergemand, M.; Murray, B. S.; Dickinson, E.; Qvist, K. B. *International Dairy Journal* **1999**, *9*, (3/6), 343-346.
185. Berthold, A.; Schubert, H.; Brandes, N.; Kroh, L.; Miller, R. *Colloids and Surfaces, A: Physicochemical and Engineering Aspects* **2007**, *301*, (1-3), 16-22.
186. Szilvay, G. R.; Paananen, A.; Laurikainen, K.; Vuorimaa, E.; Lemmetyinen, H.; Peltonen, J.; Linder, M. B. *Biochemistry* **2007**, *46*, (9), 2345-2354.
187. Hermanson, K. D.; Harasim, M. B.; Scheibel, T.; Bausch, A. R. *Physical Chemistry Chemical Physics* **2007**, *9*, (48), 6442-6446.
188. Hermanson, K. D.; Huemmerich, D.; Scheibel, T.; Bausch, A. R. *Advanced Materials* **2007**, *19*, (14), 1810-1815.
189. Zhu, Y.; Tong, W.; Gao, C.; Moehwald, H. *Journal of Materials Chemistry* **2008**, *18*, (10), 1153-1158.
190. Fainerman, V. B.; Kovalchuk, V. I.; Lucassen-Reynders, E. H.; Grigoriev, D. O.; Ferri, J. K.; Leser, M. E.; Michel, M.; Miller, R.; Moehwald, H. *Langmuir* **2006**, *22*, (4), 1701-1705.
191. Miller, R.; Fainerman, V. B.; Kovalchuk, V. I.; Grigoriev, D. O.; Leser, M. E.; Michel, M. *Advances in Colloid and Interface Science* **2006**, *128-130*, 17-26.
192. Davies, J., Dynamic Contact Angle Analysis and Protein Adsorption. In *Surface Analytical Techniques for Probing Biomaterials Processes*, Davies, J., Ed. CRC Press: Boca Raton, 1996; pp 153-174.
193. Vaknin, D.; Kjaer, K.; Ringsdorf, H.; Blankenburg, R.; Piepenstock, M.; Diederich, A.; Loesche, M. *Langmuir* **1993**, *9*, (5), 1171-4.
194. Harzallah, B.; Aguié-Beghin, V.; Douillard, R.; Bosio, L. *International Journal of Biological Macromolecules* **1998**, *23*, (1), 73-84.
195. Eaglesham, A.; Herrington, T. M.; Penfold, J. *Colloids and Surfaces* **1992**, *65*, (1), 9-16.

196. Lu, J. R.; Su, T. J.; Thomas, R. K.; Penfold, J.; Webster, J. *Journal of the Chemical Society, Faraday Transactions* **1998**, 94, (21), 3279-3287.
197. Lu, J. R.; Su, T. J.; Penfold, J. *Langmuir* **1999**, 15, (20), 6975-6983.
198. Jackler, G.; Steitz, R.; Czeslik, C. *Langmuir* **2002**, 18, (17), 6565-6570.
199. Graham, D. E.; Phillips, M. C. *Journal of Colloid and Interface Science* **1979**, 70, (3), 415-26.
200. Davies, J.; Nunnerley, C. S., Ellipsometry and Protein Adsorption. In *Surface Analytical Techniques for Probing Biomaterials Processes*, Davies, J., Ed. CRC Press: Boca Raton, 1996; pp 131-151.
201. De Feijter, J. A.; Benjamins, J.; Veer, F. A. *Biopolymers* **1978**, 17, (7), 1759-72.
202. Grigoriev, D. O.; Fainerman, V. B.; Makievski, A. V.; Kraegel, J.; Wuestneck, R.; Miller, R. *Journal of Colloid and Interface Science* **2002**, 253, (2), 257-264.
203. Fainerman, V. B.; Lucassen-Reynders, E. H.; Miller, R. *Advances in Colloid and Interface Science* **2003**, 106, 237-259.
204. Miller, R.; Dutschk, V.; Fainerman, V. B. *Journal of Adhesion* **2004**, 80, (6), 549-561.
205. Graham, D. E.; Phillips, M. C. *Journal of Colloid and Interface Science* **1979**, 70, (3), 427-39.
206. Tripp, B. C.; Magda, J. J.; Andrade, J. D. *Journal of Colloid and Interface Science* **1995**, 173, (1), 16-27.
207. Krishnan, A.; Sturgeon, J.; Siedlecki, C. A.; Vogler, E. A. *Journal of Biomedical Materials Research, Part A* **2004**, 68A, (3), 544-557.
208. Beverung, C. J.; Radke, C. J.; Blanch, H. W. *Biophysical Chemistry* **1999**, 81, (1), 59-80.
209. Fainerman, V. B.; Miller, R.; Ferri, J. K.; Watzke, H.; Leser, M. E.; Michel, M. *Advances in Colloid and Interface Science* **2006**, 123-126, 163-171.
210. Miller, R.; Grigoriev, D. O.; Kraegel, J.; Makievski, A. V.; Maldonado-Valderrama, J.; Leser, M.; Michel, M.; Fainerman, V. B. *Food Hydrocolloids* **2005**, 19, (3), 479-483.
211. Maldonado-Valderrama, J.; Wege, H. A.; Rodriguez-Valverde, M. A.; Galvez-Ruiz, M. J.; Cabrerizo-Vilchez, M. A. *Langmuir* **2003**, 19, (20), 8436-8442.
212. Gonzalez, G.; MacRitchie, F. *Journal of Colloid and Interface Science* **1970**, 32, (1), 55-61.
213. MacRitchie, F., Reversibility of Protein Adsorption. In *Proteins at Liquid Interfaces*, Möbius, D.; Miller, R., Eds. Elsevier: Amsterdam, 1998; Vol. 7, pp 149-178.
214. Miller, R.; Aksenenko, E. V.; Kragel, J.; O'Neill, M.; Makievski, A. V.; Fainerman, V. B., Dynamics of Protein Adsorption Layers at Liquid Interfaces. In *Food Colloids, Biopolymers and Materials*, Dickinson, E.; Vliet, T. v., Eds. Royal Society of Chemistry: Cambridge, 2003; pp 207-215.
215. Adamczyk, Z. *Journal of Colloid and Interface Science* **2000**, 229, (2), 477-489.
216. Adamczyk, Z. *Surface and Colloid Science* **2004**, 17, 211-360.
217. Adamczyk, Z.; Siwek, B.; Weroni, P.; Zembala, M. *Progress in Colloid & Polymer Science* **1998**, 111, (Structure, Dynamics and Properties of Disperse Colloidal Systems), 41-47.
218. Miller, R.; Fainerman, V. B.; Aksenenko, E. V.; Leser, M. E.; Michel, M. *Langmuir* **2004**, 20, (3), 771-777.
219. Joos, P.; Serrien, G. *Journal of Colloid and Interface Science* **1991**, 145, (1), 291-4.

220. Joos, P. *Biochimica et Biophysica Acta, Biomembranes* **1975**, 375, (1), 1-9.
221. Fainerman, V. B.; Zholob, S. A.; Miller, R. *Langmuir* **1997**, 13, (2), 283-289.
222. Fainerman, V. B.; Miller, R.; Makievski, A. V. *Langmuir* **1995**, 11, (8), 3054-60.
223. Miller, R.; Fainerman, V. B.; Makievski, A. V.; Kragel, J.; Grigoriev, D. O.; Kazakov, V. N.; Sinyachenko, O. V. *Advances in Colloid and Interface Science* **2000**, 86, (1,2), 39-82.
224. Fainerman, V. B.; Lucassen-Reynders, E. H.; Miller, R. *Colloids and Surfaces, A: Physicochemical and Engineering Aspects* **1998**, 143, (2-3), 141-165.
225. Fainerman, V. B.; Miller, R.; Wuestneck, R. *Journal of Colloid and Interface Science* **1996**, 183, (1), 26-34.
226. Ward, A. F. H.; Tordai, L. *Journal of Chemical Physics* **1946**, 14, 453-61.
227. Maldonado-Valderrama, J.; Fainerman, V. B.; Aksenenko, E.; Galvez-Ruiz, M. J.; Cabrerizo-Vilchez, M. A.; Miller, R. *Colloids and Surfaces, A: Physicochemical and Engineering Aspects* **2005**, 261, (1-3), 85-92.
228. Alahverdijeva, V. S.; Grigoriev, D. O.; Fainerman, V. B.; Aksenenko, E. V.; Miller, R.; Moehwald, H. *Journal of Physical Chemistry B* **2008**, 112, (7), 2136-2143.
229. Makievski, A. V.; Fainerman, V. B.; Bree, M.; Wuestneck, R.; Kraegel, J.; Miller, R. *Journal of Physical Chemistry B* **1998**, 102, (2), 417-425.
230. Lucassen-Reynders, E. H.; Fainerman, V. B.; Miller, R. *Journal of Physical Chemistry B* **2004**, 108, (26), 9173-9176.
231. Miller, R.; Leser, M. E.; Michel, M.; Fainerman, V. B. *Journal of Physical Chemistry B* **2005**, 109, (27), 13327-13331.
232. Ma, P. X. *Advanced Drug Delivery Reviews* **2008**, 60, (2), 184-198.
233. Engel, E.; Michiardi, A.; Navarro, M.; Lacroix, D.; Planell, J. A. *Trends in Biotechnology* **2008**, 26, (1), 39-47.
234. Bäuerlein, E., *Handbook of Biomineralization. Biological Aspects and Structure Formation*. Wiley-VCH: Weinheim, 2007; Vol. 1.
235. Mann, D. G. *Phycologia* **1999**, 38, (6), 437-495.
236. Round, F. E.; Crawford, R. M.; Mann, D. G., *The Diatoms. Biology and Morphology of the Genera*. Cambridge University Press: Cambridge, 1990.
237. Kroger, N.; Deutzmann, R.; Bergsdorf, C.; Sumper, M. *Proceedings of the National Academy of Sciences of the United States of America* **2000**, 97, (26), 14133-14138.
238. Kroger, N.; Deutzmann, R.; Sumper, M. *Science* **1999**, 286, (5442), 1129-1132.
239. Cha, J. N.; Shimizu, K.; Zhou, Y.; Christiansen, S. C.; Chmelka, B. F.; Stucky, G. D.; Morse, D. E. *Proceedings of the National Academy of Sciences of the United States of America* **1999**, 96, (2), 361-365.
240. Shimizu, K.; Cha, J.; Stucky, G. D.; Morse, D. E. *Proceedings of the National Academy of Sciences of the United States of America* **1998**, 95, (11), 6234-8.
241. Brott, L. L.; Naik, R. R.; Pikas, D. J.; Kirkpatrick, S. M.; Tomlin, D. W.; Whitlock, P. W.; Clarson, S. J.; Stone, M. O. *Nature* **2001**, 413, (6853), 291-3.
242. Cha, J. N.; Stucky, G. D.; Morse, D. E.; Deming, T. J. *Nature* **2000**, 403, (6767), 289-292.
243. Coelfen, H.; Antonietti, M. *Angewandte Chemie, International Edition* **2005**, 44, (35), 5576-5591.
244. Coelfen, H.; Mann, S. *Angewandte Chemie, International Edition* **2003**, 42, (21), 2350-2365.

245. Smith, B. L.; Schaffer, T. E.; Viani, M.; Thompson, J. B.; Frederick, N. A.; Kind, J.; Belcher, A.; Stucky, G. D.; Mors, D. E.; Hansma, P. K. *Nature* **1999**, 399, (6738), 761-763.
246. Coelfen, H. *Topics in Current Chemistry* **2007**, 271, (Biom mineralization II), 1-77.
247. Addadi, L.; Weiner, S. *Nature* **1997**, 389, (6654), 912-913, 915.
248. Addadi, L.; Joester, D.; Nudelman, F.; Weiner, S. *Chemistry - A European Journal* **2006**, 12, (4), 980-987.
249. Oaki, Y.; Imai, H. *Angewandte Chemie, International Edition* **2005**, 44, (40), 6571-6575.
250. Imai, H.; Oaki, Y., The Hierarchical Architecture of Nacre and its Mimetic Materials. In *Handbook of Biom mineralization. Biomimetic and Bioinspired Chemistry*, Behrens, P.; Bäuerlein, E., Eds. Wiley-VCH: Weinheim, 2007; Vol. 2, pp 89-107.
251. Gehrke, N.; Nassif, N.; Pinna, N.; Antonietti, M.; Gupta, H. S.; Coelfen, H. *Chemistry of Materials* **2005**, 17, (26), 6514-6516.
252. Oaki, Y.; Imai, H. *Advanced Functional Materials* **2005**, 15, (9), 1407-1414.
253. Fratzl, P.; Weinkamer, R. *Progress in Materials Science* **2007**, 52, (8), 1263-1334.
254. Murugan, R.; Ramakrishna, S., Nanoengineered Biomimetic Bone-Building Blocks. In *Molecular Building Blocks for Nanotechnology*, Mansoori, G. A.; George, T. F.; Assoufid, L.; Zhang, G., Eds. Springer: New York, 2007; pp 301-352.
255. Epple, M.; Bäuerlein, E., *Handbook of Biom mineralization. Medical and Clinical Aspects*. Wiley-VCH: Weinheim, 2007; Vol. 3.
256. Vallet-Regí, M.; Arcos, D., Nanostructured Hybrid Materials for Bone Implants Fabrication. In *Bio-inorganic Hybrid Nanomaterials*, Ruiz-Hitzky, E.; Ariga, K.; Lvov, Y., Eds. Wiley-VCH: Weinheim, 2008; pp 367-399.
257. Palin, E.; Liu, H.; Webster, T. J. *Nanotechnology* **2005**, 16, (9), 1828-1835.
258. Gonzalez-McQuire, R.; Green, D.; Walsh, D.; Hall, S.; Chane-Ching, J.-Y.; Oreffo, R. O. C.; Mann, S. *Biomaterials* **2005**, 26, (33), 6652-6656.
259. Wang, R. Z.; Cui, F. Z.; Lu, H. B.; Wen, H. B.; Ma, C. L.; Li, H. D. *Journal of Materials Science Letters* **1995**, 14, (7), 490-2.
260. Song, J.-H.; Kim, H.-E.; Kim, H.-W. *Journal of Biomedical Materials Research, Part B: Applied Biomaterials* **2007**, 83B, (1), 248-257.
261. Parhi, P.; Ramanan, A.; Ray, A. R. *Journal of Applied Polymer Science* **2006**, 102, (6), 5162-5165.
262. Hillig, W. B.; Choi, Y.; Murtha, S.; Natravali, N.; Ajayan, P. *Journal of Materials Science: Materials in Medicine* **2008**, 19, (1), 11-17.
263. Rusu, V. M.; Ng, C.-H.; Wilke, M.; Tiersch, B.; Fratzl, P.; Peter, M. G. *Biomaterials* **2005**, 26, (26), 5414-5426.
264. Kino, R.; Ikoma, T.; Monkawa, A.; Yunoki, S.; Munekata, M.; Tanaka, J.; Asakura, T. *Journal of Applied Polymer Science* **2006**, 99, (5), 2822-2830.
265. Mathieu, L. M.; Mueller, T. L.; Bourban, P.-E.; Pioletti, D. P.; Mueller, R.; Manson, J.-A. E. *Biomaterials* **2006**, 27, (6), 905-916.
266. Bunker, B. C.; Rieke, P. C.; Tarasevich, B. J.; Campbell, A. A.; Fryxell, G. E.; Graff, G. L.; Song, L.; Liu, J.; Virden, J. W.; McVay, G. L. *Science* **1994**, 264, (5155), 48-55.
267. Kokubo, T.; Takadama, H. *Biomaterials* **2006**, 27, (15), 2907-2915.

268. Hench, L. L.; Splinter, R. J.; Allen, W. C.; Greenlee, T. K. *Biomedical Materials Symposium* **1971**, (2), 117-41.
269. Kokubo, T. *Biomaterials* **1991**, 12, (2), 155-63.
270. Hench, L. L. *Journal of Materials Science: Materials in Medicine* **2006**, 17, (11), 967-978.
271. Fratzl, P. *Nachrichten aus der Chemie* **2007**, 55, (6), 644-646.
272. Kokubo, T.; Ito, S.; Shigematsu, M.; Sakka, S.; Yamamuro, T. *Journal of Materials Science* **1985**, 20, (6), 2001-4.
273. Kokubo, T.; Ito, S.; Sakka, S.; Yamamuro, T. *Journal of Materials Science* **1986**, 21, (2), 536-40.
274. Ohtsuki, C.; Aoki, Y.; Kokubo, T.; Bando, Y.; Neo, M.; Nakamura, T. *Journal of the Ceramic Society of Japan* **1995**, 103, (May), 449-54.
275. Kokubo, T.; Kushitani, H.; Sakka, S.; Kitsugi, T.; Yamamuro, T. *Journal of Biomedical Materials Research* **1990**, 24, (6), 721-34.
276. Orme, C. A.; Giocondi, J. L., Model Systems for Formation and Dissolution of Calcium Phosphate Minerals. In *Handbook of Biomineralization. Biomimetic and Bioinspired Chemistry*, P., B.; Bäuerlein, E., Eds. Wiley-VCH: Weinheim, 2007; Vol. 2, pp 135-157.
277. Kokubo, T.; Kushitani, H.; Ohtsuki, C.; Sakka, S.; Yamamuro, T. *Journal of Materials Science: Materials in Medicine* **1992**, 3, (2), 79-83.
278. Kokubo, T.; Kushitani, H.; Ohtsuki, C.; Sakka, S.; Yamamuro, T. *Journal of Materials Science: Materials in Medicine* **1993**, 4, (1), 1-4.
279. Kim, H. M.; Kishimoto, K.; Miyaji, F.; Kokubo, T.; Yao, T.; Suetsugu, Y.; Tanaka, J.; Nakamura, T. *Journal of Biomedical Materials Research* **1999**, 46, (2), 228-235.
280. Ohtsuki, C.; Kokubo, T.; Yamamuro, T. *Journal of Non-Crystalline Solids* **1992**, 143, (1), 84-92.
281. Tanahashi, M.; Yao, T.; Kokubo, T.; Minoda, M.; Miyamoto, T.; Nakamura, T.; Yamamuro, T. *Journal of the American Ceramic Society* **1994**, 77, (11), 2805-8.
282. Hata, K.; Kokubo, T.; Nakamura, T.; Yamamuro, T. *Journal of the American Ceramic Society* **1995**, 78, (4), 1049-53.
283. Tanahashi, M.; Hata, K.; Kokubo, T.; Minoda, M.; Miyamoto, T.; Nakamura, T.; Yamamuro, T., Effect of substrate on apatite formation by a biomimetic process. In *Bioceramics*, Yamamuro, T.; Kokubo, T.; Nakamura, T., Eds. Kobunshi-Kankokai: Kyoto, 1992; Vol. 5, pp 57-64.
284. Kontonasaki, E.; Zorba, T.; Papadopoulou, L.; Pavlidou, E.; Chatzistavrou, X.; Paraskevopoulos, K.; Koidis, P. *Crystal Research and Technology* **2002**, 37, (11), 1165-1171.
285. Tanahashi, M.; Yao, T.; Kokubo, T.; Minoda, M.; Miyamoto, T.; Nakamura, T.; Yamamuro, T. *Journal of Biomedical Materials Research* **1995**, 29, (3), 349-57.
286. Tanahashi, M.; Yao, T.; Kokubo, T.; Minoda, M.; Miyamoto, T.; Nakamura, T.; Yamamuro, T. *Journal of Materials Science: Materials in Medicine* **1995**, 6, (6), 319-26.
287. Balas, F.; Kawashita, M.; Nakamura, T.; Kokubo, T. *Biomaterials* **2006**, 27, (9), 1704-1710.
288. Stanley, W. M. *Science* **1935**, 81, 644-5.
289. Scholthof, K.-B. G.; Shaw, J. G.; Zaitlin, M., *Tobacco Mosaic Virus: One Hundred Years of Contributions to Virology*. American Phytopathological Society Press: St. Paul, Minnesota, USA, 1999.

290. Harrison, B. D.; Wilson, T. M. A. *Philosophical Transactions of the Royal Society of London, Series B: Biological Sciences* **1999**, 354, (1383), 521-529.
291. Dijkstra, J.; Khan, J. A., Description of Positive-Sense, Single-Stranded RNA Viruses. Family Comoviridae. In *Handbook of Plant Virology*, Dijkstra, J.; Khan, J. A., Eds. Food Products Press: Binghamton, 2006; pp 268-271.
292. Edwardson, J. R.; Christie, R. G., Comoviruses. In *CRC Handbook of Viruses Infecting Legumes*, CRC Press, Inc.: Boca Raton, 1991; pp 369-393.
293. Kammen, A. v.; Lent, J. v.; Wellink, J. Cowpea Mosaic Virus.
<http://www.dpvweb.net/dpv/showadpv.php?dpvno=378> (02.08.2007)
294. Lomonosoff, G. P.; Shanks, M., Comoviruses (Comoviridae). In *Encyclopedia of Virology*, Granoff, A.; Webster, R. G., Eds. Academic Press: San Diego, 1999; Vol. 1, pp 285-291.
295. Goldbach, R.; Kammen, A. v., Structure, Replication, and Expression of the Bipartite Genome of Cowpea Mosaic Virus. In *Molecular Plant Virology*, Davies, J. W., Ed. CRC Press, Inc.: Boca Raton, 1985; Vol. 2, pp 83-120.
296. Lin, T.; Chen, Z.; Usha, R.; Stauffacher, C. V.; Dai, J.-B.; Schmidt, T.; Johnson, J. E. *Virology* **1999**, 265, (1), 20-34.
297. Johnson, J. E.; Hollingshead, C. *Journal of Ultrastructure Research* **1981**, 74, (2), 223-31.
298. Edwardson, J. R.; Christie, R. G., *CRC Handbook of Viruses Infecting Legumes*. CRC Press, Inc.: Boca Raton, 1991.
299. Wellink, J., Comovirus Isolation and RNA Extraction. In *Plant Virology Protocols*, Foster, G. D.; Taylor, S. C., Eds. Humana Press: Totawa, 1998; Vol. 81, pp 205-209.
300. Dijkstra, J.; Khan, J. A., Description of Positive-Sense, Single-Stranded RNA Viruses: Family Tymoviridae. In *Handbook of Plant Virology*, Khan, J.; Dijkstra, J., Eds. Food Products Press: Binghamton, 2006; pp 282-284.
301. Hirth, L.; Givord, L., Tymoviruses. In *The Plant Viruses. Polyhedral Virions with Monopartite RNA Genomes*, Koenig, R., Ed. Plenum Publishing Corporation: New York, 1988; Vol. 3, pp 163-212.
302. Matthews, R. E. F. Turnip Yellow Mosaic Virus.
<http://www.dpvweb.net/dpv/showadpv.php?dpvno=230> (02.08.2007)
303. Koenig, R., *Polyhedral Virions with Monopartite RNA Genomes*. Plenum Publishing Corporation: New York, 1988; Vol. 3.
304. Edwardson, J. R.; Christie, R. G., Tymoviruses. In *CRC Handbook of Viruses Infecting Legumes*, CRC Press, Inc.: Boca Raton, 1991; p 429.
305. Gibbs, A., Tymoviruses. In *Encyclopedia of Virology*, Granoff, A.; Webster, R. G., Eds. Academic Press: San Diego, 1999; Vol. 3, pp 1850-1853.
306. Canady, M. A.; Larson, S. B.; Day, J.; McPherson, A. *Nature Structural Biology* **1996**, 3, (9), 771-781.
307. Gibbs, A.; Mackenzie, A. M., Tymovirus Isolation and Genomic RNA Extraction. In *Plant Virology Protocols*, Foster, G. D.; Taylor, S. C., Eds. Humana Press: Totawa, 1998; Vol. 81, pp 219-224.
308. Dijkstra, J.; Khan, J. A., Description of Positive-Sense, Single-Stranded RNA Viruses: Unassigned Genera. In *Handbook of Plant Virology*, Khan, J.; Dijkstra, J., Eds. Food Products Press: Binghamton, 2006; pp 348-351.
309. Lewandowski, D. J.; Dawson, W. O., Tobamoviruses. In *Encyclopedia of Virology*, Granoff, A.; Webster, R. G., Eds. Academic Press: San Diego, 1999; Vol. 3, pp 1780-1783.

310. Zaitlin, M. Tobacco Mosaic Virus. <http://www.dpvweb.net/dpv/showadpv.php?dpvno=370> (02.08.2007)
311. Namba, K.; Pattanayek, R.; Stubbs, G. *Journal of Molecular Biology* **1989**, 208, (2), 307-25.
312. Sachse, C.; Chen, J. Z.; Coureux, P.-D.; Stroupe, M. E.; Faendrich, M.; Grigorieff, N. *Journal of Molecular Biology* **2007**, 371, (3), 812-835.
313. Stubbs, G. *Philosophical Transactions of the Royal Society of London, Series B: Biological Sciences* **1999**, 354, (1383), 551-557.
314. Klug, A. *Philosophical Transactions of the Royal Society of London, Series B: Biological Sciences* **1999**, 354, (1383), 531-535.
315. Lomonosoff, G. P.; Wilson, T. M. A., Structure and in vitro Assembly of Tobacco Mosaic Virus. In *Molecular Plant Virology*, Davies, J. W., Ed. CRC Press, Inc.: Boca Raton, 1985; Vol. 1, pp 43-83.
316. Butler, P. J. G. *Philosophical Transactions of the Royal Society of London, Series B: Biological Sciences* **1999**, 354, (1383), 537-550.
317. Chapman, S. N., Tobamovirus Isolation and RNA Extraction. In *Plant Virology Protocols*, Foster, G. D.; Taylor, S. C., Eds. Humana Press: Totowa, 1998; Vol. 81, pp 123-129.
318. Edwardson, J. R.; Christie, R. G., Tobamoviruses. In *CRC Handbook of Viruses Infecting Legumes*, CRC Press, Inc.: Boca Raton, 1991; p 81.
319. Beachy, R. N. *Philosophical Transactions of the Royal Society of London, Series B: Biological Sciences* **1999**, 354, (1383), 659-664.
320. Yusibov, V.; Shivprasad, S.; Turpen, T. H.; Dawson, W.; Koprowski, H. *Current Topics in Microbiology and Immunology* **1999**, 240, (Plant Biotechnology), 81-94.
321. Harrison, P. M.; Arosio, P. *Biochimica et Biophysica Acta, Bioenergetics* **1996**, 1275, (3), 161-203.
322. Chasteen, N. D.; Harrison, P. M. *Journal of Structural Biology* **1999**, 126, (3), 182-194.
323. Collawn, J. F., Jr.; Lau, P. Y.; Morgan, S. L.; Fox, A.; Fish, W. W. *Archives of Biochemistry and Biophysics* **1984**, 233, (1), 260-6.
324. Heusterspreute, M.; Crichton, R. R. *FEBS Letters* **1981**, 129, (2), 322-7.
325. Banyard, S. H.; Stammers, D. K.; Harrison, P. M. *Nature* **1978**, 271, (5642), 282-4.
326. Orino, K.; Harada, S.; Natsuhori, M.; Takehara, K.; Watanabe, K. *BioMetals* **2004**, 17, (2), 129-134.
327. Takeda, S.; Ohta, M.; Ebina, S.; Nagayama, K. *Biochimica et Biophysica Acta, Gene Structure and Expression* **1993**, 1174, (2), 218-20.
328. Urushizaki, I.; Niitsu, Y.; Ishitani, K.; Matsuda, M.; Fukuda, M. *Biochimica et Biophysica Acta, Protein Structure* **1971**, 243, (2), 187-92.
329. Petsev, D. N.; Chen, K.; Gliko, O.; Vekilov, P. G. *Proceedings of the National Academy of Sciences of the United States of America* **2003**, 100, (3), 792-796.
330. Ikai, A., Serum Albumin. In *Encyclopedia of molecular biology*, Creighton, T. E., Ed. Wiley: New York, 1999; Vol. 4, pp 2339-2341.
331. Peters, T. J. *Advances in Protein Chemistry* **1985**, 37, 161-245.
332. Peters, T. J., *All about Albumin*. Academic Press: San Diego, 1996.
333. Wen, J.; Arakawa, T.; Philo, J. S. *Analytical Biochemistry* **1996**, 240, (2), 155-166.

334. Brown, W. M.; Saunders, N. R.; Koellgaard, K.; Dziegielewska, K. M. *BioEssays* **1992**, 14, (11), 749-55.
335. Dziegielewska, K. M.; Brown, W. M.; Casey, S. J.; Christie, D. L.; Foreman, R. C.; Hill, R. M.; Saunders, N. R. *Journal of Biological Chemistry* **1990**, 265, (8), 4354-7.
336. Brown, W. M.; Dziegielewska, K. M. *Protein Science* **1997**, 6, (1), 5-12.
337. Otto, H.-H.; Schirmeister, T. *Chemical Reviews* **1997**, 97, (1), 133-171.
338. Westenfeld, R.; Jahnen-Dechent, W.; Ketteler, M. *Trends in Cardiovascular Medicine* **2007**, 17, (4), 124-128.
339. Schaefer, C.; Heiss, A.; Schwarz, A.; Westenfeld, R.; Ketteler, M.; Floege, J.; Mueller-Esterl, W.; Schinke, T.; Jahnen-Dechent, W. *Journal of Clinical Investigation* **2003**, 112, (3), 357-366.
340. Ketteler, M.; Bongartz, P.; Westenfeld, R.; Ernst Wildberger, J.; Horst Mahnken, A.; Bohm, R.; Metzger, T.; Wanner, C.; Jahnen-Dechent, W.; Floege, J. *Lancet* **2003**, 361, (9360), 827-833.
341. Reynolds, J. L.; Skepper, J. N.; McNair, R.; Kasama, T.; Gupta, K.; Weissberg, P. L.; Jahnen-Dechent, W.; Shanahan, C. M. *Journal of the American Society of Nephrology* **2005**, 16, (10), 2920-2930.
342. Toroian, D.; Price, P. A. *Calcified Tissue International* **2008**, 82, (2), 116-126.
343. Heiss, A.; DuChesne, A.; Denecke, B.; Groetzinger, J.; Yamamoto, K.; Renne, T.; Jahnen-Dechent, W. *Journal of Biological Chemistry* **2003**, 278, (15), 13333-13341.
344. Heiss, A.; Jahnen-Dechent, W.; Endo, H.; Schwahn, D. *Biointerphases* **2007**, 2, (1), 16-20.
345. Xie, J.; Baumann, M. J.; McCabe, L. R. *Journal of Biomedical Materials Research, Part A* **2005**, 73A, (1), 39-47.
346. Triffitt, J. T.; Owen, M. E.; Ashton, B. A.; Wilson, J. M. *Calcified Tissue Research* **1978**, 26, (2), 155-61.
347. Heiss, W. A. Zur molekularen Topologie der Bindung natürlicher und rekombinanter Varianten von α 2-HS-Glycoprotein/Fetuin an Hydroxylapatit. Aachen, 2002.
348. Harding, S. E.; Johnson, P. *Biochemical Journal* **1985**, 231, (3), 549-55.
349. Kaper, J. M.; Litjens, E. C. *Biochemistry* **1966**, 5, (5), 1612-17.
350. Camerini-Otero, R. D.; Franklin, R. M.; Day, L. A. *Biochemistry* **1974**, 13, (18), 3763-73.
351. Fasman, G. D., *Handbook of Biochemistry and Molecular Biology*. CRC Press: Cleveland, 1976; Vol. 2, p 372-382.
352. Arosio, P.; Adelman, T. G.; Drysdale, J. W. *Journal of Biological Chemistry* **1978**, 253, (12), 4451-8.
353. Fasman, G. D., *Handbook of Biochemistry and Molecular Biology*. CRC Press: Cleveland, 1976; Vol. 2, p 383-546.
354. Raj, T.; Flygare, W. H. *Biochemistry* **1974**, 13, (16), 3336-40.
355. Anderson, J. L.; Rauh, F.; Morales, A. *Journal of Physical Chemistry* **1978**, 82, (5), 608-16.
356. Dickinson, E. *Soft Matter* **2006**, 2, (8), 642-652.
357. Appelqvist, I. A. M.; Golding, M.; Vreeker, R.; Zuidam, N. J. *Encapsulation and Controlled Release Technologies in Food Systems* **2007**, 41-81.
358. Michel, M.; Watzke, H. J.; Sagalowicz, L.; Kolodziejczyk, E.; Leser, M. E., Self-assembly in food - a new way to make nutritious products. In *Food*

- Colloids. Self-Assembly and Materials Science*, Dickinson, E.; Leser, M. E., Eds. Royal Society of Chemistry: Cambridge, 2007; pp 19-33.
359. Weiss, J.; Takhistov, P.; McClements, D. J. *Journal of Food Science* **2006**, *71*, (9), R107-R116.
360. Sanguansri, P.; Augustin, M. A. *Trends in Food Science & Technology* **2006**, *17*, (10), 547-556.
361. Rosen, M. R., *Delivery System Handbook for Personal Care and Cosmetic Products*. William Andrew Publishing: Norwich, 2005.
362. The Bone and Joint Decade. <http://www.bjdonline.org> (31.05.2008)
363. Bayliss, S. C.; Heald, R.; Fletcher, D. I.; Buckberry, L. D. *Advanced Materials* **1999**, *11*, (4), 318-321.
364. Bayliss, S. C.; Harris, P. J.; Buckberry, L. D.; Rousseau, C. *Journal of Materials Science Letters* **1997**, *16*, (9), 737-740.
365. Whitehead, M. A.; Fan, D.; Akkaraju, G. R.; Canham, L. T.; Coffey, J. L. *Journal of Biomedical Materials Research, Part A* **2007**, *83A*, (1), 225-234.
366. Li, X.; Coffey, J. L.; Chen, Y.; Pinizzotto, R. F.; Newey, J.; Canham, L. T. *Journal of the American Chemical Society* **1998**, *120*, (45), 11706-11709.
367. Offenhaeusser, A.; Boecker-Meffert, S.; Decker, T.; Helpenstein, R.; Gasteier, P.; Groll, J.; Moeller, M.; Reska, A.; Schaefer, S.; Schulte, P.; Vogt-Eisele, A. *Soft Matter* **2007**, *3*, (3), 290-298.
368. Besenbacher, F.; Duch, M. R.; Foss, M.; Pedersen, F. S.; Justesen, J. H. F.; Andersen, L. K.; Crovato, T. E. L.; Markert, L. Biocompatible material for surgical implants and cell guiding tissue culture surfaces. WO2006114098, 2006.
369. Edler, K. J.; Roser, S. J. *International Reviews in Physical Chemistry* **2001**, *20*, (3), 387-466.
370. Antonietti, M. *Philosophical Transactions of the Royal Society, A: Mathematical, Physical & Engineering Sciences* **2006**, *364*, (1847), 2817-2840.
371. Butler, J. A. V. *Proceedings of the Royal Society of London, Series A: Mathematical, Physical and Engineering Sciences* **1932**, *135*, 348-75.
372. Lucassen-Reynders, E. H. *Colloids and Surfaces, A: Physicochemical and Engineering Aspects* **1994**, *91*, 79-88.
373. Fainerman, V. B.; Miller, R. *Langmuir* **1999**, *15*, (5), 1812-1816.
374. Fainerman, V. B.; Miller, R., Adsorption and Interfacial Tension Isotherms for Proteins. In *Proteins at Liquid Interfaces*, Möbius, D.; Miller, R., Eds. Elsevier: Amsterdam, 1998; Vol. 7, pp 51-102.
375. Makievski, A. V.; Miller, R.; Fainerman, V. B.; Kragel, J.; Wustneck, R., Adsorption of proteins at the gas-liquid and oil-water interfaces as studied by the pendant drop method. In *Food Emulsions and Foams*, Dickinson, E.; Patino, J., Eds. Royal Society of Chemistry: Cambridge, 1999; pp 269-284.
376. Maldonado-Valderrama, J.; Martin-Molina, A.; Galvez-Ruiz, M. J.; Martin-Rodriguez, A.; Cabrerizo-Vilchez, M. A. *Journal of Physical Chemistry B* **2004**, *108*, (34), 12940-12945.
377. Dukhin, S. S.; Kretzschmar, G.; Miller, R., *Dynamics of Adsorption at Liquid Interfaces*. Elsevier: Amsterdam, 1995; Vol. 1.
378. Makievski, A. V.; Loglio, G.; Kraegel, J.; Miller, R.; Fainerman, V. B.; Neumann, A. W. *Journal of Physical Chemistry B* **1999**, *103*, (44), 9557-9561.
379. Fainerman, V. B.; Makievski, A. V.; Miller, R. *Colloids and Surfaces, A: Physicochemical and Engineering Aspects* **1994**, *87*, (1), 61-75.

380. Hansen, R. S. *Journal of Colloid Science* **1961**, 16, 549-60.
381. Ybert, C.; di Meglio, J. M. *Langmuir* **1998**, 14, (2), 471-475.
382. Rillaerts, E.; Joos, P. *Journal of Physical Chemistry* **1982**, 86, (17), 3471-8.
383. Makievski, A. V.; Fainerman, V. B.; Miller, R.; Bree, M.; Liggieri, L.; Ravera, F. *Colloids and Surfaces, A: Physicochemical and Engineering Aspects* **1997**, 122, (1-3), 269-273.
384. Wuestneck, R.; Kraegel, J.; Miller, R.; Fainerman, V. B.; Wilde, P. J.; Sarker, D. K.; Clark, D. C. *Food Hydrocolloids* **1996**, 10, (4), 395-405.
385. Miller, R.; Fainerman, V. B.; Wustneck, R.; Kragel, J.; Trukhin, D. V. *Colloids and Surfaces, A: Physicochemical and Engineering Aspects* **1998**, 131, (1-3), 225-230.
386. Fainerman, V. B.; Lylyk, S. V.; Makievski, A. V.; Miller, R. *Journal of Colloid and Interface Science* **2004**, 275, (1), 305-308.
387. Miller, R.; Fainerman, V. B.; Makievski, A. V.; Leser, M.; Michel, M.; Aksenenko, E. V. *Colloids and Surfaces, B: Biointerfaces* **2004**, 36, (3-4), 123-126.
388. Miller, R.; Fainerman, V. B.; Makievski, A. V.; Ferrari, M.; Loglio, G. *Handbook of Applied Surface and Colloid Chemistry* **2002**, 2, 225-238.
389. Kralchevsky, P. A.; Danov, K. D.; Denkov, N. D., Chemical Physics of Colloid Systems and Interfaces. In *Handbook of Surface and Colloid Chemistry*, Birdi, K. S., Ed. CRC Press: Boca Raton, 2003; p 156.
390. Fainerman, V. B.; Miller, R. *Journal of Colloid and Interface Science* **1995**, 175, (1), 118-21.
391. Fainerman, V. B.; Mys, V. D.; Makievski, A. V.; Petkov, J. T.; Miller, R. *Journal of Colloid and Interface Science* **2006**, 302, (1), 40-46.
392. Aksenenko, E. V.; Kovalchuk, V. I.; Fainerman, V. B.; Miller, R. *Advances in Colloid and Interface Science* **2006**, 122, (1-3), 57-66.
393. Miller, R.; Fainerman, V.; O'Neill, M.; Kragel, J.; Makievski, A., Adsorption and rheological behaviour of biopolymers at liquid interfaces. In *Plant Biopolymer Science: Food and Non-Food Applications*, Renard, D.; Valle, D.; Popineau, Y., Eds. Royal Society of Chemistry: London, 2002; Vol. 276, pp 153-165.
394. Kragel, J.; O'Neill, M.; Makievski, A. V.; Michel, M.; Leser, M. E.; Miller, R. *Colloids and Surfaces, B: Biointerfaces* **2003**, 31, (1-4), 107-114.
395. Miller, R.; Policova, Z.; Sedev, R.; Neumann, A. W. *Colloids and Surfaces, A: Physicochemical and Engineering Aspects* **1993**, 76, (1-3), 179-85.
396. Miller, R.; Sedev, R.; Schano, K. H.; Ng, C.; Neumann, A. W. *Colloids and Surfaces* **1993**, 69, (4), 209-16.
397. Fainerman, V. B.; Makievski, A. V.; Kraegel, J.; Javadi, A.; Miller, R. *Journal of Colloid and Interface Science* **2007**, 308, (1), 249-253.
398. Ferri, J. K.; Dong, W.-F.; Miller, R. *Journal of Physical Chemistry B* **2005**, 109, (31), 14764-14768.
399. Hoorfar, M.; Neumann, A. W. *Advances in Colloid and Interface Science* **2006**, 121, (1-3), 25-49.
400. Zholob, S. A.; Makievski, A. V.; Miller, R.; Fainerman, V. B. *Advances in Colloid and Interface Science* **2007**, 134-135, 322-329.
401. Song, B.; Springer, J. *Journal of Colloid and Interface Science* **1996**, 184, (1), 64-76.

402. Hansen, F. K.; Roedsrud, G. *Journal of Colloid and Interface Science* **1991**, 141, (1), 1-9.
403. Callejas-Fernández, J.; Tirado-Miranda, M.; Quesada-Pérez, M.; Odiozola-Prego, G.; Schmitt, A., Photon Spectroscopy of Colloids. In *Encyclopedia of Surface and Colloid Science*, Hubbard, A. T., Ed. Marcel Dekker, Inc.: New York, 2002; Vol. 3, pp 4072-4089.
404. Liu, T.; Chu, B., Light-Scattering by Proteins. In *Encyclopedia of Surface and Colloid Science*, Hubbard, A. T., Ed. Marcel Dekker, Inc.: New York, 2002; Vol. 3, pp 3023-3043.
405. Bloomfield, V. A., Biological Applications of Dynamic Light Scattering. In *Dynamic Light Scattering*, Pecora, R., Ed. Plenum Press: New York, 1985; p 376 ff.
406. Harding, S. E.; Sattelle, D. B.; Bloomfield, V. A., *Laser Light Scattering in Biochemistry*. Royal Society of Chemistry: Cambridge, 1992.
407. Kratochvil, P., *Classical Light Scattering From Polymer Solutions*. Elsevier: Amsterdam, 1987.
408. Debye, P. *Journal of Physical and Colloid Chemistry* **1947**, 51, 18-32.
409. Zimm, B. H. *Journal of Chemical Physics* **1948**, 16, 1099-1116.
410. Pecora, R., *Dynamic Light Scattering*. Plenum Press: New York, 1985.
411. Schmitz, K. S., *An Introduction to Dynamic Light Scattering by Macromolecules*. Academic Press: Boston, 1990.
412. Hiemenz, P. C.; Rajagopalan, R., *Principles of Colloid and Surface Chemistry*. Marcel Dekker Inc.: New York, 1997.
413. Siegert, A. J. F. *MIT Rad. Lab. Rep.* **1943**, 465.
414. Provencher, S. W. *Makromolekulare Chemie* **1979**, 180, (1), 201-9.
415. Provencher, S. W. *Computer Physics Communications* **1982**, 27, 213-227.
416. Provencher, S. W. *Computer Physics Communications* **1982**, 27, 229-242.
417. Johnsen, P.; Brown, W., An Overview of Current Methods of Analysing QLS Data. In *Laser Light Scattering in Biochemistry*, Harding, S. E.; Sattelle, D. B.; Bloomfield, V. A., Eds. Royal Society of Chemistry: Cambridge, 1992; pp 77-91.
418. Koppel, D. E. *Journal of Chemical Physics* **1972**, 57, (11), 4814-20.
419. Stephen, M. J. *Journal of Chemical Physics* **1971**, 55, (8), 3878-83.
420. Zero, K.; Pecora, R., Dynamic Depolarized Light Scattering. In *Dynamic Light Scattering*, Pecora, R., Ed. Plenum Press: New York, 1985; pp 65-75.
421. Lehner, D.; Lindner, H.; Glatter, O. *Langmuir* **2000**, 16, (4), 1689-1695.
422. Thomas, J. C.; Fletcher, G. C. *Biopolymers* **1978**, 17, (11), 2753-6.
423. Wada, A.; Suda, N.; Tsuda, T.; Soda, K. *Journal of Chemical Physics* **1969**, 50, (1), 31-5.
424. Schurr, J. M.; Schmitz, K. S. *Biopolymers* **1973**, 12, (5), 1021-45.
425. Aguilar, M.-I., *HPLC of Peptides and Proteins*. Humana Press: Totowa, 2004.
426. Folta-Stogniew, E.; Williams, K. R. *Journal of Biomolecular Techniques* **1999**, 10, (2), 51-63.
427. Oliva, A.; Llabres, M.; Farina, J. B. *Current Drug Discovery Technologies* **2004**, 1, (3), 229-242.
428. Mann, M.; Hendrickson, R. C.; Pandey, A. *Annual Review of Biochemistry* **2001**, 70, 437-473.
429. Fitzgerald, M. C.; Siuzdak, G. *Chemistry & Biology* **1996**, 3, (9), 707-715.

430. Scott, D. J.; Harding, S. E.; Rowe, A. J., *Analytical Ultracentrifugation: Techniques and Methods*. Royal Society of Chemistry: Cambridge, 2005.
431. Cole, J. L.; Lary, J. W.; Moody, T. P.; Laue, T. M. *Methods in Cell Biology* **2008**, 84, (Biophysical Tools for Biologists, Volume One), 143-179.
432. Brown, P. H.; Balbo, A.; Schuck, P. *Biomacromolecules* **2007**, 8, (6), 2011-2024.
433. Howlett, G. J.; Minton, A. P.; Rivas, G. *Current Opinion in Chemical Biology* **2006**, 10, (5), 430-436.
434. Wyatt, P. J., Combined Differential Light Scattering with Various Liquid Chromatography Separation Techniques. In *Laser Light Scattering in Biochemistry*, Harding, S. E.; Sattelle, D. B.; Bloomfield, V. A., Eds. Royal Society of Chemistry: Cambridge, 1992; pp 33-58.
435. Fee, C. J.; Van Alstine, J. M. *Bioconjugate Chemistry* **2004**, 15, (6), 1304-1313.
436. Irvine, B. G., Molecular-Weight Estimation for Native Proteins Using Size-Exclusion High-Performance Liquid Chromatography. In *The Protein Protocols Handbook*, Walker, J. M., Ed. Humana Press: Totowa, 1996; pp 473-478.
437. Liu, J.; Andya, J. D.; Shire, S. J. *AAPS Journal* **2006**, 8, (3), E580-E589.
438. Silveira, J. R.; Raymond, G. J.; Hughson, A. G.; Race, R. E.; Sim, V. L.; Hayes, S. F.; Caughey, B. *Nature* **2005**, 437, (7056), 257-261.
439. Claes, P.; Dunford, M.; Kenney, A.; Vardy, P., An On-line Dynamic Light Scattering Instrument for Macromolecular Characterization. In *Laser Light Scattering in Biochemistry*, Harding, S. E.; Sattelle, D. B.; Bloomfield, V. A., Eds. Royal Society of Chemistry: Cambridge, 1992; pp 66-76.
440. Hartmann, W. K.; Satharishi, N.; Yang, X. Y.; Mitra, G.; Soman, G. *Analytical Biochemistry* **2004**, 325, (2), 227-239.
441. Takagi, T. *J. Chromatogr.* **1990**, 506, 409-416.
442. Krull, I. S.; Mhatre, R.; Stuting, H. H. *TrAC, Trends in Analytical Chemistry* **1989**, 8, (7), 260-8.
443. Jumel, K.; Browne, P.; Kennedy, J. F., The Use of Low Angle Laser Light Scattering with Gel Permeation Chromatography for the Molecular Weight Determination of Biomolecules. In *Laser Light Scattering in Biochemistry*, Harding, S. E.; Sattelle, D. B.; Bloomfield, V. A., Eds. Royal Society of Chemistry: Cambridge, 1992; p 23 ff.
444. Huglin, M. B. *Journal of Applied Polymer Science* **1965**, 9, (12), 4003-24.
445. Eisenberg, H.; Josephs, R.; Reisler, E.; Schellman, J. A. *Biopolymers* **1977**, 16, (12), 2773-83.
446. Perlmann, G. E.; Longsworth, L. G. *Journal of the American Chemical Society* **1948**, 70, 2719-24.
447. Ball, V.; Ramsden, J. J. *Biopolymers* **1998**, 46, (7), 489-492.
448. Soria, V.; Llopis, A.; Celda, B.; Campos, A.; Figueruelo, J. E. *Polymer Bulletin* **1985**, 13, (1), 83-8.
449. Kendrick, B. S.; Kerwin, B. A.; Chang, B. S.; Philo, J. S. *Analytical Biochemistry* **2001**, 299, (2), 136-146.
450. Wyatt ASTRA V, 5.3.2.15; Santa Barbara, 2007.
451. Brenner, S.; Horne, R. W. *Biochimica et Biophysica Acta* **1959**, 34, 103-10.
452. Harris, R. J.; Horne, R., Negative Staining. In *Electron Microscopy in Biology*, Harris, R. J., Ed. Oxford University Press: Oxford, 1991; pp 203-228.
453. Spiess, E.; Zimmermann, H.-P.; Lünsdorf, H., Negative Staining of Protein Molecules and Filaments. In *Electron Microscopy in Molecular Biology*,

- Sommerville, J.; Scheer, U., Eds. Oxford University Press: Oxford, 1998; pp 147-166.
454. Harris, J. R.; Horne, R. W. *Micron* **1994**, 25, (1), 5-13.
455. Botton, G., Analytical Electron Microscopy. In *Science of Microscopy*, Hawkes, P. W.; Spence, J. C. H., Eds. Springer: New York, 2007; Vol. 1, pp 273-405.
456. Nikiforov, M. P.; Bonnell, D. A., Scanning Probe Microscopy in Materials Science. In *Science of Microscopy*, Hawkes, P. W.; Spence, J. C. H., Eds. Springer: New York, 2007; Vol. 2, pp 929-968.
457. Hansma, P. K.; Cleveland, J. P.; Radmacher, M.; Walters, D. A.; Hillner, P. E.; Bezanna, M.; Fritz, M.; Vie, D.; Hansma, H. G.; et al. *Applied Physics Letters* **1994**, 64, (13), 1738-40.
458. D'Amato, M. J.; Marcus, M. S.; Eriksson, M. A.; Carpick, R. W. *Applied Physics Letters* **2004**, 85, (20), 4738-4740.
459. Magonov, S. N.; Reneker, D. H. *Annual Review of Materials Science* **1997**, 27, 175-222.
460. Kuznetsov, Y. G.; Malkin, A. J.; Lucas, R. W.; Plomp, M.; McPherson, A. *Journal of General Virology* **2001**, 82, (9), 2025-2034.
461. Muramatsu, H.; Yamamoto, Y.; Sato, A.; Enomoto, S.; Kim, W.-S.; Chang, S.-M.; Kim, J. M. *Journal of Microscopy* **2006**, 224, (2), 146-151.
462. Hafner, J. H.; Cheung, C. L.; Woolley, A. T.; Lieber, C. M. *Progress in Biophysics & Molecular Biology* **2001**, 77, (1), 73-110.
463. Hansma, H. G.; Hoh, J. H. *Annual Review of Biophysics and Biomolecular Structure* **1994**, 23, 115-39.
464. Allen, S.; Davies, M. C.; Roberts, C. J.; Tendler, S. J. B.; Williams, P. M. *Trends in Biotechnology* **1997**, 15, (3), 101-105.
465. Malkin, A. J.; Marco, P.; McPherson, A., Unraveling the Architecture of Viruses by High-Resolution Atomic Force Microscopy. In *DNA Viruses*, Liebermann, P. M., Ed. Humana Press: Totowa, 2005; pp 85-108.
466. Kuznetsov, Y. G.; Malkin, A. J.; Land, T. A.; DeYoreo, J. J.; Barba, A. P.; Konnert, J.; McPherson, A. *Biophysical Journal* **1997**, 72, (5), 2357-2364.
467. Kuznetsov, Y. G.; Low, A.; Fan, H.; McPherson, A. *Virology* **2004**, 323, (2), 189-196.
468. Kuznetsov, Y. G.; McPherson, A. *Virology* **2006**, 352, (2), 329-337.
469. Kuznetsov, Y. G.; Malkin, A. J.; Lucas, R. W.; McPherson, A. *Colloids and Surfaces, B: Biointerfaces* **2000**, 19, (4), 333-346.
470. Malkin, A. J.; Kuznetsov, Y. G.; Lucas, R. W.; McPherson, A. *Journal of Structural Biology* **1999**, 127, (1), 35-43.
471. Malkin, A. J.; Land, T. A.; Kuznetsov, Y. G.; McPherson, A.; De Yoreo, J. J. *Physical Review Letters* **1995**, 75, (14), 2778-81.
472. McPherson, A.; Kuznetsov, Y. G.; Malkin, A.; Plomp, M. *Journal of Structural Biology* **2003**, 142, (1), 32-46.
473. Nettikadan, S. R.; Johnson, J. C.; Vengasandra, S. G.; Muys, J.; Henderson, E. *Nanotechnology* **2004**, 15, (3), 383-389.
474. Silva, L. P. *Current Protein and Peptide Science* **2005**, 6, (4), 387-395.
475. Hansma, H. G.; Kim, K. J.; Laney, D. E.; Garcia, R. A.; Argaman, M.; Allen, M. J.; Parsons, S. M. *Journal of Structural Biology* **1997**, 119, (2), 99-108.
476. Dupres, V.; Verbelen, C.; Dufrene, Y. F. *Biomaterials* **2007**, 28, (15), 2393-2402.

477. Forman, J. R.; Clarke, J. *Current Opinion in Structural Biology* **2007**, 17, (1), 58-66.
478. Attard, P. *Journal of Physics: Condensed Matter* **2007**, 19, (47), 473201/1-473201/33.
479. Xie, X. N.; Chung, H. J.; Sow, C. H.; Wee, A. T. S. *Materials Science & Engineering, R: Reports* **2006**, R54, (1-2), 1-48.
480. Ngunjiri, J.; Garino, J. C. *Analytical Chemistry* **2008**, 80, (5), 1361-1369.
481. Yang, J.; Shao, Z. *Micron* **1995**, 26, (1), 35-49.
482. Dijkstra, J.; Jager, C. P. d., *Practical Plant Virology*. Springer: Berlin, 1998.
483. Foster, G. D.; Taylor, S. C., *Plant Virology Protocols*. Humana Press Inc.: Totowa, 1998.
484. Wang, Q., *personal communication/laboratory manual*.
485. Song, B.; Springer, J. *Journal of Colloid and Interface Science* **1996**, 184, (1), 77-91.
486. Goebel, A.; Lunkenheimer, K. *Langmuir* **1997**, 13, (2), 369-372.
487. Laemmli, U. K. *Nature* **1970**, 227, (5259), 680-685.
488. Fuerstenau, S. D.; Benner, W. H.; Thomas, J. J.; Brugidou, C.; Bothner, B.; Siuzdak, G. *Angewandte Chemie, International Edition* **2001**, 40, (3), 541-544.
489. Siuzdak, G.; Bothner, B.; Yeager, M.; Brugidou, C.; Fauquet, C. M.; Hoey, K.; Chang, C.-M. *Chemistry & Biology* **1996**, 3, (1), 45-8.
490. Sommerville, J.; Scheer, U., *Electron Microscopy in Molecular Biology. A Practical Approach*. Oxford University Press: Oxford, 1987.
491. Harris, R. J., *Electron Microscopy in Biology. A Practical Approach*. Oxford University Press: Oxford, 1991.
492. Massover, W. H. *Micron* **1993**, 24, (4), 389-437.
493. Bloomfield, V. A. *Annual Review of Biophysics and Bioengineering* **1981**, 10, 421-50.
494. Harding, S. E., Total Intensity and Quasi-elastic Light Scattering Applications in Microbiology. In *Laser Light Scattering in Biochemistry*, Harding, S. E.; Sattelle, D. B.; Bloomfield, V. A., Eds. Royal Society of Chemistry: Cambridge, 1992; pp 365-385.
495. Camerini-Otero, R. D.; Pusey, P. N.; Koppel, D. E.; Schaefer, D. W.; Franklin, R. M. *Biochemistry* **1974**, 13, (5), 960-70.
496. Harvey, J. D. *Virology* **1973**, 56, (1), 365-8.
497. Johnson, P.; Brown, W., An Investigation of Rigid Rod-like particles in Dilute Solution. In *Laser Light Scattering in Biochemistry*, Harding, S. E.; Sattelle, D. B.; Bloomfield, V. A., Eds. Royal Society of Chemistry: Cambridge, 1992; pp 161-183.
498. Wilcoxon, J.; Schurr, J. M. *Biopolymers* **1983**, 22, (3), 849-67.
499. Santos, N. C.; Castanho, M. A. R. B. *Biophysical Journal* **1996**, 71, (3), 1641-1650.
500. Sano, Y. *Journal of General Virology* **1987**, 68, (9), 2439-2442.
501. Weber, F. N., Jr.; Elton, R. M.; Kim, H. G.; Rose, R. D.; Steere, R. L.; Kupke, D. W. *Science* **1963**, 140, 1090-2.
502. Steere, R. L. *Science* **1963**, 140, 1089-90.
503. Petsev, D. N.; Thomas, B. R.; Yau, S. T.; Vekilov, P. G. *Biophysical Journal* **2000**, 78, (4), 2060-2069.
504. Hauser, H. *Hoppe-Seyler's Zeitschrift fuer Physiologische Chemie* **1969**, 350, (11), 1331-9.

505. Linder, M. C.; Kakavandi, H. R.; Miller, P.; Wirth, P. L.; Nagel, G. M. *Archives of Biochemistry and Biophysics* **1989**, 269, (2), 485-96.
506. Stefanini, S.; Chiancone, E.; Arosio, P.; Finazzi-Agro, A.; Antonini, E. *Biochemistry* **1982**, 21, (10), 2293-9.
507. Baker, T. S.; Olson, N. H.; Fuller, S. D. *Microbiology and Molecular Biology Reviews* **1999**, 63, (4), 862-922.
508. Haugland, R. P., *Handbook of Fluorescent Probes and Research Products*. Molecular Probes, Inc.: Eugene, 2002.
509. Pawley, J. B., *Handbook of Biological Confocal Microscopy*. Springer: Berlin, 2006.
510. Taylor, K. M.; Spall, V. E.; Jonathan, P.; Butler, G.; Lomonosoff, G. P. *Virology* **1999**, 255, (1), 129-137.
511. Miller, R.; Fainerman, V. B.; Aksenenko, E. V. *Colloids and Surfaces, A: Physicochemical and Engineering Aspects* **2004**, 242, (1-3), 123-128.
512. Fainerman, V. B.; Miller, R.; Aksenenko, E. V. *Advances in Colloid and Interface Science* **2002**, 96, (1-3), 339-359.
513. Aksenenko, E. V., Software Tools to Interpret the Thermodynamics and Kinetics of Surfactant Adsorption. In *Surfactants: Chemistry, Interfacial Properties, Applications*, Fainerman, V. B.; Möbius, D.; Miller, R., Eds. Elsevier: Amsterdam, 2001; Vol. 13, pp 619-648.
514. Adsorption Software.
<http://www.thomascat.info/thomascat/Scientific/AdSo/AdSo.htm> (21.04.2008)
515. Maldonado-Valderrama, J.; Fainerman, V. B.; Galvez-Ruiz, M. J.; Martin-Rodriguez, A.; Cabrerizo-Vilchez, M. A.; Miller, R. *Journal of Physical Chemistry B* **2005**, 109, (37), 17608-17616.
516. Miller, R.; Aksenenko, E. V.; Fainerman, V. B.; Pison, U. *Colloids and Surfaces, A: Physicochemical and Engineering Aspects* **2001**, 183-185, 381-390.
517. Wuestneck, R.; Fainermann, V. B.; Wuestneck, N.; Pison, U. *Journal of Physical Chemistry B* **2004**, 108, (5), 1766-1770.
518. Hashimoto, F.; Tsukahara, S.; Watarai, H. *Langmuir* **2003**, 19, (10), 4197-4204.
519. Humpolickova, J.; Gielen, E.; Benda, A.; Fagulovala, V.; Vercammen, J.; vande Ven, M.; Hof, M.; Ameloot, M.; Engelborghs, Y. *Biophysical Journal* **2006**, 91, (3), L23-L25.
520. Schwille, P.; Korlach, J.; Webb, W. W. *Cytometry* **1999**, 36, (3), 176-182.
521. Scheybani, T.; Yoshimura, H.; Baumeister, W.; Nagayama, K. *Langmuir* **1996**, 12, (2), 431-5.
522. Heenan, R. K.; Eastoe, J. *Journal of Applied Crystallography* **2000**, 33, (3), 749-752.
523. Estrela-Lopis, I.; Leporatti, S.; Typlt, E.; Clemens, D.; Donath, E. *Langmuir* **2007**, 23, (13), 7209-7215.
524. Endo, H. *Physica B: Condensed Matter* **2006**, 385-386, (Pt. 1), 682-684.
525. Porod, G., *Small Angle X-Ray Scattering*. Academic Press: London, 1982; p 17.
526. Gallas, J. M.; Littrell, K. C.; Seifert, S.; Zajac, G. W.; Thiyagarajan, P. *Biophysical Journal* **1999**, 77, (2), 1135-1142.
527. Lee, B.; Lo, C.-T.; Thiyagarajan, P.; Winans, R. E.; Li, X.; Niu, Z.; Wang, Q. *Langmuir* **2007**, 23, (22), 11157-11163.
528. Lacefield, W. R. *Annals of the New York Academy of Sciences* **1988**, 523, 72-80.
529. Santos, M. H.; de Oliveira, M.; de Freitas Souza, L. P.; Mansur, H. S.; Vasconcelos, W. L. *Materials Research* **2004**, 7, (4), 625-630.

-
530. Lazic, S. *Journal of Crystal Growth* **1995**, 147, (1/2), 147-54.
531. Hsieh, M. F.; Perng, L. H.; Chin, T. S.; Perng, H. G. *Biomaterials* **2001**, 22, (19), 2601-2607.
532. Rabiei, A.; O'Neill, A. T.; Neville, B. P. *Materials Research Society Symposium Proceedings* **2005**, 851, 517-526.
533. LeGeros, R. Z. *Clinical Materials* **1993**, 14, (1), 65-88.
534. Porter, A. E.; Patel, N.; Skepper, J. N.; Best, S. M.; Bonfield, W. *Biomaterials* **2003**, 24, (25), 4609-4620.
535. Rhee, S.-H.; Tanaka, J. *Biomaterials* **1999**, 20, (22), 2155-2160.
536. Chung, R.-J.; Hsieh, M.-F.; Panda, R. N.; Chin, T.-S. *Surface and Coatings Technology* **2003**, 165, (2), 194-200.
537. Sikiric, M.; Babic-Ivancic, V.; Milat, O.; Sarig, S.; Fueredi-Milhofer, H. *Langmuir* **2000**, 16, (24), 9261-9266.
538. Bigi, A.; Boanini, E.; Walsh, D.; Mann, S. *Angewandte Chemie, International Edition* **2002**, 41, (12), 2163-2166.
539. Green, D. W.; Leveque, I.; Walsh, D.; Howard, D.; Yang, X.; Partridge, K.; Mann, S.; Oreffo, R. O. C. *Advanced Functional Materials* **2005**, 15, (6), 917-923.
540. Schueth, F. *Angewandte Chemie, International Edition* **2003**, 42, (31), 3604-3622.

Acknowledgement

Prof. Alexander Böker (University of Bayreuth): Ich möchte mich für die große Freiheit und das damit verbundene Vertrauen bedanken, dass ich während meiner gesamten Doktorarbeit als große Wertschätzung empfunden habe.

Prof. Axel H. E. Müller (University of Bayreuth): Ich möchte mich für die ausdauernde Begleitung und Interesse an meiner Arbeit, beginnend mit der Diplomarbeit bis zum Schluss der Doktorarbeit, sehr bedanken.

Prof. Qian Wang (University of South Carolina, Columbia, USA): Thank you for all the kindness during my stay in your group and the chance to get in touch and to learn something about virus production and purification. I would like to include your coworkers into my thanks for the preparation and supply with virus solutions.

Dr. Eugene Aksenenko (Institute of Colloid Chemistry and Chemistry of Water, Kiev, Ukraine) and the team leaders Dr. Reinhard Miller (MPIKG Golm, Germany) and Prof. Valentine B. Fainerman (Donetsk Medical University, Ukraine): Providing the software package for modelling the protein adsorption and support.

Alexander Baumgartner (University of Bayreuth): Help with the synthesis of glass A, X-ray measurement of the glasses and hydroxy apatite coatings (particularly Fig. 52).

Dr. Greg Fowler (University of Sheffield, Great Britain): Antibody labelling and fluorescence imaging (particularly Fig. 50).

Nicole Schwenger: Preparation of microtome cuts (particularly Fig. 49)

Further I would like to thank the following colleagues and instrument responsables for their introduction into some measurement techniques and technical assistance:

Dr. Per Rigler (University of Basel, Switzerland): CLSM

Markus Hund, Dr. Violetta Olszowka (University of Bayreuth): AFM

Dr. Markus Drechsler, Dr. Stefan Geimer (University of Bayreuth): TEM, negative staining

Benjamin Gossler, Werner Reichstein (University of Bayreuth/BIMF): SEM

Tobias Mummert (University of Bayreuth): SDS-PAGE

Erklärung

Die vorliegende Arbeit wurde von mir selbständig verfasst und ich habe dabei keine anderen als die angegebenen Hilfsmittel und Quellen benutzt. Ferner habe ich nicht versucht, anderweitig mit oder ohne Erfolg eine Dissertation einzureichen oder mich der Doktorprüfung zu unterziehen.

Bayreuth,

(Günther Jutz)

